ABSTRACT

Title of dissertation: SIMULATION MODELING OF FLIGHT DYNAMICS, CONTROL AND TRAJECTORY OPTIMIZATION OF ROTORCRAFT TOWING SUBMERGED LOADS

Ananth Sridharan, Doctor of Philosophy, 2014

Dissertation directed by: Professor Roberto Celi
Department of Aerospace Engineering

This work presents the mathematical modeling and analysis of helicopters towing submerged loads using long cables for sub-surface object detection when surface-based vessels cannot operate safely. A geometrically exact model of rotating beams is derived, and used to represent both the cable dynamics and rotor blade dynamics. Flight dynamics and trim conditions for an axially flexible straight cable and a curved cable are separately formulated for a general case of helical climbing turns, and used to cross-validate each other. In steady flight, the trim longitudinal dynamics of the submerged load produces down-forces from towed body fins, increasing the apparent weight of the tow system. Cable and towed body drag manifest as increases in the effective equivalent flat-plate area, necessitating excessive nose-down helicopter trim pitch attitudes (-6°) and causing pilot discomfort. Excessive pitch attitudes can be avoided using aft offset of the helicopter tow point, or the deployment of longer cables in combination with pitching fins to regulate towed body

depth. In steady level turning flight, cable and towed body drag result in the submerged load turning with a consistently smaller radius than the helicopter. Depth regulation in turning flight using pitching fins is less effective than in forward flight due to increased cable drag opposing larger down-forces.

Analysis of linearized models showed that the helicopter frequency response to pilot inputs is unaffected by the addition of the cable and towed body above 1 rad/s. The low-frequency response magnitude reduces with increasing hydrodynamic drag on the cable and towed body, and is unaffected by cable structural properties due to over-damped stabilization from hydrodynamics.

The swashplate inputs required to guide the towed body along a "teardrop" shaped trajectory are obtained using a two-stage process. The motions of the tow point that guide the submerged load along the target path are obtained using an optimization process. The system target states are generated based on these tow point motions, and an LQR controller is used to guide the helicopter along *its* target path. Trim rotor inflows from the vortex wake model are obtained at the various equilibrium points used to construct helicopter target states, interpolated and applied as "delta" corrections to the dynamic inflow model. Blade elastic twist has a significant effect on rotor power predictions and the steady hub loads, while flap bending elasticity acts as a vibration absorber to attenuate the oscillatory component of hub rolling and pitching moments.

SIMULATION MODELING OF FLIGHT DYNAMICS, CONTROL AND TRAJECTORY OPTIMIZATION OF ROTORCRAFT TOWING SUBMERGED LOADS

by

Ananth Sridharan

Dissertation submitted to the Faculty of the Graduate School of the
University of Maryland, College Park in partial fulfillment
of the requirements for the degree of
Doctor of Philosophy
2014

Advisory Committee:

Professor Roberto Celi, Chair/Advisor
Alfred Gessow Professor Inderjit Chopra
Minta Martin Professor J. Gordon Leishman
Associate Professor James Baeder
Professor Doron Levy

DEDICATED TO

My parents Mahalakshmi and Sridharan, for all that they gave up so that I could come this far; without their constant support, I would not possess a fraction of the tenacity, confidence, curiosity or sense of humor that I do today.

Acknowledgments

It has been great fun meeting open-minded people from all over the world at UMD, and eye-opening to interact, work with and learn from a truly international community of students and teachers.

First and foremost, I'd like to thank Professors Roberto Celi and Inderjit Chopra for the opportunity to attend graduate school at UMD. They have set high standards for technical proficiency, teaching excellence and level-headed crisis control that I one day hope to meet. They gave me time to grow while constantly encouraging me to expand my thinking process, for which I do not have words to thank them enough. The one quality that I admire the most in my advisor is his extraordinary patience. His vision and faith in my abilities far exceeded my own, and he always saw the way forward when all I could observe was a hazy fog (DVE).

I have enjoyed the many occasions on which I interacted with Prof. Leishman. His constant emphasis on critical thinking and clear communication helped hone my writing skills, especially during the Helicopter Design class, and I look forward to reading his future books and papers.

During the last year of my study, I had the opportunity to perform collaborative work with Dr. Baeder. His office became an unofficial meeting spot for both technical and non-technical conversations, and I wish I could have taken all his classes.

I would also like to thank Professor Doron Levy - his lectures on solving PDEs still stand out as one of the clearest explanations of the weighted residual method.

He went out of his way to be available for my pre-defense on extremely short notice, and I am extremely grateful to him for his time investment.

I have interacted with Dr. V.T. Nagaraj (or simply VT to familiars) on a regular basis. Our common interests in Carnatic music sparked many conversations, and his reminiscences of classical concerts and the quirky antics of some musicians were entertaining to listen to. I have adopted one of his frequently used design mantras - *So What?* - for evaluating many things, both technical and not.

Family and friends played a key role in shaping my attitude throughout. In the interests of being impartial, I do not mention any one name, simply to avoid writing down a hundred more.

I would like to acknowledge financial support from the U.S. Naval Air Research Wing (NAVAIR) and the U.S. Army/Navy/NASA-funded Vertical Lift Research Center of Excellence Program at the Alfred Gessow Rotorcraft Center, UMD for all the projects discussed herein. Mr. Mike Fallon and Ken Kahill of NAVAIR, and Alan Schwartz (Carderock) have given insightful comments and suggestions that motivated the separate chapter on tear-drop maneuvers.

Table of Contents

List of Tables

List of Figures

List of Abbreviations

A	Cross-section area
$\mathbf{A}$, $\mathbf{B}$	System state and control matrices
$\mathbf{C}$, $\mathbf{D}$	System output and feed-through matrix
e_A	Chordwise offset of cross-section CG towards LE from EA
E	Young's modulus, isotropic material
EI	Flexural bending stiffness
$\mathbf{f}$	System of equations
f_{L}	Equivalent flat-plate area of submerged load
f_v	Beam lag bending equation
f_w	Beam flap bending equation
f_ϕ	Beam torsion equation
g	Acceleration due to gravity
$\mathbf{E}$, $\mathbf{F}$, $\mathbf{G}$	Taylor series coefficient matrices for linearization
G	Shear Modulus, isotropic material
$\mathbf{H}$	Transfer function
$H_{w,i}$	Finite element bending shape function
$H_{\phi,i}$	Finite element torsion shape function
$\boldsymbol{i}$, $\boldsymbol{j}$, $\boldsymbol{k}$	Unit vectors along undeformed beam axes
$\boldsymbol{i}'$, $\boldsymbol{j}'$, $\boldsymbol{k}'$	Unit vectors along deformed beam axes
$\boldsymbol{i}_{\mathrm{B}}$, $\boldsymbol{j}_{\mathrm{B}}$, $\boldsymbol{k}_{\mathrm{B}}$	Unit vectors along body-fixed directions
$\boldsymbol{i}_{\mathrm{C}}$, $\boldsymbol{j}_{\mathrm{C}}$, $\boldsymbol{k}_{\mathrm{C}}$	Unit vectors along cable undeformed axes
$\boldsymbol{i}_{\mathrm{G}}$, $\boldsymbol{j}_{\mathrm{G}}$, $\boldsymbol{k}_{\mathrm{G}}$	Unit vectors along earth-fixed directions
$\boldsymbol{i}_{\mathrm{H}}$, $\boldsymbol{j}_{\mathrm{H}}$, $\boldsymbol{k}_{\mathrm{H}}$	Unit vectors along hub non-rotating coordinates
$\boldsymbol{i}_{\mathrm{P}}$, $\boldsymbol{j}_{\mathrm{P}}$, $\boldsymbol{k}_{\mathrm{P}}$	Unit vectors along blade preconed undeformed axes
$\mathbf{I}$	Second mass moment of inertia
J	Polar area moment of inertia
k_{m2}, k_{m3}	Cross-section radii of gyration
$\mathbf{K}$	Feedback gain matrix
L	Airfoil lift
D	Airfoil drag
M	Airfoil pitching moment
m	Beam mass per unit span
M_x, M_y, M_z	Structural moments in deformed axes
$\widetilde{M}_x$, $\widetilde{M}_y$, $\widetilde{M}_z$	Structural moments in undeformed axes
N_b	Number of rotor blades
N_e	Number of beam finite elements
N_m	Number of rotor modes
$\mathbf{p}$	Vector of external forces per unit span in deformed beam axes
$\mathbf{q}$	Vector of external moments per unit span in deformed beam axes
$\mathbf{q}_w$	Vector of beam flap bending nodal degrees of freedom
$\mathbf{q}_v$	Vector of beam lag bending nodal degrees of freedom
$\mathbf{q}_\phi$	Vector of beam torsion nodal degrees of freedom
p_{F}, q_{F}, r_{F}	Rigid body angular velocity components about body axes
$\mathrm{q}_{()}$	Dynamic pressure of component ()

$\mathbf{Q}$	Weighting for states in LQR
r	Non-dimensional coordinate along deformed beam axes
$\mathbf{R}$	Weighting for controls in LQR
R	Beam length (rotor radius)
S_x, S_y, S_z	Structural forces in deformed axes
$\widetilde{S}_x$, $\widetilde{S}_y$, $\widetilde{S}_z$	Structural forces in undeformed axes
$\mathbf{T}_{DU}$	Rotation matrix from undeformed to deformed beam axes
$\mathbf{u}$	Vector of control inputs
U_R, U_T, U_P	Components of flow velocity in blade deformed axes
u_{F}, v_{F}, w_{F}	Rigid body velocity components along body axes
u	Non-dimensional axial fore-shortening
v	Non-dimensional lag displacement
$\mathbf{V}$	Eigenvector matrix
V_∞	Free-stream velocity
V_{tip}	Rotor tip speed
w	Non-dimensional flap displacement
x	Non-dimensional radial position along undeformed beam axis
$\mathbf{y}$	Vector of system states
$(\,)_{\mathrm{F}}$	( ) of the helicopter fuselage
$(\,)_{\mathrm{L}}$	( ) of the submerged load
$(\,)^+$	Spatial derivative along deformed beam axis
$(\,)'$	Spatial derivative along undeformed beam axis
α	Airfoil angle of attack
α_{F}	Fuselage angle of attack
α_s	Shaft aft tilt angle with respect to fuselage
β_{F}	Fuselage sideslip angle
β_s	Shaft lateral tilt with respect to fuselage
δ	Numerical precision for solution convergence
$\Delta X, \Delta Y, \Delta Z$	Separation distance between helicopter and load CG
η_0, ζ_0	Coordinates of a point in the cross-section of an undeformed beam
η, ζ	Coordinates of a point in the cross-section of a deformed beam
ϵ_{ij}, i,j = 1,2,3	Strains
$\epsilon_{\phi,i}$	Beam torsion equation residual
$\epsilon_{v,i}$	Beam flap equation residual
$\epsilon_{w,i}$	Beam lag equation residual
γ	Flight path angle
γ_I	Flow inclination to cable axis
$\gamma_{w,i}$	Beam bending trial function
$\gamma_{\phi,i}$	Beam torsion trial function
$\boldsymbol{\eta}$	Vector of generalized displacements for a beam
$\boldsymbol{\epsilon}$	Vector of residuals
$\boldsymbol{\kappa}$	Skew-symmetric curvature matrix
$\kappa_1, \kappa_2, \kappa_3$	Torsion, flap bending and lag bending curvatures
λ	Rotor inflow ratio
ν	Poisson's ratio

Ω	Rotor rotational speed
ϕ_{F},θ_{F},ψ_{F}	Euler roll, pitch and yaw angles of fuselage
ϕ_{L},θ_{L},ψ_{L}	Euler roll, pitch and yaw angles of submerged load
ψ	Azimuth angle of blade 1
$\psi_{\mathrm{b,i}}$	Azimuth mounting offset angle of blade i with respect to blade 1
ϕ	Beam elastic twist
ρ	Density of air
ρ_f	Density of water
σ_{ij}, i,j = 1,2,3	Stress components
$\boldsymbol{\tau}_c, \boldsymbol{\tau}_s$	Time constants for dynamic inflow
θ_t	Beam pre-twist
$\theta_0, \theta_{1c}, \theta_{1s}$	Main rotor swashplate collective and cyclic pitch controls
θ_{TR}	Tail rotor collective pitch control
ξ	Spherical angle of flight path
ξ_1, β_1, θ_1	Euler angles used to construct the $\mathbf{T}_{DU}$ matrix

BVI	Blade-Vortex Interaction
CG	Center of Gravity
DTRC	David Taylor Research Center
EA	Elastic Axis
LE	Leading Edge
ODE	Ordinary Differential Equation
PDE	Partial Differential Equation

1 Introduction

The rotorcraft mission that is the focus of this work is to tow an underwater object, by attaching it to a helicopter with long cables, for sub-surface object detection. Using an aerial platform for tow operations continues to be explored as a viable alternative to traditional ship-based tow procedures (Refs. [1], [2], [3], [4], [5]). The primary application of such a configuration is in shallow water and locations which may have mines, where surface-based vessels are vulnerable to damage.

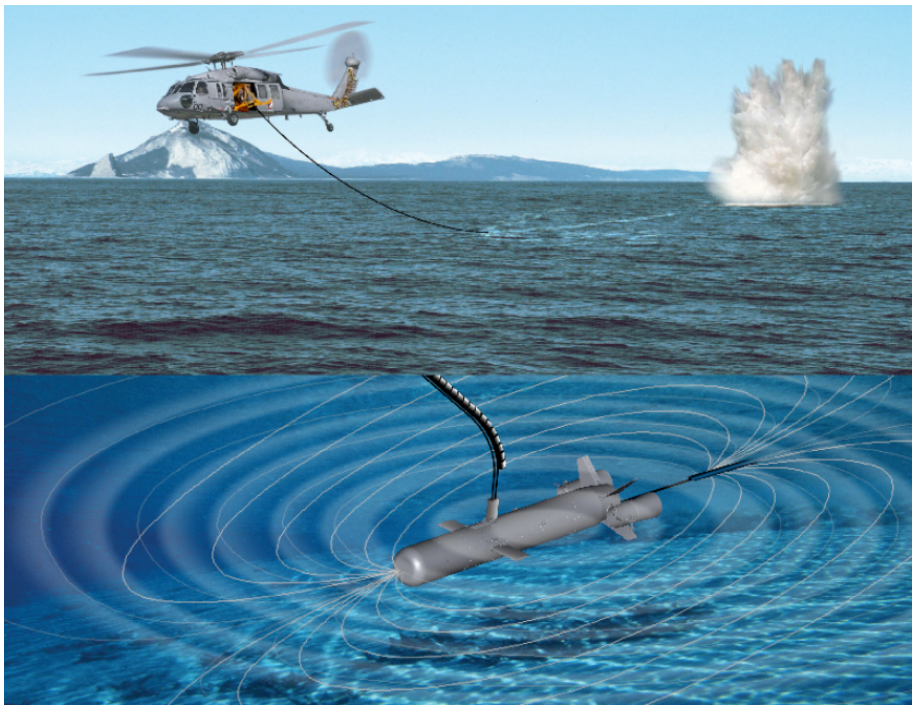

Figure 1.1: The Helicopter-based Tow Mission For Submerged Loads - from Ref. [6]

This application is unique in comparison to other roles that rotorcraft have come to occupy over the years, and presents its own specific challenges to overcome. The towed body is fitted with pitching hydrofoils to maintain a specified depth below the water surface. The interaction of depth control system and hydrodynamics of the load, dynamics of the helicopter rotor and the long cable lengths involved (350-500 ft) may trigger physical phenomena that pose a risk to flight safety. Further, the large hydrodynamic drag on the submerged components (including the cable) results in increased engine power requirements and large nose-down trim pitch attitudes, resulting in inefficient operation, reduced life and pilot discomfort.

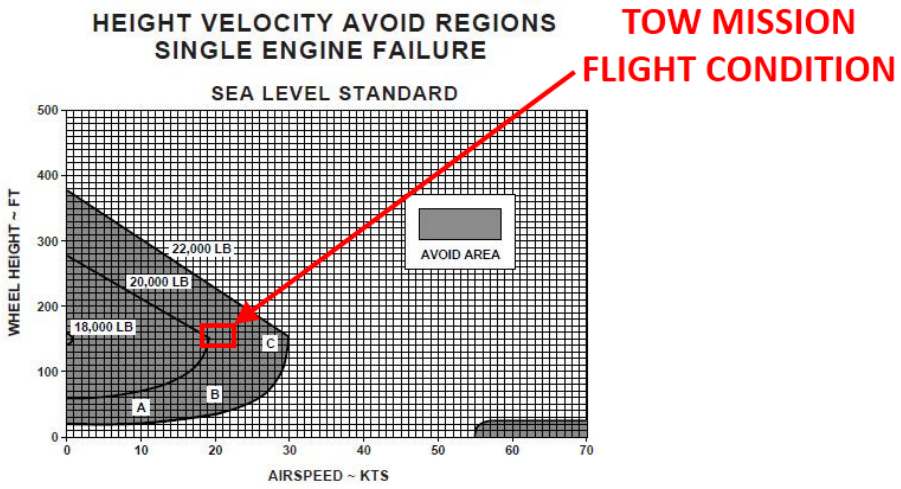

Figure 1.2: Height-Velocity Curve : UH-60 BlackHawk (Ref. [7])

The tow mission is typically executed at an altitude of 150 ft at 20-25 knots. This flight condition is on the verge of violating the height-velocity curve restrictions (known as the "dead-man curve") shown in Fig. 1.2. The helicopter altitude is constrained from increasing beyond a reasonable limit by cable weight and engine power restrictions, and from decreasing by safety of flight issues. The vehicle possesses insufficient altitude and airspeed to safely execute autorotation following

engine failure, and operates on a knife-edge balancing safety and efficiency. Through careful selection of design parameters and control co-ordination techniques, the system efficiency can be increased and adverse effects of dynamic interactions can be alleviated or avoided entirely.

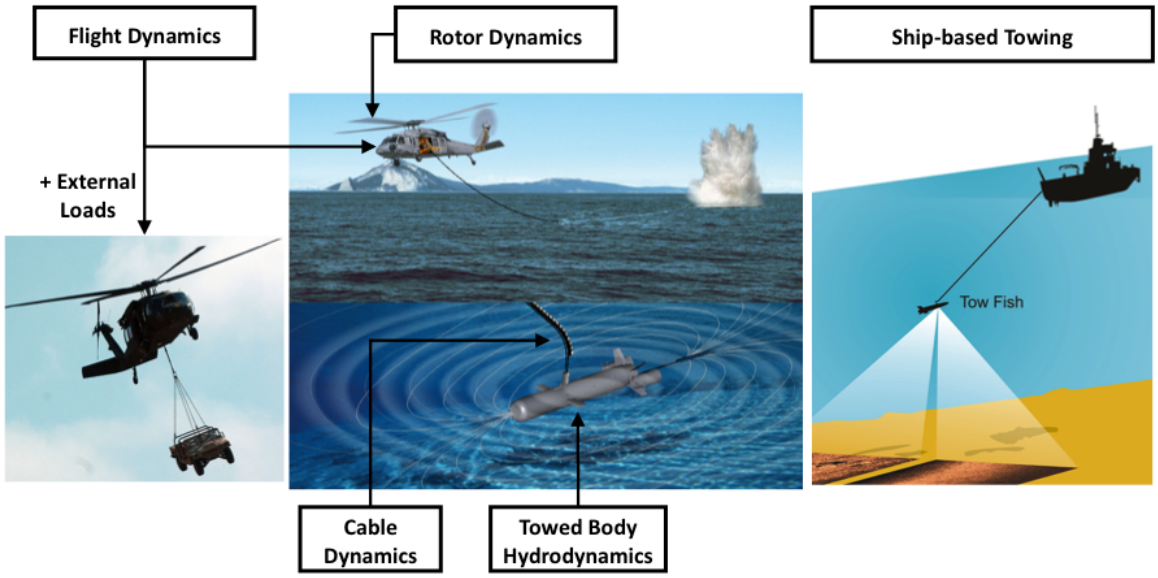

Figure 1.3: Tow System Components and Related Applications (Refs. [6], [8], [9])

The tow mission brings together aspects of two different fields. The first field is helicopter flight, in which the relevant areas of study are rotor dynamics, flight dynamics and sling load operations. The second area is sub-surface sensing from auxiliary devices towed from ships using long cables. The dominant physical phenomena in this application are cable flexibility, hydrodynamics of the towed body and fluid forces on the cable. These areas of interest are illustrated in Fig. 1.3. Prior work in each of these areas has allowed the scientific community to identify reliable analytical tools to model the physical phenomena of interest. While

the building blocks for the helicopter tow mission have been individually studied, certain assumptions were made, tailored to the specific systems under consideration, that limit their direct applicability to the present problem. The next section will summarize the state-of-the-art in four key areas :

- **Rotor Dynamics**
- **Helicopter Flight Dynamics**
- **Sling Load Operations**
- **Cable and Towed Body Modeling**

1.1 Previous Work in Rotor Dynamics Modeling

Over the last few decades, significant advances have been made in simulation modeling of rotor blade structures and aerodynamics. The general term used for detailed rotor dynamics modeling is *Comprehensive Analysis*, which refers to a class of techniques that encompass rotor trim, time marching simulations and stability analysis. The modeling of most problems in structural dynamics can be broken down into two components : the structural model, which is concerned with the reaction forces in the flexible material, and the forcing model, that deals with inertia, gravity and aerodynamics.

The primary contributions to the so-called "external" loads acting on the rotor blade are the inertial forces and aerodynamic forces. The inertial loads can be obtained from the motions of the structure using Newton's II law, as given in

Chapter 2 for Euler-Bernoulli beams, and are common to all manner of structures. The aerodynamic models are specific to rotors and blades, and are discussed in the following section.

Aerodynamic forces on a rotor blade are generated by virtue of its motion relative to the free-stream flow. These motions include blade rotation, pitch control inputs, geometric and elastic twist, flap/lag transverse motions, hub translations (forward flight and climb/descent) and hub rotations due to fuselage pitch, roll and yaw. The airload distributions generated by the rotor blades give rise to sheets of trailed and shed vorticity that roll up into discrete tip vortices. The various elements of vorticity in the flowfield are responsible for the induced inflow over the rotor disk. **The problems of quantifying the induced velocity in the flowfield and structural motions are inherently coupled, and iterative methods are employed to obtain solutions that yield flowfields that are consistent with the structural response and vice versa**.

Rotor Blade Structures

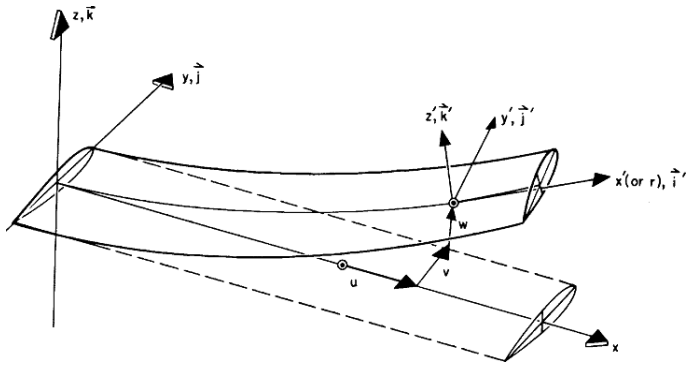

Figure 1.4: Beam Model of an Elastic Rotor Blade - Ref. [10]

Most rotor blades are slender structures (radius to chord ratios over 10) and have been successfully modeled as Euler-Bernoulli beams with elastic flap, lag and torsion (Refs. [10], [11], [12], [13]). Initial analyses invoked small-angle assumptions based on ordering schemes to reduce the number of terms in analytical expansions (Ref. [10]). Variants of the beam theory were derived (Ref. [11]) to accommodate so-called "moderate rotations" and partial numerical formulations of the beam equations. Further systematic efforts (Refs. [14], [15]) allowed for lifting the various assumptions made during the formulation of the beam equations, and expanded the generality of the analysis. These "implicit formulations" were developed to express the governing beam equations in state-space form using a numerical representation, which is extremely useful for stability analysis and the circumvention of ordering schemes. However, as highlighted in Ref. [15], the inherent "implicitness" of the formulation does not guarantee the accommodation of large deflections. A survey of the beam theories used for rotorcraft analyses may be found in Ref. [16].

Beam theories that make no assumptions regarding the relative magnitudes of various rotations and displacements, or those that place limitations only on the maximum strains in the material, are referred to as geometrically exact representations (Refs. [17], [18]). With the advent of these improved formulations, they quickly gained a place as tools of choice in most rotorcraft comprehensive analyses.

Successful validation with flight tests and wind-tunnel tests have demonstrated that, for the purposes of predicting rotor performance and vibrations (Refs. [19], [20], [21]), beam models are sufficient representations of blade elasticity. Examples of Comprehensive Analyses that use beam models include CAMRAD II (Ref. [22]),

RCAS (Ref. [23]), UMARC (Ref. [19]), UMARC II (Ref. [21]) and KTRAN-RDYNE-GENHEL (Sikorsky). In the last analysis, KTRAN (Ref. [24]) models structural dynamics, RDYNE (Ref. [25]) is used for structural/aerodynamics and GENHEL (Ref. [26]) is used for the vehicle flight dynamics. In addition to the examples mentioned here, various organizations such as Westland, Bell and Eurocopter use their in-house codes for performance and vibration analysis.

Rotor Aerodynamics

The simplest wake model for a rotor is obtained from momentum theory, where the rotor disk is treated as a pressure discontinuity and the induced inflow is assumed to be uniform. For steady axial flight, the Blade Element Momentum Theory (Ref. [27]) can be used to impose fewer assumptions on the spanwise distribution of the inflow, but is restricted to hover, climb and windmilling descent with a well-defined steady wake boundary.

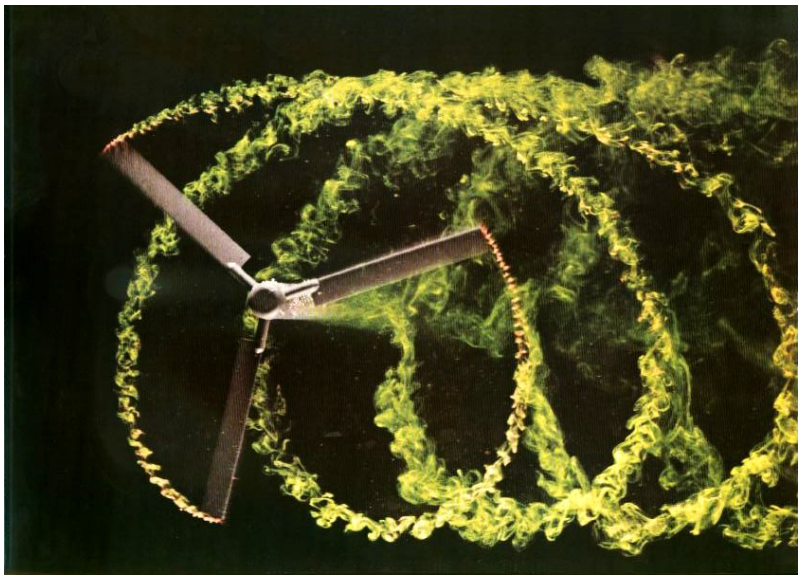

Figure 1.5: Visualization of Tip Vortices - Ref. [28]

As the rotor transitions into forward flight, the discrete tip vortices interact strongly with each other between advance ratios of 0 and 0.1 and the inflow distribution is non-uniform. At slightly higher advance ratios (0.15 or higher), the rotor wake is swept away by the free-stream flow, and the inflow distribution over the disk can be approximated using a constant component superimposed with a radially linear longitudinal and lateral skew (Refs. [27], [29]). These models were extended to include additional variations in spanwise and azimuthal distributions of induced inflow, resulting in a generalized finite-state model based on unsteady potential flow theory (Ref. [30]). The reduced-order wake models relate the inflow distribution over the rotor disk to the aerodynamic load distributions along the span and around the azimuth based on assumed shape functions, and may be adequate for aeroelastic stability analysis. However, the *quantitative* accuracy of such models comes into question during the so-called "transition" flight regimes ($\mu \leqslant 0.1$) and certain stages of descending flight. In these operating conditions, non-uniformities in the rotor inflow distribution are significant, and the assumptions used to construct these reduced-order models are violated by the nature of the resulting wake geometry.

With improvements in computational power, it became possible to utilize vortex models of the rotor wake. These refined models are used to represent the rotor wake using the fundamental physical elements, i.e. individual vortices, that comprise the flowfield. A comprehensive survey of vortex wake methodologies may be found in the literature (Refs. [27] and [19]), and the milestones related to time-marching wake are summarized here.

Initial vortex wake models were based on experimental measurements of wake geometry (Refs. [31], [32]), which resulted in significant improvements in rotor hover performance predictions. A relaxation wake model (Ref. [33]) was used to obtain periodic (steady-state) solutions for the wake geometry, valid for a single tip vortex corresponding to a bound circulation distribution with one maximum. These works were refined (Ref. [34]) and extended to forward flight (Ref. [35]), and formed the basis of time-marching wake algorithms that accommodate multiple rotors (Ref. [36]), multiple trailers and associated local maxima in the bound circulation distribution (Ref. [37]) and dissimilar blades (Ref. [38]). These time marching vortex wake models are necessary for the analysis of unsteady flight conditions (i.e. maneuvers), and may also be used in steady flight conditions.

As a result of concerted efforts by various researchers, these models have evolved as useful tools that provide an accurate representation of the flowfield, and can be coupled to both the rotor dynamics and the vehicle flight dynamics.

1.2 Previous Work in Flight Dynamic Modeling

The field of helicopter flight dynamics is concerned with understanding the aerodynamic and structural couplings between rotor motion, airframe translations and rotations, and the time-varying flowfield that manifests as a result of these interactions. Over the years, commercial software developers, helicopter manufacturers, academic institutions and research labs have developed flight dynamic analyses of increasing fidelity levels. A detailed review of these tools may be found in Refs. [39]

and [20], and is summarized here for completeness. All these analyses can perform trim and time integration to simulate a maneuver in response to prescribed pilot inputs. With the exception of CHARM, the other simulations can also obtain linearized dynamic models for stability analysis.

The final entry in Table 1.1 has been developed starting from the GENHEL model (Ref. [26]) over the years at the University of Maryland. The original GENHEL model was augmented with a dynamic inflow model and the ODEs were recast into state-space form in Ref. [40]. Ref. [41] details the implementation of a fully numerical structural formulation for elastic blades with coupled flap-lag-torsion dynamics, modal reduction and the addition of a finite-state wake model (Ref. [30]). In Ref. [39], the structural/flight dynamics were coupled with a vortex wake model (Ref. [42]), Keller's extended momentum theory was implemented for inflow computations and a quasi-steady forcing model was introduced for blade section aerodynamics. Aerodynamic modeling refinements were found to be necessary to improve prediction of the vehicle off-axis response. During the work of Ref. [43], the ODEs were expressed in implicit form for improved modularity. The flight dynamics were coupled with the time marching vortex wake of Ref. [44] in Ref. [20] for trim and time marching, and serves as a starting point for the present analysis.

(*The details of FLIGHTLAB are from Ref. [46], last updated 15 Feb 2008)

Table 1.1: Rotorcraft Flight Dynamic Models

Name	Fuselage	Rotor	Wake
CAMRAD II	Rigid body	w,v,ϕ	Johnson Wake (Ref. [37])
CHARM	Rigid body	w,v,ϕ,u	Fast vortex (Ref. [45])
COPTER	Flexible	w,v,ϕ	Scully vortex wake
FLIGHTLAB	Rigid body	w,v,uncoupled ϕ	3-state Dynamic Inflow
HOST	Rigid body	Elastic	Pitt-Peters
RCAS	Flexible	w,v,ϕ	Peters-He, Vortex wake
UMARC	Flexible	u,v,w,ϕ	Pitt-Peters, Vortex wake
HeliUM	**Rigid body**	w,v,ϕ	**Peters-He, Vortex Wake**

1.3 Previous Work in Sling Load Modeling

Helicopters present an attractive option for short-haul cargo transport, especially for ship-to-ship transfer or in areas where wheeled or tracked vehicles cannot progress due to the nature of the terrain (e.g. logging operations and emergency rescues in mountainous regions). To that end, they are fitted with cargo hooks for lifting external loads using cables. The addition of a pendulous mass beneath the helicopter affects the system dynamics (Ref. [47]), increases pilot workload (especially for large rotorcraft - Ref. [48]) and sometimes imposes stability-based restrictions on the maximum flight speeds (Ref. [49]). Subsequent efforts focused on modeling, predicting and alleviating the aerodynamics-induced instabilities (Ref. [50]) and understanding the Handling Qualities (HQ) requirements for helicopters with sling

loads (Refs. [51]).

Flight-test based HQ ratings for isolated helicopters have been found to correlate well with frequency-domain characteristics of the fuselage on-axis attitude responses. However, the addition of an external load modifies the system dynamics, with increasing load mass (in relation to helicopter mass) and long sling cables having pronounced effects on the on-axis response. Previous studies (e.g. Refs. [52], [53]) have identified a dipole signature (closely spaced pole-zero pair) in the phase and reduction in magnitude in the vicinity of the natural pendulum frequency of the load, resulting in a "double crossing" of the magnitude and phase bandwidth cutoffs. It was found in Ref. [53] that bandwidth parameters obtained from the aircraft translational rate response were found to correlate well with trends in HQ ratings obtained from flight tests. The work of Refs. [51] and [54] collectively highlighted two significant findings:

- The metrics formulated in Ref. [53] based on vehicle translational rate response did not completely correlate with flight test results
- Another criterion based on a bandwidth and a magnitude deformation parameter of the vehicle attitude response correlated well with the HQ ratings from flight tests

Given the large hydrodynamic forces acting on the towed body, the total force exerted by the towed body on the helicopter is similar in magnitude to that experienced when carrying a heavy sling load ($m_{load} \geqslant 0.2\ m_{helo}$). Therefore, frequency response criteria pertaining to sling loads may yield additional insight into the Han-

dling Qualities of the helicopter tow system, discussed in Chapter 6.

Payload Delivery Systems using Fixed-Wing Aircraft

Two-body problems joined by a curved cable are of practical interest to airborne delivery systems using fixed-wing aircraft. In these applications, the cargo (payload) is suspended from the aircraft using a long tow cable and the pilot maintains a level circular hold pattern (steady level turn). The cumulative effects of weight, aerodynamic drag and long cables result in the payload assuming a steady circular path of extremely small turn radius, i.e. it is near-stationary and may be safely detached. When the turn radius is sufficiently small, the delivery is termed "pin-point". This problem was studied in Ref. [55], and an interesting trend was found - that the nature of the solution was multi-valued, i.e. there are multiple payload paths for the same aircraft turn rate. These multivalued solution regions are intricately linked to the regions of pin-point deliveries. The cable was assumed to act as an inextensible catenary, and the forces on the payload considered were steady aerodynamic drag and gravity.

Reference [56] also investigates the aforementioned problem using a flexible cable modeled with finite elements. "Jump" discontinuities and regions of multivalued solutions were observed to occur for specific combinations of aircraft turn radius and cable length. Dynamic instabilities based on linearized analyses were also observed. Experimental measurements on circularly towed aerial tethers were recorded in Ref. [57], while simulation modeling and optimal control is performed

in Ref. [58].

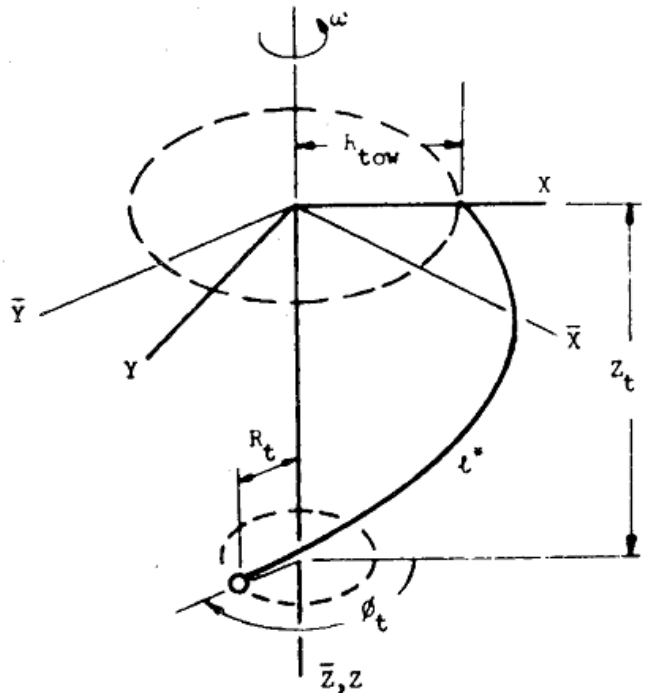

Figure 1.6: Schematic of Aircraft-based Cargo Delivery - Ref. [56]

Reference [59] discusses dynamic modeling and control of a small maneuverable flight vehicle towed by a fixed-wing aircraft. The cable is modeled using a multibody formulation with multiple straight-line segments. Nonlinear control laws using dynamic inversion are formulated in Ref. [60] for a maneuverable towed target, and optimal control of a similar system is studied in Ref. [61].

Helicopters Towing Hydroplaning and Submerged Loads

Reference [62] analyzes towing a sea pallet fitted with hydrofoils using a HSS-2 helicopter, and addresses steady-state performance analysis. Significant power savings may be obtained by allowing the payload to float on the water surface on a hydroplaning sled, and towing the sled using a helicopter. Using FlightLAB (Ref. [46])

to model the helicopter dynamics, a lumped-mass model of the cable and a rigid-body model of the towed body with table-lookup hydrodynamics for quasi-steady forces and moments, Ref. [63] represents the most relevant comprehensive analytical work for the rotorcraft tow mission. Trim and OEI conditions were analyzed for the tow system. The location of the cable attachment point on the helicopter was also found to play an important for speed stability (longitudinal static stability).

Reference [64] documents flight tests of a U.S. Navy H-53 helicopter towing a floating oil-spill containment barrier. Large transient cable forces are attributed to vortex shedding. By choosing cables with cross-sections of different dimensions, the tow ropes were effectively used as vibration absorbers to improve pilot comfort. In Ref. [65], the development of a hydroplaning hull sled for delivery of pollution response equipment is discussed. Payload transport was demonstrated for an HH-3F helicopter, initially using the (more powerful) Navy RH-53 as a test platform to verify the behavior of the sled. A maximum speed of 53 knots was achieved for the the HH-3F helicopter. Reference [66] discusses systematic development of tow procedures through flight tests of a hydroplaning body using an HH-3F helicopter. The helicopter trim attitude is increasingly nose-down with higher speeds (less than -6 deg), leading to pilot fatigue. **The challenges of operating rotorcraft with submerged loads extend beyond overcoming dynamic interactions and human factors must also be considered**.

1.4 Previous Work in Cable and Towed Body Modeling

Cable modeling has received considerable attention in the field of Ocean Engineering due to its use in underwater mooring and tow lines. A floating platform (ship) is used to tow single or multiple cables for applications ranging from fishing to submarine detection using sonar. Due to the relative masses of the tow platform and the towed cable, two-way couplings are usually neglected, and the motion of the ship is often imposed as a kinematic constraint (boundary condition) for the root end of the cable. Initial efforts focused on modeling the cable as multiply jointed rigid straight-line segments. This methodology captures global curvature effects without resorting to (at the time) computationally expensive simulations (Ref. [67]).

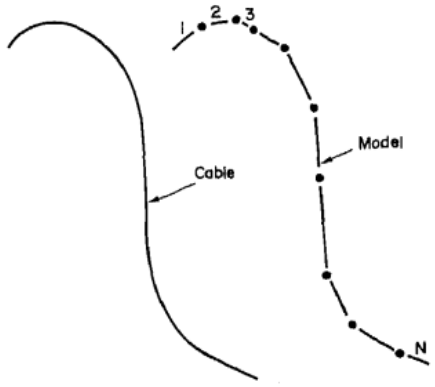

Figure 1.7: Cable Model with Multiple Jointed Links - Ref. [68]

Reference [69] details the modeling of cables using the approach mentioned above, and showed that transitioning from straight-line tow to circular motion and back resulted in large differences in turn radii for the tow point and towed body. These differences were found to be larger for increased tow speed, and that transient drag forces played an important role in determining the depth of the towed body.

In Ref. [68], results from these "rigid-link" models were compared to analytical solutions of the PDEs governing the motion of a catenary with a concentrated tip mass. The natural frequencies showed excellent agreement with analytical solutions with increasing number of elements. However, the transient behavior predictions (in air) did not yield satisfactory solutions in comparison to analytical results, but these were attributed to small-angle assumptions used to obtain the analytical solution. Comparisons with experimental results in a water tank were also presented which showed overall good agreement. A versatile variant of this model was formulated in Ref. [70] to accommodate multiple cables of dynamically changing length.

One shortcoming of these rigid-link models is that they ignore the cable flexural stiffness and invariably exhibit slope discontinuities, which play an important role in determining the variation of cable hydrodynamic loading as a function of the flow incidence angle (Ref. [71]). These inaccuracies diminish with an increasing number of segments, but still persist as an inherent part of the approach.

Reference [72] discusses the modeling of three-dimensional motion of a towed system under steady conditions, neglecting cable elastic torsion, bending resistance, side forces, added mass, inertial loads and axial elongation. A conservative estimate using parameters specific to a particular tow system is made to justify the dropping of various terms in the governing equations, and a lumped parameter approach is adopted for the analysis. Since inertial loads were dropped, only steady-state configurations can be obtained.

Reference [73] adopts an approach called "the method of lines" to solve the governing equations, similar to that in Ref. [74]. This analysis accounted for cable

inertia but neglected flexural stiffness of the cable. A comparison with experiments revealed that while the cable positions were representative, the errors in trail angle and depth were of the order of 5-10% of the cable length. The simulation consistently over-predicted the sink rate of the cable. The transient peaks in the tension at the fixed point showed similar trends.

In Ref. [75], the numerical solution scheme of Ref. [76] was improved to solve the governing equations using a finite-difference approach. Comparisons between the analyses and with experimental data showed good agreement.

Reference [77] demonstrated the use of a finite element method to model the inherent curvature in the tow cable. The PDEs were reduced to ODEs (similar to the treatment of rotor blades) and an ODE solver (Ref. [78]) tailored for stiff problems was used to obtain numerical solutions. This effort was among the first to address problems in tow cable dynamics using standardized methods and acceptable numerical errors. Further, the differences in experimental errors associated with at-sea testing vs. controlled laboratory testing were noted to govern the accuracy of measurements.

Reference [79] presents a finite-element based approach for modeling the cable dynamics of a deep-sea ROV (Remotely Operated Vehicle) system. Each element is modeled with axial extension at the end nodes, with linear shape functions. This model was developed for studying snap loads in rough seas where the vertical motions of the ship cause alternate tensing and slackening of the cable. Comparisons with test data showed good agreement, especially when including refined hydrodynamic forcing on the cable due to the wake of the cage.

The fluid-structure coupling problem for cables is addressed in Ref. [80]. A finite-difference based structural discretization and solutions of the governing PDEs is presented, together with verification and validation of the formulation was presented. The governing equations were derived neglecting the flexural stiffness terms, and buckling effects are therefore absent.

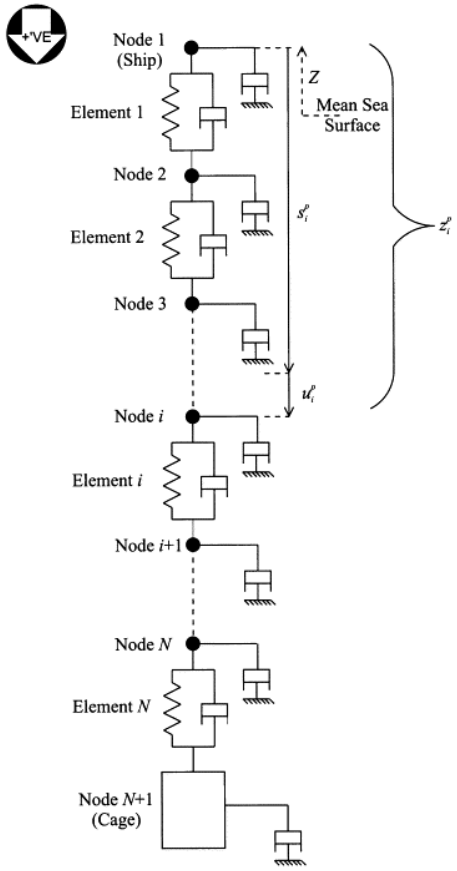

Figure 1.8: Axially Extensible Cable Model of Ref. [79]

A cable model is developed in Ref. [81] that accounts for flexural stiffness contributions to the governing equations based on a simplified beam assumption. This model was improved in Ref. [82] to include nonlinear stress-strain relationships and arbitrarily large rotations, this avoiding the singularities associated with the Euler rotation sequence. This model is used with finite-difference spatial discretization

and various time marching schemes to study the transient behavior of the cable, along with simulations of cable break in Ref. [83]. Reference [84] present an investigation of cable and towed-body response under transient conditions and water currents, for a fixed tow vehicle trajectory. For the large cable length considered (4000 m), the turn radius of the submerged body is consistently smaller than that of the tow vehicle, and the separation between the two increases with the turn rate of the platform.

Cable Hydrodynamic Characteristics

A concise description of the dominant flow phenomena around submerged cables, together with experimental data is given in Ref. [85], the key conclusions of which are summarized below.

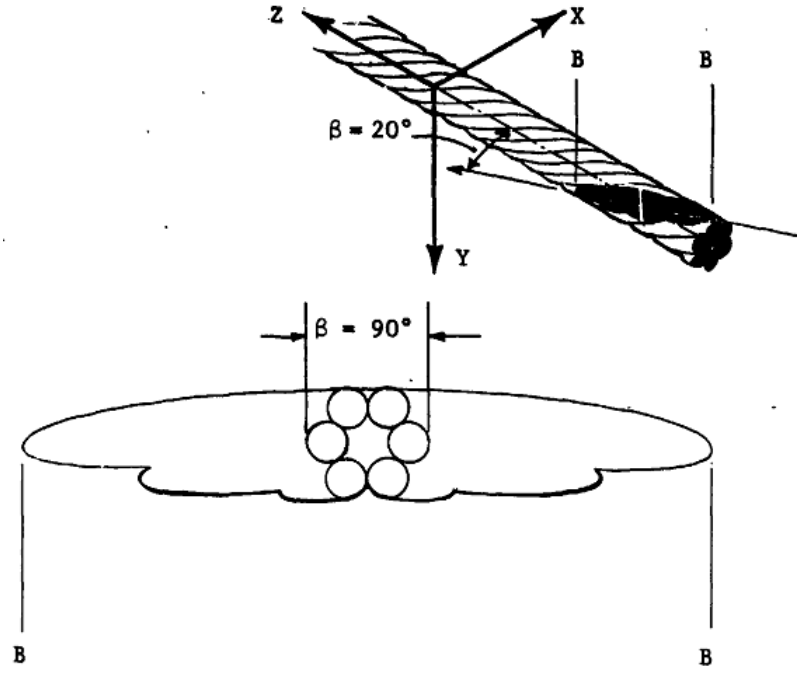

Figure 1.9: Tow Cable Cross-Section - Ref. [85]

Tow cables are constructed from multiple strands that are wound around each other, shown in Fig. 1.9. When hydrodynamic fairings are not used, the resulting outer shape is not symmetric, resulting in a steady non-zero lift force in addition to steady drag. Unsteady flow separation on the upper and lower portions of the rear of the cross-section, known as vortex shedding, creates fluctuating lift and drag forces on the cross-section. This shedding may be symmetric or asymmetric depending on the Reynolds number, as shown in Fig. 1.10.

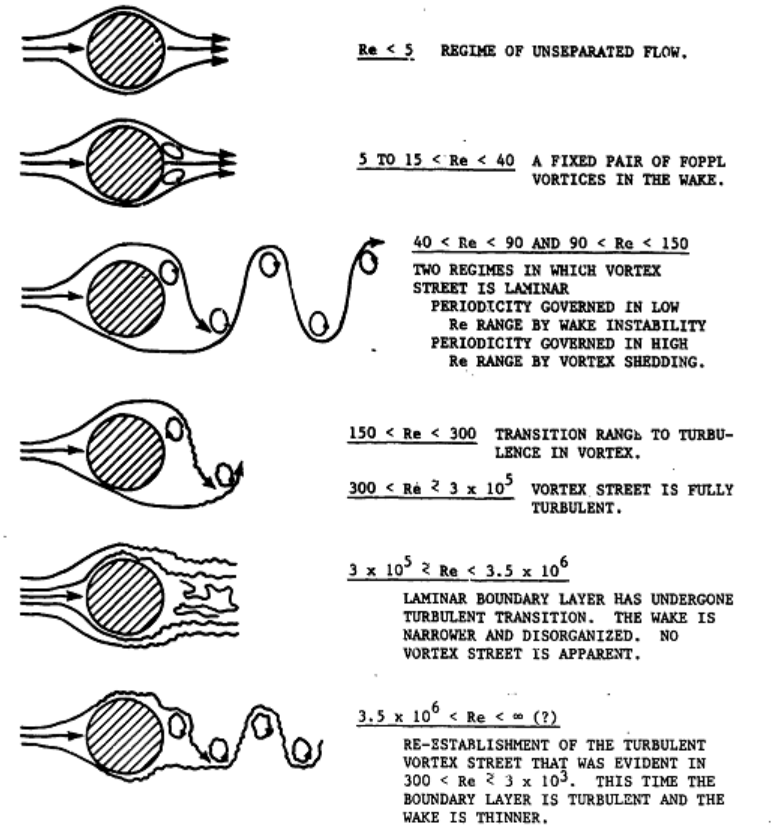

Figure 1.10: Flow Around Circular Cylinders at Various Reynolds Numbers - Ref. [85]

In the present investigations, the target tow speed is 25 knots. For a cable diameter of 0.025 m, the Reynolds number in water is 3.1×10^5, where laminar to

turbulent transition of the flow in the cable boundary layer is incipient, as shown in Fig. 1.11 for a circular cylinder with its axis normal to the flow.

The Independence Principle states that the fluid dynamic properties of a yawed cylinder are governed by the normal component of the flow. Therefore, metrics such as the Reynolds number and Strouhal number may be appropriately modified to use the flow component normal to the cable axis.

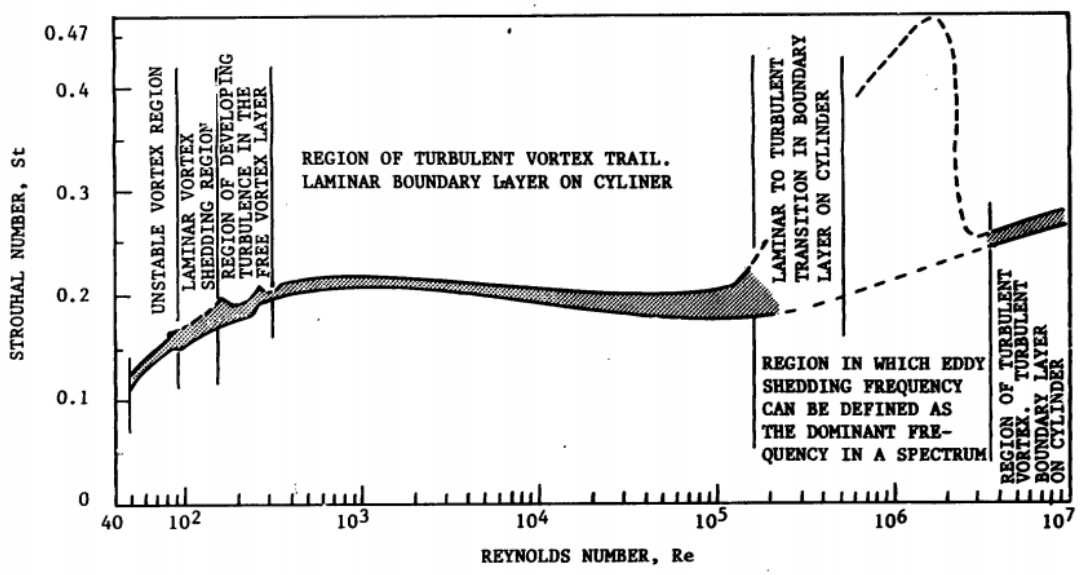

Figure 1.11: Strouhal Number for a Circular Cable - Ref. [85]

The motion of the cable in response to unsteady loads induced by vortex shedding is labeled **strumming**, which consists of one cycle normal to the flow and two cycles in line with the flow. Lock-in phenomena may also occur when the natural frequencies of the cable are close to the vortex shedding frequency. During lock-in vibrations, the vortex shedding frequency of the cable is modified by the structural motions, resulting in a larger resonance band, extending from 75-125% of the original natural frequency.

Experimental measurements were also obtained in Ref. [85] to determine the variation of cable hydrodynamic forces at various flow inclinations. Based on the data, a normalized hydrodynamic loading function is proposed, of the form

$$\begin{aligned} f_N &= \frac{F_N(\beta, Re)}{R(Re)} \\ f_T &= \frac{F_T(\beta, Re)}{R(Re)} \\ f_L &= \frac{F'_L(\beta, Re)}{R(Re)} \end{aligned}$$

The subscripts N,T,L represent the normal, tangential (along cable axis) and lift forces per unit span acting on the cable. $R(Re)$ represents the drag force per unit span for a cable with its axis perpendicular to the flow ($\beta = 90°$) and F'_L is the maximum lift force per unit span. Re is the Reynolds number based on diameter and β is the inclination angle between the flow direction and the cable axis. The advantage of this normalized representation is that at a given speed (Reynolds number), the force coefficients are dependent only on the inclination angle β. The variation of each of these force coefficients F_N, f_T and F_R are discussed below.

Normal Force

The normal drag coefficient of circular cylinders is initially sensitive to Reynolds numbers from 0 to 10^4, and nominally constant above 10^4 up to turbulent transition at Re=3×10^5. The measurements of Ref. [85] indicate that for stranded cables, normal force sensitivity to Reynolds numbers extends up to 6×10^4. Since the tow mission of interest (for a 1-inch cable at 25 knots inclined at 45° to the flow) has an operating Reynolds number of 2×10^5, the effects of Reynolds number on this

force are not considered to be significant. The tests of Ref. [71] indicated very small changes in normal force with Reynolds number above 10^4.

The variation of normal loading with flow inclination is given by

$$f_N(\beta) \quad = \quad A_0 + A_1 \cos\beta + B_1 \sin\beta + A_2 \cos 2\beta + B_2 \sin 2\beta$$

This representation was independently determined by Ref. [71] based on tow tests conducted using ships. Ref. [85] suggests various coefficients that are specific to each cable tested. However, Ref. [71] determined a common functional form for two different cables (shown in Fig. 1.12 using ϕ instead of β along the x-axis), given by

$$f_N(\beta) \quad = \quad -0.424 + 0.869 \cos\beta + 0.979 \sin\beta - 0.445 \cos 2\beta - 434 \sin 2\beta$$

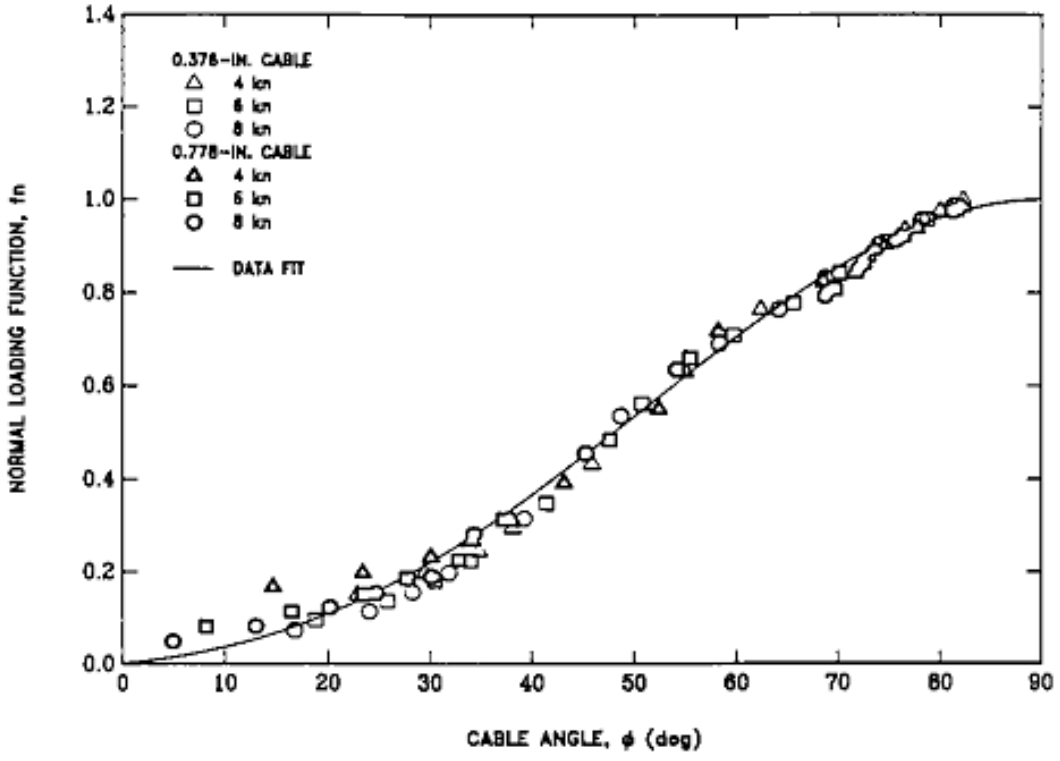

Figure 1.12: Normal Loading Function - Ref. [71]

Lift Force

Measurements of the steady lift force acting on a cable with its axis normal to the flow direction showed scatter of the order of the measured value. Further, attempts to fit similar loading functions for the lift force variation with flow inclination resulted in significant error. The average lift force was found to be 5% or smaller in comparison to the normal force. With increasing Reynolds number, the normal force coefficients decreased rapidly, dropping to as much as 0.05 based on the cable diameter and normal flow velocity. With the presence of hydrodynamic fairings, this lift force (at zero sideslip) will vanish, and is ignored in the present analysis.

Tangential Force

The tangential force, primarily a result of viscous forces on the cable surface, was not measured in Ref. [85]. Ref. [71] estimated a constant value of 0.0249 with respect to the cable diameter and total flow speed, using data collected from ship-based tow tests and a static catenary analysis program at the David Taylor Research Center (DTRC).

Towed Body Modeling

The submerged load (underwater sensor) is treated as a rigid body with 6DOF motions. The towed bodies of interest are streamlined to reduce drag, and fitted with hydrofoil surfaces to enable maneuvering as shown in Fig. 1.13. The hydrody-

namic forces on the hull, hydrodynamic depressors and aft tailplanes are modeled component-wise and added together, assuming negligible interference effects.

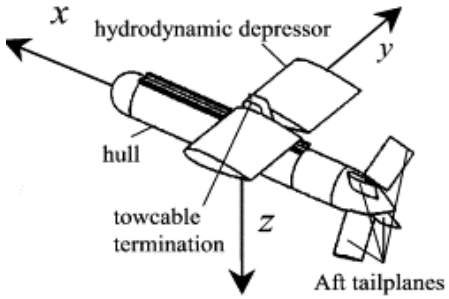

Figure 1.13: Typical Submerged Loads - from Ref. [86]

The hydrodynamic forces on each of these components is computed using experimental data (in the case of bluff bodies) or semi-empirical models (for the hydrofoils) based on the flow velocities and orientations at a reference point. Added mass effects (also known as virtual mass) are taken into account when considering unsteady motions by augmenting the inertial loads with acceleration-dependent hydrodynamic forces. These virtual mass forces are based on experimental data for bluff bodies or unsteady thin airfoil theory for lifting surfaces.

The approach outlined above has been used almost universally for modeling towed body dynamics (e.g. Ref. [67]). Research on underwater towed bodies has primarily focused on surface-based platforms, where two-way interactions are negligible. In recent work, a dynamical model and control strategy for an underwater vehicle towed by a *semi-submersible* is formulated in Ref. [87]. Two-way couplings are considered between the bodies at either end of a tow cable that is modeled using rigid jointed sections, and validation of the same is shown in Ref. [88]. Hydrodynamic lift and drag, as well as added mass of the two vehicles are accounted for in

a component-wise manner. Using pitching fins, depth control is achieved with PID feedback, and turns by using proportional rudder feedback based on heading errors to target way points. The turn maneuver simulations in Ref. [88] also demonstrated that the two bodies did not turn with the same radius.

Modeling Deficiencies

- The use of independent controls for depth and heading may be sufficient when both the tow platform and the towed body are immersed in water, where damping is significant. For aerial platforms (rotorcraft), such an assumption cannot be made. The bare airframe (open-loop) dynamics are unstable at low speeds, couplings are non-negligible and off-axis responses are significant.

- Till date, Ref. [82] is the most comprehensive cable model that accounts for flexural stiffness contributions and material non-linearities. However, the governing equations have been derived for a circular cross-section, assuming no structural or inertial cross-couplings. Further, the original PDEs are integrated numerically, and not available in state-space form for stability analysis.

- Previous work (Ref. [63]) used dynamic inflow at model the rotor wake at low advance ratios (μ=0.06), which may yield quantitatively inaccurate predictions of rotor power.

A deficiency exists in state-of-the-art simulation modeling of the helicopter tow system, and the over-arching goal of the present work is to improve the analysis fidelity. Specifically, the objectives are

Objectives

- Construct improved mathematical models of the rotorcraft tow system with components operating in different media
- Study trim configurations of helicopter and towed body in steady forward and turning flight conditions, and identify means of reducing engine power required during tow
- Perform stability analysis on the tow system and identify the dominant parameters that affect vehicle frequency response characteristics (for insight into Handling Qualities)
- Formulate an approach to obtain the helicopter swashplate control inputs that are required to guide the submerged load along a prescribed path

1.5 Key Contributions

1. Formulated coupled flight dynamics model of helicopter and hydrodynamics of curved cable and towed body, together with kinematic-kinetic couplings to account for boundary conditions and load transfers in state-space form
2. Improved cable modeling by extending the beam formulation to include non-circular cross-sections
3. Formulated trim conditions for the tow system with simplified straight cable as well as curved cable in steady forward flight and a helical ascending turn

4. Identified key physical mechanisms to reduce rotorcraft power required and the dominant parameters that affect vehicle frequency response characteristics

5. Applied a two-step approach for obtaining the pilot stick inputs required to guide the *towed body* along a prescribed search pattern using optimization and feedback control

1.6 Scope and Organization of Thesis

The present work is focused on systematic development of improved simulation modeling of helicopters towing submerged loads using flexible cables, while retaining a state-space formulation for stability analysis (as in Refs. [40], [39], [20]) .

- In Chapter 2, I detail the mathematical models used to represent the dynamics of the helicopter fuselage, main rotor blade structures and wake, empennage, tail rotor, tow cable and towed body are given, along with implementation details for the dynamic couplings

- In Chapter 3, I formulate the trim conditions for the tow system using both simplified straight cables as well as flexible (curved) cables, and detail how the cable and towed body model fit into the overall structure of the simulation

- In Chapter 4, I provide the helicopter physical parameters used in this work, together with verification and validation of the helicopter, wake and cable models

- In Chapter 5, I show trim results for steady forward flight and steady turning

flight, and identify the physical mechanisms that govern rotorcraft performance, together with design and operational recommendations for reducing power required

- In Chapter 6, I examine characteristics of the system frequency response to pilot stick inputs using linearized dynamics in the neighborhood of equilibrium (trim) conditions

- In, Chapter 7, I present an approach for trajectory tracking using optimization and feedback controls to determine the pilot stick inputs required to guide the *towed body* along a prescribed path

- Chapter 8 summarizes the key results and conclusions drawn from this work, and suggests directions for future work

- Appendix A gives additional details on rotation matrices and their time derivatives. Appendix B briefly touches on parallelization techniques used to accelerate computations. Appendix C provides expressions for the kinematic integral twist and its time derivatives, in addition to details on numerical quadrature

2 Mathematical Model

This chapter provides a brief description of the structural and aerodynamic models used for simulating the dynamics of individual components of the helicopter-cable-towed body system. The first section provides the equations of motion governing the motion of rigid bodies, i.e. the helicopter airframe and towed body. The second section outlines the geometrically exact beam formulation, and covers the structural, inertial and aerodynamic loads on flexible components, i.e. rotor blades and cable. The next section provides a brief description of aerodynamic forces acting on the fuselage, empennage and tail rotor. The final section covers the boundary conditions used to determine the dynamics of the cable and towed body.

2.1 Overview

Except for the free-vortex wake model, the equations of motion governing the system dynamics are formulated in state-space form as a system of first-order nonlinear coupled ODEs of the form

$$\mathbf{f}(\mathbf{y}\ ,\ \dot{\mathbf{y}}\ ,\ \mathbf{u}\ ,\ t) \quad = \quad \boldsymbol{\epsilon} \quad = \quad \mathbf{0}$$

$\mathbf{y}$ is a vector of system states, $\mathbf{u}$ is a vector of control inputs and t is the current time in seconds. Numerical solutions of these equations with optional simplifications (e.g.

zero body-axis accelerations for trim) can be used to study vehicle performance in steady flight, perform stability analysis and simulate unsteady maneuvers.

The state vector consists of the following components

$$\mathbf{y} = \left\{ \mathbf{y}_{\text{F}}^{\text{T}} \quad \mathbf{y}_{\lambda}^{\text{T}} \quad \mathbf{y}_{\text{rotor}}^{\text{T}} \quad \mathbf{y}_{\text{cable}}^{\text{T}} \quad \mathbf{y}_{\text{load}}^{\text{T}} \right\}^{\text{T}} \tag{2.1}$$

- $\mathbf{y}_{\text{F}}$ represents the vector of the 12 airframe rigid-body states
- $\mathbf{y}_{\lambda}$ represents the induced inflow coefficients for all rotary-wings present in the system.
- $\mathbf{y}_{\text{rotor}}$ represents the vector of rotor deflection states for all blades.
- $\mathbf{y}_{\text{cable}}$ represents the vector of deflection states for the flexible cable
- $\mathbf{y}_{\text{load}}$ is the vector of rigid-body states of the submerged load

The vector of control inputs is

$$\mathbf{u} = \left\{ \quad \delta_0 \quad \delta_{\text{lat}} \quad \delta_{\text{lon}} \quad \delta_{\text{ped}} \quad \theta_{\text{F1}} \quad \theta_{\text{F2}} \quad \right\}^{\text{T}}$$

The first four controls are manipulable by the helicopter pilot and represent, in order, the positions of the collective lever, lateral and longitudinal cyclic stick and the foot pedal. The last two controls represent the pitch inputs for the towed body fins, used to simultaneously regulate depth and lateral separation from the helicopter.

2.2 Coordinate Systems

Various reference frames are used in dynamic simulations, depending on the component being analyzed. Earth-fixed axes to track vehicle displacements, body

axes for force and moment equilibrium equations, hub-fixed axes for hubloads and rotating axes for blade deflections are some examples. To transfer displacements and loads across various interconnected components, consistency must be maintained, i.e. quantities must be transferred from one axis system to another through coordinate transformations to use in the governing equations for that component. Mathematically, this rotation can be expressed as the pre-multiplication of a vector (X,Y,Z components) with a rotation matrix.

One method to perform a rotation from one system to another is to use an Euler angle sequence. The three rotations occur in the following order:

- Yaw angle ψ about the Z axis (the new system is X_1,Y_1,Z_1=Z)
- Pitch angle θ about the Y_1 axis (the new system is X_2,Y_2=Y_1,Z_2)
- Roll angle ϕ about the X_2 axis (the new system is X_3=X_2,Y_3,Z_3)

The rotations are "positive" in the anti-clockwise sense. For example, a yaw rotation is positive if the (new) X_1 axis lies between the (old) X and Y axes (for a rotation angle less than 90°). The rotation matrices for the yaw, pitch and roll rotations are given below.

$$\mathbf{T}_\psi = \begin{bmatrix} \cos\psi & \sin\psi & 0 \\ -\sin\psi & \cos\psi & 0 \\ 0 & 0 & 1 \end{bmatrix}$$

$$\mathbf{T}_\theta = \begin{bmatrix} \cos\theta & 0 & -\sin\theta \\ 0 & 1 & 0 \\ \sin\theta & 0 & \cos\theta \end{bmatrix}$$

$$\mathbf{T}_{\phi} \quad = \quad \begin{bmatrix} 1 & 0 & 0 \\ 0 & \cos\phi & \sin\phi \\ 0 & -\sin\phi & \cos\phi \end{bmatrix}$$

Since the sequence occurs in the order $Z \rightarrow Y \rightarrow X$, the rotation matrices must be premultiplied in that order. Thus, the final rotation matrix from co-ordinate system "G" to "A" through angles (ψ,θ,ϕ) is

$$\mathbf{T}_{AG} \quad = \quad \mathbf{T}_{\phi} \quad \mathbf{T}_{\theta} \quad \mathbf{T}_{\psi} \quad = \quad \mathbf{R}(\psi, \theta, \phi)$$

The first subscript on the left hand side is the label of target co-ordinate system *to which* we are converting quantities, and the second subscript is the label of the source co-ordinate system *from which* we are converting quantities. The reverse rotation from co-ordinate system "A" to "G" follows the exact opposite sequence in reverse, i.e. angles (-ϕ,-θ,-ψ) about the (X,Y,Z) axes. In that case, the rotation matrix is given by

$$\mathbf{T}_{GA} \quad = \quad \mathbf{T}_{-\phi} \quad \mathbf{T}_{-\theta} \quad \mathbf{T}_{-\psi}$$

Using trigonometric identities, it can be shown that

$$\mathbf{T}_{-\phi} \quad = \quad \mathbf{T}_{\phi}^{\mathrm{T}}$$

$$\mathbf{T}_{-\theta} \quad = \quad \mathbf{T}_{\theta}^{\mathrm{T}}$$

$$\mathbf{T}_{-\psi} \quad = \quad \mathbf{T}_{\psi}^{\mathrm{T}}$$

Thus, the rotation from "A" to "G" is simplified to

$$\mathbf{T}_{GA} \quad = \quad \mathbf{T}_{\phi}^{\mathrm{T}} \quad \mathbf{T}_{\theta}^{\mathrm{T}} \quad \mathbf{T}_{\psi}^{\mathrm{T}}$$

Using the matrix property

$$(\mathbf{A}\ \mathbf{B}\ \mathbf{C})^{\mathrm{T}} \quad = \quad \mathbf{C}^{\mathrm{T}}\mathbf{B}^{\mathrm{T}}\mathbf{A}^{\mathrm{T}} \tag{2.2}$$

$$\mathbf{T}_{GA} \quad = \quad (\mathbf{T}_{\psi} \quad \mathbf{T}_{\theta} \quad \mathbf{T}_{\phi})^{\mathrm{T}} \quad = \quad \mathbf{T}_{AG}^{\mathrm{T}}$$

These rotation matrices do not depend explicitly on time, and the time derivatives of the forward and backward rotations are also transposes of each other.

Time Derivatives of Rotation Matrices

Often, the time derivatives of these rotation matrices are required for transferring displacements and loads across co-ordinate systems. Instead of expanding the matrix multiplication and then differentiating a long expression, it is more elegant to derive expressions for the time derivatives of individual rotations first, and then apply the matrix multiplication to build the total rate of change of a rotation matrix. To that end,

$$\begin{aligned} \dot{\mathbf{T}}_{AG} \quad &= \quad \frac{d}{dt}\left(\mathbf{T}_{\phi} \quad \mathbf{T}_{\theta} \quad \mathbf{T}_{\psi}\right) \\ &= \quad \dot{\mathbf{T}}_{\phi} \quad \mathbf{T}_{\theta} \quad \mathbf{T}_{\psi} \quad + \quad \mathbf{T}_{\phi} \quad \dot{\mathbf{T}}_{\theta} \quad \mathbf{T}_{\psi} \quad + \quad \mathbf{T}_{\phi} \quad \mathbf{T}_{\theta} \quad \dot{\mathbf{T}}_{\psi} \end{aligned} \tag{2.3}$$

The second time derivative is obtained by differentiation

$$\begin{aligned} \ddot{\mathbf{T}}_{AG} \quad &= \quad \frac{d}{dt}\left(\dot{\mathbf{T}}_{AG}\right) \\ &= \quad \ddot{\mathbf{T}}_{\phi} \quad \mathbf{T}_{\theta} \quad \mathbf{T}_{\psi} \quad + \quad \mathbf{T}_{\phi} \quad \ddot{\mathbf{T}}_{\theta} \quad \mathbf{T}_{\psi} \quad + \quad \mathbf{T}_{\phi} \quad \mathbf{T}_{\theta} \quad \ddot{\mathbf{T}}_{\psi} \quad + \\ &\quad 2\left(\dot{\mathbf{T}}_{\phi} \quad \dot{\mathbf{T}}_{\theta} \quad \mathbf{T}_{\psi} \quad + \quad \dot{\mathbf{T}}_{\phi} \quad \mathbf{T}_{\theta} \quad \dot{\mathbf{T}}_{\psi} \quad + \quad \mathbf{T}_{\phi} \quad \dot{\mathbf{T}}_{\theta} \quad \dot{\mathbf{T}}_{\psi}\right) \end{aligned} \tag{2.4}$$

All that remains is to obtain the time derivatives of the sequential rotations, which

are given below.

$$\dot{\mathbf{T}}_{\psi} = \begin{bmatrix} -\sin\psi & \cos\psi & 0 \\ -\cos\psi & -\sin\psi & 0 \\ 0 & 0 & 0 \end{bmatrix} \dot{\psi}$$

$$\dot{\mathbf{T}}_{\theta} = \begin{bmatrix} -\sin\theta & 0 & -\cos\theta \\ 0 & 0 & 0 \\ \cos\theta & 0 & -\sin\theta \end{bmatrix} \dot{\theta}$$

$$\dot{\mathbf{T}}_{\phi} = \begin{bmatrix} 0 & 0 & 0 \\ 0 & -\sin\phi & \cos\phi \\ 0 & -\cos\phi & -\sin\phi \end{bmatrix} \dot{\phi}$$

$$\ddot{\mathbf{T}}_{\psi} = \begin{bmatrix} -\sin\psi & \cos\psi & 0 \\ -\cos\psi & -\sin\psi & 0 \\ 0 & 0 & 0 \end{bmatrix} \ddot{\psi} + \begin{bmatrix} -\cos\psi & -\sin\psi & 0 \\ \sin\psi & -\cos\psi & 0 \\ 0 & 0 & 0 \end{bmatrix} \dot{\psi}^2$$

$$\ddot{\mathbf{T}}_{\theta} = \begin{bmatrix} -\sin\theta & 0 & -\cos\theta \\ 0 & 0 & 0 \\ \cos\theta & 0 & -\sin\theta \end{bmatrix} \ddot{\theta} + \begin{bmatrix} -\cos\theta & 0 & \sin\theta \\ 0 & 0 & 0 \\ -\sin\theta & 0 & -\cos\theta \end{bmatrix} \dot{\theta}^2$$

$$\ddot{\mathbf{T}}_{\phi} = \begin{bmatrix} 0 & 0 & 0 \\ 0 & -\sin\phi & \cos\phi \\ 0 & -\cos\phi & -\sin\phi \end{bmatrix} \ddot{\phi} + \begin{bmatrix} 0 & 0 & 0 \\ 0 & -\cos\phi & -\sin\phi \\ 0 & \sin\phi & -\cos\phi \end{bmatrix} \dot{\phi}^2$$

Various coordinate systems are used in this analysis. Each of these axes systems simplify calculations of certain force and moment components used in the dynamics simulation, and are detailed in the following sections.

2.2.1 Earth-Fixed Axes

The earth-fixed axes represent an inertial reference system used to track the motion of objects in space. The origin of this axis system is chosen to be a fixed point on the ground. The unit vector triad along the earth-fixed axes is represented by ($\boldsymbol{i}_{\mathrm{G}}$, $\boldsymbol{j}_{\mathrm{G}}$, $\boldsymbol{k}_{\mathrm{G}}$). The earth-fixed axes are oriented so that $\boldsymbol{i}_{\mathrm{G}}$ points North, $\boldsymbol{j}_{\mathrm{G}}$ points East and $\boldsymbol{k}_{\mathrm{G}}$ points towards the ground. The position vector of the helicopter CG in space is given by

$$\mathbf{r}_{\mathrm{CG}} \quad = \quad x_{\mathrm{CG}}\boldsymbol{i}_{\mathrm{G}} \quad + \quad y_{\mathrm{G}}\boldsymbol{j}_{\mathrm{G}} \quad + \quad z_{\mathrm{CG}}\boldsymbol{k}_{\mathrm{G}}$$

2.2.2 Helicopter Body-Fixed Axes

The body axes for the helicopter, shown in Fig. 2.1, are obtained from the earth-fixed axes using three translations to shift the origin to the helicopter CG, followed by three Euler rotations ψ_{F}, θ_{F}, ϕ_{F} in the order Z$\rightarrow$Y$\rightarrow$X, positive for nose-right, pitch-up and roll-right motions respectively. The unit vectors along the body axes are given by

$$\begin{Bmatrix} \boldsymbol{i}_{\mathrm{B}} \\ \boldsymbol{j}_{\mathrm{B}} \\ \boldsymbol{k}_{\mathrm{B}} \end{Bmatrix} \quad = \quad \mathbf{T}_{BG} \quad \begin{Bmatrix} \boldsymbol{i}_{\mathrm{G}} \\ \boldsymbol{j}_{\mathrm{G}} \\ \boldsymbol{k}_{\mathrm{G}} \end{Bmatrix} \tag{2.5}$$

The rotation matrix from gravity to helicopter body axes is given by

$$\mathbf{T}_{BG} = \begin{bmatrix} 1 & 0 & 0 \\ 0 & \cos\phi_{\mathrm{F}} & \sin\phi_{\mathrm{F}} \\ 0 & -\sin\phi_{\mathrm{F}} & \cos\phi_{\mathrm{F}} \end{bmatrix} \begin{bmatrix} \cos\theta_{\mathrm{F}} & 0 & -\sin\theta_{\mathrm{F}} \\ 0 & 1 & 0 \\ \sin\theta_{\mathrm{F}} & 0 & \cos\theta_{\mathrm{F}} \end{bmatrix} \begin{bmatrix} \cos\psi_{\mathrm{F}} & \sin\psi_{\mathrm{F}} & 0 \\ -\sin\psi_{\mathrm{F}} & \cos\psi_{\mathrm{F}} & 0 \\ 0 & 0 & 1 \end{bmatrix} \tag{2.6}$$

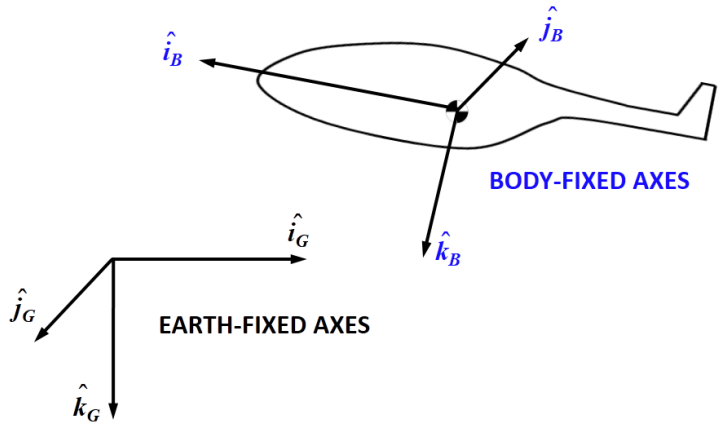

Figure 2.1: Earth-fixed axes and helicopter body axes

2.2.3 Helicopter Hub Non-Rotating Axes

The hub non-rotating axes, shown in Fig. 2.2, are obtained from the helicopter body axes using a translation of the origin, followed by two Euler rotations α_s, β_s in the order $Y \rightarrow X$, followed by a 180° rotation about the intermediate Y-axis. The first two rotations are positive when the shaft tilt causes the hub to move aft and starboard, respectively. The origin of this axis system is at the center of the hub. The unit vectors along the hub non-rotating axes are

$$\begin{Bmatrix} \boldsymbol{i}_{\mathrm{H}} \\ \boldsymbol{j}_{\mathrm{H}} \\ \boldsymbol{k}_{\mathrm{H}} \end{Bmatrix} = \mathbf{T}_{HB} \begin{Bmatrix} \boldsymbol{i}_{\mathrm{B}} \\ \boldsymbol{j}_{\mathrm{B}} \\ \boldsymbol{k}_{\mathrm{B}} \end{Bmatrix} \tag{2.7}$$

The rotation matrix *from* the helicopter body axes *to* the hub non-rotating axes is

$$\mathbf{T}_{HB} = \begin{bmatrix} -1 & 0 & 0 \\ 0 & 1 & 0 \\ 0 & 0 & -1 \end{bmatrix} \begin{bmatrix} 1 & 0 & 0 \\ 0 & \cos\beta_s & \sin\beta_s \\ 0 & -\sin\beta_s & \cos\beta_s \end{bmatrix} \begin{bmatrix} \cos\alpha_s & 0 & -\sin\alpha_s \\ 0 & 1 & 0 \\ \sin\alpha_s & 0 & \cos\alpha_s \end{bmatrix} \tag{2.8}$$

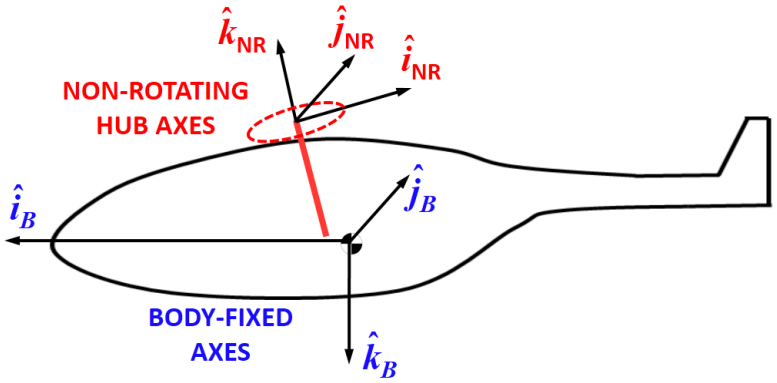

Figure 2.2: Helicopter hub non-rotating axes

2.2.4 Blade Rotating Unpreconed Axes

The blade rotating unpreconed axes, shown in Fig. 2.3, are obtained from the hub non-rotating axes using one rotation ψ_j about the hub non-rotating Z-axis $\boldsymbol{k}_{\text{H}}$. The origin of the blade rotating unpreconed axes is at the center of the hub, and is coincident with the origin of the hub non-rotating axes. The quantity ψ_j is the azimuth angle of the j^{th} blade, zero when the blade passes over the tail boom, positive counter-clockwise and is given by $\psi_j = \Omega_{\text{MR}} t + \frac{2\pi}{N_b}(j-1)$. The unit vectors along the blade rotating unpreconed axes are given by

$$\begin{Bmatrix} \boldsymbol{i}_{\text{R}} \\ \boldsymbol{j}_{\text{R}} \\ \boldsymbol{k}_{\text{R}} \end{Bmatrix} = \mathbf{T}_{RH} \begin{Bmatrix} \boldsymbol{i}_{\text{H}} \\ \boldsymbol{j}_{\text{H}} \\ \boldsymbol{k}_{\text{H}} \end{Bmatrix} \tag{2.9}$$

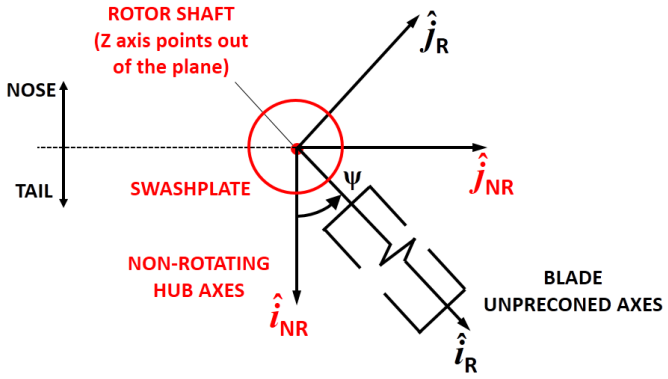

Figure 2.3: Helicopter blade rotating unpreconed axes

The rotation matrix *from* the hub non-rotating axes *to* the blade rotating unpreconed axes is

$$\mathbf{T}_{RH} = \begin{bmatrix} \cos\psi_j & \sin\psi_j & 0 \\ -\sin\psi_j & \cos\psi_j & 0 \\ 0 & 0 & 1 \end{bmatrix} \tag{2.10}$$

2.2.5 Blade Preconed Undeformed Axes

The blade pre-coned undeformed axes, shown in Fig.2.4 are obtained from the unpreconed axes using one rotation through an angle $-\beta_p$ about the $\boldsymbol{j}_{\mathrm{R}}$ unpreconed rotating axis, and is positive for vertically upward motion of the blade tip. The origin of the blade preconed axes is coincident with that of the unpreconed axes. The unit vectors along the blade rotating unpreconed axes are given by

$$\begin{Bmatrix} \boldsymbol{i} \\ \boldsymbol{j} \\ \boldsymbol{k} \end{Bmatrix} = \mathbf{T}_{UR} \begin{Bmatrix} \boldsymbol{i}_{\mathrm{R}} \\ \boldsymbol{j}_{\mathrm{R}} \\ \boldsymbol{k}_{\mathrm{R}} \end{Bmatrix} \tag{2.11}$$

The rotation matrix *from* the unpreconed axes *to* the preconed axes is given by

$$\mathbf{T}_{UR} = \begin{bmatrix} \cos\beta_p & 0 & \sin\beta_p \\ 0 & 1 & 0 \\ -\sin\beta_p & 0 & \cos\beta_p \end{bmatrix} \tag{2.12}$$

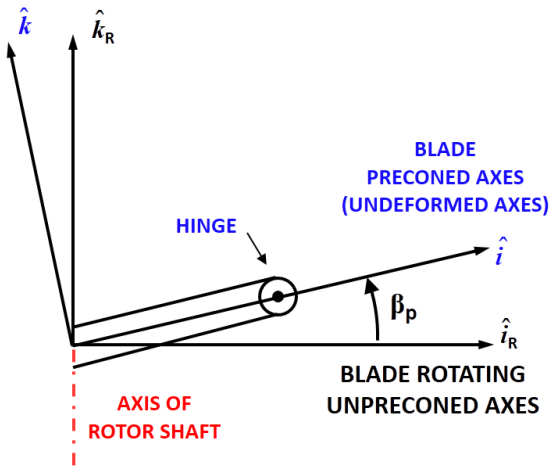

Figure 2.4: Pre-cone Rotation

2.2.6 Blade Deformed Axes

The blade *deformed* axes are unique to each point on the elastic axis, and are obtained using three translations along the preconed undeformed axes, followed by three consecutive rotations. The first translation is along the $\boldsymbol{i}$ axis through a distance $e + x + u$, where e is the hinge offset, u is the axial fore-shortening due to bending and x is the spanwise position of the beam cross-section. The second translation is along the $\boldsymbol{j}$ axis through the in-plane lead displacement v, and the third translation is along the $\boldsymbol{k}$ axis through the out-of-plane flap bending displacement w as shown in Fig. 2.5. The origin of the deformed axes defining the orientation of a blade cross-section is at the intersection of the deformed elastic axis with that

cross-section. The unit vectors along the deformed axes are

$$\begin{Bmatrix} \boldsymbol{i}' \\ \boldsymbol{j}' \\ \boldsymbol{k}' \end{Bmatrix} = \mathbf{T}_{DU} \begin{Bmatrix} \boldsymbol{i} \\ \boldsymbol{j} \\ \boldsymbol{k} \end{Bmatrix} \tag{2.13}$$

The transformation matrix *from* the undeformed axes *to* the deformed axes is

$$\mathbf{T}_{DU} = \begin{bmatrix} c_{\beta_1} c_{\xi_1} & c_{\beta_1} s_{\xi_1} & s_{\beta_1} \\ -c_{\xi_1} s_{\beta_1} s_{\theta_1} - c_{\theta_1} s_{\xi_1} & c_{\xi_1} c_{\theta_1} - s_{\xi_1} s_{\beta_1} s_{\theta_1} & c_{\beta_1} s_{\theta_1} \\ -c_{\xi_1} s_{\beta_1} c_{\theta_1} + s_{\theta_1} s_{\xi_1} & -c_{\xi_1} s_{\theta_1} - s_{\xi_1} s_{\beta_1} c_{\theta_1} & c_{\beta_1} c_{\theta_1} \end{bmatrix} \tag{2.14}$$

Here, $c_{()} = \cos()$ and $s_{()} = \sin()$. The angles ξ_1, β_1 and θ_1 may be identified from the spatial gradients of the elastic axis deflections and the elastic twist. The $\boldsymbol{i}'$ axis is tangent to the deformed elastic axis. In accordance with the Euler-Bernoulli hypothesis, plane cross-sections normal to the undeformed elastic axis before beam bending remain plane and normal to the deformed elastic axis after bending. Thus, the cross-section (after bending and twist), is completely contained in the $\boldsymbol{j}' - \boldsymbol{k}'$ plane.

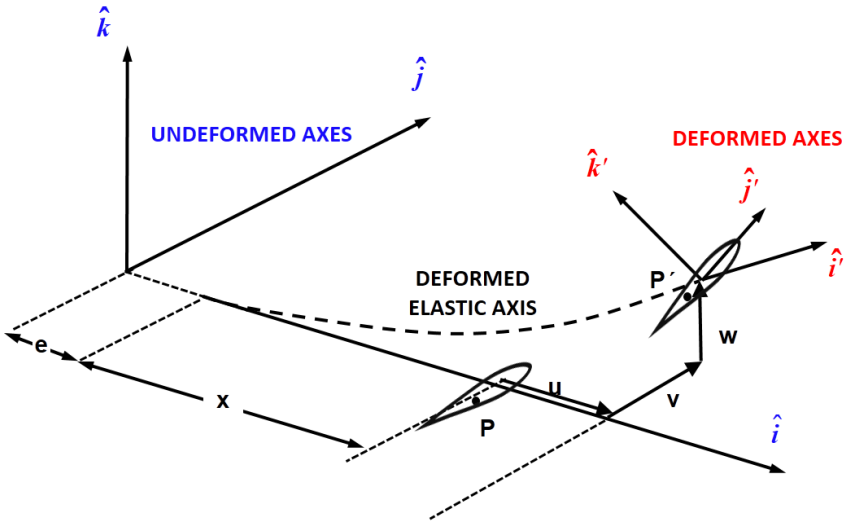

Figure 2.5: Undeformed and Deformed Axes

2.2.7 Cable Undeformed Axes

The cable undeformed axes are obtained from the earth-fixed axes after two sets of translations followed by two sequential rotations. The first set of translations shifts the origin from the earth-fixed axes to the helicopter center of gravity. The second set of translations shifts the origin from the helicopter CG to the cable attachment point on the airframe. After these translations, the earth-fixed axes are rotated through the Euler angles $(\psi_{\mathrm{F}}, -\frac{\pi}{2})$ in the sequence $Z \rightarrow Y$, and are given by

$$\begin{Bmatrix} \boldsymbol{i}_{\mathrm{C}} \\ \boldsymbol{j}_{\mathrm{C}} \\ \boldsymbol{k}_{\mathrm{C}} \end{Bmatrix} = \mathbf{T}_{CG} \begin{Bmatrix} \boldsymbol{i}_{\mathrm{G}} \\ \boldsymbol{j}_{\mathrm{G}} \\ \boldsymbol{k}_{\mathrm{G}} \end{Bmatrix} \tag{2.15}$$

The direction $\boldsymbol{i}_{\mathrm{C}}$ points vertically down and is identical to $\boldsymbol{k}_{\mathrm{G}}$, while $\boldsymbol{j}_{\mathrm{C}}$ and $\boldsymbol{k}_{\mathrm{C}}$ are defined so that cable lateral trail on the starboard side and longitudinal trail aft are positive.

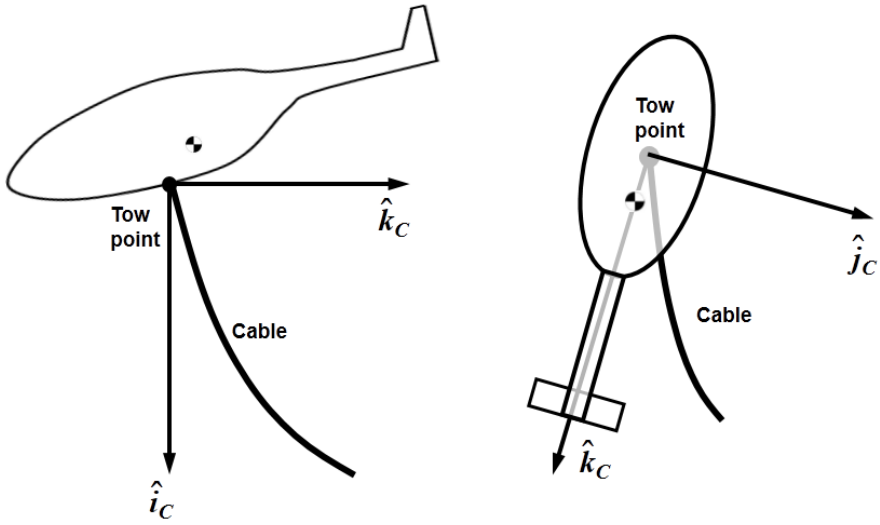

Figure 2.6: Cable Undeformed Axes

The rotation matrix *from* earth-fixed axes *to* the cable undeformed axes is

$$\mathbf{T}_{CG} = \begin{bmatrix} 0 & 0 & 1 \\ 0 & 1 & 0 \\ -1 & 0 & 0 \end{bmatrix} \begin{bmatrix} \cos\psi_{\text{F}} & \sin\psi_{\text{F}} & 0 \\ -\sin\psi_{\text{F}} & \cos\psi_{\text{F}} & 0 \\ 0 & 0 & 1 \end{bmatrix} \tag{2.16}$$

2.2.8 Cable Deformed Axes

The transformation from cable undeformed axes to cable deformed axes are defined in a manner similar to the transformation from blade undeformed axes to blade deformed axes. The cable deformed axes are obtained using three translations along the cable undeformed axes, followed by three consecutive rotations. The first translation is along the $\boldsymbol{i}_{\text{C}}$ axis through a distance $x_{\text{C}}+u_{\text{C}}$, where u_{C} is the axial foreshortening due to bending and x_{C} is the spanwise position of the cable cross-section. The second translation is along the $\boldsymbol{j}_{\text{C}}$ axis through the lateral trail displacement v_{C}, and the third translation is along the $\boldsymbol{k}_{\text{C}}$ axis through the longitudinal trail displacement w_{C}. The origin of the cable deformed axes is at the intersection of the deformed cable elastic axis and the cross-section of interest. The unit vectors along the deformed axes are given by

$$\begin{Bmatrix} \boldsymbol{i}'_{\text{C}} \\ \boldsymbol{j}'_{\text{C}} \\ \boldsymbol{k}'_{\text{C}} \end{Bmatrix} = \mathbf{T}_{DU} \begin{Bmatrix} \boldsymbol{i}_{\text{C}} \\ \boldsymbol{j}_{\text{C}} \\ \boldsymbol{k}_{\text{C}} \end{Bmatrix} \tag{2.17}$$

The transformation matrix *from* the cable undeformed axes *to* the cable deformed axes is given by Eq. (2.14), with the Euler angles β_1, ξ_1 and θ_1 defined by the bending displacements of the cable with respect to the cable undeformed axes. The choice

of cable undeformed axes allows for use of the geometrically exact beam theory to model the cable deflections for the tow mission. The 90° limit imposed by the use of positive square roots in the derivation of the $\mathbf{T}_{DU}$ matrix is reached only when the local cable elastic axis lies in a plane parallel to the water surface. Since the helicopter is always above the load and the scale of cable lengths (hundreds of feet) limit the transient accelerations during maneuvers, it is reasonable to assume that the cable slopes will never reach this limit (although there is no loss of modeling accuracy as they *approach* it, unlike traditional small deflection theories).

2.2.9 Submerged Load Body Axes

The body axes for the submerged load, shown in Fig. 2.7, are obtained from the earth-fixed axes using three translations to shift the origin to the towed body CG, followed by three Euler rotations ψ_{L}, θ_{L}, ϕ_{L} in the order Z→Y→X, positive for nose-right, pitch-up and roll-right motions respectively. The unit vectors along the load body axes are given by

$$\begin{Bmatrix} \boldsymbol{i}_{\text{L}} \\ \boldsymbol{j}_{\text{L}} \\ \boldsymbol{k}_{\text{L}} \end{Bmatrix} = \mathbf{T}_{LG} \begin{Bmatrix} \boldsymbol{i}_{\text{G}} \\ \boldsymbol{j}_{\text{G}} \\ \boldsymbol{k}_{\text{G}} \end{Bmatrix} \tag{2.18}$$

The rotation matrix from earth-fixed to load body axes is given by

$$\mathbf{T}_{LG} = \begin{bmatrix} 1 & 0 & 0 \\ 0 & \cos\phi_{\text{L}} & \sin\phi_{\text{L}} \\ 0 & -\sin\phi_{\text{L}} & \cos\phi_{\text{L}} \end{bmatrix} \begin{bmatrix} \cos\theta_{\text{L}} & 0 & -\sin\theta_{\text{L}} \\ 0 & 1 & 0 \\ \sin\theta_{\text{L}} & 0 & \cos\theta_{\text{L}} \end{bmatrix} \begin{bmatrix} \cos\psi_{\text{L}} & \sin\psi_{\text{L}} & 0 \\ -\sin\psi_{\text{L}} & \cos\psi_{\text{L}} & 0 \\ 0 & 0 & 1 \end{bmatrix} \tag{2.19}$$

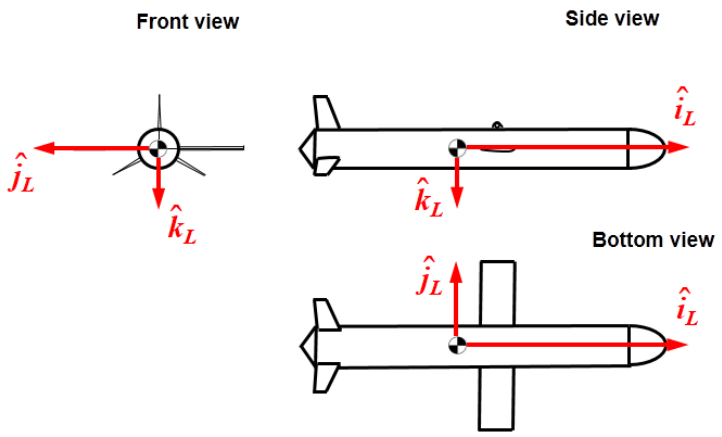

Figure 2.7: Submerged Load Body Axes

2.3 Helicopter Rigid Body Dynamics

The helicopter fuselage is assumed to be rigid, and the inertial loads can be computed from the body-axis components of the airframe linear and angular velocities. These components are obtained from the partition of the system state vector that contains the fuselage states, given by

$$\mathbf{y}_{\mathrm{F}} = \left\{ u_{\mathrm{F}} \quad v_{\mathrm{F}} \quad w_{\mathrm{F}} \quad p_{\mathrm{F}} \quad q_{\mathrm{F}} \quad r_{\mathrm{F}} \quad \phi_{\mathrm{F}} \quad \theta_{\mathrm{F}} \quad \psi_{\mathrm{F}} \quad \mathrm{x_{CG}} \quad \mathrm{y_{CG}} \quad \mathrm{z_{CG}} \right\}^{\mathrm{T}}$$

The terms ($\mathrm{x_{CG}}$, $\mathrm{y_{CG}}$, $\mathrm{z_{CG}}$) represent the positions of the helicopter CG in earth-fixed axes, (u_{F}, v_{F}, w_{F}, p_{F}, q_{F}, r_{F}) are the components of linear and angular velocity of the helicopter CG along and about body-fixed axes and (ψ_{F}, θ_{F}, ϕ_{F}) are the Euler angles used in the Z→Y→X sequence to define the fuselage orientation with respect to earth-fixed axes.

Since the fuselage is rigid, the position and orientation of the lifting surfaces (main rotor, tail rotor, horizontal and vertical stabilizers) and cable attachment

point remain constant as measured along body-fixed axes. Further, the moments of inertia of a rigid object remain constant when measured about body-fixed axes. Therefore, it is convenient to formulate force and moment equilibrium equations along the fuselage body axes. The force equilibrium equations are

$$X = \mathrm{m}_{\mathrm{F}}(\dot{u}_{\mathrm{F}} + q_{\mathrm{F}} w_{\mathrm{F}} - r_{\mathrm{F}} v_{\mathrm{F}} + g \sin\theta_{\mathrm{F}}) \tag{2.20}$$

$$Y = \mathrm{m}_{\mathrm{F}}(\dot{v}_{\mathrm{F}} + r_{\mathrm{F}} u_{\mathrm{F}} - p_{\mathrm{F}} w_{\mathrm{F}} - g \sin\phi_{\mathrm{F}} \cos\theta_{\mathrm{F}}) \tag{2.21}$$

$$Z = \mathrm{m}_{\mathrm{F}}(\dot{w}_{\mathrm{F}} + p_{\mathrm{F}} v_{\mathrm{F}} - q_{\mathrm{F}} u_{\mathrm{F}} - g \cos\phi_{\mathrm{F}} \cos\theta_{\mathrm{F}}) \tag{2.22}$$

Here, p_{F}, q_{F} and r_{F} represent the angular velocity components about the body axes, and can be expressed in terms of the Euler angles (ϕ_{F}, θ_{F}, ψ_{F}) and their time derivatives as

$$p_{\mathrm{F}} = \dot{\phi}_{\mathrm{F}} - \dot{\psi}_{\mathrm{F}} \sin\theta_{\mathrm{F}} \tag{2.23}$$

$$q_{\mathrm{F}} = \dot{\theta}_{\mathrm{F}} \cos\phi_{\mathrm{F}} + \dot{\psi}_{\mathrm{F}} \cos\theta_{\mathrm{F}} \sin\phi_{\mathrm{F}} \tag{2.24}$$

$$r_{\mathrm{F}} = -\dot{\theta}_{\mathrm{F}} \sin\phi_{\mathrm{F}} + \dot{\psi}_{\mathrm{F}} \cos\theta_{\mathrm{F}} \cos\phi_{\mathrm{F}} \tag{2.25}$$

The moment equilibrium equations are

$$L = I_{xx}\dot{p}_{\mathrm{F}} - I_{xy}(\dot{q}_{\mathrm{F}} - p_{\mathrm{F}} r_{\mathrm{F}}) - I_{xz}(\dot{r}_{\mathrm{F}} + p_{\mathrm{F}} q_{\mathrm{F}}) - I_{yz}(q_{\mathrm{F}}^2 - r_{\mathrm{F}}^2) - (I_{yy} - I_{zz}) q_{\mathrm{F}} r_{\mathrm{F}} \tag{2.26}$$

$$M = I_{yy}\dot{q}_{\mathrm{F}} - I_{yz}(\dot{r}_{\mathrm{F}} - q_{\mathrm{F}} p_{\mathrm{F}}) - I_{yx}(\dot{p}_{\mathrm{F}} + q_{\mathrm{F}} r_{\mathrm{F}}) - I_{zx}(r_{\mathrm{F}}^2 - p_{\mathrm{F}}^2) - (I_{zz} - I_{xx}) r_{\mathrm{F}} p_{\mathrm{F}} \tag{2.27}$$

$$N = I_{zz}\dot{r}_{\mathrm{F}} - I_{zx}(\dot{p}_{\mathrm{F}} - r_{\mathrm{F}} q_{\mathrm{F}}) - I_{zy}(\dot{q}_{\mathrm{F}} + r_{\mathrm{F}} p_{\mathrm{F}}) - I_{xy}(p_{\mathrm{F}}^2 - q_{\mathrm{F}}^2) - (I_{xx} - I_{yy}) p_{\mathrm{F}} q_{\mathrm{F}} \tag{2.28}$$

Since the positions of the helicopter CG are tracked with respect to the earth, the components of this position vector are assigned as states $\mathrm{x_{CG}}$, $\mathrm{y_{CG}}$, $\mathrm{z_{CG}}$. The corresponding ODEs are given by

$$\frac{d}{dt}\begin{Bmatrix} \mathrm{x_{CG}} \\ \mathrm{y_{CG}} \\ \mathrm{z_{CG}} \end{Bmatrix} = \mathbf{T}_{GB}\begin{Bmatrix} u_{\mathrm{F}} \\ v_{\mathrm{F}} \\ w_{\mathrm{F}} \end{Bmatrix} \tag{2.29}$$

The terms on the left hand side of Eqs. (2.20) -(2.22) and (2.26) - (2.28) (X, Y, Z) and (L, M, N) represent the cumulative forces and moments about the center of gravity, respectively, exerted by airframe aerodynamics, main rotor loads, tail rotor loads, empennage aerodynamics and cable force, and are given by

$$\begin{aligned}
X &= X_{\mathrm{MR}} + X_{\mathrm{TR}} + X_{\mathrm{HT}} + X_{\mathrm{VT}} + X_{\mathrm{F}} + X_{\mathrm{cable}} \\
Y &= Y_{\mathrm{MR}} + Y_{\mathrm{TR}} + Y_{\mathrm{HT}} + Y_{\mathrm{VT}} + Y_{\mathrm{F}} + Y_{\mathrm{cable}} \\
Z &= Z_{\mathrm{MR}} + Z_{\mathrm{TR}} + Z_{\mathrm{HT}} + Z_{\mathrm{VT}} + Z_{\mathrm{F}} + Z_{\mathrm{cable}} \\
L &= L_{\mathrm{MR}} + L_{\mathrm{TR}} + L_{\mathrm{HT}} + L_{\mathrm{VT}} + L_{\mathrm{F}} + L_{\mathrm{cable}} \\
M &= M_{\mathrm{MR}} + M_{\mathrm{TR}} + M_{\mathrm{HT}} + M_{\mathrm{VT}} + M_{\mathrm{F}} + M_{\mathrm{cable}} \\
N &= N_{\mathrm{MR}} + N_{\mathrm{TR}} + N_{\mathrm{HT}} + N_{\mathrm{VT}} + N_{\mathrm{F}} + N_{\mathrm{cable}}
\end{aligned}$$

The mathematical models for loads generated by each of these components are discussed in the following sections. Sections 2.4.4, 2.5.5, 2.5.4, 2.5.3 provide details on calculation of force and moment contributions from the main rotor, tail rotor, empennage and fuselage aerodynamics, respectively, to the total loads acting at the vehicle CG. The loads experienced by the cable and towed body manifest as a single concentrated force at the tow point, and are discussed in Section 2.6.

2.4 Flexible Blade Dynamics

The rotor blade motions are influenced by gravity, aerodynamics, inertia (including centrifugal forces), structural properties and pitch control inputs. A geometrically exact representation is used to model the main rotor blade dynamics as flexible rotating Euler-Bernoulli beams with flap, lag and torsion. The system states corresponding to motions of the rotor blades are given by

$$\mathbf{y}_{\text{rotor}} = \left\{ \boldsymbol{\eta}_1^{\text{T}} \quad \boldsymbol{\eta}_2^{\text{T}} \quad \cdots \quad \boldsymbol{\eta}_{\text{Nb}}^{\text{T}} \quad \dot{\boldsymbol{\eta}}_1^{\text{T}} \quad \dot{\boldsymbol{\eta}}_2^{\text{T}} \quad \cdots \quad \dot{\boldsymbol{\eta}}_{\text{Nb}}^{\text{T}} \right\}^{\text{T}}$$

The vector of generalized displacements for the " j^{th} " blade is given by

$$\boldsymbol{\eta}_j = \left\{ \eta_{j,1} \quad \eta_{j,2} \quad \cdots \quad \eta_{j,\text{Nm}} \right\}^{\text{T}}$$

$\eta_{j,i}$ represents the " i^{th} " generalized displacement of blade " j ". These generalized displacements are the coefficients of the normal modes corresponding to the rotating beam structure of the blade, the computation of which is discussed in Section 2.4.7. A detailed derivation of the beam dynamics is given in the following section.

2.4.1 The Blade Structural Model

The first step in the dynamic analysis of a rigid or flexible structure is to identify the motions of a generic point "P". For a flexible body, the displacement of a point contains contributions from both rigid-body translations/rotations and flexible motions. The flexible motion contributions that displace "P" to P′ are used to determine the displacement field and the internal strains produced by elastic deflections. Since the structures of interest are treated as slender beams, the displacement

of P can be broken down into two components : the motion of the elastic axis (and therefore the rigid translation of the cross-section containing P), and the motion of P relative to the elastic axis.

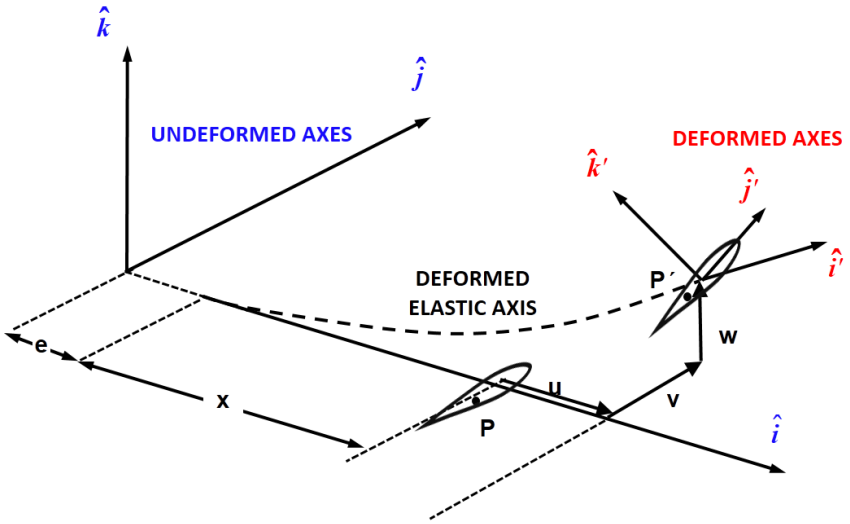

Figure 2.8: Undeformed and Deformed Axes

The Euler-Bernoulli hypothesis is invoked here, which assumes that plane cross-sections normal to the *undeformed* elastic axis before bending remain plane and normal to the *deformed* elastic axis after bending. Further, the effects of shear deformation on bending are neglected. As a result of these assumptions, points that were originally located within a cross-section normal to the elastic axis before bending, remain on the same cross-section that is normal to the new elastic axis direction after bending. This implies that a cross-section rotates *as a whole* in a rigid-body sense about the deformed elastic axis. The axial displacement u will be related to the bending displacements v, w, assuming that the elastic axis does not stretch. Therefore, the location of a point within a cross-section after bending can be computed from two translations of the elastic axis (v, w), and elastic twist of the cross-section(ϕ).

The process of beam bending can be conceptualized in two stages for every cross-section. In the first stage, the entire cross-section is translated rigidly (u,v,w) along the undeformed axes without any rotations. In the second stage, the elastic axis is held fixed in space and the entire cross-section is reoriented using a Z→Y→X rotation sequence through angles (ξ_1, β_1, θ_1), with the rotation matrix given in Eq. (2.14). The relationship between the $\mathbf{T}_{DU}$ matrix and the elastic deflections v, w, ϕ is given below.

2.4.1.1 Undeformed to Deformed Frame Transformation

Detailed derivations of the $\mathbf{T}_{DU}$ matrix are given in the literature, both with and without ordering schemes (Refs. [10], [12]). To second-order, near-identical governing equations were obtained in Ref. [11]. Minor differences still exist between the derivations obtained by the two authors. Hodges and Dowell (Ref. [10]) isolated and clearly distinguished between the derivatives along the deformed and undeformed axis while obtaining strain components and then applied the ordering scheme, while Rosen and Friedmann (Ref. [11]) applied an ordering scheme *before* obtaining expressions for the strain tensor. This work closely follows the Hodges and Dowell beam formulation, giving allowances for finite rotations.

The position vector of a point on the elastic axis at a distance x from the root end of a flexible beam, after elastic bending, is given by

$$\mathbf{r} \quad = \quad (x+u)\boldsymbol{i} \; + \; v\boldsymbol{j} \; + \; w\boldsymbol{k} \tag{2.30}$$

By definition, the unit vector tangent to the deformed elastic axis $\boldsymbol{i}'$ is the gradient

of the elastic axis deflection along the curvilinear coordinate r along the deformed elastic axis (Ref. [10]). Thus,

$$\frac{\partial \mathbf{r}}{\partial r} \;=\; \boldsymbol{i}' \;=\; \mathbf{T}_{11}\boldsymbol{i} \;+\; \mathbf{T}_{12}\boldsymbol{j} \;+\; \mathbf{T}_{13}\boldsymbol{k} \tag{2.31}$$

Here, $\mathbf{T}_{ij}$ is the element in row i and column j of the $\mathbf{T}_{DU}$ matrix, given in Eq. (2.14). Substituting Eq. (2.30) in Eq. (2.31) and comparing components along $\boldsymbol{i}$, $\boldsymbol{j}$ and $\boldsymbol{k}$, it is clear that

$$(x+u)^+ \;=\; T_{11} \tag{2.32}$$

$$(v)^+ \;=\; T_{12} \tag{2.33}$$

$$(w)^+ \;=\; T_{13} \tag{2.34}$$

Comparing the terms in Eqs. (2.14), (2.33), (2.34) and applying trigonometry yields

$$\sin\beta_1 \;=\; w^+ \tag{2.35}$$

$$\cos\beta_1 \;=\; \sqrt{1-w^{+2}} \tag{2.36}$$

$$\sin\xi_1 \;=\; \frac{v^+}{\sqrt{1-w^{+2}}} \tag{2.37}$$

$$\cos\xi_1 \;=\; \frac{\sqrt{1-v^{+2}-w^{+2}}}{\sqrt{1-w^{+2}}} \tag{2.38}$$

An implicit assumption made in this formulation through the use of the positive square root is that the bending slopes do not exceed 90° in magnitude. The third rotation angle θ_1 may be obtained from the $\mathbf{T}_{DU}$ matrix. Consider a point on the elastic axis at a location r. The deformed beam axes at $r+dr$ can be obtained using three rotations ($\kappa_3\ dr$, $\kappa_2\ dr$, $\kappa_1\ dr$) about the deformed beam axes ($\boldsymbol{i}'$, $\boldsymbol{j}'$, $\boldsymbol{k}'$) at r. The gradient of these rotations along the span of the beam are, by definition, the

curvatures (Ref. [89]) κ_3, κ_2, κ_1. Since these rotations are infinitesimal in nature, terms in dr^2 and dr^3 can be neglected and so we obtain an expression for the spatial derivative (along r) of the unit vectors defining the deformed beam axes

$$\frac{\partial}{\partial r}\begin{Bmatrix} \boldsymbol{i}' \\ \boldsymbol{j}' \\ \boldsymbol{k}' \end{Bmatrix} = \begin{bmatrix} 0 & \kappa_3 & -\kappa_2 \\ -\kappa_3 & 0 & \kappa_1 \\ \kappa_2 & -\kappa_1 & 0 \end{bmatrix} \begin{Bmatrix} \boldsymbol{i}' \\ \boldsymbol{j}' \\ \boldsymbol{k}' \end{Bmatrix} = \boldsymbol{\kappa} \quad \mathbf{T}_{DU} \begin{Bmatrix} \boldsymbol{i} \\ \boldsymbol{j} \\ \boldsymbol{k} \end{Bmatrix} \tag{2.39}$$

Where

$$\boldsymbol{\kappa} = \begin{bmatrix} 0 & \kappa_3 & -\kappa_2 \\ -\kappa_3 & 0 & \kappa_1 \\ \kappa_2 & -\kappa_1 & 0 \end{bmatrix} \tag{2.40}$$

Differentiate Eq. (2.13) once with respect to r to obtain

$$\frac{\partial}{\partial r}\begin{Bmatrix} \boldsymbol{i}' \\ \boldsymbol{j}' \\ \boldsymbol{k}' \end{Bmatrix} = \frac{\partial \mathbf{T}_{DU}}{\partial r} \begin{Bmatrix} \boldsymbol{i} \\ \boldsymbol{j} \\ \boldsymbol{k} \end{Bmatrix} \tag{2.41}$$

Comparing the expressions on the right hand side of Eqs. (2.39) and (2.41)

$$\boldsymbol{\kappa} \quad \mathbf{T}_{DU} = \mathbf{T}^{+}_{DU}$$

Rearranging and using $\mathbf{T}^{\mathrm{T}}_{DU} = \mathbf{T}^{-1}_{DU} = \mathbf{T}_{UD}$, we obtain

$$\boldsymbol{\kappa} = \mathbf{T}^{+}_{DU} \quad \mathbf{T}^{\mathrm{T}}_{DU} \tag{2.42}$$

After carrying out matrix multiplications, we obtain expressions for the curvatures

$$\left.\begin{aligned} \kappa_1 &= \theta_1^{+} + \xi_1^{+} w^{+} = (\theta_t + \phi)^{+} \\ \kappa_2 &= -\beta_1^{+} \cos\theta_1 + \xi_1^{+} \cos\beta_1 \sin\theta_1 \\ \kappa_3 &= \xi_1^{+} \cos\beta_1 \cos\theta_1 + \beta_1^{+} \sin\theta_1 \end{aligned}\right\} \tag{2.43}$$

θ_t is the rigid pre-twist of the beam and ϕ is the elastic twist. Substituting for ξ_1^+ from Eq. (2.35) and integrating along the deformed elastic axis, we obtain

$$\theta_1 = \theta_t + \phi - \int_0^r \frac{w^+}{\sqrt{1 - v^{+^2} - w^{+^2}}} \left(v^{++} + \frac{v^+ w^+ w^{++}}{1 - w^{+^2}} \right) dr \tag{2.44}$$

2.4.1.2 Strain, Stress and Structural Loads

The strain tensor components are derived using the displacement field. The expressions are repeated from Ref. [10], neglecting axial stretch and warping effects. The strain tensor components acting at a point (η,ζ) on a cross-section of the beam are

$$\begin{aligned}
2\epsilon_{11} &= (-\eta\kappa_3 + \zeta\kappa_2)^2 \quad + \quad \kappa_1^2(\zeta^2 + \eta^2) \quad + \quad 2(-\eta\kappa_3 + \zeta\kappa_2) \\
&\quad + \quad (v^{+^2} + w^{+^2} - u^{+^2}) \quad + \quad 2u^+\sqrt{1 - v^{+^2} - w^{+^2}} \\
&\quad - \quad \theta^{+^2}(\eta_0^2 + \zeta_0^2) \qquad\qquad (2.45) \\
2\epsilon_{12} &= -\zeta\kappa_1 \quad + \quad \left(\frac{d\eta_0}{d\eta}\right)\theta^+\zeta_0 \\
2\epsilon_{13} &= \eta\kappa_1 \quad - \quad \left(\frac{d\zeta_0}{d\zeta}\right)\theta^+\eta_0 \\
2\epsilon_{22} &= 1 \quad - \quad \left(\frac{d\eta_0}{d\eta}\right)^2 \\
2\epsilon_{23} &= 0 \\
2\epsilon_{33} &= 1 \quad - \quad \left(\frac{d\zeta_0}{d\zeta}\right)^2
\end{aligned}$$

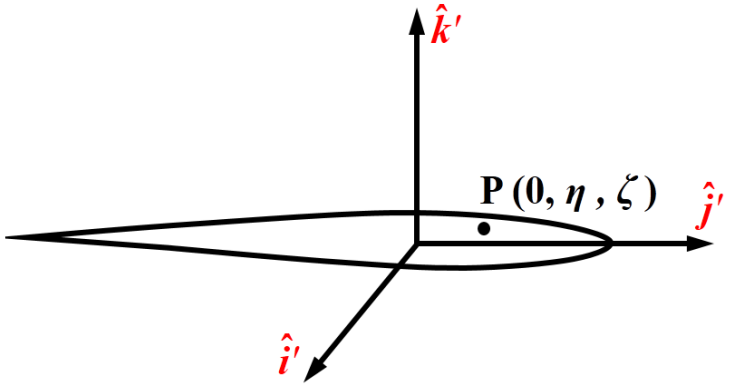

Figure 2.9: Coordinates of a Point in a Cross-Section along Beam Deformed Axes

Application of Hooke's law for an isotropic material yields

$$\left.\begin{aligned}
\begin{bmatrix}\sigma_{11}\\ \sigma_{22}\\ \sigma_{33}\end{bmatrix} &= \frac{E}{(1+\nu)(1-2\nu)}\begin{bmatrix}1-\nu & \nu & \nu\\ \nu & 1-\nu & \nu\\ \nu & \nu & 1-\nu\end{bmatrix}\begin{bmatrix}\epsilon_{11}\\ \epsilon_{22}\\ \epsilon_{33}\end{bmatrix}\\
\begin{bmatrix}\sigma_{23}\\ \sigma_{31}\\ \sigma_{12}\end{bmatrix} &= G\begin{bmatrix}\epsilon_{23}\\ \epsilon_{31}\\ \epsilon_{12}\end{bmatrix}
\end{aligned}\right\} \tag{2.46}$$

The uni-axial stress assumption, which is valid for long slender beams, is invoked at this stage. Under this assumption,

$$\sigma_{22} \;=\; \sigma_{33} \;=\; \sigma_{23} \;\overset{\text{def}}{=}\; 0$$

This assumption is used to obtain the derivatives $\frac{d\eta_0}{d\eta}$ and $\frac{d\zeta_0}{d\zeta}$ as

$$\frac{d\eta_0}{d\eta} \;=\; \frac{d\zeta_0}{d\zeta} \;=\; \sqrt{1 \;+\; 2\nu\epsilon_{11}} \tag{2.47}$$

The material stresses are obtained by inverting Eqs. (2.46) as

$$\left.\begin{array}{rcl} \sigma_{11} & = & E\epsilon_{11} \\ \sigma_{12} & = & G\epsilon_{12} \\ \sigma_{13} & = & G\epsilon_{13} \end{array}\right\} \tag{2.48}$$

The structural loads at a cross-section are obtained by integrating the stresses over the area. The elastic force vector is

$$\mathbf{F}_s = S_x\boldsymbol{i}' + S_y\boldsymbol{j}' + S_z\boldsymbol{k}'$$

$$\left.\begin{array}{rcl} S_x & = & \int\int_A \sigma_{11}dA \\ S_y & = & 2\int\int_A \sigma_{12}dA \\ S_z & = & 2\int\int_A \sigma_{13}dA \end{array}\right\} \tag{2.49}$$

The components of the elastic moment about the deformed beam axes are obtained by integrating over the cross-section, moments of the material stresses about the deformed elastic axis. The total elastic moment is

$$\mathbf{M}_s = M_x\boldsymbol{i}' + M_y\boldsymbol{j}' + M_z\boldsymbol{k}'$$

Where

$$\left.\begin{array}{rcl} M_x & = & 2\int\int_A (\ \eta\sigma_{13} - \zeta\sigma_{12}\ )\,dA \\ M_y & = & \int\int_A \zeta\sigma_{11}dA \\ M_z & = & -\int\int_A \eta\sigma_{11}dA \end{array}\right\} \tag{2.50}$$

The relationship between (ζ,η) and (ζ_0,η_0) can be determined using an assumption of small axial strain ϵ_{11}. Most materials can withstand 0.2% of strain ($\epsilon_{11} = 0.002$) before exhibiting inelastic behavior and hysteresis. Further, the Poisson‘s ratio ν

is less than unity for typical materials used in rotor blade and cable construction (metals and carbon composites). Thus, an upper limit for the derivatives $\frac{d\eta_0}{d\eta}$ and $\frac{d\zeta_0}{d\zeta}$ can be obtained from Eq. (2.47) as

$$\frac{d\eta_0}{d\eta} \quad = \quad \frac{d\zeta_0}{d\zeta} \quad <= \quad \sqrt{1 \quad + \quad 2 \times 0.002} \approx 1.001 \tag{2.51}$$

Based on the upper limit obtained above, a further approximation can be made - the location of points in a cross-section remain fixed with respect to the elastic axis, for the purposes of obtaining structural loads via integration over the cross-section. Thus, it is reasonable to assume that the cross-section coordinates after bending (η, ζ) are identical to their counterparts (η_0, ζ_0) before bending.

$$\eta \quad \approx \quad \eta_0 \qquad \text{and} \qquad \zeta \quad \approx \quad \zeta_0$$

Substituting for the stresses from Eq. (2.48), the structural moment components about the deformed elastic axes are obtained as

$$M_x \quad = \quad G \int\int_A [\qquad [\eta^2 + \zeta^2] \quad (\kappa_1 - \theta^+) \quad + \quad 2\eta\zeta(\nu\epsilon_{11}) \qquad] \quad dA \tag{2.52}$$

$$\left.\begin{aligned} 2M_y \quad = \quad & E \int\int_A [\quad \eta^2\zeta(\kappa_3^2 + \kappa_1^2 - \theta^{+^2}) \quad + \quad \zeta^3(\kappa_2^2 + \kappa_1^2 - \theta^{+^2}) \\ & + \quad \eta\zeta(-2\kappa_3) \quad + \quad \zeta^2(2\kappa_2) \quad + \quad \eta\zeta^2(-2\kappa_3\kappa_2) \\ & + \quad \zeta(v^{+^2} + w^{+^2} - u^{+^2} + 2u^+\sqrt{1 - v^{+^2} - w^{+^2}})] \quad dA \end{aligned}\right\} \tag{2.53}$$

$$\left.\begin{aligned} 2M_z \quad = \quad & E \int\int_A [\quad \eta^3 \left(\theta^{+^2} - \kappa_3^2 - \kappa_1^2\right) \quad + \quad \zeta^2\eta \left(\theta^{+^2} - \kappa_2^2 - \kappa_1^2\right) \\ & + \quad 2\eta^2(\kappa_3) \quad - \quad 2\zeta\eta(\kappa_2) \quad + \quad 2\eta^2\zeta(\kappa_3\kappa_2) \\ & - \quad \eta \left(v^{+^2} + w^{+^2} - u^{+^2} + 2u^+\sqrt{1 - v^{+^2} - w^{+^2}}\right)] \quad dA \end{aligned}\right\} \tag{2.54}$$

In each of the integrals, the terms in the parentheses are constant across a cross-section. Another assumption is introduced at this stage - that the *load-carrying members of the cross-section* are symmetric about the η axis. Thus, all integrals over odd polynomials in ζ vanish, and the expressions reduce to

$$\begin{aligned}
M_x &= G\int\int_A \quad (\eta^2+\zeta^2) \quad (\kappa_1-\theta^+) \quad dA \\
2M_y &= E\int\int_A [\quad \zeta^2(2\kappa_2) \quad + \quad \eta\zeta^2(-2\kappa_3\kappa_2)] \quad dA \\
2M_z &= E\int\int_A [\quad \eta^3\left(\theta^{+^2}-\kappa_3^2-\kappa_1^2\right) \quad + \quad \zeta^2\eta\left(\theta^{+^2}-\kappa_2^2-\kappa_1^2\right) \quad + \quad 2\eta^2(\kappa_3) \\
&\qquad - \quad \eta\left(v^{+^2}+w^{+^2}-u^{+^2}+2u^+\sqrt{1-v^{+^2}-w^{+^2}}\right)] \quad dA
\end{aligned}$$

The cross-section integrals are second and third moments of area, and the above expressions can be reduced to

$$\begin{aligned}
M_x &= GJ(\phi^+) \\
M_y &= EI_{\eta\eta}(\kappa_2) \quad - EI_{\eta\eta\zeta}(\kappa_3\kappa_2) \\
M_z &= \frac{1}{2}EI_{\zeta\zeta\zeta}\left(\theta^{+^2}-\kappa_3^2-\kappa_1^2\right) \quad + \quad \frac{1}{2}EI_{\eta\eta\zeta}\left(\theta^{+^2}-\kappa_2^2-\kappa_1^2\right) \quad + \quad EI_{\zeta\zeta}(\kappa_3) \\
&\quad - \quad \frac{1}{2}EAe_A\left(v^{+^2}+w^{+^2}-u^{+^2}+2u^+\sqrt{1-v^{+^2}-w^{+^2}}\right) \qquad (2.55)
\end{aligned}$$

The terms in parentheses are functions of deflection and beam pre-twist. The terms outside the parentheses are cross-section properties, i.e. the area moments of inertia and are given by

$$\begin{aligned}
I_{\zeta\zeta} &= \int\int_A \quad \eta^2 \quad dA \\
I_{\eta\eta} &= \int\int_A \quad \zeta^2 \quad dA
\end{aligned}$$

$$
\begin{aligned}
J &= I_{\zeta\zeta} + I_{\eta\eta} \\
I_{\zeta\zeta\zeta} &= \int\int_A \eta^3 \quad dA \\
I_{\eta\eta\zeta} &= \int\int_A \zeta^2\eta \quad dA \\
A &= \int\int_A dA \\
Ae_A &= \int\int_A \eta \quad dA
\end{aligned}
$$

Spatial Derivatives : Deformed and Undeformed Elastic Axis

The relationship between the spatial derivatives $\frac{\partial}{\partial r}$ and $\frac{\partial}{\partial x}$ is obtained using geometry. The differential along the deformed elastic axis may be written as

$$dr = \sqrt{(dx+du)^2 + dv^2 + dw^2} \tag{2.56}$$

Dividing Eq. (2.56) by dx, we obtain

$$\frac{dr}{dx} = \sqrt{(1+u')^2 + v'^2 + w'^2}$$

Using

$$\frac{dr}{dx} = \frac{1}{\frac{dx}{dr}} = \frac{1}{x^+}$$

We obtain

$$x^+ = \frac{1}{\sqrt{(1+u')^2 + v'^2 + w'^2}} \tag{2.57}$$

Thus,

$$()^+ = \frac{\partial}{\partial r}() = \frac{\partial}{\partial x}()x^+ = ()'x^+ \tag{2.58}$$

Squaring Eq. (2.56) and dividing by dr^2, we obtain

$$1 = (x+u)^{+^2} + v^{+^2} + w^{+^2} \tag{2.59}$$

Substituting Eq. (2.59) in Eq. (2.55), the component of the structural moment about the $\boldsymbol{k}'$ axis simplifies to

$$\begin{aligned} M_z &= \frac{1}{2}EI_{\zeta\zeta\zeta}\left(\theta^{+^2} - \kappa_3^2 - \kappa_1^2\right) + \frac{1}{2}EI_{\eta\eta\zeta}\left(\theta^{+^2} - \kappa_2^2 - \kappa_1^2\right) \\ &+ EI_{\zeta\zeta}(\kappa_3) - \frac{1}{2}EAe_A\left(1 - x^{+^2}\right) \end{aligned} \tag{2.60}$$

2.4.1.3 Ordering Scheme

Some of the area moments of inertia can be neglected because they are small *in comparison* to other terms. The cross-sections of interest have dimensions that are 10% of the span along the η coordinate, and 1% span along the ζ coordinate. Estimates for the higher moments of inertia may be obtained assuming rectangular cross-sections, and the relative magnitudes of the terms in the equations may be compared based on curvatures corresponding to a strain limit of 0.002. This analysis provides estimates for the orders of magnitude of individual terms (expressed in Newton-meters), for a beam of length "R" and allows us to identify the dominant terms, if any. The κ in Eqs. (2.61) refers to the bending curvatures only, and the twist rate κ_1 must be handled separately.

$$\left.\begin{aligned} EI_{\eta\eta\zeta}\kappa^2 &= E\kappa^2 \int\int_A \zeta^2\eta \; dA \approx 10^{-2}R^3 \\ EI_{\zeta\zeta\zeta}\kappa^2 &= E\kappa^2 \int\int_A \eta^3 \; dA \approx 10^{0}R^3 \\ EI_{\eta\eta}\kappa &= E\kappa \int\int_A \zeta^2 \; dA \approx 10^{1}R^3 \\ EI_{\zeta\zeta}\kappa &= E\kappa \int\int_A \eta^2 \; dA \approx 10^{3}R^3 \end{aligned}\right\} \tag{2.61}$$

An inspection of Eqs. (2.55) reveals that in the $\boldsymbol{j}'$ component, the dominant term is $\mathrm{EI}_{\eta\eta}\,\kappa_2$, which is at least three orders of magnitude higher than $\mathrm{EI}_{\eta\eta\zeta}\,\kappa_3\kappa_2$. Similarly, the $\boldsymbol{k}'$ component is dominated by $\mathrm{EI}_{\zeta\zeta}$, which is at least three orders of magnitude larger than the two terms involving third moments of inertia and squares of bending curvatures. With this rationalization, the structural moment components about the deformed elastic axes can be reduced (using Eq. (2.60) for the $\boldsymbol{k}'$ component) to

$$\left.\begin{array}{rcl} M_x &=& GJ(\phi^+) \\ M_y &=& EI_y(\kappa_2) \\ M_z &=& EI_{\zeta\zeta}(\kappa_3) - \frac{1}{2}EAe_A\left(1-x^{+^2}\right) - EB_2\left(\theta^+\phi^+ + \frac{1}{2}\phi^{+^2}\right) \end{array}\right\} \tag{2.62}$$

Here, $I_y = I_{\eta\eta}$ is the flap-wise moment of area for the cross-section about the *neutral* axis, and $EB_2 = I_{\eta\eta\zeta} + I_{\zeta\zeta\zeta}$. The twist rate terms are preserved with the present ordering scheme to retain the ability to model dynamics of beams with large geometric pre-twist (e.g. propeller and tilt-rotor blades). The terms in parentheses depend on the deflection (v,w) and twist (ϕ) of the elastic axis, while the terms outside the parentheses are functions of the cross-section shape and material properties.

2.4.1.4 Conversion of Structural Loads to Undeformed Frame

The $\mathbf{T}_{DU}$ matrix can be used to convert the structural forces and moments to the undeformed frame, which is used to formulate the governing equations. The quantities of interest are the structural moments and their derivatives. The spatial derivative of the components of the structural moment about the undeformed axes are

$$\begin{Bmatrix} \widetilde{M}_x^+ \\ \widetilde{M}_y^+ \\ \widetilde{M}_z^+ \end{Bmatrix} = \left(\mathbf{T}_{DU}^{\mathrm{T}}\right)^+ \begin{Bmatrix} M_x \\ M_y \\ M_z \end{Bmatrix} + \mathbf{T}_{DU}^T \begin{Bmatrix} M_x^+ \\ M_y^+ \\ M_z^+ \end{Bmatrix} \tag{2.63}$$

2.4.1.5 Governing Equations

The next step is to relate the structural moments to the axial and shear forces at a cross-section, accomplished by applying force and moment equilibrium to a section of the elastic axis that is acted upon by external forces and moments. The external loads per unit span due to the cumulative effects of inertia, gravity, buoyancy and fluid forces are denoted by $\mathbf{p}$ and $\mathbf{q}$ respectively. Applying force equilibrium for an element of length dr, we obtain

$$\mathbf{p} + \mathbf{F}_s^+ = \mathbf{0}$$

Moment equilibrium, when applied to a point on the elastic axis segment of length dr, yields after neglecting squares in the infinitesimal dr

$$\mathbf{q} + \mathbf{M}_s^+ + \boldsymbol{i}' \times \mathbf{F}_s = \mathbf{0} \tag{2.64}$$

$\mathbf{F}_s$ represents the structural force vector. Resolving into components along the undeformed axes, we obtain

$$\begin{Bmatrix} \tilde{p}_x \\ \tilde{p}_y \\ \tilde{p}_z \end{Bmatrix} = -\begin{Bmatrix} \widetilde{S}_x^+ \\ \widetilde{S}_y^+ \\ \widetilde{S}_z^+ \end{Bmatrix} \tag{2.65}$$

$$\cdot \begin{Bmatrix} \tilde{q}_x \\ \tilde{q}_y \\ \tilde{q}_z \end{Bmatrix} + \begin{Bmatrix} \widetilde{M}_x^+ \\ \widetilde{M}_y^+ \\ \widetilde{M}_z^+ \end{Bmatrix} + \begin{Bmatrix} T_{12}\widetilde{S}_z - T_{13}\widetilde{S}_y \\ T_{13}\widetilde{S}_x - T_{11}\widetilde{S}_z \\ T_{11}\widetilde{S}_y - T_{12}\widetilde{S}_x \end{Bmatrix} = \mathbf{0} \tag{2.66}$$

The shear forces can be expressed in terms of the structural moments and the axial force using Eq. (2.66) as

$$\left.\begin{aligned} \widetilde{S}_y &= \frac{T_{12}}{T_{11}}\widetilde{S}_x - \left(\widetilde{M}_z^+ + \tilde{q}_z\right)\frac{1}{T_{11}} \\ \widetilde{S}_z &= \frac{T_{13}}{T_{11}}\widetilde{S}_x + \left(\widetilde{M}_y^+ + \tilde{q}_y\right)\frac{1}{T_{11}} \end{aligned}\right\} \tag{2.67}$$

T_{ij} is the entry in row i and column j of the T_{DU} matrix given in Eq. (2.14). Substituting expressions for the shear forces in Eq. (2.67) in the X-component of Eq. (2.66) yields

$$\widetilde{M}_x^+ + \frac{T_{12}}{T_{11}}\left(\widetilde{M}_y^+ + \tilde{q}_y\right) + \frac{T_{13}}{T_{11}}\left(\widetilde{M}_z^+ + \tilde{q}_z\right) + \tilde{q}_x = 0$$

The expressions on the left hand side are exactly equal to the spatial gradient of the torsion moment along the deformed elastic axis. After multiplying by T_{11}, the equation reduces to

$$\mathbf{M}_s^+ \cdot \boldsymbol{i}' + q_x = 0 \tag{2.68}$$

Premultiply Eq. (2.63) by $\mathbf{T}_{DU}$ to obtain

$$\mathbf{T}_{DU}\widetilde{\mathbf{M}}_s^+ = \mathbf{T}_{DU}\mathbf{T}_{DU}^{T+}\mathbf{M}_s + \mathbf{T}_{DU}\mathbf{T}_{DU}^{T}\mathbf{M}_s^+ \tag{2.69}$$

The equation can be simplified further, using the following identities

$$\mathbf{T}_{DU}\ \mathbf{T}_{DU}^{\mathrm{T}} = \mathbf{I}$$

$$\mathbf{T}_{DU}^+\ \mathbf{T}_{DU}^{\mathrm{T}} + \mathbf{T}_{DU}\mathbf{T}_{DU}^{T+} = \mathbf{0}$$

$$\boldsymbol{\kappa} = \mathbf{T}_{DU}^+\ \mathbf{T}_{DU}^{\mathrm{T}} = -\,\mathbf{T}_{DU}\ \mathbf{T}_{DU}^{T+}$$

To yield

$$\mathbf{T}_{DU}\widetilde{\mathbf{M}}_s^+ \quad = \quad -\boldsymbol{\kappa}\mathbf{M}_s \quad + \quad \mathbf{M}_s^+ \tag{2.70}$$

The first row of the left hand side is $\mathbf{M}_s^+ \cdot \boldsymbol{i}'$, and can be substituted into Eq. (2.68) to obtain the beam torsion equation as

$$M_z\kappa_2 \quad - \quad M_y\kappa_3 \quad + \quad M_x^+ \quad + \quad q_x \quad = \quad 0 \tag{2.71}$$

If the slope of the vertical deflection is an odd multiple of $\frac{\pi}{2}$, the rotation matrix becomes singular and the first and third Euler rotations occur about the same axis. We will assume that this situation will not occur, since the physical configuration corresponding to a 90° slope with respect to the equilibrium position is difficult (if not impossible) to achieve for rotor blades, and for the cases of cable deflection considered. Thus, multiplications and divisions by T_{11} are permissible under these assumptions. Substituting the shear forces given by Eq. (2.67) in the force balance equation 2.65, we obtain

$$\tilde{p}_z \quad + \quad \frac{\partial}{\partial r}\left[\quad \frac{T_{13}}{T_{11}}\widetilde{S}_x \quad + \quad \left(\frac{\partial \widetilde{M}_y}{\partial r} \quad + \quad \tilde{q}_y\right)\frac{1}{T_{11}} \quad \right] \quad = \quad 0 \tag{2.72}$$

$$\tilde{p}_y \quad + \quad \frac{\partial}{\partial r}\left[\quad \frac{T_{12}}{T_{11}}\widetilde{S}_x \quad - \quad \left(\frac{\partial \widetilde{M}_z}{\partial r} \quad + \quad \tilde{q}_z\right)\frac{1}{T_{11}} \quad \right] \quad = \quad 0 \tag{2.73}$$

At this stage, the governing equations have been formulated in terms of the structural moments about the undeformed axes, which can be obtained from their deformed-frame counterparts using a coordinate transformation. The outstanding quantity that is undetermined is the term $EAe_A\frac{1}{2}(1 - x^{+^2})$ in the Z-component of Eqs. (2.62), which represents the coupling between axial force and "lag" bending due to chord-wise offset of the cross-section centroid. (A similar term would exist

in the flap bending moment if we had not assumed one axis of symmetry for the cross-section.) The term $\frac{1}{2}(1-x^{+^2})$ is the axial strain at the elastic axis $\epsilon_{11}(\eta=\zeta=0)$, or simply $\epsilon_{11}(0,0)$, which can be obtained through the following manipulations. Integrating the force equilibrium relations Eq. (2.65), we obtain the structural reaction components along the undeformed axes as

$$\left.\begin{array}{rcl} \widetilde{S}_x &=& -\int_r^R \tilde{p}_x(s)ds \\ \widetilde{S}_y &=& -\int_r^R \tilde{p}_y(s)ds \\ \widetilde{S}_z &=& -\int_r^R \tilde{p}_z(s)ds \end{array}\right\} \tag{2.74}$$

These components can be expressed in the deformed frame using a coordinate transformation (premultiplying by the $\mathbf{T}_{DU}$ matrix). The force component along the deformed elastic axis is

$$S_x = -\left(T_{11}\int_r^R \tilde{p}_x(s)ds + T_{12}\int_r^R \tilde{p}_y(s)ds + T_{13}\int_r^R \tilde{p}_z(s)ds \right) \tag{2.75}$$

The structural force S_x may also be obtained by integrating the axial strain over the cross-section, given by Eqs. (2.49) and (2.45) as

$$\begin{aligned} S_x = \int\int_A [& \frac{1}{2}\eta^2(\kappa_3^2+\kappa_1^2-\theta^{+^2}) + \frac{1}{2}\zeta^2(\kappa_2^2+\kappa_1^2-\theta^{+^2}) + \eta\zeta(-\kappa_2\kappa_3) \\ & + \eta(-\kappa_3) + \zeta(\kappa_2) + \epsilon_{11}(0,0)] \; dA \end{aligned}$$

Using the area moments of inertia to denote the integrals,

$$\begin{aligned} S_x = & \frac{1}{2}EI_{\zeta\zeta}(\kappa_3^2+\kappa_1^2-\theta^{+^2}) + \frac{1}{2}EI_{\eta\eta}(\kappa_2^2+\kappa_1^2-\theta^{+^2}) \\ & + EA\,[e_A(-\kappa_3)+\epsilon_{11}(0,0)] \end{aligned}$$

An order of magnitude analysis similar to Eq. (2.61) can be performed to isolate the dominant terms (based on an assumption of maximum bending strain)

$$S_x = EA\,[e_A(-\kappa_3)+\epsilon_{11}(0,0)] + EJ\left[\theta^+\phi^+ + \frac{1}{2}\phi^{+^2}\right] \tag{2.76}$$

Substituting for S_x from Eq. 2.75 in Eq. (2.76), we obtain the force along the elastic axis as

$$\begin{aligned} EA\epsilon_{11}(0,0) &= EA\frac{1}{2}(1-x^{+^2}) \\ &= S_x + EAe_A\kappa_3 - EJ\left(\theta^+\phi^+ + \frac{1}{2}\phi^{+^2}\right) \end{aligned} \tag{2.77}$$

Substitute the expression for $\epsilon_{11}(0,0)$ from Eq. (2.77) in Eq. (2.62) to yield an expression for the lag structural moment as

$$M_z = EI_z\kappa_3 - e_AS_x - EB_2^*\left(\theta^+\phi^+ + \frac{1}{2}\phi^{+^2}\right) \tag{2.78}$$

Where

$$I_z = I_{\zeta\zeta} - Ae_A^2 \quad ; \quad EB_2^* = EB_2 - EJe_A$$

I_z is the lag-wise second moment of area of the cross-section about the *neutral axis*, which is offset a distance e_A ahead of the elastic axis along the η coordinate. This completes the structural loads formulation, and all quantities have been expressed in terms of the external loads **p**,**q** and the deflections (v, w, ϕ).

2.4.1.6 Beam Dynamics : External Loading

Expressions for the external forces **p** and moments **q** per unit span are obtained in this section. The sources of external loading are fluid forces (aero or hydrodynamics), gravity, buoyancy and inertia. A mechanical damper is used to stabilize the rotor lag modes, and introduces point loads at its attachment point on the blade. The contributions to the external loads from each of these components are given in this section.

2.4.1.7 Lag Damper Loads

The rotor blade used in the present study is attached to the hub using coincident flap and lag hinges, and is fitted with a mechanical lag damper to provide structural damping for the in-plane motions, i.e. the first lag mode. The moments provided by the damper to the rotor blade are computed using a linear spring constant and a tabulated damping coefficient (Ref. [26]). Since the other end of the damper is attached to the airframe, its loads are internal to the entire aircraft.

2.4.1.8 Rotor Blade Boundary Condition

The rotor blades are mounted using a nexus, or *hub*, which rotates about a fixed axis on a shaft that is driven by a gas turbine engine, using a gearbox to reduce RPM and increase torque. Rotor hubs are mounted above the vehicle center of gravity due to safety requirements. Additionally, the rotor shaft is often mounted with a forward tilt with respect to the body. This shaft mount angle is critical for orienting a component the rotor thrust into the wind in forward flight without affecting longitudinal moment balance. Finally, a precone angle is given to the blade spar to reduce the flap bending moments.

In this analysis, the connections from body to shaft, shaft to hub and hub to blade are assumed to be rigid. The variations of rotor speed due to engine dynamics are assumed to be small and neglected. Therefore, the blade root motions can be obtained using rigid-body kinematics using the helicopter motions, hub offset from vehicle CG, shaft tilt and rotor rotational speed from the states corresponding to

the airframe rigid-body motions $\mathbf{y}_{\mathrm{RB}}$. The position of the rotor hub is

$$\mathbf{r}_{\mathrm{hub}} = \mathbf{r}_{\mathrm{CG}} + \begin{Bmatrix} \boldsymbol{i}_{\mathrm{G}} \\ \boldsymbol{j}_{\mathrm{G}} \\ \boldsymbol{k}_{\mathrm{G}} \end{Bmatrix}^{\mathrm{T}} \mathbf{T}_{GB} \begin{Bmatrix} \Delta \mathrm{x} \\ \Delta \mathrm{y} \\ \Delta \mathrm{z} \end{Bmatrix}_{\mathrm{hub}} \tag{2.79}$$

Where $\mathbf{T}_{GB} = \mathbf{T}_{BG}^{\mathrm{T}}$ is the rotation matrix from the earth-fixed axes to the helicopter body axes, obtained from Eq. (2.6). Rotor hub offsets from the vehicle CG are represented by $(\Delta \mathrm{x},\ \Delta \mathrm{y},\ \Delta \mathrm{z})_{\mathrm{hub}}$, measured in body-fixed axes. Differentiate Eq. (2.79) once with respect to time to obtain the hub velocity with respect to the earth as

$$\mathbf{v}_{\mathrm{hub}} = \mathbf{v}_{\mathrm{CG}} + \begin{Bmatrix} \boldsymbol{i}_{\mathrm{G}} \\ \boldsymbol{j}_{\mathrm{G}} \\ \boldsymbol{k}_{\mathrm{G}} \end{Bmatrix}^{\mathrm{T}} \dot{\mathbf{T}}_{GB} \begin{Bmatrix} \Delta \mathrm{x} \\ \Delta \mathrm{y} \\ \Delta \mathrm{z} \end{Bmatrix}_{\mathrm{hub}} \tag{2.80}$$

Traditional analyses operate in the body-fixed axes system, and the effects of angular rotation are usually accounted for using a cross-product $\omega \times \mathbf{r}_{\mathrm{hub}}$. In the present analysis, the premultiplication by $\dot{\mathbf{T}}_{GB}$ automatically accounts for these rotations and simultaneously converts the velocities to earth-fixed axes. Differentiate Eq. (2.80) once with respect to time to obtain the hub acceleration with respect to the earth as

$$\mathbf{a}_{\mathrm{hub}} = \mathbf{a}_{\mathrm{CG}} + \begin{Bmatrix} \boldsymbol{i}_{\mathrm{G}} \\ \boldsymbol{j}_{\mathrm{G}} \\ \boldsymbol{k}_{\mathrm{G}} \end{Bmatrix}^{\mathrm{T}} \ddot{\mathbf{T}}_{GB} \begin{Bmatrix} \Delta \mathrm{x} \\ \Delta \mathrm{y} \\ \Delta \mathrm{z} \end{Bmatrix}_{\mathrm{hub}} \tag{2.81}$$

The time derivatives of $\mathbf{T}_{GB}$ are given in Eqs. (2.3) and (2.4). The final component used in the formulation of beam external loads is the rotation from the earth-fixed

axes ($\boldsymbol{i}_{\text{G}}$, $\boldsymbol{j}_{\text{G}}$, $\boldsymbol{k}_{\text{G}}$, Section 2.2.1) to the blade undeformed axes ($\boldsymbol{i}$, $\boldsymbol{j}$, $\boldsymbol{k}$, Section 2.2.5). The coordinate transformation matrix and its time derivatives are given by

$$\begin{aligned}
\mathbf{T}_{UG} &= \mathbf{T}_{UH}\ \mathbf{T}_{HG} \\
\dot{\mathbf{T}}_{UG} &= \dot{\mathbf{T}}_{UH}\ \mathbf{T}_{HG} + \mathbf{T}_{UH}\ \dot{\mathbf{T}}_{HG} \\
\ddot{\mathbf{T}}_{UG} &= \ddot{\mathbf{T}}_{UH}\ \mathbf{T}_{HG} + 2\,\dot{\mathbf{T}}_{UH}\ \dot{\mathbf{T}}_{HG} + \mathbf{T}_{UH}\ \ddot{\mathbf{T}}_{HG}
\end{aligned} \tag{2.82}$$

Where

$$\begin{aligned}
\mathbf{T}_{HG} &= \mathbf{T}_{HB}\ \mathbf{T}_{BG} & \qquad \mathbf{T}_{UH} &= \mathbf{T}_{UR}\ \mathbf{T}_{RH} \\
\dot{\mathbf{T}}_{HG} &= \mathbf{T}_{HB}\ \dot{\mathbf{T}}_{BG} & \qquad \dot{\mathbf{T}}_{UH} &= \mathbf{T}_{UR}\ \dot{\mathbf{T}}_{RH} \\
\ddot{\mathbf{T}}_{HG} &= \mathbf{T}_{HB}\ \ddot{\mathbf{T}}_{BG} & \qquad \ddot{\mathbf{T}}_{UH} &= \mathbf{T}_{UR}\ \ddot{\mathbf{T}}_{RH}
\end{aligned}$$

- The matrix $\mathbf{T}_{BG}$ represents the rotation from earth-fixed axes to helicopter body axes, given in Eq. (2.6). The time derivatives of rotation matrices are obtained using Eqs. (2.3) and (2.4) by substituting $\phi = \phi_{\text{F}}$, $\theta = \theta_{\text{F}}$, $\psi = \psi_{\text{F}}$, $\dot{\phi} = \dot{\phi}_{\text{F}}$, $\dot{\theta} = \dot{\theta}_{\text{F}}$, $\dot{\psi} = \dot{\psi}_{\text{F}}$, $\ddot{\phi} = \ddot{\phi}_{\text{F}}$, $\ddot{\theta} = \ddot{\theta}_{\text{F}}$ and $\ddot{\psi} = \ddot{\psi}_{\text{F}}$.

- The terms $\mathbf{T}_{HB}$ and $\mathbf{T}_{UR}$ represent the rotations from body axes to hub non-rotating axes, and rotating blade unpreconed axes to rotating blade preconed undeformed axes, are time-invariant by definition and given in Eqs. (2.8) and (2.12) respectively.

- The matrix $\mathbf{T}_{RH}$ represents the rotation from the hub non-rotating axes to the blade rotating unpreconed axes, given in Eq. (2.10). The time derivatives of this matrix are obtained using Eqs. (2.3) and (2.4) by substituting $\phi = \theta = \dot{\phi} = \dot{\theta} = \ddot{\phi} = \ddot{\theta} = \ddot{\psi} = 0$, $\psi = \psi_j$ and $\dot{\psi} = \Omega_{\text{MR}}$.

2.4.2 Inertial Loads

Consider a flexible rotor blade mounted to a hub attachment that is translating and rotating with the helicopter. The accelerations of an arbitrary point "P" are obtained and integrated over the cross-sections to yield the sectional loads per unit span. To include the effect of helicopter hub accelerations, the coordinates of "P" are written in an earth-fixed reference as

$$\mathbf{r}_{\mathrm{P}} \quad = \quad \mathbf{r}_{\mathrm{hub}} \quad + \quad \mathbf{r}_{ea} \quad + \quad \mathbf{r}_{cs} \tag{2.83}$$

In Eq. (2.83), $\mathbf{r}_{\mathrm{hub}}$ represents the position of the hub with respect to the earth, given in Eq. (2.79) ; $\mathbf{r}_{ea}$ represents the deformed positions of the elastic axis in the undeformed frame ; $\mathbf{T}_{GU}$ is the rotation matrix from the undeformed beam axes ($\boldsymbol{i}$, $\boldsymbol{j}$, $\boldsymbol{k}$, Section 2.2.5) to the inertial axes ($\boldsymbol{i}_{\mathrm{G}}$, $\boldsymbol{j}_{\mathrm{G}}$, $\boldsymbol{k}_{\mathrm{G}}$, Section 2.2.1) ; x is the radial distance of the cross-section from the root before deformation ; (u, v, w) are the displacements of the elastic axis along the undeformed axes ; $\mathbf{T}_{GD} = \mathbf{T}_{GU}\ \mathbf{T}_{UD}$ is the rotation matrix from the beam deformed axes ($\boldsymbol{i}'$, $\boldsymbol{j}'$, $\boldsymbol{k}'$, Section 2.2.6) to the earth-fixed axes, given by Eqs. (2.14) and (2.82) ; $\mathbf{r}_{cs}$ represents the coordinates of a point in the cross-section with respect to the deformed elastic axis ; and (η, ζ) are the coordinates of P along the ($\boldsymbol{j}'$, $\boldsymbol{k}'$) axes.

$$\mathbf{r}_{ea} \quad = \quad \left\{ \begin{array}{c} \boldsymbol{i}_{\mathrm{G}} \\ \boldsymbol{j}_{\mathrm{G}} \\ \boldsymbol{k}_{\mathrm{G}} \end{array} \right\}^{\mathrm{T}} \quad \mathbf{T}_{GU} \quad \left\{ \begin{array}{c} x+u \\ v \\ w \end{array} \right\}$$

$$\mathbf{r}_{cs} = \begin{Bmatrix} \boldsymbol{i}_{\mathrm{G}} \\ \boldsymbol{j}_{\mathrm{G}} \\ \boldsymbol{k}_{\mathrm{G}} \end{Bmatrix}^{\mathrm{T}} \mathbf{T}_{GD} \begin{Bmatrix} 0 \\ \eta \\ \zeta \end{Bmatrix}$$

Differentiate Eq. (2.83) once with respect to time, to obtain

$$\mathbf{v}_p = \mathbf{v}_{\mathrm{hub}} + \dot{\mathbf{r}}_{\mathrm{ea}} + \dot{\mathbf{r}}_{\mathrm{cs}} \tag{2.84}$$

Where $\mathbf{v}_{\mathrm{hub}}$ is given in Eq. (2.80), and

$$\dot{\mathbf{r}}_{\mathrm{ea}} = \begin{Bmatrix} \boldsymbol{i}_{\mathrm{G}} \\ \boldsymbol{j}_{\mathrm{G}} \\ \boldsymbol{k}_{\mathrm{G}} \end{Bmatrix}^{\mathrm{T}} \left[\mathbf{T}_{GU} \begin{Bmatrix} \dot{u} \\ \dot{v} \\ \dot{w} \end{Bmatrix} + \dot{\mathbf{T}}_{GU} \begin{Bmatrix} x+u \\ v \\ w \end{Bmatrix} \right]$$

$$\dot{\mathbf{r}}_{cs} = \begin{Bmatrix} \boldsymbol{i}_{\mathrm{G}} \\ \boldsymbol{j}_{\mathrm{G}} \\ \boldsymbol{k}_{\mathrm{G}} \end{Bmatrix}^{\mathrm{T}} \left[\dot{\mathbf{T}}_{GD} \begin{Bmatrix} 0 \\ \eta \\ \zeta \end{Bmatrix} \right]$$

Differentiate Eq. (2.84) once with respect to time, to obtain

$$\mathbf{a}_p = \mathbf{a}_{\mathrm{hub}} + \ddot{\mathbf{r}}_{\mathrm{ea}} + \ddot{\mathbf{r}}_{\mathrm{cs}} \tag{2.85}$$

Where $\mathbf{a}_{\mathrm{hub}}$ is given by Eq. (2.81), and

$$\ddot{\mathbf{r}}_{\mathrm{ea}} = \begin{Bmatrix} \boldsymbol{i}_{\mathrm{G}} \\ \boldsymbol{j}_{\mathrm{G}} \\ \boldsymbol{k}_{\mathrm{G}} \end{Bmatrix}^{\mathrm{T}} \left[\mathbf{T}_{GU} \begin{Bmatrix} \ddot{u} \\ \ddot{v} \\ \ddot{w} \end{Bmatrix} + 2\dot{\mathbf{T}}_{GU} \begin{Bmatrix} \dot{u} \\ \dot{v} \\ \dot{w} \end{Bmatrix} + \ddot{\mathbf{T}}_{GU} \begin{Bmatrix} x+u \\ v \\ w \end{Bmatrix} \right]$$

$$\ddot{\mathbf{r}}_{\mathrm{cs}} = \begin{Bmatrix} \boldsymbol{i}_{\mathrm{G}} \\ \boldsymbol{j}_{\mathrm{G}} \\ \boldsymbol{k}_{\mathrm{G}} \end{Bmatrix}^{\mathrm{T}} \ddot{\mathbf{T}}_{GD} \begin{Bmatrix} 0 \\ \eta \\ \zeta \end{Bmatrix}$$

The inertial force per unit span is obtained by integrating the acceleration over the cross-section area as

$$\mathbf{F}_I^+ \quad = \quad -\int\int_A \quad \mathbf{a}_p \quad \rho_{\mathrm{b}} dA \tag{2.86}$$

Here, ρ_{b} represents the mass density of the rotor blade material. Since the beam equations are formulated in the undeformed reference frame, the accelerations need to be expressed in that frame. The components of the inertial force per unit span along the undeformed beam axes are

$$\begin{Bmatrix} \tilde{p}_x \\ \tilde{p}_y \\ \tilde{p}_z \end{Bmatrix}_I \quad = \quad -m\mathbf{T}_{UG} \left[\quad \begin{Bmatrix} \ddot{x}_0 \\ \ddot{y}_0 \\ \ddot{z}_0 \end{Bmatrix} \quad + \quad \begin{Bmatrix} \ddot{x}_{\mathrm{ea}} \\ \ddot{y}_{\mathrm{ea}} \\ \ddot{z}_{\mathrm{ea}} \end{Bmatrix} \quad + \quad \ddot{\mathbf{T}}_{GD} \begin{Bmatrix} 0 \\ e_A \\ 0 \end{Bmatrix} \quad \right] \tag{2.87}$$

The term m represents the mass per unit span of the rotor blade at the spanwise position of interest. The acceleration components $\mathbf{a}_{hub}$ and $\ddot{\mathbf{r}}_{\mathrm{ea}}$ are functions of the root-end motion, orientation of the undeformed frame with respect to the inertial reference and motion of the elastic axis, while $\ddot{\mathbf{r}}_{\mathrm{cs}}$ depends on the coordinates (η, ζ) of a point in the cross-section. For convenience, the first two acceleration terms are handled together, while the third term $\mathbf{r}_{\mathrm{cs}}$ is treated separately. Using a process similar to that followed for inertial forces, the moment per unit span about the deformed beam axes exerted by inertial forces on a cross-section are

$$\mathbf{M}_I^+ \quad = \quad \mathbf{M}_{I1}^+ \quad + \quad \mathbf{M}_{I2}^+$$

Where

$$\mathbf{M}_{I1}^+ \quad = \quad -\int\int_A \quad (\eta \boldsymbol{j}' + \zeta \boldsymbol{k}') \ \times \ (\mathbf{a}_{\mathrm{hub}} + \mathbf{a}_{\mathrm{ea}}) \quad \rho_{\mathrm{b}} dA$$

$$\mathbf{M}^{+}_{I2} \quad = \quad -\int\int_{A} \quad (\eta \boldsymbol{j}' + \zeta \boldsymbol{k}') \ \times \ \mathbf{a}_{\mathrm{cs}} \quad \rho_{\mathrm{b}} dA$$

The first integral $\mathbf{M}^{+}_{I1}$ contains accelerations that represent the motions of the root and elastic axis, which are independent of the cross-section coordinates (η, ζ). The components of $\mathbf{M}_{I1}$ along earth-fixed axes are

$$\begin{Bmatrix} M^{+}_{x} \\ M^{+}_{y} \\ M^{+}_{z} \end{Bmatrix}_{I1} \quad = \quad -\int\int_{A} \quad \begin{Bmatrix} r_y a_{z1} - r_z a_{y1} \\ r_z a_{x1} - r_x a_{z1} \\ r_x a_{y1} - r_y a_{x1} \end{Bmatrix} \rho_{\mathrm{b}} dA$$

Where

$$\begin{Bmatrix} r_x \\ r_y \\ r_z \end{Bmatrix} \quad = \quad \begin{Bmatrix} T^{*}_{12}\eta + T^{*}_{13}\zeta \\ T^{*}_{22}\eta + T^{*}_{23}\zeta \\ T^{*}_{32}\eta + T^{*}_{33}\zeta \end{Bmatrix}$$

$$\begin{Bmatrix} a_{x1} \\ a_{y1} \\ a_{z1} \end{Bmatrix} \quad = \quad (\mathbf{a}_{\mathrm{hub}} + \ddot{\mathbf{r}}_{\mathrm{ea}}) \cdot \begin{Bmatrix} \boldsymbol{i}_{\mathrm{G}} \\ \boldsymbol{j}_{\mathrm{G}} \\ \boldsymbol{k}_{\mathrm{G}} \end{Bmatrix}$$

$\mathbf{T}^{*}_{ij}$ is the element in row i and column j of the matrix $\mathbf{T}_{GD}$. Assuming that the cross-section has a symmetric mass distribution about the η axis, the integrals can be reduced to

$$\begin{Bmatrix} M^{+}_{x} \\ M^{+}_{y} \\ M^{+}_{z} \end{Bmatrix}_{I1} \quad = \quad m e_A \begin{Bmatrix} a_{y1} T^{*}_{32} - a_{z1} T^{*}_{22} \\ a_{z1} T^{*}_{12} - a_{x1} T^{*}_{32} \\ a_{x1} T^{*}_{22} - a_{y1} T^{*}_{12} \end{Bmatrix} \tag{2.88}$$

Where $m\ e_A = \int\int_A\ \eta\ \rho_{\mathrm{b}}\ dA$. The components of $\mathbf{M}_{I2}$ along earth-fixed axes are

$$\begin{Bmatrix} M_x^+ \\ M_y^+ \\ M_z^+ \end{Bmatrix}_{I2} = -\int\int_A \begin{Bmatrix} r_y a_{z2} - r_z a_{y2} \\ r_z a_{x2} - r_x a_{z2} \\ r_x a_{y2} - r_y a_{x2} \end{Bmatrix} \rho_{\mathrm{b}} dA \tag{2.89}$$

Where

$$\begin{Bmatrix} a_{x2} \\ a_{y2} \\ a_{z2} \end{Bmatrix} = \begin{Bmatrix} \ddot{T}^*_{12}\eta + \ddot{T}^*_{13}\zeta \\ \ddot{T}^*_{22}\eta + \ddot{T}^*_{23}\zeta \\ \ddot{T}^*_{32}\eta + \ddot{T}^*_{33}\zeta \end{Bmatrix} \tag{2.90}$$

$\ddot{T}^*_{ij}$ is the element in row i and column j in the matrix $\ddot{\mathbf{T}}_{GD}$. Expanding the expression for the X-component, we obtain

$$\begin{aligned} (M_x^+)_{I2} &= -\int\int_A \left(r_y a_{z2} - r_z a_{y2}\right) dA \\ &= -\int\int_A \left(T^*_{22}\eta + T^*_{23}\zeta\right)\left(\ddot{T}^*_{32}\eta + \ddot{T}^*_{33}\zeta\right)\rho_{\mathrm{b}} dA \\ &\quad + \int\int_A \left(T^*_{32}\eta + T^*_{33}\zeta\right)\left(\ddot{T}^*_{22}\eta + \ddot{T}^*_{23}\zeta\right)\rho_{\mathrm{b}} dA \end{aligned}$$

The integrals over the cross-section can be represented using mass moments of inertia, and the expression reduces to

$$(M_x^+)_{I2} = mk^2_{m2}\left(T^*_{32}\ddot{T}^*_{22} - T^*_{22}\ddot{T}^*_{32}\right) + mk^2_{m3}\left(T^*_{33}\ddot{T}^*_{23} - T^*_{23}\ddot{T}^*_{33}\right)$$

Cross-section symmetry about the $\boldsymbol{j}'$ axis has been used to eliminate the integrals in odd powers of ζ, and the non-zero integrals have been represented using

$$mk^2_{m2} = \int\int_A \eta^2\ \rho_{\mathrm{b}} dA \qquad\qquad mk^2_{m3} = \int\int_A \zeta^2\ \rho_{\mathrm{b}} dA$$

The terms k_{m2} and k_{m3} are the radii of gyration of the cross-section about the $\boldsymbol{k}'$ and $\boldsymbol{j}'$ axes respectively. Working similarly, the components of $\mathbf{M}_{I2}$ along $\boldsymbol{j}_{\mathrm{G}}$ and

$\boldsymbol{k}_{\mathrm{G}}$ are obtained. The three components (along earth-fixed axes) are

$$\begin{aligned}
(M_x^+)_{I2} &= mk_{m2}^2\left(T_{32}^*\ddot{T}_{22}^* - T_{22}^*\ddot{T}_{32}^*\right) + mk_{m3}^2\left(T_{33}^*\ddot{T}_{23}^* - T_{23}^*\ddot{T}_{33}^*\right) \\
(M_y^+)_{I2} &= mk_{m2}^2\left(T_{12}^*\ddot{T}_{32}^* - T_{32}^*\ddot{T}_{12}^*\right) + mk_{m3}^2\left(T_{13}^*\ddot{T}_{33}^* - T_{33}^*\ddot{T}_{13}^*\right) \\
(M_z^+)_{I2} &= mk_{m2}^2\left(T_{22}^*\ddot{T}_{12}^* - T_{12}^*\ddot{T}_{22}^*\right) + mk_{m3}^2\left(T_{23}^*\ddot{T}_{13}^* - T_{13}^*\ddot{T}_{23}^*\right)
\end{aligned} \tag{2.91}$$

The components of inertial moment per unit span about the undeformed beam axes are obtained by using a coordinate transformation on Eqs. (2.88) and (2.91), yielding

$$\begin{Bmatrix} \tilde{q}_x \\ \tilde{q}_y \\ \tilde{q}_z \end{Bmatrix}_I = \mathbf{T}_{UG}\left[\begin{Bmatrix} M_x^+ \\ M_y^+ \\ M_z^+ \end{Bmatrix}_{I1} + \begin{Bmatrix} M_x^+ \\ M_y^+ \\ M_z^+ \end{Bmatrix}_{I2} \right] \tag{2.92}$$

2.4.2.1 Gravity and Buoyancy

The effects of gravity and buoyancy are computed simultaneously, since these forces act along the $\boldsymbol{k}_{\mathrm{G}}$ axis but in opposite directions. The gravitational acceleration at a beam section is

$$\mathbf{a}_g = g\ \boldsymbol{k}_{\mathrm{G}} \tag{2.93}$$

Archimedes' principle states that the buoyancy force (upward) exerted by a fluid on a partially or completely immersed object is equal to the weight of the fluid displaced by that object. Denoting the fluid density by ρ_f and the material density of the beam by ρ_{b}, the buoyancy acceleration is

$$\mathbf{a}_b = -\frac{\rho_f}{\rho_{\mathrm{b}}} g\ \boldsymbol{k}_{\mathrm{G}} \tag{2.94}$$

Following a procedure similar to that adopted for inertial loads, the cumulative effects of gravity and buoyancy forces and moments per unit span are obtained

$$\begin{Bmatrix} \tilde{p}_x \\ \tilde{p}_y \\ \tilde{p}_z \end{Bmatrix}_{env} = \mathbf{T}_{UG} \begin{Bmatrix} 0 \\ 0 \\ 1 \end{Bmatrix} mg \left(1 - \frac{\rho_f}{\rho_b}\right) \tag{2.95}$$

$$\begin{Bmatrix} \tilde{q}_x \\ \tilde{q}_y \\ \tilde{q}_z \end{Bmatrix}_{env} = \mathbf{T}_{UG} \begin{Bmatrix} T^*_{22} \\ -T^*_{12} \\ 0 \end{Bmatrix} mg \left(1 - \frac{\rho_f}{\rho_b}\right) e_A \tag{2.96}$$

The buoyancy and gravity forces create moments about the elastic axis of a beam when the centroid has an offset e_A. This can be thought of physically as the total force on the cross-section acting at the mass centroid, which then produces a moment about the elastic axis.

2.4.3 Aerodynamic Loads

The aerodynamic forces acting on a rotor blade are obtained from the motions of the structure relative to the fluid. Since ambient winds are assumed to be absent, the fluid forces depend only on the absolute motions of the structure (and induced inflow, in the case of rotor blades) in the present analysis. From Eq. (2.84), the absolute velocity of a point in a cross-section of the beam can be resolved into

components along the deformed beam axes as

$$\begin{Bmatrix} v_1 \\ v_2 \\ v_3 \end{Bmatrix} = \mathbf{T}_{DG} \begin{Bmatrix} \dot{x}_0 \\ \dot{y}_0 \\ \dot{z}_0 \end{Bmatrix} + \mathbf{T}_{DU} \begin{Bmatrix} \dot{u} \\ \dot{v} \\ \dot{w} \end{Bmatrix} + \mathbf{T}_{DG}\, \dot{\mathbf{T}}_{GU} \begin{Bmatrix} x+u \\ v \\ w \end{Bmatrix}$$
$$+ \mathbf{T}_{DG}\, \dot{\mathbf{T}}_{GD} \begin{Bmatrix} 0 \\ \eta \\ \zeta \end{Bmatrix}$$

The velocity of air relative to the structure is equal in magnitude and opposite in direction to the velocity of the structure relative to the fluid. In the case of a rotor blade, the induced inflow must be accounted for in computing the velocity of the air relative to the blade sections. The velocity components for a counter-clockwise turning rotor are shown in Fig. 2.10, given by

$$\begin{Bmatrix} U_R \\ U_T \\ U_P \end{Bmatrix} = \begin{Bmatrix} -v_1 \\ v_2 \\ -v_3 \end{Bmatrix} + \begin{Bmatrix} V_{xi} \\ -V_{yi} \\ V_{zi} \end{Bmatrix}$$
$$\begin{Bmatrix} V_{xi} \\ V_{yi} \\ V_{zi} \end{Bmatrix} = \mathbf{T}_{DH} \begin{Bmatrix} \lambda_{xi} \\ \lambda_{yi} \\ \lambda_{zi} \end{Bmatrix}$$

U_T is the tangential velocity along the airfoil reference line, U_P is the "upwash" velocity for the airfoil section, U_R is the spanwise flow velocity, defined positive outward as shown in Fig. 2.10. (V_{xi}, V_{yi}, V_{zi}) are the induced velocity components in the deformed frame, and the inflow components (non-dimensionalized by tip

speed) along the hub non-rotating axes are (λ_{xi}, λ_{yi}, λ_{zi}). $\mathbf{T}_{DH} = \mathbf{T}_{DU}\ \mathbf{T}_{UR}\ \mathbf{T}_{RH}$ is the transformation matrix from the hub non-rotating axes to the blade deformed frame, obtained from Eqs. (2.14), (2.12) and (2.10).

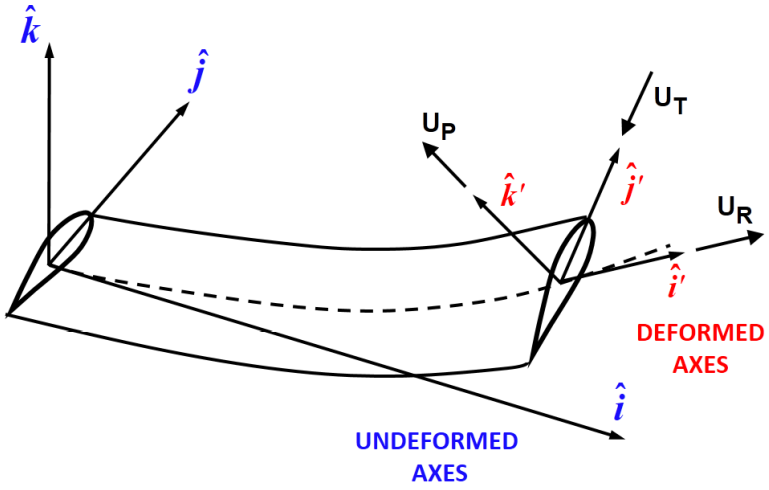

Figure 2.10: Velocity Components in Deformed Axes

Fluid Forces on an Airfoil Section

Main rotor blades are composed of airfoil cross-sections. These beam sections operate in a three-dimensional flow environment when the flow velocity has a component normal to the cross-section. For rotor blades, flow along the longitudinal direction is often referred to as "radial flow". The presence of a flow velocity component along the elastic axis implies that the resultant velocity vector is not contained in the same plane as the airfoil cross-sections, as shown in Fig. 2.11. The angle of attack of the section in a plane containing the resultant velocity is

$$\alpha \quad = \quad \tan^{-1} \frac{U_P}{\sqrt{U_T^2 + U_R^2}} \tag{2.97}$$

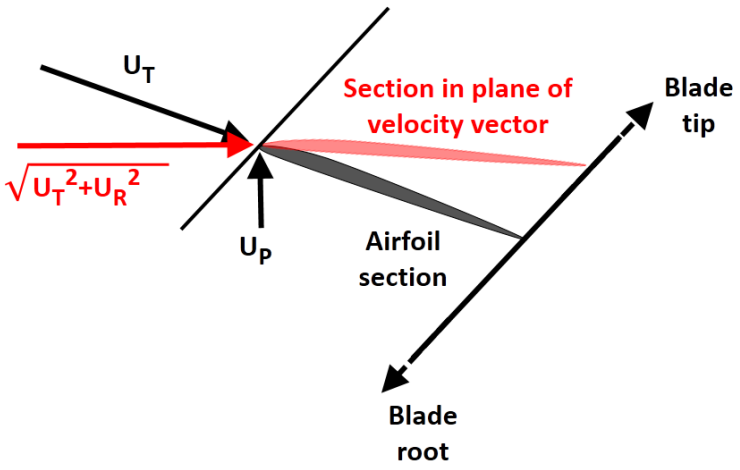

Figure 2.11: Blade Airfoil Section in Radial Flow

The skew angle γ_{I} that occurs due to radial flow is defined as the angle between the components U_T and U_R, given by

$$\gamma_{\text{I}} = \tan^{-1}\frac{U_R}{U_T}$$

Empirical corrections are implemented as given in Ref. [90] to compute the lift, drag and moment coefficients in yawed (radial) flow as

$$\begin{aligned} \frac{dL}{dr} &= \frac{dL_C}{dr} + \frac{dL_{NC}}{dr} \\ \frac{dD}{dr} &= \frac{1}{2}\,\rho\,V_\infty^2\,c\,C_d(\alpha, M) \\ \frac{dM_A}{dr} &= \frac{dM_C}{dr} + \frac{dM_{NC}}{dr} \end{aligned} \tag{2.98}$$

V_∞ is the free-stream velocity magnitude at the elastic axis, given by

$$V_\infty = \sqrt{U_T^2 + U_P^2 + U_R^2}$$

L_C^+ is the lift per unit span from circulatory forces (Ref. [27]) that acts at the aerodynamic center, obtained from the angle of attack at three-quarter chord as

$$L_C^+ = \frac{1}{2}\,\rho\,V_\infty^2\,c\,C_\ell(\alpha\cos\gamma_{\text{I}}, M) \qquad \text{at aerodynamic center}$$

The non-circulatory component of lift distribution (Ref. [27]) is given by

$$\begin{aligned} L^+_{NC} &= L^+_2 + L^+_3 \qquad \text{Where} \\ L^+_2 &= \frac{\pi}{4}\,\rho\,c^2\,\ddot{h}\Big|_{0.5\text{ c}} \qquad \text{at mid-chord} \\ L^+_3 &= \frac{\pi}{4}\,\rho\,c^2\,V_\infty\,\dot{\alpha} \qquad \text{at 3/4 chord} \end{aligned}$$

$\ddot{h}\Big|_{0.5\text{ c}}$ is the plunge acceleration at mid-chord. The aerodynamic moment per unit span about the elastic axis due to circulatory forces is

$$M^+_C = \frac{1}{2}\,\rho\,V^2_\infty\,c^2\,C_m(\alpha\cos\gamma_{\text{I}}, M) + x_{\text{ac}}L^+_C - \frac{\pi}{16}\,\dot{\alpha}\,\rho\,V_\infty\,c^3$$

x_{ac} is the chordwise offset of the aerodynamic center from the elastic axis, positive towards the leading edge. The non-circulatory component of pitching moment distribution about the elastic axis is

$$M^+_{NC} = L^+_2 x_{\text{mc}} + L^+_3 x_{0.75\text{c}} - \frac{\pi\rho c^4}{128}\ddot{\alpha} \tag{2.99}$$

(x_{mc}, $x_{0.75\text{c}}$) are the locations of the mid-chord and three-quarter chord points, respectively, with respect the the elastic axis and are positive when these locations are between the leading edge and the elastic axis. The last term in the non-circulatory moments is dropped, since its magnitude is small compared to the quasi-steady contributions for rotor blades in the frequency range of interest ($\omega \leq 10$ rad/s). The terms C_ℓ, C_d and C_m are the airfoil lift, drag and moment coefficients obtained from experiment-based tables. The force components in the beam deformed axes are

$$\begin{Bmatrix} p_x \\ p_y \\ p_z \end{Bmatrix}_{\text{aero}} = \frac{1}{V_\infty} \begin{Bmatrix} D^+U_R - L^+U_P\sin\gamma_{\text{I}} \\ -D^+U_T + L^+U_P\cos\gamma_{\text{I}} \\ D^+U_P + L^+\sqrt{U^2_T + U^2_R} \end{Bmatrix} \tag{2.100}$$

$$\left\{\begin{array}{c} q_x \\ q_y \\ q_z \end{array}\right\}_{\text{aero}} = \left\{\begin{array}{c} M_A^+ \cos\gamma_{\text{I}} \\ M_A^+ \sin\gamma_{\text{I}} \\ 0 \end{array}\right\} \tag{2.101}$$

These loads are converted to the undeformed frame using the $\mathbf{T}_{UD}$ rotation matrix, obtained from Eq. (2.14), to yield

$$\left\{\begin{array}{c} \tilde{p}_x \\ \tilde{p}_y \\ \tilde{p}_z \end{array}\right\}_{\text{aero}} = \mathbf{T}_{UD} \left\{\begin{array}{c} p_x \\ p_y \\ p_z \end{array}\right\}_{\text{aero}} \tag{2.102}$$

$$\left\{\begin{array}{c} \tilde{q}_x \\ \tilde{q}_y \\ \tilde{q}_z \end{array}\right\}_{\text{aero}} = \mathbf{T}_{UD} \left\{\begin{array}{c} q_x \\ q_y \\ q_z \end{array}\right\}_{\text{aero}} \tag{2.103}$$

2.4.4 Hub Loads

The forces and moments transmitted to the hub are obtained by integrating the loads along the span and summing the contributions from each of the blades. The force components along the rotating undeformed axes from the j^{th} blade are

$$\begin{aligned} X_{\text{R}}(j) &= \int_0^R \tilde{p}_x \, dr \\ Y_{\text{R}}(j) &= \int_0^R \tilde{p}_y \, dr \\ Z_{\text{R}}(j) &= \int_0^R \tilde{p}_z \, dr \end{aligned}$$

Where $\tilde{p}_x, \tilde{p}_y, \tilde{p}_z$ represent the load components per unit span along the rotating undeformed blade axes, containing the sum of inertial, aerodynamic, gravitational

and buoyancy loads given in Eqs. (2.87) and (2.102). The moment components along the rotating undeformed axes from the j^{th} blade are

$$\begin{aligned} L_{\text{R}}(j) &= \int_0^R [\tilde{q}_x \ + \ v \ \tilde{p}_z \ - \ w \ \tilde{p}_y] \ dr \\ M_{\text{R}}(j) &= \int_0^R [\tilde{q}_y \ + \ w \ \tilde{p}_x \ - \ (x+u) \ \tilde{p}_z] \ dr \\ N_{\text{R}}(j) &= \int_0^R [\tilde{q}_z \ + \ (x+u) \ \tilde{p}_y \ - \ v \ \tilde{p}_x] \ dr \end{aligned}$$

Where $\tilde{q}_x$, $\tilde{q}_y$, $\tilde{q}_z$ represent the moment components per unit span along the rotating undeformed blade axes, containing the sum of inertial and aerodynamic loads given in Eqs. (2.92) and (2.103). The hub loads are obtained by resolving the blade loads along the hub non-rotating axes and summing the contributions from individual blades. The hub force and moment components are

$$\begin{Bmatrix} X_{\text{NR}} \\ Y_{\text{NR}} \\ Z_{\text{NR}} \end{Bmatrix} = \sum_{j=1}^{N_b} \mathbf{T}_{RH}^{\text{T}} \ \mathbf{T}_{UR}^{\text{T}} \begin{Bmatrix} F_{\text{XR}} \\ F_{\text{YR}} \\ F_{\text{ZR}} \end{Bmatrix}$$

$$\begin{Bmatrix} L_{\text{NR}} \\ M_{\text{NR}} \\ N_{\text{NR}} \end{Bmatrix} = \sum_{j=1}^{N_b} \mathbf{T}_{RH}^{\text{T}} \ \mathbf{T}_{UR}^{\text{T}} \begin{Bmatrix} M_{\text{XR}} \\ M_{\text{YR}} \\ M_{\text{ZR}} \end{Bmatrix}$$

Where the matrices $\mathbf{T}_{RH}^{\text{T}}$ and $\mathbf{T}_{UR}^{\text{T}}$ are obtained from Eqs. (2.10) and (2.12), and the azimuth angle of the j^{th} blade is $\psi_j \ = \ \psi_1 \ + \ \dfrac{2\pi}{N_b}(j-1)$. Finally, the hub loads are converted to the helicopter body axes using the transformation matrix $\mathbf{T}_{BH} = \mathbf{T}_{HB}^{\text{T}}$ from Eq. (2.8), to yield the contributions from the main rotor to the

vehicle force and moment equilibrium Eqs. (2.20) - (2.28) as

$$\begin{Bmatrix} X_{\text{MR}} \\ Y_{\text{MR}} \\ Z_{\text{MR}} \end{Bmatrix} = \mathbf{T}_{BH} \begin{Bmatrix} X_{\text{NR}} \\ Y_{\text{NR}} \\ Z_{\text{NR}} \end{Bmatrix} \tag{2.104}$$

$$\begin{Bmatrix} L_{\text{MR}} \\ M_{\text{MR}} \\ N_{\text{MR}} \end{Bmatrix} = \mathbf{T}_{BH} \begin{Bmatrix} L_{\text{NR}} \\ M_{\text{NR}} \\ N_{\text{NR}} \end{Bmatrix} + \begin{Bmatrix} \Delta \text{y}_{\text{hub}}\ Z_{\text{MR}} - \Delta \text{z}_{\text{hub}}\ Y_{\text{MR}} \\ \Delta \text{z}_{\text{hub}}\ X_{\text{MR}} - \Delta \text{x}_{\text{hub}}\ Z_{\text{MR}} \\ \Delta \text{x}_{\text{hub}}\ Y_{\text{MR}} - \Delta \text{y}_{\text{hub}}\ X_{\text{MR}} \end{Bmatrix} \tag{2.105}$$

2.4.5 Approximate Solution and the Galerkin Method

Equations 2.71, 2.72 and 2.73 are nonlinear *Partial Differential Equations*, since the non-structural (external) loads **p** and **q** include inertial accelerations and fluid forces that depend on the time derivatives of v, w and ϕ. Galerkin's method of weighted residuals is used to transform these equations into a system of *Ordinary Differential Equations* to reduce the computational cost for obtaining a solution. As a result, the beam equations are rendered compatible to use in a state-space formulation (system of coupled ODEs). The solutions of these ODEs are called *weak* solutions, since they satisfy the original PDEs in an *average* sense instead of at every point along the beam. The problem of beam bending and torsion is solved using separation of variables, and the deflections can be parameterized using spatial and temporally-varying components as

$$v = \sum_{i=1}^{N_v} q_{v,i} \gamma_{v,i}$$

$$
\begin{aligned}
w &= \sum_{i=1}^{N_w} q_{w,i}\gamma_{w,i} \\
\phi &= \sum_{i=1}^{N_\phi} q_{\phi,i}\gamma_{\phi}
\end{aligned}
$$

$\gamma_{v,i}$, $\gamma_{w,i}$ and $\gamma_{\phi,i}$ are the trial functions that depend on the span-wise position r, and $q_{v,i}$, $q_{w,i}$, $q_{\phi,i}$ are the trial function coefficients that depend only on time. Let the original PDEs in Eqs. (2.71) - (2.73) be represented by

$$
\begin{aligned}
f_\phi(v,w,\phi) &= 0 \\
f_{\mathrm{w}}(v,w,\phi) &= 0 \\
f_{\mathrm{v}}(v,w,\phi) &= 0
\end{aligned}
$$

Trial functions that are admissible for each equation are used to obtain the weighed residuals, and the problem of solving the PDE is converted to that of finding the coefficients $q_{v,i}$, $q_{w,i}$ and $q_{\phi,i}$ such that

$$
\left.
\begin{aligned}
\int_0^R f_\phi(v,w,\phi)\gamma_{v,i}\, dr &= 0 \\
\int_0^R f_{\mathrm{w}}(v,w,\phi)\gamma_{w,i}\, dr &= 0 \\
\int_0^R f_{\mathrm{v}}(v,w,\phi)\gamma_{\phi,i}\, dr &= 0
\end{aligned}
\right\} \tag{2.106}
$$

Consider the elastic twist equation 2.71. A weak solution must satisfy

$$
\int_0^R \left(M_z\kappa_2 - M_y\kappa_3 + M_x^+ + q_x\right)\gamma_{\phi,i} dr = \epsilon_{\phi,i} = 0 \tag{2.107}
$$

For practical purposes, we will further relax the condition that the residuals $\epsilon_{\phi,i}$ be exactly zero. Instead, the weak solutions are assumed to be obtained when the residuals decrease (in magnitude) below a specified threshold δ_0. This threshold is set to a small number relative to the magnitudes of the terms in the original PDE.

The numerical values of the structural moments can be computed from the elastic deflections (v, w, ϕ) and used without further manipulation to compute the residuals of the modified PDEs. However, terms involving spatial derivatives (e.g. M_x^+) needs to be handled differently. When lower-order polynomial trial functions are used, repeated differentiation results in loss of information and erroneous computation of the spatial gradient for structural loads. To avoid these errors, the residuals of the modified PDEs are computed using regular span-wise integration for terms that are "directly" available, and using integration by parts for the derivatives with respect to r. Following this approach,

$$\begin{aligned}
\epsilon_{\phi,i} &= \int_0^R \left[\left(M_z\kappa_2 - M_y\kappa_3 + q_x\right)\gamma_{\phi,i} - M_x\gamma_{\phi,i}^+ \right] dr \\
&\quad + M_x\gamma_{\phi,i}\Big|_0^R
\end{aligned}$$

$$\begin{aligned}
\epsilon_{w,i} &= \int_0^R \left[\tilde{p}_z\gamma_{w,i} - \left(\frac{T_{13}\widetilde{S}_x + \tilde{q}_y}{T_{11}}\right)\gamma_{w,i}^+ + \left(\frac{\gamma_{w,i}^+}{T_{11}}\right)^+ \widetilde{M}_y \right] dr \\
&\quad + \frac{T_{13}\widetilde{S}_x + \tilde{q}_y + \widetilde{M}_y^+}{T_{11}}\gamma_{w,i}\Big|_0^R - \frac{\gamma_{w,i}^+}{T_{11}}\widetilde{M}_y\Big|_0^R
\end{aligned}$$

$$\begin{aligned}
\epsilon_{v,i} &= \int_0^R \left[\tilde{p}_y\gamma_{v,i} - \left(\frac{T_{12}\widetilde{S}_x - \tilde{q}_z}{T_{11}}\right)\gamma_{v,i}^+ - \left(\frac{\gamma_{v,i}^+}{T_{11}}\right)^+ \widetilde{M}_z \right] dr \\
&\quad + \frac{T_{12}\widetilde{S}_x - \tilde{q}_z - \widetilde{M}_z^+}{T_{11}}\gamma_{v,i}\Big|_0^R + \frac{\gamma_{v,i}^+}{T_{11}}\widetilde{M}_z\Big|_0^R
\end{aligned}$$

Using Eq. (2.67), the boundary-value terms may be identified as tip loads, and the residuals of the modified PDEs can be simplified to

$$\epsilon_{\phi,i} = \int_0^R \left(M_z\kappa_2 - M_y\kappa_3 + q_x\right)\gamma_{\phi,i} dr$$

$$- \quad \int_0^R \gamma_{\phi,i}^+ M_x dr \quad + \quad M_x \gamma_{\phi,i} \Big|_0^R \tag{2.108}$$

$$\begin{aligned} \epsilon_{w,i} \quad = \quad & \int_0^R \quad \tilde{p}_z \gamma_{w,i} dr \quad + \quad \left(\widetilde{S}_z \gamma_{w,i} - \frac{\widetilde{M}_y \gamma_{w,i}^+}{T_{11}} \right) \Big|_0^R \\ & - \quad \int_0^R \frac{T_{13} \widetilde{S}_x + \tilde{q}_y}{T_{11}} \gamma_{w,i}^+ dr \quad + \quad \int_0^R \left(\frac{\gamma_{w,i}^+}{T_{11}} \right)^+ \widetilde{M}_y dr \end{aligned} \tag{2.109}$$

$$\begin{aligned} \epsilon_{v,i} \quad = \quad & \int_0^R \quad \tilde{p}_y \gamma_{v,i} dr \quad + \quad \left(\widetilde{S}_y \gamma_{v,i} + \frac{\widetilde{M}_z \gamma_{v,i}^+}{T_{11}} \right) \Big|_0^R \\ & - \quad \int_0^R \frac{T_{12} \widetilde{S}_x - \tilde{q}_z}{T_{11}} \gamma_{v,i}^+ dr \quad - \quad \int_0^R \left(\frac{\gamma_{v,i}^+}{T_{11}} \right)^+ \widetilde{M}_z dr \end{aligned} \tag{2.110}$$

Table 2.1: Boundary conditions for beams

Boundary condition	Mathematical Representation
Root restraint	$\gamma_{w,i}(0) = \gamma_{v,i}(0) = 0$
Torsion restraint	$\gamma_{\phi,i}(0) = 0$
Cantilever	$\gamma_{w,i}^+(0) = \gamma_{v,i}^+(0) = 0$
Hinge	$\widetilde{M}_y(0) = \widetilde{M}_z(0) = 0$
Swivel	$\widetilde{M}_x(0) = 0$
Free end	$\mathbf{M}_S = \mathbf{F}_S = \mathbf{0}$

Physical considerations will be used to handle the boundary-value terms at the lower limit, i.e. $r = 0$ or the root end. The constraint conditions for the ends of the beam that are modeled are cantilever supports and hinges. Based on these

conditions, the choice of admissible trial functions is limited to those that satisfy properties given in Table 2.1.

2.4.6 Finite Element Discretization

The trial functions $\gamma_{v,i}$, $\gamma_{w,i}$, $\gamma_{\phi,i}$ must be continuous along the span to accurately reflect the nature of the physical deflections. Since the beam exhibits smoothly changing gradients of transverse deflections (slopes), the first derivatives $\gamma^+_{w,i}$, $\gamma^+_{v,i}$ must also be continuous. Therefore, polynomials are a natural choice to represent beam deflections. In cases where certain sections of the beam have higher curvatures than others, higher-order polynomials become necessary to accurately represent beam deflections but are susceptible to Runge oscillations during interpolation. Therefore, the trial functions are built using *local* polynomials, or *shape functions*, that are smoothly fitted over multiple segments, or *finite elements*, of the beam. A natural choice of shape functions for the transverse deflections (v, w) within an element is the set of Hermite polynomials

$$\begin{aligned} H_{w,1}(s) &= 2s^3 - 3s^2 + 1 \\ H_{w,2}(s) &= l_e(s^3 - 2s^2 + s) \\ H_{w,3}(s) &= 1 - H_{w,1}(s) \\ H_{w,4}(s) &= l_e(s^3 - s^2) \end{aligned}$$

s represents the non-dimensional span location along an element of length l_e. The shape functions for the "lag" deflection (v) are identical to $H_{w,i}$ given above, since the transverse deflections have identical representation constraints. For torsion,

the twist angle (ϕ) must be continuous, but the twist rate (ϕ^+) need not. Thus, quadratic shape functions are sufficient to accurately represent linear variations in twist rate along an element, and are given by

$$\begin{aligned} H_{\phi,1}(s) &= 2s^2 - 3s + 1 \\ H_{\phi,2}(s) &= -4s^2 + 4s \\ H_{\phi,3}(s) &= 2s^2 - s \end{aligned}$$

The shape functions for bending $H_{w,i}$ and torsion $H_{\phi,i}$ are shown in Fig. 2.12. The trial functions $\gamma_{w,i}$, $\gamma_{\phi,i}$ are obtained using *admissible* linearly independent combinations of the shape functions, i.e. those that preserve continuity along the span and, in the case of the transverse bending, differentiability also. The trial functions for transverse bending $\gamma_{w,i}$ and $\gamma_{v,i}$ are identical, since they are constructed from the same shape functions.

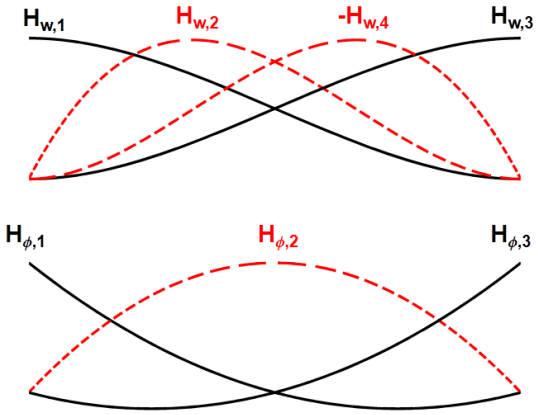

Figure 2.12: Shape Functions in a Finite Element

Figures 2.13 and 2.14 show the trial functions for transverse bending and torsion, respectively, for a beam with four finite elements, together with the coefficients $q_{w,i}$ and $q_{\phi,i}$ that represent the numerical value of the trial function coefficients at

the intersection of finite elements, called *nodes*.

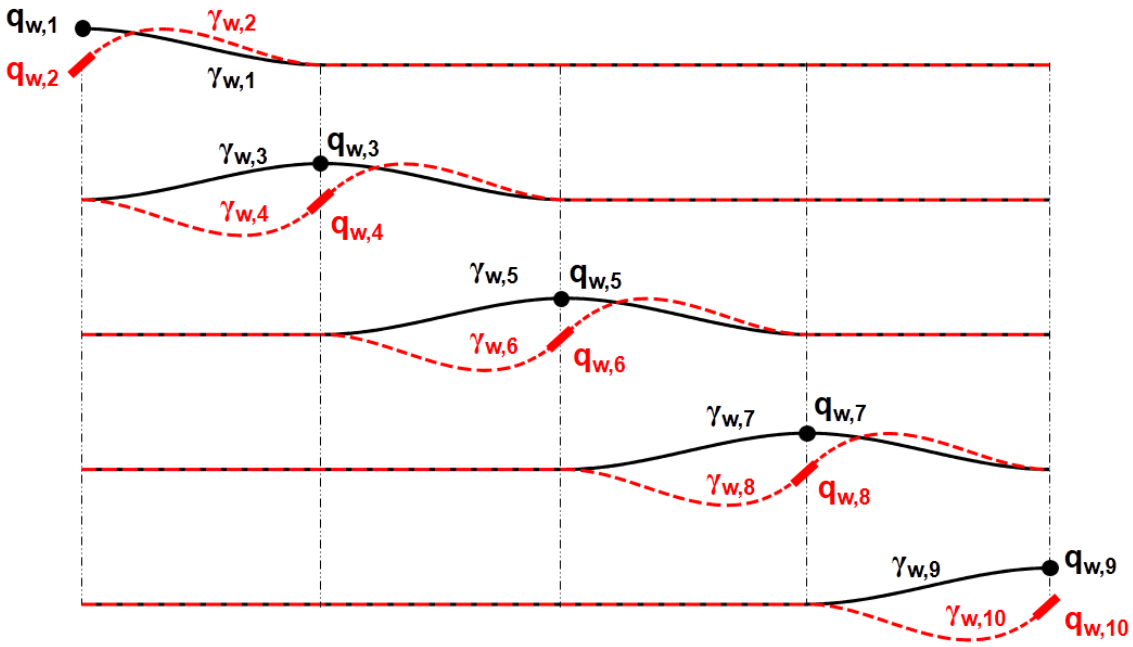

Figure 2.13: Trial Functions for Beam Bending with 4 Finite Elements

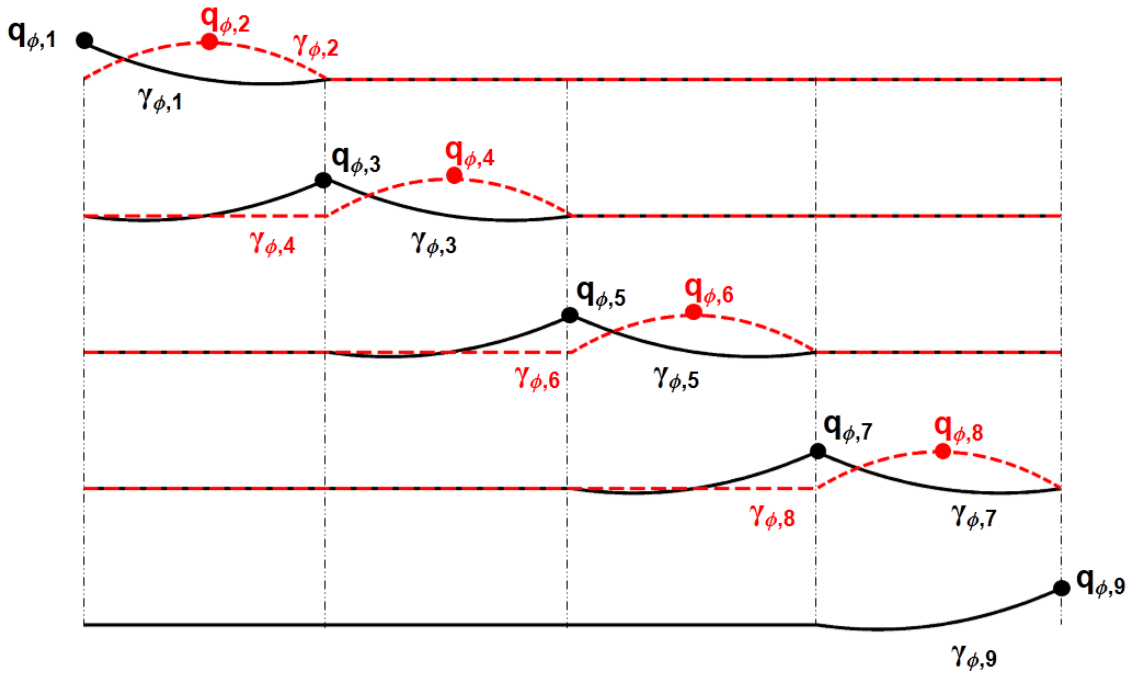

Figure 2.14: Trial Functions for Beam Torsion with 4 Finite Elements

After applying boundary conditions, the appropriate degrees of freedom and trial functions are eliminated from the system of equations before computing the residuals $\epsilon_{w,i}$, $\epsilon_{v,i}$ and $\epsilon_{\phi,i}$ of the modified PDEs.

2.4.7 Modal Reduction

The flap, lag and torsion dynamics of each rotor blade is represented using $6N_e$+5 ODEs, where N_e is the number of finite elements. For a four-bladed rotor each with four finite elements, this results in 116 ODEs for the rotor dynamics. With increasing variations in the spatial distribution of aerodynamic and inertial loads (e.g. high-speed forward flight or BVI conditions), additional finite elements are required to obtain accurate blade force distributions, and the subsequent blade response and vehicle motions. However, additional finite elements also result in increased computational cost, in terms of the number of ODEs used to represent the system dynamics. One technique to **reduce the computational cost without compromising the accuracy of the load distributions** is modal reduction.

The operating condition of the physical system (typical helicopter blades) are such that its structural dynamics are strongly linear, with mild contributions from non-linear components (due to axial fore-shortening and elastic flap-lag-torsion couplings). Therefore, the deflections of the rotor blade can be approximated to a linear combination of the natural mode shapes. These mode shapes are obtained from eigenvector solutions of the linearized structural dynamics for the rotating blade in vacuum, and are orthogonal to each other. Each mode is associated with a natural

frequency. Higher natural frequencies are associated with larger spatial variations in the deflections (more zero crossings and larger bending curvatures/twist rates) and therefore more elastic energy. For typical rotor blades, the energy required to excite the high-frequency modes is relatively enormous, and is typically not encountered in flight, where the external forces are continuous and near-monotonic along the span. With this rationalization, **the blade response is approximated to a linear combination of a finite number of natural mode shapes**. **Modal reduction effectively decouples the computational complexity of the rotor ODEs from the spatial resolution of the external loads while preserving the dominant blade motions**. For the purpose of modal reduction, it is convenient to use the original form of the beam equations, given by

$$\mathbf{g}_{\text{rotor}}(\mathbf{q}, \dot{\mathbf{q}}, \ddot{\mathbf{q}}, \mathbf{u}) \quad = \quad \boldsymbol{\epsilon}_{\text{beam}} \quad = \quad \mathbf{0}$$

The beam equation residuals can be subdivided into the contributions from the flap, lag and torsion equations as

$$\boldsymbol{\epsilon}_{\text{beam}} \quad = \quad \left\{ \quad \boldsymbol{\epsilon}_{\phi}^{\mathrm{T}} \quad \boldsymbol{\epsilon}_{w}^{\mathrm{T}} \quad \boldsymbol{\epsilon}_{v}^{\mathrm{T}} \quad \right\}^{\mathrm{T}}$$

$\epsilon_{\phi,i}, \epsilon_{w,i}$ and $\epsilon_{v,i}$ are given by Eqs. (2.108) – (2.110)

$$\boldsymbol{\epsilon}_{\phi} \quad = \quad \left\{ \quad \epsilon_{\phi,1} \quad \epsilon_{\phi,2} \quad \cdots \quad \epsilon_{\phi,n} \quad \right\}^{\mathrm{T}}$$

$$\boldsymbol{\epsilon}_{w} \quad = \quad \left\{ \quad \epsilon_{w,1} \quad \epsilon_{w,2} \quad \cdots \quad \epsilon_{w,n} \quad \right\}^{\mathrm{T}}$$

$$\boldsymbol{\epsilon}_{v} \quad = \quad \left\{ \quad \epsilon_{v,1} \quad \epsilon_{v,2} \quad \cdots \quad \epsilon_{v,n} \quad \right\}^{\mathrm{T}}$$

The nodal degrees of freedom are

$$\mathbf{q} \quad = \quad \left\{ \quad \mathbf{q}_{w}^{\mathrm{T}} \quad \mathbf{q}_{v}^{\mathrm{T}} \quad \mathbf{q}_{\phi}^{\mathrm{T}} \quad \right\}^{\mathrm{T}}$$

Where

$$\begin{aligned}
\mathbf{q}_w &= \left\{ \quad q_{w,1} \quad q_{w,2} \quad \cdots \quad q_{w,n} \quad \right\}^{\mathrm{T}} \\
\mathbf{q}_v &= \left\{ \quad q_{v,1} \quad q_{v,2} \quad \cdots \quad q_{v,n} \quad \right\}^{\mathrm{T}} \\
\mathbf{q}_\phi &= \left\{ \quad q_{\phi,1} \quad q_{\phi,2} \quad \cdots \quad q_{\phi,n-1} \quad \right\}^{\mathrm{T}}
\end{aligned}$$

$\mathbf{q}_w$, $\mathbf{q}_v$ represent the flap and lag nodal degrees of freedom respectively, each of which number $n = 2N_e + 2$. The torsion nodal degrees of freedom are $\mathbf{q}_\phi$ which number $n - 1 = 2N_e + 1$. Figures 2.13 and 2.14 show the nodal degrees of freedom for flap bending and torsion, respectively, for four finite elements.

The entries in row i and column j of the stiffness and mass matrix are approximated using finite differences, and are given by

$$\begin{aligned}
K_{i,j} &= \frac{\partial \boldsymbol{\epsilon}_{\mathrm{beam}}(i)}{\partial \mathbf{q}(j)} \approx \frac{\Delta \boldsymbol{\epsilon}_{\mathrm{beam}}(i)}{\Delta \mathbf{q}(j)} \\
M_{i,j} &= \frac{\partial \boldsymbol{\epsilon}_{\mathrm{beam}}(i)}{\partial \ddot{\mathbf{q}}(j)} \approx \frac{\Delta \boldsymbol{\epsilon}_{\mathrm{beam}}(i)}{\Delta \ddot{\mathbf{q}}(j)}
\end{aligned}$$

$\Delta \boldsymbol{\epsilon}_{\mathrm{beam}}(i)$ represents the change in the residual of the i^{th} beam equation. $\Delta \mathbf{q}(j)$ and $\Delta \ddot{\mathbf{q}}(j)$ represent, respectively, perturbations in the j^{th} nodal degree of freedom and its second time derivative. The linearized beam dynamics in vacuum may then be written as a series of coupled second-order ODEs given by

$$\mathbf{M}\ \ddot{\mathbf{q}}(t) \quad + \quad \mathbf{K}\ \mathbf{q}(t) \quad = \quad \mathbf{0} \tag{2.111}$$

Since $\mathbf{M}$ and $\mathbf{K}$ are time-invariant, the solution for the nodal degrees of freedom $\mathbf{q}$ is of the form

$$\mathbf{q}(t) \quad = \quad \mathbf{q_0}\ \sin \omega t$$

Substituting this solution into Eq. (2.111) yields the following Eigenvalue problem

$$\mathbf{M}\,\omega^2\,\mathbf{q_0} \quad = \quad \mathbf{K}\,\mathbf{q_0}$$

An inspection of the above expression reveals that the square roots of the Eigenvalues represent the natural frequencies of the rotating beam. The Eigenvectors represent the natural mode shapes of the rotating beam. When the cumulative spanwise distribution of the external loads resembles a particular mode shape, the blade response consists predominantly of that mode shape. The Eigenvectors for the modes of interest are assembled into a matrix $\mathbf{V}$, and the nodal degrees of freedom can be computed from the mode coefficients $\boldsymbol{\eta}$ as

$$\mathbf{q} \quad = \quad \boldsymbol{\eta}^{\mathrm{T}}\,\mathbf{V}$$

The mode coefficients $\boldsymbol{\eta}$ are the generalized displacements of the rotor blades when modal reduction is used. If modal reduction is not selected, then $\mathbf{V}$ is set to an identity matrix of the appropriate size, and the generalized displacements are the nodal degrees of freedom ($\mathbf{q}_\phi$, $\mathbf{q}_w$, $\mathbf{q}_v$) of the flexible beam.

Modal reduction can be conceptualized as a second-stage Galerkin method applied to the modified beam PDEs. The nodal degrees of freedom are expressed as a linear combination of the normal mode shapes. In Galerkin's method, the trial functions must be equal to the shape functions used to represent the nodal deflections. (For modal reduction, the term "function" may be somewhat misleading, since the shape functions - Eigenvectors - consist of discrete values of the beam deflection at the finite element nodes.) Therefore, the residuals of the

modified PDEs are weighted by the Eigenvector matrix to yield the beam residuals corresponding to the generalized coordinates as

$$\boldsymbol{\epsilon}_{\text{modes}} \quad = \quad \mathbf{V}^{\text{T}} \; \boldsymbol{\epsilon}_{\text{beam}} \tag{2.112}$$

2.5 Aerodynamic Models

This section provides a brief description of the aerodynamic loads acting on the helicopter fuselage, empennage and tail rotor, together with rotor inflow models (dynamic inflow and free-vortex wake) used to quantify the induced inflow of the main rotor. Two inflow models - dynamic inflow and vortex wake - are discussed in the following sections. Vortex wake models provide a numerical representation of the flowfield through summation of velocities induced by individual vortex filaments. Semi-analytic dynamic inflow models relate the aerodynamic thrust distribution over the rotor disk to the inflow coefficients. When a 3-state dynamic inflow model is used to represent the main rotor flowfield, the inflow state vector is given by

$$\mathbf{y}_{\lambda} \quad = \quad \left\{ \; \overline{\lambda}_0 \qquad \overline{\lambda}_{1\text{c}} \qquad \overline{\lambda}_{1\text{s}} \qquad \lambda_{_{\text{TR}}} \; \right\}^{\text{T}}$$

$\overline{\lambda}_0$ represents the average induced inflow ratio of the main rotor, scaled by a constant factor $\sqrt{3}$ (Ref. [30]) ; $\overline{\lambda}_{1\text{c}}$, $\overline{\lambda}_{1\text{s}}$ are the (scaled) longitudinal and lateral skews of the induced inflow ratio ; and λ_{TR} represents the induced inflow ratio of the tail rotor.

2.5.1 Main Rotor Dynamic Inflow

The aim of dynamic inflow models is to capture, in an approximate manner, the time-varying inflow distribution on a rotor disk operating in flight conditions

that are slowly varying as a function of time. The general form of these models (Refs. [30]) consists of two sets of coupled first-order ordinary differential equations, given by

$$\begin{aligned} \boldsymbol{\tau}_c \quad \dot{\boldsymbol{\lambda}}_c \quad + \quad \boldsymbol{\lambda}_c \quad &= \quad \mathbf{f}_c(\ C_\ell(r,\psi),\ \cos\psi,\ \cos 2\psi,\ \cos 3\psi, \cdots) \\ \boldsymbol{\tau}_s \quad \dot{\boldsymbol{\lambda}}_s \quad + \quad \boldsymbol{\lambda}_s \quad &= \quad \mathbf{f}_s(\ C_\ell(r,\psi),\ \sin\psi\ , \sin 2\psi\ , \sin 3\psi\ , \cdots) \end{aligned} \tag{2.113}$$

Here, r represents the non-dimensional radial distance from the shaft, and ψ represents the azimuthal position of a point on the rotor disk. The first set of equations represent the longitudinal inflow dynamics, i.e. variations along the flight direction, including the uniform component. The second set of equations represent the lateral skew in inflow. Dynamic inflow models traditionally focus on rotors in forward flight, which reduce to hover at zero flight speed. A comprehensive summary of these models may be found in Ref. [91]. The uniform inflow λ_0 and longitudinal skew λ_{1c} are coupled to each other, and each is individually uncoupled from the lateral skew component λ_{1s}. The inflow at a point (r, ψ) is given by

$$\lambda(r,\psi) \quad = \quad \lambda_0 \quad + \quad r\,(\lambda_{1c}\cos\psi \quad + \quad \lambda_{1c}\sin\psi)$$

λ_0, λ_{1c} and λ_{1s} are obtained from the inflow states $\overline{\lambda}_0$, $\overline{\lambda}_{1c}$ and $\overline{\lambda}_{1s}$ and coefficients of the radial basis functions as given in Ref. [30].

2.5.2 Time Marching Free Vortex Wake

For the tow mission, the flight speeds of interest range from hover ($\mu = 0$) to transition flight conditions (μ <0.1) where blade-vortex interactions cause significant azimuthal and radial variations in the inflow distribution. Cross-couplings between

rotor-airframe lateral and longitudinal modes are introduced by the wake, and these dynamics are not modeled by "reduced-order" (in a comparative sense) dynamic inflow equations. To accurately represent the coupled dynamics of helicopter flight and the rotor wake, an in-house free-vortex wake methodology (Refs. [44], [92]) is used to model the rotor wake. For completeness, a brief summary is presented here, borrowing heavily and paraphrased from detailed descriptions in Ref. [92].

Mathematical Model of Vortex Wake

The tip vortex trailed from a rotor blade is naturally curved, but is discretized into multiple straight-line segments. Lagrangian markers are placed at the intersections of these line segments, and the approximate trailer geometry is obtained using a piecewise linear reconstruction as shown in Fig. 2.15. This choice of discretization has been shown to be second-order accurate (Refs [44], [93], [94]) and that to maintain overall second-order accuracy, the wake discretizations must be less than 5°.

The markers so defined are allowed to convect to force-free locations in space based on the vortex-induced velocities and free-stream conditions. The motion of these particles is governed by the three-dimensional incompressible form of the Navier-Stokes equation written in velocity-vorticity form. For the purposes of convecting vortex particles, viscous effects can be ignored since they are usually confined to much smaller length scales (e.g. airfoil boundary layers). Under inviscid incompressible flow conditions, the problem of tracking the location of vortex markers in

space reduces to

$$\frac{d\mathbf{r}_p}{dt} = \mathbf{V}_i \qquad \mathbf{r}_p(t_0) = \mathbf{r}_0$$

Here, $\mathbf{r}_0$ is the initial position of the marker. For the wake trailed from a helicopter blade rotating at constant angular speed Ω_{MR}, the left hand side can be expressed as a function of the blade azimuth ψ and wake age ζ. The convection equation is

$$\frac{\partial \mathbf{r}_p}{\partial \psi} + \frac{\partial \mathbf{r}_p}{\partial \zeta} = \frac{\mathbf{V}_i}{\Omega_{\text{MR}}}$$

Using five-point central and second-order backward difference representations, respectively, for the spatial and temporal derivatives results in the following approximation

$$D_\zeta + D_\psi \approx \frac{1}{\Omega_{\text{MR}}}\mathbf{V}_i$$

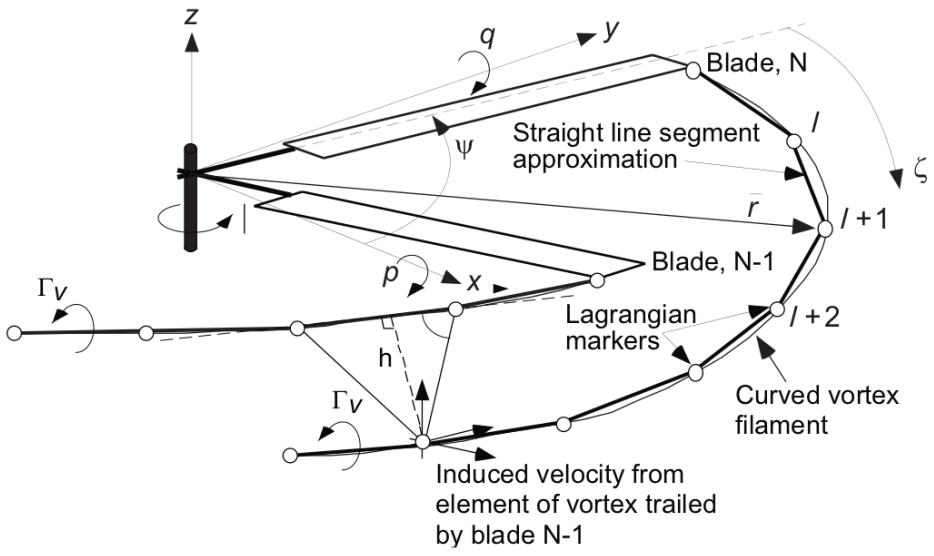

Figure 2.15: Free-Vortex Wake Model of a Rotor

Blade Bound Vortices and Near Wake

Each blade is modeled as a distribution of vortex singularities in the flowfield (Refs. [42], [44], [92]). To accurately capture spanwise variation of lift and the associated trailed wake strengths, a Weissinger-L lifting surface model is used to represent the *effect of the blade* on the rest of the flowfield. Each blade is divided into multiple spanwise segments, each with a bound line vortex located at quarter-chord as shown in Fig. 2.16.

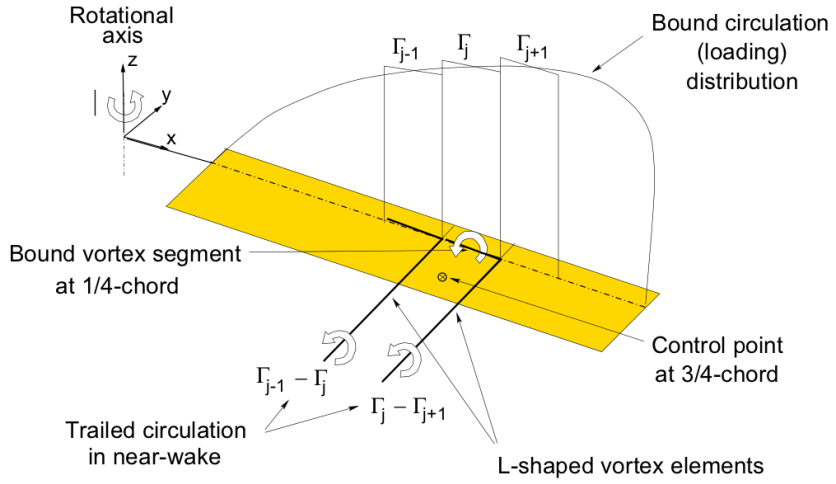

Figure 2.16: Bound Vortices on a Helicopter Blade

The strengths of the trailed vortex segments are obtained using Helmholtz's laws of vorticity conservation (Ref. [95]), given by

$$\Gamma_t|_j \quad = \quad \Gamma_b|_j \quad - \quad \Gamma_b|_{j+1}$$

The so-called "near wake" of the rotor blade consists of the trailed line vortices obtained from the Weissinger-L model. As in Ref. [92], the near wake is assumed to be rigid and aligned with the local airfoil chordline. These trailers are truncated after a short distance $\Delta\psi_w = 30°$. It is assumed that at an azimuth $\Delta\psi_w$ behind

the rotor blade, the vortex sheet has completely rolled up into free-vortex trailers, or elements of circulation, that comprise the far wake.

The bound circulation strengths $\mathbf{\Gamma}_b$ are obtained by enforcing the flow tangency criterion at the three-quarter chord points (or *control points*) at the mid-span locations of each blade segment. Mathematically, this is achieved by setting to zero the total velocity normal to the airfoil reference line, i.e.

$$\mathbf{V}(i) \cdot \mathbf{n}(i) \quad = \quad 0 \qquad\qquad i = 1, 2, 3, ..., N_{\mathrm{S}}$$

$\mathbf{V}(i)$ represents the velocity vector and $\mathbf{n}(i)$ represents the unit vectors normal to the airfoil reference line corresponding to control point i. The total velocity $\mathbf{V}(i)$ can be obtained by summing the contributions from hub translations, hub rotations, free-wake trailers, (rigid) near-wake trailers and bound vortices as

$$\mathbf{V}(i) \quad = \quad \mathbf{V}_{\mathrm{hub}}(i) \; + \; \boldsymbol{\omega}_{\mathrm{hub}} \; \times \; \mathbf{r}(i) \; + \; \mathbf{V}_{_{\mathrm{FW}}}(i) \; + \; \mathbf{V}_{_{\mathrm{NW}}}(i) \; + \; \mathbf{V}_{_{\mathrm{B}}}(i) \qquad (2.114)$$

$\mathbf{r}(i)$ represents the position vector of the point of interest from the center of the hub in non-rotating hub axes. The velocity components $\mathbf{V}_{_{\mathrm{NW}}}$ and $\mathbf{V}_{_{\mathrm{B}}}$ at all control points can be summed and expressed as a matrix-vector product of influence coefficients and bound vortex strengths, i.e.

$$\mathbf{V}_{_{\mathrm{NW}}}(i) \quad + \quad \mathbf{V}_{_{\mathrm{B}}}(i) \quad = \quad \sum_{j=1}^{N_{\mathrm{S}}} \mathbf{I}_{\mathrm{b}}(i,j) \quad \mathbf{\Gamma}_{\mathrm{b}}(j) \qquad (2.115)$$

Substituting Eq. (2.115) in Eq. (2.114), the bound vortex strengths can be obtained by solving a system of linear equations given by

$$\mathbf{I}_b(i,j)\; \mathbf{\Gamma}_b(j) \quad = \quad -(\mathbf{V}_{\mathrm{hub}} \; + \; \boldsymbol{\omega}_{\mathrm{hub}} \; \times \; \mathbf{r} \; + \; \mathbf{V}_{FW})(i) \cdot \mathbf{n}(i) \qquad (i = 1, 2, 3, ..., N_{\mathrm{S}}) \qquad (2.116)$$

2.5.3 Fuselage Aerodynamics

The aerodynamic forces and moments acting on the body of the fuselage are computed based on the flow velocity components at a "reference point" on the fuselage (Ref. [26]), given by

$$\begin{aligned} u_{\text{ref}} &= u_{\text{F}} + \text{y}_{\text{ref}}\, r_{\text{F}} - \text{z}_{\text{ref}}\, q_{\text{F}} + u_{\text{int}_{\text{F}}} \\ v_{\text{ref}} &= v_{\text{F}} + \text{z}_{\text{ref}}\, p_{\text{F}} - \text{x}_{\text{ref}}\, r_{\text{F}} + v_{\text{int}_{\text{F}}} \\ w_{\text{ref}} &= w_{\text{F}} + \text{x}_{\text{ref}}\, q_{\text{F}} - \text{y}_{\text{ref}}\, r_{\text{F}} + w_{\text{int}_{\text{F}}} \end{aligned}$$

The position vector of the fuselage reference point relative to the vehicle center of gravity is given by

$$\mathbf{r}_{\text{ref}} = x_{\text{ref}}\, \boldsymbol{i}_{\text{B}} + y_{\text{ref}}\, \boldsymbol{j}_{\text{B}} + z_{\text{ref}}\, \boldsymbol{k}_{\text{B}}$$

$(u,\, v,\, w)_{\text{int}_{\text{F}}}$ are interference velocity components along body axes, and are computed from the average main rotor downwash $\lambda_0 \Omega_{\text{MR}} R$, nose-down tilt of the rotor tip path plane β_{1c} and wake skew angle χ as

$$\begin{aligned} u_{\text{int}_{\text{F}}} &= \lambda_0 \Omega_{\text{MR}} R \quad \nu_x(\beta_{1c},\, \chi) \\ v_{\text{int}_{\text{F}}} &= 0 \\ w_{\text{int}_{\text{F}}} &= \lambda_0 \Omega_{\text{MR}} R \quad \nu_z(\beta_{1c},\, \chi) \end{aligned} \tag{2.117}$$

The functions $\nu_x(\beta_{1c},\, \chi)$ and $\nu_z(\beta_{1c},\, \chi)$ are obtained from look-up tables, and the wake skew angle is obtained from the free-stream velocity components along shaft axes $(u,\, v,\, w)_{\text{S}}$ as

$$\chi = \tan^{-1} \frac{u_{\text{S}}}{\lambda \Omega_{\text{MR}} R - w_{\text{S}}} + \beta_{1c}$$

Using the velocity components at the fuselage reference point, the flow incidence angles α_{F}, β_{F} are obtained as

$$\begin{aligned} \alpha_{\text{F}} &= \tan^{-1} \frac{w_{\text{F}}}{u_{\text{F}}} \\ \beta_{\text{F}} &= \tan^{-1} \frac{v_{\text{F}}}{\sqrt{u_{\text{F}}^2 + w_{\text{F}}^2}} \end{aligned} \tag{2.118}$$

α_{F} is positive when the fuselage is tilted nose-up with respect to the free-stream flow, and β_{F} is positive when the starboard side is facing the free-stream flow. Using these two flow angles and the dynamic pressure at the fuselage reference point q_{F}, the aerodynamic coefficients in the wind-axes system are obtained using a table look-up procedure based on wind-tunnel measurements (Ref. [26]), and transformed to the body axes (Ref. [20]). Representing the body-axes fuselage forces and moments at the fuselage reference point by $\mathbf{F}_{\text{F}}$ and $\mathbf{M}_{\text{F}}$ respectively, the loads at the vehicle center of gravity are given by

$$\begin{Bmatrix} X \\ Y \\ Z \end{Bmatrix}_{\text{F}} = q_{\text{F}} \begin{Bmatrix} C_X \\ C_Y \\ C_Z \end{Bmatrix}_{\text{F}}$$

$$\begin{Bmatrix} L \\ M \\ N \end{Bmatrix}_{\text{F}} = q_{\text{F}} \begin{Bmatrix} C_L \\ C_M \\ C_N \end{Bmatrix}_{\text{F}} + \mathbf{r}_{\text{ref}} \times \mathbf{F}_{\text{F}}$$

Where

$$q_{\text{F}} = \frac{1}{2} \rho \left(u_{\text{F}}^2 + v_{\text{F}}^2 + w_{\text{F}}^2 \right)$$

2.5.4 Empennage Aerodynamics

The aerodynamic loads acting on the horizontal and vertical tail are computed using a procedure similar to that followed for the fuselage. The velocity at the reference point for each lifting surface is computed from the fuselage translation velocity $\mathbf{V}_b$, angular velocity $\boldsymbol{\omega}_b$ and the position of the reference points with respect to the vehicle center of gravity $\mathbf{r}_{\text{H}}$, $\mathbf{r}_{\text{V}}$ as

$$\begin{aligned} \mathbf{V}_{\text{HT}} &= K_{\text{H}}\mathbf{V}_b + \boldsymbol{\omega} \times \mathbf{r}_{\text{H}} + \mathbf{V}_{\text{int}_{\text{H}}} \\ \mathbf{V}_{\text{VT}} &= K_{\text{V}}\mathbf{V}_b + \boldsymbol{\omega} \times \mathbf{r}_{\text{V}} + \mathbf{V}_{\text{int}_{\text{V}}} \end{aligned} \tag{2.119}$$

K_{H} and K_{V} are used to empirically model the dynamic pressure loss at the tail surfaces, which occurs as a result of operating in the wake of the airframe. $\mathbf{V}_{\text{int}_{\text{H}}}$ and $\mathbf{V}_{\text{int}_{\text{V}}}$ represent the velocities at the tail surfaces induced by the main rotor wake, (obtained from wind-tunnel tests) and are given by

$$\begin{aligned} \mathbf{V}_{\text{int}_{\text{H}}} &= \lambda_0\Omega_{\text{MR}}R \left[\nu_{x_{\text{H}}}(\beta_{1c},\chi)\ \boldsymbol{i}_{\text{B}} + \nu_{z_{\text{H}}}(\beta_{1c},\chi)\ \boldsymbol{k}_{\text{B}}\right] \\ \mathbf{V}_{\text{int}_{\text{V}}} &= \lambda_0\Omega_{\text{MR}}R \left[\nu_{x_{\text{V}}}(\beta_{1c},\chi)\ \boldsymbol{i}_{\text{B}} + \nu_{z_{\text{V}}}(\beta_{1c},\chi)\ \boldsymbol{k}_{\text{B}}\right] \end{aligned} \tag{2.120}$$

The functions ν_{x_H}, ν_{z_H}, ν_{x_V}, ν_{z_V} are obtained from look-up tables based on the wake skew angle χ and the tip-path plane tilt β_{1c} with respect to the fuselage. Using (u, v, w)$_{\text{H}}$ and (u, v, w)$_{\text{V}}$ to represent the velocity components at the horizontal and vertical stabilizers, respectively, along vehicle body axes, the angles of attack and sideslip at the tail surfaces are computed as

$$\begin{aligned} \alpha_{\text{H}} &= \tan^{-1}\frac{w_{\text{H}}}{u_{\text{H}}} + \theta_{\text{HT}} \\ \beta_{\text{H}} &= \tan^{-1}\frac{v_{\text{H}}}{\sqrt{u_{\text{H}}^2 + w_{\text{H}}^2}} \end{aligned}$$

$$
\begin{aligned}
\alpha_{_{\rm V}} &= \tan^{-1}\frac{w_{_{\rm V}}}{u_{_{\rm V}}} \\
\beta_{_{\rm V}} &= \tan^{-1}\frac{v_{_{\rm V}}}{\sqrt{u_{_{\rm V}}^2 + w_{_{\rm V}}^2}}
\end{aligned}
$$

The pitch of the horizontal stabilizer $\theta_{_{\rm HT}}$ is scheduled to change with the fuselage speed in a prescribed manner. An approach similar to that followed for the fuselage aerodynamics is utilized for computing the forces on the horizontal and vertical stabilizers. Using the incidence angles α and β for each surface and the dynamic pressure at the reference points, the aerodynamic lift and drag coefficients are obtained using a table look-up procedure based on wind-tunnel measurements, and transformed to the helicopter body axes. Using ($\mathbf{F}_{_{\rm HT}}$, $\mathbf{F}_{_{\rm VT}}$) and ($\mathbf{M}_{_{\rm HT}}$, $\mathbf{M}_{_{\rm HT}}$) to represent the body-axes forces and moments, respectively, at the reference points, the loads at the vehicle center of gravity are given by

$$
\begin{aligned}
\begin{Bmatrix} X \\ Y \\ Z \end{Bmatrix}_{\rm emp} &= q_{_{\rm HT}} \begin{Bmatrix} C_X \\ C_Y \\ C_Z \end{Bmatrix}_{_{\rm HT}} + q_{_{\rm VT}} \begin{Bmatrix} C_X \\ C_Y \\ C_Z \end{Bmatrix}_{_{\rm VT}} \\
\begin{Bmatrix} L \\ M \\ N \end{Bmatrix}_{\rm emp} &= \mathbf{r}_{_{\rm HT}} \times \mathbf{F}_{_{\rm HT}} + \mathbf{r}_{_{\rm VT}} \times \mathbf{F}_{_{\rm VT}}
\end{aligned}
$$

The dynamic pressures are given by

$$
q_{_{\rm HT}} = \frac{1}{2}\ \rho\ \mathbf{V}_{_{\rm HT}} \cdot \mathbf{V}_{_{\rm HT}} \qquad \text{and} \qquad q_{_{\rm VT}} = \frac{1}{2}\ \rho\ \mathbf{V}_{_{\rm VT}} \cdot \mathbf{V}_{_{\rm VT}} \tag{2.121}
$$

2.5.5 Tail Rotor Aerodynamics

The tail rotor model is based on a simplified implementation of the closed-form solution given by Ref. [96], which relates the free-stream velocity to the rotor thrust, torque and induced inflow. The velocity at the tail rotor reference point (hub) is

$$\mathbf{V}_{\text{TR}} \quad = \quad \mathbf{V}_b \quad + \quad \boldsymbol{\omega} \times \mathbf{r}_{\text{TR}} \quad + \quad \mathbf{V}_{\text{int}_{\text{TR}}} \tag{2.122}$$

$\mathbf{V}_{\text{int}_{\text{TR}}}$ represents the induced velocity at the tail rotor reference point due by the wake of the main rotor and fuselage, given by

$$\mathbf{V}_{\text{int}_{\text{TR}}} \quad = \quad \lambda_0 \Omega_{\text{MR}} R \quad [\nu_{x_{\text{TR}}}(\beta_{1c}, \chi)\ \boldsymbol{i}_{\text{B}} \quad + \quad \nu_{z_{\text{TR}}}(\beta_{1c}, \chi)\ \boldsymbol{k}_{\text{B}}] \tag{2.123}$$

The functions $\nu_{x_{\text{TR}}}$, $\nu_{z_{\text{TR}}}$ are obtained from look-up tables based on the wake skew angle χ and the tip-path plane tilt β_{1c} with respect to the fuselage. The velocity $\mathbf{V}_{\text{TR}}$ at the tail rotor reference point $\mathbf{r}_{\text{TR}}$ is resolved into components along the tail rotor axes. The tail rotor axes system are obtained using two rotations in the sequence $Z \rightarrow Y$ through angles (Γ_{TR}, Λ_{TR}) starting from the helicopter body axes. The rotation matrix from fuselage body axes to tail rotor axes is given by

$$\mathbf{T}_{TR,B} \quad = \quad \begin{bmatrix} \cos\Lambda_{\text{TR}} & 0 & -\sin\Lambda_{\text{TR}} \\ 0 & 1 & 0 \\ \sin\Lambda_{\text{TR}} & 0 & \cos\Lambda_{\text{TR}} \end{bmatrix} \begin{bmatrix} \cos\Gamma_{\text{TR}} & \sin\Gamma_{\text{TR}} & 0 \\ -\sin\Gamma_{\text{TR}} & \cos\Gamma_{\text{TR}} & 0 \\ 0 & 0 & 1 \end{bmatrix}$$

The velocity components in the tail rotor reference frame are

$$\begin{Bmatrix} u \\ v \\ w \end{Bmatrix}_{\text{TR}} \quad = \quad \mathbf{T}_{TR,B} \begin{bmatrix} \mathbf{V}_{\text{TR}} \cdot \begin{Bmatrix} \boldsymbol{i}_{\text{B}} \\ \boldsymbol{j}_{\text{B}} \\ \boldsymbol{k}_{\text{B}} \end{Bmatrix} \end{bmatrix} \tag{2.124}$$

The tail rotor thrust (assumed to act along the shaft direction) is

$$T_{\text{TR}} \quad = \quad \pi \quad R_{\text{TR}}^4 \quad \Omega_{\text{TR}}^2 \quad |V|_{\text{TR}} \quad v_{i,\text{TR}} \quad K_{\text{TR}} \tag{2.125}$$

$v_{i,\text{TR}} = \lambda_{\text{TR}} \Omega_{\text{TR}} R_{\text{TR}}$ is the average induced velocity of the tail rotor, K_{TR} accounts for blockage effects of the vertical fin and $|V|_{\text{TR}}$ is the magnitude of the total velocity (including induced inflow) at the tail rotor, given by

$$|V|_{\text{TR}} \quad = \quad \sqrt{u_{\text{TR}}^2 \quad + \quad v_{\text{TR}}^2 \quad + \quad (w_{\text{TR}} - \lambda_{\text{TR}} \Omega_{\text{TR}} R_{\text{TR}})^2}$$

The tail rotor torque due to induced and profile drag is

$$Q_{\text{TR}} \quad = \quad C_{Q_{\text{TR}}} \quad \rho \quad \pi \quad \Omega_{\text{TR}}^2 \quad R_{\text{TR}}^5$$

The forces and moment components in fuselage body axes exerted by the tail rotor on the airframe center of gravity are obtained using a coordinate transformation

$$\begin{Bmatrix} X \\ Y \\ Z \end{Bmatrix}_{\text{TR}} \quad = \quad \mathbf{T}_{TR,B}^{\text{T}} \quad \begin{Bmatrix} 0 \\ -T_{\text{TR}} \\ 0 \end{Bmatrix}$$

$$\begin{Bmatrix} L \\ M \\ N \end{Bmatrix}_{\text{TR}} \quad = \quad \mathbf{T}_{TR,B}^{\text{T}} \quad \begin{Bmatrix} 0 \\ -Q_{\text{TR}} \\ 0 \end{Bmatrix}$$

$$+ \quad \mathbf{r}_{\text{TR}} \times (X_{\text{TR}} \, \boldsymbol{i}_{\text{B}} + Y_{\text{TR}} \, \boldsymbol{j}_{\text{B}} + Z_{\text{TR}} \, \boldsymbol{k}_{\text{B}})$$

Tail Rotor Dynamic Inflow

The induced inflow of the tail rotor is assumed to be uniform over the disk, and is represented using a 1-state Pitt-Peters dynamic inflow model (Ref. [29]). The

ODE governing the inflow dynamics is

$$\frac{4R_{\text{TR}}}{3\pi|V_{\text{TR}}|}\dot{\lambda}_{\text{TR}} \quad + \quad \lambda_{\text{TR}} \quad = \quad \frac{C_{T_{\text{TR}}}\Omega_{\text{TR}}R_{\text{TR}}}{2|V_{\text{TR}}|} \tag{2.126}$$

$C_{T_{TR}}$ is the thrust coefficient of the tail rotor.

2.6 Cable Dynamics

The treatment of cable structural dynamics is very similar to the rotor blade formulation, and represents a special case of non-rotating beam with zero hinge offset. The partition of the system state vector containing the cable states is

$$\mathbf{y}_{\text{cable}} \quad = \quad \left\{ \begin{array}{cccccccc} \eta_{\text{C1}} & \dot{\eta}_{\text{C1}} & \eta_{\text{C2}} & \dot{\eta}_{\text{C2}} & \cdots & \eta_{\text{C Nmc}} & \dot{\eta}_{\text{C Nmc}} \end{array} \right\}^{\text{T}}$$

η_{CN} represents the " N^{th} " generalized coordinate of the cable. The discontinuity in loading at the air/water free surface precludes the use of modal reduction, since an infinite number of modes is required to represent the response to a step discontinuity in spanwise loading. The beam bending nodal degrees of freedom, as obtained after finite element discretization in Section 2.4.6, are used as the generalized displacement coordinates in the presence of hydrodynamics. Structural loads are computed as given in Section 2.4.1. The inertial loads are obtained using the formulation given in Section 2.4.2. The motion at the root of the cable are obtained from helicopter translations and rotations as follows.

The cable is attached to the helicopter at the tow point using a spherical bearing that transmits only forces and no moments. The tow point position vector

is defined as

$$\mathbf{r}_{\text{tow}} = \mathbf{r}_{\text{CG}} + \begin{Bmatrix} \boldsymbol{i}_{\text{G}} \\ \boldsymbol{j}_{\text{G}} \\ \boldsymbol{k}_{\text{G}} \end{Bmatrix}^{\text{T}} \mathbf{T}_{GB} \begin{Bmatrix} \Delta\text{x} \\ \Delta\text{y} \\ \Delta\text{z} \end{Bmatrix}_{\text{hook}} \tag{2.127}$$

Here, $\mathbf{r}_{\text{CG}}$ is the position of the helicopter CG in space, $\mathbf{T}_{GB}$ is the rotation matrix from earth-fixed axes to helicopter body axes, obtained from Eq. (2.6) and $(\Delta\text{x}, \Delta\text{y}, \Delta\text{z})_{\text{hook}}$ represents the coordinates of the cable attachment point in helicopter body axes with respect to the airframe CG. The velocity and acceleration of the tow point are obtained by differentiating Eq. (2.127) once and twice, respectively, with respect to time to yield

$$\mathbf{v}_{\text{tow}} = \mathbf{v}_{\text{CG}} + \begin{Bmatrix} \boldsymbol{i}_{\text{G}} \\ \boldsymbol{j}_{\text{G}} \\ \boldsymbol{k}_{\text{G}} \end{Bmatrix}^{\text{T}} \dot{\mathbf{T}}_{GB} \begin{Bmatrix} \Delta\text{x} \\ \Delta\text{y} \\ \Delta\text{z} \end{Bmatrix}_{\text{hook}} \tag{2.128}$$

$$\mathbf{a}_{\text{tow}} = \mathbf{a}_{\text{CG}} + \begin{Bmatrix} \boldsymbol{i}_{\text{G}} \\ \boldsymbol{j}_{\text{G}} \\ \boldsymbol{k}_{\text{G}} \end{Bmatrix}^{\text{T}} \ddot{\mathbf{T}}_{GB} \begin{Bmatrix} \Delta\text{x} \\ \Delta\text{y} \\ \Delta\text{z} \end{Bmatrix}_{\text{hook}} \tag{2.129}$$

Here, $\mathbf{v}_{\text{CG}}$ and $\mathbf{a}_{\text{CG}}$ represent the velocity and acceleration, respectively of the helicopter CG, and $\dot{\mathbf{T}}_{GB}$, $\ddot{\mathbf{T}}_{GB}$ are obtained as specified in Section 2.4.1.8. The final component used in the formulation of cable inertial, hydrodynamic, buoyancy and gravitational loads is the rotation from the earth-fixed axes ($\boldsymbol{i}_{\text{G}}$, $\boldsymbol{j}_{\text{G}}$, $\boldsymbol{k}_{\text{G}}$, Section 2.2.1) to the cable undeformed axes ($\boldsymbol{i}_{\text{C}}$, $\boldsymbol{j}_{\text{C}}$, $\boldsymbol{k}_{\text{C}}$, Section 2.2.7). The coordinate transformation matrix is given by Eq. (2.16) as $\mathbf{T}_{UG} = \mathbf{T}_{CG}$, and its two

time derivatives may be obtained from Eqs. (2.3) and (2.4) with the substitutions $\phi = \dot{\phi} = \ddot{\phi} = \dot{\theta} = \ddot{\theta} = 0$, $\theta = -\frac{\pi}{2}$, $\psi = \psi_{_F}$, $\dot{\psi} = \dot{\psi}_{_F}$ and $\ddot{\psi} = \ddot{\psi}_{_F}$.

Hydrodynamic Forces on Tow Cable

The tow cable is attached to the helicopter on one end and the submerged load on the other end. A part of the tow cable is above the water surface and experiences aerodynamic forces, while the rest of the cable experiences hydrodynamic forces, both normal and tangential to the axis of the cable. The cable section velocities are obtained using the procedure outlined in Section 2.4.3, and the cable sectional hydrodynamic loads are used in place of airfoil lift, drag and pitching moment. The tangential force is given by

$$F_r^+ \quad = \quad \frac{1}{2}\,\rho\,V_\infty^2\,D\,C_r$$

D is the cable diameter and C_r is the radial force coefficient, which was determined to be 0.025 (Ref. [71]). The force normal to the cable axis in the $U_{_T}$-$U_{_P}$ plane is given by

$$F_n^+ \quad = \quad \frac{1}{2}\,\rho\,V_\infty^2\,D\,C_n$$

The normal force coefficient is determined from experiments as

$$\begin{aligned} C_n \quad = \quad & C_{_{\mathrm{Do}}}(-0.424 \;+\; 0.869\cos\gamma_{_I} \;+\; 0.979\sin\gamma_{_I} \\ & \qquad -\; 0.455\cos 2\gamma_{_I} \;-\; 0.434\sin 2\gamma_{_I}) \end{aligned}$$

The normal drag coefficient is $C_{_{\mathrm{Do}}} = 1.73$ for bare cables, obtained from experiments (Ref. [71]). Since pitching moment data is unavailable, the moment coefficient is

set to zero for all flow conditions. The various forces at a point on a bare cable are shown in Fig. 2.17.

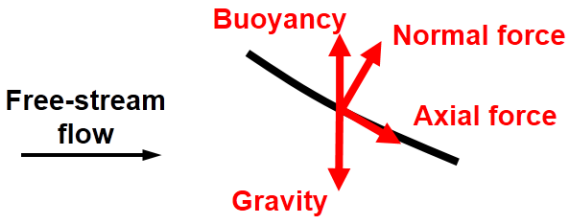

Figure 2.17: Forces on Bare Cables

The tremendous drag created by hydrodynamics on the submerged sections of the cable necessitates the use of fairings to reduce the engine power required in forward flight. The normal drag coefficient is therefore set to C_{Do}=0.1 to better model the profile drag of a fairing. The hydrodynamic force distributions are obtained in the cable deformed axes, and converted to the undeformed axes as in Eq. (2.102). The contributions from external and structural loads are computed and substituted into the governing Eqs. (2.109) and (2.110) for transverse bending to compute the ODE residuals.

The submerged load is treated as a tip mass for the tow cable. Using the helicopter rigid-body states and cable generalized displacements, the motions of the towed body are obtained. These motions are used to obtain the total forces acting on the submerged load that manifest as tip forces for the cable. The cumulative forces on the towed body and cable are transmitted to the helicopter as towing tension. These forces are obtained using a procedure similar to the computation of hub loads as given in Section 2.4.4, with the following modifications

- The matrix product $\mathbf{T}_{RH}^{\mathrm{T}}\mathbf{T}_{UR}^{\mathrm{T}}$ is replaced with $\mathbf{T}_{GC}$

- The matrix $\mathbf{T}_{BH}$ is replaced with $\mathbf{T}_{BG}$

2.6.1 Towed Body Dynamics

The primary function of the towed body is to detect submerged objects in its vicinity using sensors placed inside a waterproof frame. The hull is shaped like a modified torpedo and streamlined to reduce drag. Two active fins near the load CG can pitch relative to the body and produce lift (or down-force) for depth regulation. Three stationary fins are mounted at the tail end in an inverted-Y configuration to help orient the nose of the towed body into the free-stream flow and reduce pitch attitude excursions from a design point. It is assumed that the submerged load is attached to the tow cable using a spherical bearing that allows all three rotations. A schematic of a towed body is shown in Fig. 2.7.

The submerged load is modeled as a rigid distributed mass that is attached to the tip of the tow cable using a spherical bearing that allows rotations about all three axes. The orientations of the towed body are determined using Euler rotations, and moment equilibrium is enforced using Eqs. (2.26) - (2.28). The treatment of the towed body dynamics is distinctly different from the fuselage rigid-body dynamics, where the body-axis translations and rotations are immediately available from the system state vector. For the towed body, translations must be obtained from the tip deflections of the cable to preserve the state-space formulation and prevent using an overdetermined system of equations. The towed body states are obtained from the

appropriate partition of the system state vector, given by

$$\mathbf{y}_{\text{load}} \quad = \quad \left\{ \; p_{\text{L}} \quad q_{\text{L}} \quad r_{\text{L}} \qquad \phi_{\text{L}} \quad \theta_{\text{L}} \quad \psi_{\text{L}} \; \right\}^{\text{T}}$$

(p_{L}, q_{L}, r_{L}) are the components of angular velocity of the submerged load about body-fixed axes and (ψ_{L}, θ_{L}, ϕ_{L}) are the Euler angles used in the Z→Y→X sequence to define the towed body orientation with respect to the earth-fixed axes. When using a simplified axially flexible straight cable model, the curved cable states vanish and six additional towed body states (position vector components along gravity-axes and velocity components along body-axes) are added to the vector of load states.

If the attachment between the tow cable and submerged load does not allow all three rotations, then the bending slopes and twist at the tip must also be used to determine the load attitudes that are constrained by the cable attachment, and the appropriate moment equilibrium equations must be dropped from the formulation. The cumulative forces and moments on the towed body due to inertia, gravity, buoyancy and hydrodynamics manifest as tip loads for the flexible beam that is defined by the cable structure.

2.6.2 Towed Body Translations

The position of the cable attachment point on the load is given by

$$\left.\begin{array}{rcl} \mathbf{r}_{\text{load hook}} & = & \mathbf{r}_{\text{load CG}} \quad + \quad \mathbf{r}_{\text{hook wrt CG}} \\ & = & \mathbf{r}_{\text{cable tip}} \end{array}\right\} \tag{2.130}$$

The first expression identifies the cable attachment point on the towed body using the CG locations in space and the hook location with respect to the CG of the load.

The second expression identifies the same point using the helicopter tow point and the cable tip deflections. The expressions can be rearranged to obtain the position of the load CG in space as

$$\mathbf{r}_{\mathrm{L}} = \mathbf{r}_{\mathrm{tow}} + \begin{Bmatrix} \boldsymbol{i}_{\mathrm{G}} \\ \boldsymbol{j}_{\mathrm{G}} \\ \boldsymbol{k}_{\mathrm{G}} \end{Bmatrix}^{\mathrm{T}} \left[\mathbf{T}_{GC} \begin{Bmatrix} x_{\mathrm{C}} + u_{\mathrm{C}} \\ v_{\mathrm{C}} \\ w_{\mathrm{C}} \end{Bmatrix} - \mathbf{T}_{GL} \begin{Bmatrix} \Delta\mathrm{x} \\ \Delta\mathrm{y} \\ \Delta\mathrm{z} \end{Bmatrix}_{\mathrm{LH}} \right] \tag{2.131}$$

The first term on the right hand side represents the coordinates of the helicopter tow point, given by Eq. (2.127). The second term represents the position of the cable tip with respect to the tow point, and the third term represents the coordinates of the load CG with respect to the tip of the cable. $(\Delta\mathrm{x},\ \Delta\mathrm{y},\ \Delta\mathrm{z})_{\mathrm{LH}}$ represent the coordinates of the cable attachment point on the load with respect to the CG of the load along body-fixed axes, and are time-invariant. Differentiating Eq. (2.131) with respect to time, we obtain the velocity of the load CG as

$$\mathbf{v}_{\mathrm{L}} = \mathbf{v}_{\mathrm{tow}} + \begin{Bmatrix} \boldsymbol{i}_{\mathrm{G}} \\ \boldsymbol{j}_{\mathrm{G}} \\ \boldsymbol{k}_{\mathrm{G}} \end{Bmatrix}^{\mathrm{T}} \left[\mathbf{T}_{GC} \begin{Bmatrix} \dot{u}_{\mathrm{C}} \\ \dot{v}_{\mathrm{C}} \\ \dot{w}_{\mathrm{C}} \end{Bmatrix}_{\mathrm{tip}} - \dot{\mathbf{T}}_{GL} \begin{Bmatrix} \Delta\mathrm{x} \\ \Delta\mathrm{y} \\ \Delta\mathrm{z} \end{Bmatrix}_{\mathrm{LH}} + \dot{\mathbf{T}}_{GC} \begin{Bmatrix} x_{\mathrm{C}} + u_{\mathrm{C}} \\ v_{\mathrm{C}} \\ w_{\mathrm{C}} \end{Bmatrix}_{\mathrm{tip}} \right] \tag{2.132}$$

Differentiate Eq. (2.132) with respect to time to obtain the load CG acceleration as

$$\mathbf{a}_{\mathrm{L}} = \mathbf{a}_{\mathrm{tow}} + \begin{Bmatrix} \boldsymbol{i}_{\mathrm{G}} \\ \boldsymbol{j}_{\mathrm{G}} \\ \boldsymbol{k}_{\mathrm{G}} \end{Bmatrix}^{\mathrm{T}} \left[\mathbf{T}_{GC} \begin{Bmatrix} \ddot{u}_{\mathrm{C}} \\ \ddot{v}_{\mathrm{C}} \\ \ddot{w}_{\mathrm{C}} \end{Bmatrix}_{\mathrm{tip}} - \ddot{\mathbf{T}}_{GL} \begin{Bmatrix} \Delta\mathrm{x} \\ \Delta\mathrm{y} \\ \Delta\mathrm{z} \end{Bmatrix}_{\mathrm{LH}} + \ddot{\mathbf{T}}_{GC} \begin{Bmatrix} x_{\mathrm{C}} + u_{\mathrm{C}} \\ v_{\mathrm{C}} \\ w_{\mathrm{C}} \end{Bmatrix}_{\mathrm{tip}} + 2\,\dot{\mathbf{T}}_{GC} \begin{Bmatrix} \dot{u}_{\mathrm{C}} \\ \dot{v}_{\mathrm{C}} \\ \dot{w}_{\mathrm{C}} \end{Bmatrix}_{\mathrm{tip}} \right] \tag{2.133}$$

The velocity and acceleration components of the load CG along body-fixed axes can be obtained from Eqs. (2.132) and (2.133) using a transformation matrix as

$$\begin{aligned} \begin{Bmatrix} u_{\mathrm{L}} \\ v_{\mathrm{L}} \\ w_{\mathrm{L}} \end{Bmatrix} &= \mathbf{T}_{LG} \begin{Bmatrix} \mathbf{v}_{\mathrm{L}} \cdot \boldsymbol{i}_{\mathrm{G}} \\ \mathbf{v}_{\mathrm{L}} \cdot \boldsymbol{j}_{\mathrm{G}} \\ \mathbf{v}_{\mathrm{L}} \cdot \boldsymbol{k}_{\mathrm{G}} \end{Bmatrix} \\ \begin{Bmatrix} a_{\mathrm{x}} \\ a_{\mathrm{y}} \\ a_{\mathrm{z}} \end{Bmatrix}_{\mathrm{L}} &= \mathbf{T}_{LG} \begin{Bmatrix} \mathbf{a}_{\mathrm{L}} \cdot \boldsymbol{i}_{\mathrm{G}} \\ \mathbf{a}_{\mathrm{L}} \cdot \boldsymbol{j}_{\mathrm{G}} \\ \mathbf{a}_{\mathrm{L}} \cdot \boldsymbol{k}_{\mathrm{G}} \end{Bmatrix} \end{aligned} \tag{2.134}$$

$\mathbf{T}_{LG}$ is the rotation matrix from earth-fixed axes to the load body-fixed axes, given by Eq. (2.19). The acceleration components in Eq. (2.134) are

$$\left.\begin{aligned} a_{\mathrm{x_L}} &= \dot{u}_{\mathrm{L}} + q_{\mathrm{L}} w_{\mathrm{L}} - r_{\mathrm{L}} v_{\mathrm{L}} + g \sin\theta_{\mathrm{L}} \\ a_{\mathrm{y_L}} &= \dot{v}_{\mathrm{L}} + r_{\mathrm{L}} u_{\mathrm{L}} - p_{\mathrm{L}} w_{\mathrm{L}} - g \cos\theta_{\mathrm{L}} \sin\phi_{\mathrm{L}} \\ a_{\mathrm{z_L}} &= \dot{w}_{\mathrm{L}} + p_{\mathrm{L}} v_{\mathrm{L}} - q_{\mathrm{L}} u_{\mathrm{L}} - g \cos\theta_{\mathrm{L}} \cos\phi_{\mathrm{L}} \end{aligned}\right\} \tag{2.135}$$

Eqs. (2.135) can be substituted in Eqs. (2.20) - (2.22) and the resulting expressions can be manipulated to isolate the cable force components along the body-fixed axes of the submerged load as

$$\begin{aligned} X_{\mathrm{c}} &= m_{\mathrm{L}} a_{\mathrm{x_L}} - X_{\mathrm{ext}} \\ Y_{\mathrm{c}} &= m_{\mathrm{L}} a_{\mathrm{y_L}} - Y_{\mathrm{ext}} \\ Z_{\mathrm{c}} &= m_{\mathrm{L}} a_{\mathrm{z_L}} - Z_{\mathrm{ext}} \end{aligned}$$

The components of total force exerted *by* the towed body *on* the cable are obtained using two transformations : from the load body axes to the earth-fixed axes, and then from the earth-fixed axes to cable undeformed axes, which are then applied as tip loads for the beam structure defining the flexible cable. Thus,

$$\left\{ \begin{array}{c} \widetilde{S}_{\mathrm{x_L}} \\ \widetilde{S}_{\mathrm{y_L}} \\ \widetilde{S}_{\mathrm{z_L}} \end{array} \right\}_{\mathrm{tip}} = \mathbf{T}_{CG} \quad \mathbf{T}_{GL} \quad \left\{ \begin{array}{c} X_{\mathrm{c}} \\ Y_{\mathrm{c}} \\ Z_{\mathrm{c}} \end{array} \right\} \tag{2.136}$$

The final step consists of obtaining expressions for the external loads (X_{ext}, Y_{ext}, Z_{ext}) due to gravity, buoyancy, and hydrodynamics of the hull and fins.

2.6.3 External Loads on Towed Body

The external forces and moments on the towed body are gravity, buoyancy, hull drag, and fin lift and drag. Effects of flow interference between the body and fins, and radial flow over the individual fins are neglected. Gravity, hull drag and buoyancy are treated as point loads that act at specific locations on the towed body

(load CG for gravity and hull drag, center of buoyancy for the third force), given by

$$\begin{aligned}
\mathbf{F}_{\mathrm{g}} &= m_{\mathrm{L}} g \quad \boldsymbol{k}_G \\
\mathbf{F}_{\mathrm{b}} &= -\rho_{\mathrm{w}} \, \mathrm{V}_{\mathrm{L}} \, g \quad \boldsymbol{k}_G \\
\mathbf{F}_{\mathrm{hull}} &= \frac{1}{2}\rho_{\mathrm{w}} \sqrt{u_{\mathrm{L}}^2 + v_{\mathrm{L}}^2 + w_{\mathrm{L}}^2} \; \mathrm{f}_{\mathrm{L}} \quad (u_{\mathrm{L}} \, \boldsymbol{i}_{\mathrm{L}} + v_{\mathrm{L}} \, \boldsymbol{j}_{\mathrm{L}} + w_{\mathrm{L}} \, \boldsymbol{k}_{\mathrm{L}})
\end{aligned}$$

m_{L} is the load mass, ρ_{w} is the water density, V_{L} is the load volume and f_{L} is the equivalent flat-plate area of the towed body.

Fin Forces

Steady hydrodynamic lift and drag on the fins are implemented in a table-lookup form, shown in Fig. 2.19. The components of flow velocity at a reference point on each fin are resolved along fin-fixed axes, which are shown in Fig. 2.18.

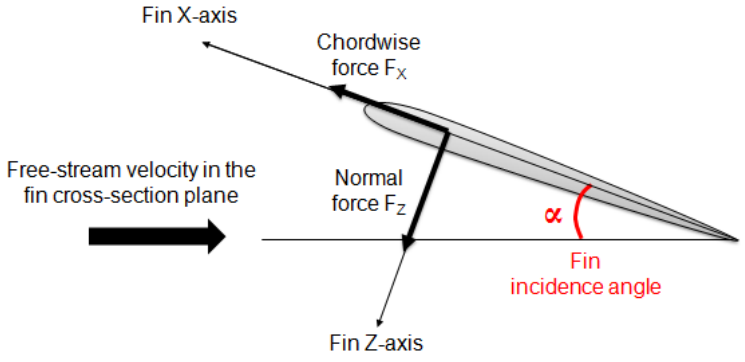

Figure 2.18: Flow and forces on a fin

Force coefficients along fin-fixed axes (with respect to fin plan-form area and free-stream dynamic pressure at the fin reference point) are obtained based on aerodynamics of three-dimensional flat plates (Ref. [97]) in three distinct flow regimes:

- Attached flow regime

This is a small-angle regime ($|\alpha| \leq \alpha_1$) in which the flow stays attached and lift increases linearly with fin incidence angle α, up to a certain upper bound α_1. The chordwise force is due to a combination of profile and induced drag. In fin-fixed axes, the force coefficients (with respect to fin area and free-stream dynamic pressure at a reference point) are

$$\begin{aligned} C_{F_Z} &= -C_{L_\alpha}\alpha \\ C_{F_X} &= -\cos\alpha\left[\frac{C_{F_Z}^2}{\pi A R e_{Ost}} + C_{Do}\right] \end{aligned}$$

- Fully stalled flow regime

  This is the large angle condition ($180 \geq |\alpha| \geq \alpha_2$) in which flow over the lifting surface is completely stalled once the incidence angle exceeds a "second" stall angle, and flow over the airfoil resembles that over a bluff body, with significant profile drag (C_{Dp}).

$$\begin{aligned} C_{F_X} &= -C_{Do}\cos\alpha \\ C_{F_Z} &= -\sin^2\alpha\frac{\alpha}{|\alpha|}C_{Dp} \end{aligned}$$

- Stall transition regime

  The intermediate angles between the post-stall and attached flow regime ($\alpha_1 \leq \alpha \leq \alpha_2$ and $-\alpha_1 \geq \alpha \geq -\alpha_2$) is called the stall transition regime. Over this range of incidence angles, the flow transitions from fully attached to fully detached flow. The forces for this range of incidence angles are obtained using linear interpolation from the ends of the bounding regimes, as

$$C_{F_X} = C_{x1} + \frac{C_{x2} - C_{x1}}{\alpha_2 - \alpha_1}(|\alpha| - \alpha_1)$$

$$C_{F_Z} = C_{z1} + \frac{C_{z2} - C_{z1}}{\alpha_2 - \alpha_1}(|\alpha| - \alpha_1)$$

Where

$$C_{x1} = -\cos^2 \alpha_1 \left[C_{Do} + \frac{C_{L_\alpha}^2 \alpha_1^2}{\pi A R e_{Ost}} \right]$$

$$C_{x2} = -\cos^2 \alpha_2 C_{Do}$$

and

$$C_{z1} = -C_{L_\alpha} \alpha_1 \frac{\alpha}{|\alpha|}$$

$$C_{z2} = -\sin^2 \alpha_2 \frac{\alpha}{|\alpha|} C_{Dp}$$

The moments created by all external forces about the load CG are summed and used in the rigid-body moment equilibrium equations. The right hand side of Eqs. (2.26) - (2.28) are computed using the towed body inertias, Euler angles, angular velocities and accelerations, obtained from the state vector partition corresponding to the towed body $\mathbf{y}_{\text{load}}$.

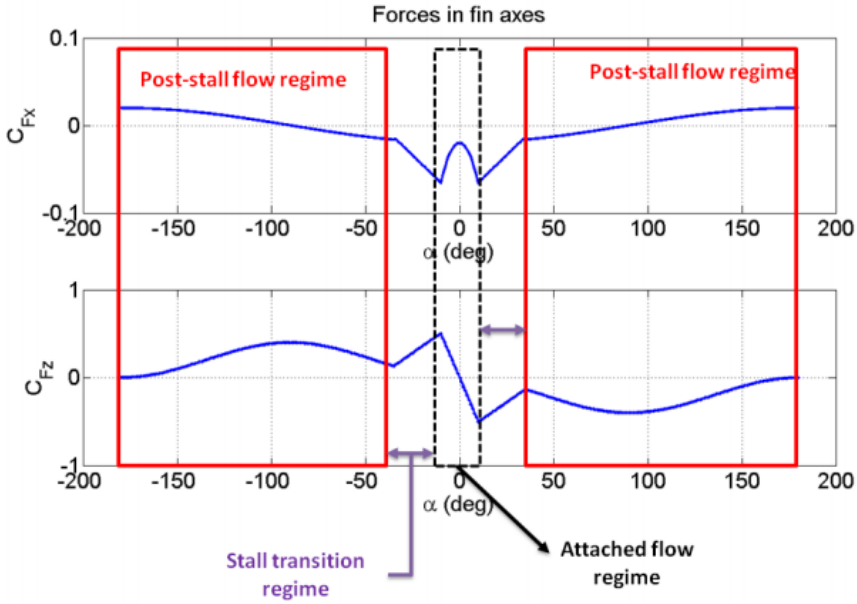

Figure 2.19: Lift and drag coefficients of fins

2.7 Summary

Each element in the state vector $\mathbf{y}$ has a corresponding differential equation in vector $\mathbf{f}$ of equations used to model the system dynamics. The vector of ODEs can be subdivided into

- 12 non-linear equations that enforce force and moment equilibrium for the fuselage rigid-body motions, and kinematic compatibility between time derivatives of Euler angles and body-axis angular rates. The corresponding ODE residuals are represented by $\boldsymbol{\epsilon}_{\text{F}}$, and the ODEs are given in Eqs. (2.20) - (2.28) and (2.29), Section 2.3.

- 4 dynamic inflow equations for the main and tail rotors, when using a 3-state Peters-He model to compute the main rotor induced inflow. If the free wake model is used instead of the Peters-He model, then the main rotor dynamic inflow equations are removed from the system and the wake geometry is evolved separately using a time-marching process. The corresponding ODE residuals are $\boldsymbol{\epsilon}_{\lambda_{\text{MR}}}$ and $\boldsymbol{\epsilon}_{\lambda_{\text{TR}}}$, given by Eqs. (2.113) and (2.126), Section 2.4.3.

- $2 \times N_b \times N_m$ equations for rotor blade dynamics that represent the mode-weighted Euler-Bernoulli beam equations. The corresponding ODE residuals are $\boldsymbol{\epsilon}_{\text{rotor}}$, given by Eqs. (2.112), Section 2.4.7.

- $2 \times N_{mc}$ equations for the flexible cable that represent the weighted residuals of the Euler-Bernoulli transverse beam bending equations. The corresponding ODE residuals are $\boldsymbol{\epsilon}_{\text{cable}}$, given by Eqs. (2.109) and (2.110), Section 2.4.5.

- 6 equations that enforce moment equilibrium and kinematic compatibility for the towed body Euler angles. The corresponding ODE residuals are $\boldsymbol{\epsilon}_{\mathrm{L}}$, given by Eqs. (2.26) - (2.28). When a simplified axially flexible cable model is used, the cable equations are eliminated from the system and the force equilibrium equations are included, given in Eqs. (2.20) - (2.22), Section 2.3.

The vector of ODE residuals $\boldsymbol{\epsilon}$ is assembled from the individual components and is given by

$$\boldsymbol{\epsilon} = \left\{ \begin{array}{ccccccc} \boldsymbol{\epsilon}_{\mathrm{F}}^{\mathrm{T}} & \boldsymbol{\epsilon}_{\lambda_{\mathrm{MR}}}^{\mathrm{T}} & \epsilon_{\lambda_{\mathrm{TR}}}^{\mathrm{T}} & \boldsymbol{\epsilon}_{\mathrm{rotor}}^{\mathrm{T}} & \boldsymbol{\epsilon}_{\mathrm{cable}}^{\mathrm{T}} & \boldsymbol{\epsilon}_{\mathrm{L}}^{\mathrm{T}} \end{array} \right\}^{\mathrm{T}} \tag{2.137}$$

3 Solution Methods

This chapter describes the numerical techniques used to solve the differential equations governing the motion of rigid and flexible structures that comprise the helicopter-cable-towed body system. The first section details the computation of "trim" (steady flight) configurations, in which the vehicle acceleration components along body axes are zero and the rotor response is periodic. The second section covers extraction of linearized models about equilibrium configurations which are useful for stability analysis and evaluating characteristics of the vehicle frequency response to pilot inputs. The third section describes the numerical procedure used to simulate the evolution of the system dynamics as a function of time in response to user-specified pilot inputs, starting from an initial condition. The final section covers the procedure used to include the free-vortex wake during trim and time marching.

The ODEs of interest are strongly coupled to each other, especially for the rotor dynamics. Explicit expressions for the accelerations (second time derivatives of displacements) as a function of forcing and velocities are lengthy and cumbersome to manipulate. One way to simplify the beam equations is to make small-angle assumptions and use an ordering scheme (Ref. [19]), which then restricts the validity

of the analysis to small angles. Alternately, it is possible to use the original form of the governing ODEs

$$\mathbf{f}(\dot{\mathbf{y}},\ \mathbf{y},\ \mathbf{u},\ t\ ) \quad = \quad \overline{\boldsymbol{\epsilon}} \quad = \quad \mathbf{0} \tag{3.1}$$

with a *class* of techniques that, given an initial guess $\mathbf{y}_0(t)$, obtain a solution $\mathbf{y}(t)$ such that $e(\overline{\boldsymbol{\epsilon}}) < \delta$, where $e(\overline{\boldsymbol{\epsilon}})$ is an error metric and δ is a user-specified threshold that is used to terminate the solution process to required numerical precision. Thus, the task of simulating vehicle dynamics is simplified to that of programming the logic for computing *numerical* values of $\overline{\boldsymbol{\epsilon}}$ for a given $\mathbf{y}, \dot{\mathbf{y}}, \mathbf{u}$ and leveraging open-source subprograms from NETLIB for obtaining trim solutions and simulating maneuvering flight (Ref. [98]).

3.1 Definition of Trim

The term "trim" is used to refer to a steady flight condition in which the translational and angular acceleration components along and about the body axes are zero. Therefore, trim includes steady level flight, steady climbing flight, steady level turns and steady climbing/descending turns of constant radii. The concept of rotorcraft trim evolved from the corresponding definition for fixed-wing platforms, and so it is useful to define aircraft trim first.

3.1.1 Aircraft Trim

Trim for a fixed-wind aircraft is defined as a steady flight condition in which the control settings, orientations and velocity of the vehicle produce forces (inertial

and aerodynamic) that exactly cancel out contibutions from gravity and buoyancy, thus allowing the aircraft to remain in its state of rest or uniform motion " indefinitely ". The force distributions on a fixed-wing aircraft in trim are steady, hence the aerodynamic and inertial loads at any two instants in time will be near-identical. There may still be fluctuations in these loads at extremely high frequencies (determined by the RPMs of the various rotors inside the engine), but the amplitudes of these fluctuations are so small that their effect on aircraft trim is negligible.

Unlike a fixed wing, the aerodynamic and inertial loads generated by each rotor blade are not steady. In forward flight, rotor blades experience time-varying dynamic pressures and operating angles of attack, and therefore undergoes unsteady motion in response to these time-varying force and moment distributions along the span. These unsteady motions result in time-varying inertial blade loads in addition to the fluctuating aerodynamic loads, hence the forces transmitted to the airframe are vibratory in nature. With these considerations, rotor trim can be defined.

3.1.2 Rotor trim

When the controls for a rotor (collective and cyclic pitch inputs) are held constant, the rotor is said to be trimmed if the blade response is periodic, i.e. it has reached steady-state, and the forces and moments, when averaged over this period, do not change over successive cycles. Often, the time period is assumed to be that reqiured for one rotor revolution, due to the cyclic variation of the free-stream velocities as seen by the blade and the kinematics of the pitch control system.

3.1.3 Rotorcraft Trim

Just as fixed-wing trim is not significantly affect by engine vibrations, it is assumed that, for the purposes of enforcing body force and moment equilibrium, rotorcraft trim is insensitive to the *oscillatory* forces and moments transmitted to the hub. Instead, the *time-averaged* forces and moments will be used to represent the contributions from rotor loads to Eqs. (2.20) - (2.28). This assumption is justified since the vibratory loads manifest at sufficiently large frequencies that the airframe response is negligible and the vehicle trim state is unaffected (Ref. [40]). When the blade motion is periodic *and* the time-averaged forces and moments generated by the rotor are sufficient for establishing vehicle force and moment equilibrium, the system is said to be in *coupled trim* or *propulsive trim*.

The most general case of trim considered is a steady coordinated helical climbing turn of constant radius (Ref. [99]). This flight condition is defined by three parameters : the flight speed V, the flight path angle γ (positive for climb) and the turn rate $\dot{\psi}$ (positive for nose-right turns). Using this definition,

- Steady level turning flight is a special case in which $\gamma = 0$ (constant altitude)
- Steady climbing flight is a special case in which $\dot{\psi} = 0$
- Steady level forward flight is a special case in which $\gamma = 0$ and $\dot{\psi} = 0$
- Hover is a special case in which $\gamma = 0$, $V = 0$ and $\dot{\psi} = 0$

Mathematically, trim is enforced by imposing additional conditions on the govering ODE set Eq. (3.1). For the rotorcraft trim problem, the differential equations

reduce to nonlinear algebraic equations that may be represented as

$$\mathbf{F}(\mathbf{X}) \quad = \quad \overline{\boldsymbol{\epsilon}}_{\text{trim}} \quad = \quad \mathbf{0} \tag{3.2}$$

The problem of trim is then converted to solving a set of algebraic equations for the so-called *trim unknowns*. The trim unknowns include the rotor response, vehicle attitudes, rotor induced inflow ratios and the pilot controls. Solution of the trim equations is achieved by manipulation of the trim variables $\mathbf{X}$ using a numerical solver (Ref. [100]) until an error metric $\text{e}(|\overline{\boldsymbol{\epsilon}}|_{\text{trim}})$ falls below a user-specified threshold δ_{trim}. To avoid formulating an over-determined or under-determined system of equations, the number of trim variables $\mathbf{X}$ must be equal to the number of trim equations $\mathbf{F}$. The trim equations and corresponding trim variables are given in the following section.

3.2 Trim Equations and Trim Variables

- **The components of time-averaged fuselage translational and rotational accelerations along and about the body axes must be zero**, as given in Eqs. (2.20) - (2.28). Using " T " to represent time period for one rotor revolution, the first six trim equations are

$$\int_0^T \dot{u}_{\text{F}}\, dt \quad = \quad \epsilon_{\text{RB1}} \quad = \quad 0 \tag{3.3}$$

$$\int_0^T \dot{v}_{\text{F}}\, dt \quad = \quad \epsilon_{\text{RB2}} \quad = \quad 0 \tag{3.4}$$

$$\int_0^T \dot{w}_{\text{F}}\, dt \quad = \quad \epsilon_{\text{RB3}} \quad = \quad 0 \tag{3.5}$$

$$\int_0^T \dot{p}_{\text{F}}\, dt \quad = \quad \epsilon_{\text{RB4}} \quad = \quad 0 \tag{3.6}$$

$$\int_0^T \dot{q}_{\text{F}}\, dt \quad = \quad \epsilon_{\text{RB5}} \quad = \quad 0 \tag{3.7}$$

$$\int_0^T \dot{r}_{\text{F}}\, dt \quad = \quad \epsilon_{\text{RB6}} \quad = \quad 0 \tag{3.8}$$

Equations (3.3) - (3.8) constitute the six trim conditions that enforce vehicle force and moment equilibrium under steady flight conditions. The corresponding trim variables are the pilot controls (δ_0, δ_{lat}, δ_{lon}, δ_{ped}) and the fuselage pitch and roll attitudes (ϕ_{F}, θ_{F}). The last two trim variables are indirect controls, in the sense that they cannot be immediately adjusted by the pilot. Instead, the vehicle has to be *flown into* these orientations using the four direct controls that influence the lift distributions over the rotor disks.

- **The rotor must be trimmed**, i.e. the motions of all blades must be individually periodic. Since we assume that all blades are identical, it follows that **all blades must exhibit identical motions** with phase offsets corresponding to their relative azimuthal spacing. Therefore, the problem of obtaining the motion of all blades of a particular rotor is simplified to that of obtaining the motion of a reference blade. Without loss of generality, the first blade is chosen to be the reference blade.

  A further assumption is made at this stage to simplify the analysis - that the resulting periodic blade motion is well-represented using a Fourier series in integer multiples of the rotor frequency Ω. This method is often called *harmonic balance*, and can capture the dominant blade motions (with regard to flight dynamics) using the first few harmonics. **A Galerkin method with harmonic balance is used to obtain the time-resolution of the**

rotating blade modes. The generalized coordinates of a blade at azimuth ψ can be approximated to

$$\boldsymbol{\eta}_j(\psi) \quad \approx \quad \boldsymbol{\eta}_0 \quad + \quad \sum_{k=1}^{\mathrm{Nh}} (\boldsymbol{\eta}_{\mathrm{kc}} \ \cos k\psi \quad + \quad \boldsymbol{\eta}_{\mathrm{ks}} \ \sin k\psi) \tag{3.9}$$

$\boldsymbol{\eta}_0$ represents the steady part of the generalized coordinates, and the amplitudes of the sine and cosine components for the " k^{th} " harmonic are ($\boldsymbol{\eta}_{kc}$, $\boldsymbol{\eta}_{ks}$). The Nm(1+2 Nh) Fourier coefficients are the trim variables that define the rotor blade motions with respect to the undeformed rotating preconed axes. These Fourier coefficients are used to compute the blade deflections which are substituted into the beam equations, to yield the mode-weighted ODE residuals

$$\overline{\boldsymbol{\epsilon}}_{\mathrm{blade\ 1}} \quad = \quad \mathbf{f}_{\mathrm{beam}}(\mathbf{y}_1, \ \dot{\mathbf{y}}_1, \ \mathbf{u}, \ t) \tag{3.10}$$

Here, $\mathbf{f}_{\mathrm{beam}}$ represents the ODEs governing rotating beam dynamics, i.e. the mode-weighted flap, lag and torsion equations. $\mathbf{y}_1$ represents a subset of the state vector that contains the 12 rigid-body fuselage states and the generalized coordinates (together with their first time derivatives) for the reference blade. Since we are using Galerkin's method, the corresponding trim equations are obtained by weighting the beam equations with the azimuthal shape functions and integrating over one revolution. The algebraic equation residuals corresponding to the steady, cosine and sine components of blade motions are

$$\boldsymbol{\epsilon}_{\mathrm{steady}} \quad = \quad \int_0^T \boldsymbol{\epsilon}_{\mathrm{blade\ 1}}(t) \qquad\qquad dt \tag{3.11}$$

$$\boldsymbol{\epsilon}_{\mathrm{cos,k}} \quad = \quad \int_0^T \boldsymbol{\epsilon}_{\mathrm{blade\ 1}}(t) \quad \cos k\Omega t \quad dt \tag{3.12}$$

$$\boldsymbol{\epsilon}_{\sin,\mathrm{k}} \quad = \quad \int_0^T \boldsymbol{\epsilon}_{\text{blade }1}(t) \quad \sin k\Omega t \quad dt \tag{3.13}$$

- **The components of helicopter linear, angular velocities along fuselage body axes, and roll and pitch attitudes must be time-invariant**

  For trimmed flight, the vehicle must move at constant speed V. The orientation of the free-stream velocity vector relative to the airframe can be described using the spherical angles α_{F} and β_{F} as defined in Eq. (2.118). The translation velocity components along helicopter body axes are

$$\left.\begin{aligned} u_{\mathrm{F}} &= \mathrm{V}\ \cos\alpha_{\mathrm{F}} \cos\beta_{\mathrm{F}} \\ v_{\mathrm{F}} &= \mathrm{V}\ \sin\beta_{\mathrm{F}} \\ w_{\mathrm{F}} &= \mathrm{V}\ \sin\alpha_{\mathrm{F}} \cos\beta_{\mathrm{F}} \end{aligned}\right\} \tag{3.14}$$

  The helicopter yaw rate $\dot{\psi}_{\mathrm{F}}$ must be constant and the Euler pitch and roll attitudes must be time-invariant. Applying these conditions to Eqs. (2.23), the angular velocity components along body axes are obtained as

$$\left.\begin{aligned} p_{\mathrm{F}} &= -\dot{\psi}_{\mathrm{F}} \sin\theta_{\mathrm{F}} \\ q_{\mathrm{F}} &= \dot{\psi}_{\mathrm{F}} \cos\theta_{\mathrm{F}} \sin\phi_{\mathrm{F}} \\ r_{\mathrm{F}} &= \dot{\psi}_{\mathrm{F}} \cos\theta_{\mathrm{F}} \cos\phi_{\mathrm{F}} \end{aligned}\right\} \tag{3.15}$$

  At low forward speeds, the reduced dynamic pressure on the vertical stabilizer renders it ineffective for producing anti-torque. Therefore, **below a certain threshold airspeed, the helicopter is constrained to fly with zero sideslip angle**, i.e.

$$\beta_{\mathrm{F}} \quad = \quad 0$$

Above the threshold airspeed, all turns must be coordinated to increase ride comfort and reduce the danger of entering a spin. Mathematically, turn coordination is enforced by setting the cumulative component of inertial and gravitational forces along the $\boldsymbol{j}_{\mathrm{B}}$ direction to zero. Substituting Eqs. (3.14) and Eqs. (3.15) in Eq. (2.21) yields the residual of the turn coordination equation as

$$\epsilon_{\text{coord}} \quad = \quad \mathrm{V}\dot{\psi}_{\mathrm{F}} \cos\beta_{\mathrm{F}}(\cos\alpha_{\mathrm{F}} \cos\theta_{\mathrm{F}} \cos\phi_{\mathrm{F}} \; + \; \sin\theta_{\mathrm{F}} \sin\alpha_{\mathrm{F}}) - g \sin\phi_{\mathrm{F}} \cos\theta_{\mathrm{F}} \tag{3.16}$$

Another kinematic relationship exists between the climb angle γ, the Euler angles $(\psi, \theta, \phi)_{\mathrm{F}}$ and the wind angles $(\alpha, \beta)_{\mathrm{F}}$. To determine this relationship, consider the velocity components of the helicopter along fuselage body axes, as given in Eqs. (3.14). The velocity components along the earth-fixed axes can be obtained using the rotation matrix from body axes to gravity axes as

$$\begin{Bmatrix} \dot{\mathrm{x}}_{\mathrm{F}} \\ \dot{\mathrm{y}}_{\mathrm{F}} \\ \dot{\mathrm{z}}_{\mathrm{F}} \end{Bmatrix} \quad = \quad \mathbf{T}_{GB} \begin{Bmatrix} u_{\mathrm{F}} \\ v_{\mathrm{F}} \\ w_{\mathrm{F}} \end{Bmatrix} \tag{3.17}$$

The component along $\boldsymbol{k}_{\mathrm{G}}$ is given by the third row of the right hand side. By definition, the same velocity component is equal to

$$\dot{\mathrm{z}}_{\mathrm{F}} \quad = \quad -V \sin\gamma$$

The negative sign accounts for the fact that $\boldsymbol{k}_{\mathrm{G}}$ points downward and a positive γ indicates a steady increase in altitude. **The equation of flight path** can be obtained by comparing the two expressions for $\dot{\mathrm{z}}_{\mathrm{F}}$ above, and dividing by

the velocity magnitude V. The residual of this trim equation is

$$\left.\begin{aligned} \epsilon_{\text{FP}} \quad = \quad & \cos\alpha_{\text{F}} \cos\beta_{\text{F}} \sin\theta_{\text{F}} \quad - \quad \sin\gamma_{\text{F}} \\ & - \cos\theta_{\text{F}} (\sin\beta_{\text{F}} \sin\phi_{\text{F}} \; + \; \sin\alpha_{\text{F}} \cos\beta_{\text{F}} \cos\phi_{\text{F}}) \end{aligned}\right\} \tag{3.18}$$

The trim variables corresponding to the turn coordination and flight path equations are (α_{F}, β_{F}). Perfect hover with identically zero forward speed is simulated by replacing the flight path equation with

$$\epsilon_{\text{FP}} \quad = \quad \alpha_{\text{F}} \qquad\qquad \textbf{at hover}$$

- **The inflow ratios are time-invariant** when averaged over one revolution of the main rotor. The corresponding trim equation residuals are

$$\begin{aligned} \epsilon_{\lambda_{TR}} \quad &= \quad \int_0^T \dot{\lambda}_{\text{TR}} \; dt \\ \epsilon_{\lambda_{0,MR}} \quad &= \quad \int_0^T \dot{\lambda}_{0_{\text{MR}}} \; dt \\ \epsilon_{\lambda_{1c,MR}} \quad &= \quad \int_0^T \dot{\lambda}_{1\text{c}_{\text{MR}}} \; dt \\ \epsilon_{\lambda_{1s,MR}} \quad &= \quad \int_0^T \dot{\lambda}_{1\text{s}_{\text{MR}}} \; dt \end{aligned}$$

3.3 Trim with Simplified Cable Model

When a simplified cable model is used, it is assumed that the cable is straight and acts like a linear spring in tension. The towed body formulation is similar to the helicopter fuselage formulation, and the state vector contains both positions and orientations of the submerged load. The trim variables are the components of the towed body CG relative to the helicopter CG along earth-fixed axes (X_{L}, Y_{L},

$Z_{\rm L}$), the Euler pitch and roll angles ($\theta_{\rm L}$, $\phi_{\rm L}$) and the angles ($\alpha_{\rm L}$, $\beta_{\rm L}$), which are analogous to the wind-axes angles ($\alpha_{\rm F}$, $\beta_{\rm F}$) for the airframe. The corresponding trim equations are zero accelerations along and about the load body axes, and the flight path equation (3.18) applied to the towed body. The Euler angle $\psi_{\rm L}$ can be obtained in terms of the wind-axes angles ($\alpha_{\rm L}$, $\beta_{\rm L}$), the Euler roll and pitch attitudes ($\phi_{\rm L}$, $\theta_{\rm L}$) and the flight path angles ($\gamma_{\rm L}$, $\xi_{\rm L}$) and the helicopter angle of flight path ($\gamma_{\rm F}$) using kinematic consistency conditions, as follows.

Consider a time instant in which an object is moving with a non-zero velocity V, and the velocity orientations with the gravity axes described by the spherical angles γ and ξ, shown in Fig 3.1.

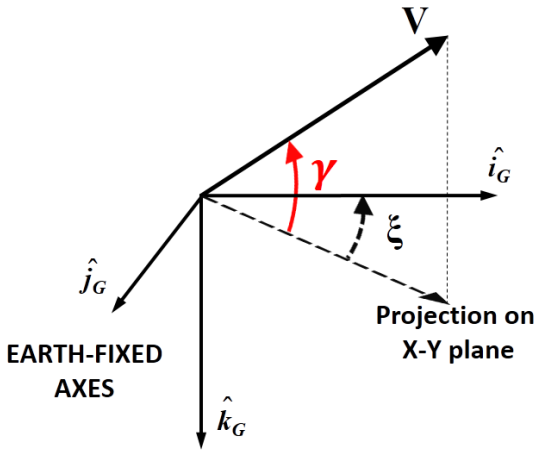

Figure 3.1: Flight path angles

The load velocity components along earth-fixed axes are

$$\dot{x}_{\rm g} = {\rm V}\cos\gamma\cos\xi$$

$$\dot{y}_{\rm g} = {\rm V}\cos\gamma\sin\xi$$

$$\dot{z}_{\rm g} = -{\rm V}\sin\gamma$$

The velocity of the object may also be resolved along body-fixed axes to yield

$$\begin{aligned} u &= \mathrm{V}\cos\alpha\cos\beta \\ v &= \mathrm{V}\sin\beta \\ w &= \mathrm{V}\sin\alpha\cos\beta \end{aligned}$$

The gravity-axes velocity components may also be obtained from their body-axes counterparts using a rotation matrix as

$$\begin{Bmatrix} \dot{x}_{\mathrm{g}} \\ \dot{y}_{\mathrm{g}} \\ \dot{z}_{\mathrm{g}} \end{Bmatrix} = \begin{Bmatrix} V\cos\gamma\cos\xi \\ V\cos\gamma\sin\xi \\ -V\sin\gamma \end{Bmatrix} = \mathbf{T}_{GB} \begin{Bmatrix} u \\ v \\ w \end{Bmatrix} = \mathbf{T}_{GB} \begin{Bmatrix} V\cos\alpha\cos\beta \\ V\sin\beta \\ V\sin\alpha\cos\beta \end{Bmatrix}$$

The above expressions can be broken down into components, yielding 3 equations

$$\left.\begin{aligned} \cos\gamma\cos\xi = {} & \cos\alpha\cos\beta\cos\theta\cos\psi + \sin\theta\sin\phi\sin\beta\cos\psi \\ & - \cos\phi\sin\psi\sin\beta \\ & + \sin\alpha\cos\beta(\sin\theta\cos\phi\cos\psi + \sin\phi\sin\psi) \end{aligned}\right\} \quad (3.19)$$

$$\left.\begin{aligned} \cos\gamma\sin\xi = {} & \cos\alpha\cos\beta\cos\theta\sin\psi + \sin\theta\sin\phi\sin\psi\sin\beta \\ & + \cos\phi\cos\psi\sin\beta \\ & + \sin\alpha\cos\beta(\sin\theta\cos\phi\sin\psi - \sin\phi\cos\psi) \end{aligned}\right\} \quad (3.20)$$

$$\left.\begin{aligned} -\sin\gamma = {} & \sin\beta\cos\theta\sin\phi - \cos\alpha\cos\beta\sin\theta \\ & + \sin\alpha\cos\beta\cos\theta\cos\phi \end{aligned}\right\} \quad (3.21)$$

Eq. (3.21) is the flight path angle equation, and is used as the trim equation corresponding to the wind-axes angle α for both the helicopter and the towed body.

The heading angle ψ can be computed using Eqs. (3.19) and (3.20) by grouping the unknowns, to obtain simultaneous equations in $\cos\psi$ and $\sin\psi$

$$\begin{aligned} a_{11}\cos\psi \;+\; a_{12}\sin\psi &= b_1 \\ a_{11}\sin\psi \;-\; a_{12}\cos\psi &= b_2 \end{aligned}$$

The coefficients are

$$\begin{aligned} a_{11} &= \cos\theta\cos\alpha\cos\beta \;+\; \sin\theta\sin\phi\sin\beta \;+\; \sin\alpha\cos\beta\sin\theta\cos\phi \\ a_{12} &= -\sin\beta\cos\phi \;+\; \sin\alpha\cos\beta\sin\phi \\ b_1 &= \cos\gamma\cos\xi \\ b_2 &= \cos\gamma\sin\xi \end{aligned}$$

The simultaneous equations can be used to obtain ψ in terms of a_{11}, a_{12}, b_1 and b_2.

- When a_{11} is very small, the equations reduce to

$$\tan\psi = -\frac{b_1}{b_2} = -\cot\xi$$

- When a_{12} is very small, the equations reduce to

$$\tan\psi = \frac{b_2}{b_1} = \tan\xi$$

- When both a_{11} and a_{12} are non-negligible,

$$\tan\psi = \frac{b_1 a_{12} \;+\; b_2 a_{11}}{b_1 a_{11} \;-\; b_2 a_{12}}$$

This relationship is valid for a general rigid body, and is applied to both the helicopter fuselage and the towed body for the trim formulation in turning flight.

Two-body Turn Kinematics

In steady turning flight, the positions and orientations of the helicopter and submerged load remain fixed relative to each other. However, it is not necessary that the load travels along the same path as the helicopter - it may travel along a circle of larger or smaller radius. The instantaneous velocity vectors of the helicopter and towed body may also be oriented along different directions. The present trim formulation in turning flight can accommodate these possible scenarios.

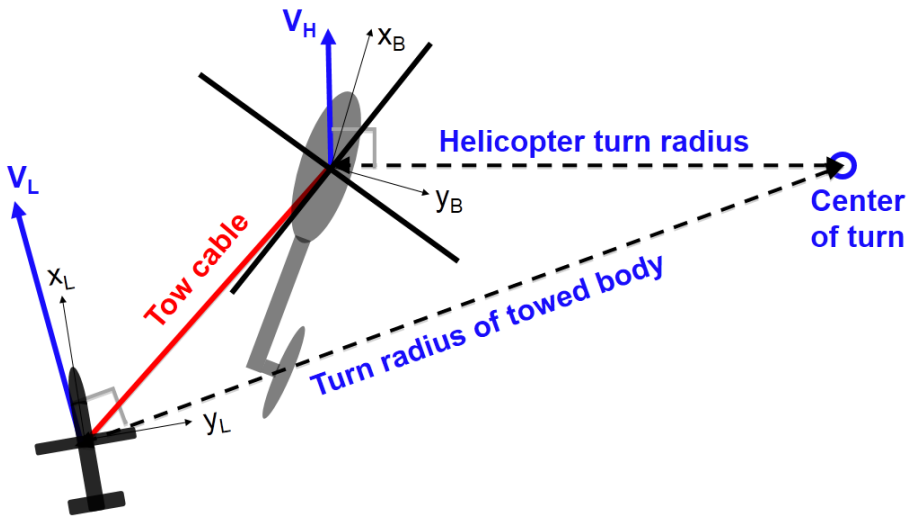

Figure 3.2: Helicopter with towed body

For the helicopter in trim, the spherical angle ξ_{F} is set to zero without loss of generality. Henceforth, the $_{\text{L}}$ subscript is dropped and the variable ξ will be used to refer to the load spherical angle. The load spherical angle ξ is obtained from kinematics, shown in Fig. 3.3, as

$$\tan\xi = -\frac{\Delta X}{R_{\text{H}} + \Delta Y} \tag{3.22}$$

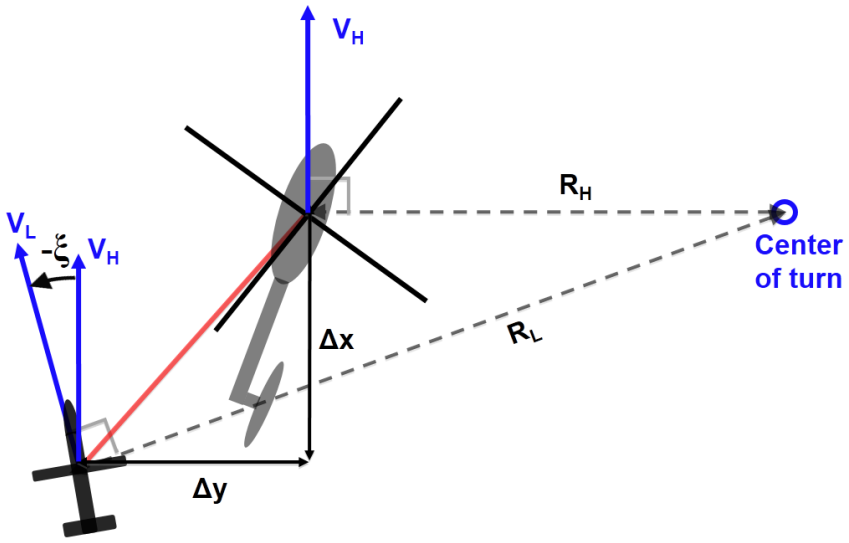

Figure 3.3: Right-handed turn with towed body

This formulation is for a nose-right turn, but the general method may be applied for nose-left turns as well. In trim, the load and helicopter have the same vertical velocity, i.e. rate of climb. Mathematically, this is expressed as

$$\dot{z}_{g_F} \quad = \quad \dot{z}_{g_F} \quad = \quad V \sin \gamma_F \quad = \quad V_L \sin \gamma_L \tag{3.23}$$

The helicopter turn radius can be computed from known trim parameters as

$$R_H \quad = \quad \frac{V}{|\dot{\psi}_H|} \tag{3.24}$$

The turn radius of the submerged load can be computed using the trim variables $(\Delta X, \Delta Y, \Delta Z)$ as

$$R_L \quad = \quad \sqrt{(R_H + \Delta Y)^2 + \Delta X^2} \tag{3.25}$$

The CGs of the helicopter and the load both execute circular motions of different radii in the plane of the turn, about the same center. The velocity of the CG of the towed body in the plane of the turn is obtained from kinematics by

$$V_{L2} \quad = R_L \, \dot{\psi}_H \tag{3.26}$$

The magnitude of the load velocity is obtained from Eqs. (3.23) and (3.26) as

$$V_{\mathrm{L}} \quad = \quad \sqrt{\mathrm{V}^2 \sin^2 \gamma_{\mathrm{F}} \; + \; \mathrm{V}_{\mathrm{L2}}^2}$$

The trim variables (X_{L}, Y_{L}) are directly related to the trail distances ΔX and ΔY as

$$\Delta Y \quad = \quad -Y_{\mathrm{L}} \tag{3.27}$$

$$\Delta X \quad = \quad -X_{\mathrm{L}} \tag{3.28}$$

Modification for Left-handed Turns

A left-handed turn is shown in Fig. 3.4. The treatment of nose-left turns is very similar to that of nose-right turns, and the following equations have to be modified to maintain consistency.

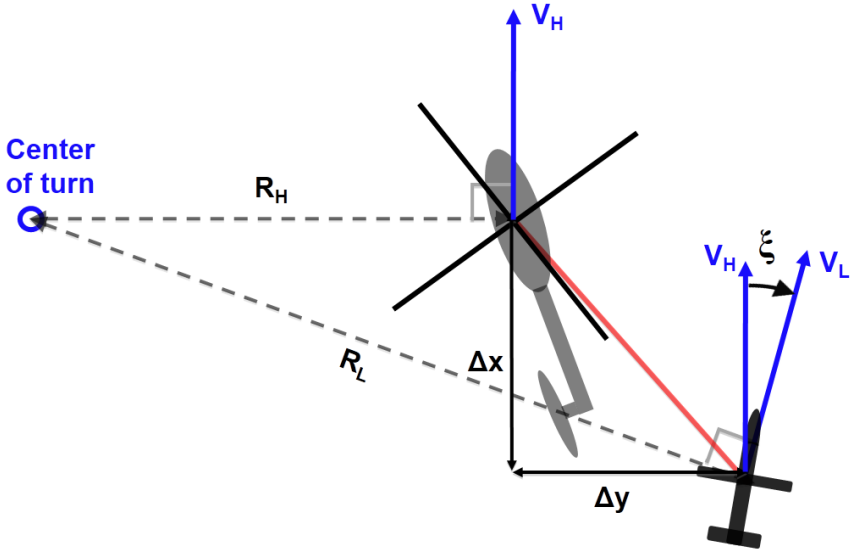

Figure 3.4: Left-handed turn with towed body

Method 1:

The first method of ensuring compatibility of left-handed turns with the present formulation is to mirror the lateral trail distances, i.e.

- Eq. (3.27) has to be modified as $\Delta Y = Y_{\text{L}}$
- Eq. (3.22) has to be modified as $\tan\xi = \frac{\Delta X}{R_{\text{H}}+\Delta Y}$

Method 2:

Another way to ensure compatibility for right and left-handed turns is to allow the turn radius to become negative for left-handed turns. Thus, Eq. (3.24) is modified as

$$R_{\text{H}} = \frac{\text{V}}{\dot{\psi}_{\text{H}}}$$

All other expressions may be retained in their original form. This implementation allows for "on-line" computation of the load velocity during the trim process, depending on the solver-adjusted value for the load positions.

3.4 Trim with Curved Cables

The curved cable is treated as a flexible beam with its own mass and fluid force distributions along the span. In turning flight, the cable (and towed body) may be subject to additional inertial forces due to centrifugal loading. These inertial loads are automatically accounted for by defining the cable deflections in a rotating coordinate system that is aligned with the helicopter heading ψ_{F}. This choice of

reference frame substitutes one lengthy set of coupling terms in the cable equations (specifically, the role of helicopter turn rate in the cable centrifugal accelerations) with a one-step matrix multiplication for rotating reference frames. This formulation is also identical to that used to analyze rotor blades, hence it involves no additional implementation overhead.

The towed body is treated as a distributed mass attached to the tip of the cable. The load trim variables are the Euler angles (ψ_{L}, θ_{L}, ϕ_{L}) and the trim equations correspond to zero angular acceleration components about load body axes.

The trim variables for the curved cable are the generalized coordinates $\boldsymbol{\eta}_{\text{c}}$, and the corresponding trim equations are the beam flap, lag and torsion equations (2.108) - (2.110).

3.5 Free-Vortex Wake Model in Trim

When the free wake model is used in trim, all the trim conditions given in the previous sections are enforced. The main rotor inflow equations are initially used to generate a starting guess for the trim controls, rotor response and fuselage orientations. Once trim is achieved with dynamic inflow, the main rotor inflow equations are removed from the trim equations and a " loose-coupling " procedure is used to periodically exchange information over one rotor revolution between the aerodynamics and rotor/flight dynamics. A detailed description of the implementation of information exchange between the aerodynamics and flight/structural dynamics may be found in Ref. [20]. Reference [101] provides additional details on the

loose-coupling trim procedure, and a brief summary is given here for completeness.

1. With the trim controls, fuselage velocity and blade motions from the previous iteration, the free wake solution is marched forward in time until the L1 norm of the inflow over the rotor disk reduces below a threshold value δ_{inflow}.

2. The inflow distribution over the rotor disk is computed from the converged free wake geometry and frozen.

3. Using this *frozen* inflow distribution, the trim procedure is applied a solution for simultaneous vehicle equilibrium and rotor response periodicity. Once trim is achieved with the inflow distribution from step 2, the structural/flight dynamics are *frozen*.

4. Steps 1-3 are repeatedly performed until the L1 norm of trim variables (excluding 2/rev and higher rotor harmonics) reduce below a threshold δ_{TV}.

3.6 Extraction of Linearized Models

Models that represent the linearized dynamics of a system in the neighborhood of an equilibrium point (trim condition) can be used to gain insight into system stability characteristics. Consider the dynamics represented by Eqs. (3.1). Expanding the left hand side in a Taylor series, we obtain

$$\mathbf{f} \quad + \quad \frac{\partial \mathbf{f}}{\partial \dot{\mathbf{y}}} \Delta \dot{\mathbf{y}} \quad + \quad \frac{\partial \mathbf{f}}{\partial \mathbf{y}} \Delta \mathbf{y} \quad + \quad \frac{\partial \mathbf{f}}{\partial \mathbf{u}} \Delta \mathbf{u} \quad + \quad \cdots \quad = \quad \boldsymbol{\epsilon} \tag{3.29}$$

At equilibrium (trim), $\mathbf{f} = \boldsymbol{\epsilon} \stackrel{\text{def}}{=} \mathbf{0}$. Let the Jacobian matrices be

$$\mathbf{E} \quad = \quad \left.\frac{\partial \boldsymbol{\epsilon}}{\partial \dot{\mathbf{y}}}\right|_{\text{trim}} \quad ; \quad \mathbf{F} \quad = \quad \left.\frac{\partial \boldsymbol{\epsilon}}{\partial \mathbf{y}}\right|_{\text{trim}} \quad ; \quad \mathbf{G} \quad = \quad \left.\frac{\partial \boldsymbol{\epsilon}}{\partial \mathbf{u}}\right|_{\text{trim}}$$

Neglecting the higher-order terms, we obtain the linearized system dynamics about equilibrium, given by

$$\mathbf{E}\,\Delta\dot{\mathbf{y}} \quad + \quad \mathbf{F}\,\Delta\mathbf{y} \quad + \quad \mathbf{G}\,\Delta\mathbf{u} \quad = \quad \mathbf{0} \tag{3.30}$$

Rearranging the equations and isolating $\Delta\dot{\mathbf{y}}$, we obtain

$$\Delta\dot{\mathbf{y}} \quad = \quad \mathbf{A}\,\Delta\mathbf{y} \quad + \mathbf{B}\,\Delta\mathbf{u} \tag{3.31}$$

Where

$$\mathbf{A} \quad = \quad -\,\mathbf{E}^{-1}\mathbf{F}$$

$$\mathbf{B} \quad = \quad -\,\mathbf{E}^{-1}\mathbf{G}$$

Using Eq. (3.31) and an appropriate state-to-output conversion matrix $\mathbf{C}$, transfer functions between *pilot inputs* and system outputs for the relevant physical quantities can be constructed as

$$\mathbf{H}(s) \quad = \quad \mathbf{C}\ (s\,\mathbf{I}\ -\ \mathbf{A}\ )^{-1}\ \mathbf{B}\ +\ \mathbf{D} \tag{3.32}$$

$\mathbf{D}$ is called the " feed-through matrix ", which represents the direct influence of the inputs on the outputs. For mechanical systems such as rotorcraft and fixed-wing aircraft, the nature of the aerodynamics and rotor dynamics introduces time delays between application of input and establishment of steady-state response. The control inputs influence the force distributions over the rotor disks, modifying the rotor and airframe accelerations. These accelerations, integrated over time, manifest as changes in the positions and velocities which are the system states and outputs. **Therefore, the feed-through matrix D is identically zero**.

3.7 LQR and the Riccati Equation

Feedback control inputs based on linearized models are used in the present analysis to track prescribed vehicle motions and obtain the control inputs required to fly a certain trajectory. To obtain the feedback gains $\mathbf{K}$ from the linearized dynamics, the Linear Quadratic Regulator (LQR) (Ref. [102]) is used, which provides a methodology to stabilize and control a linear system by minimizing a designer-weighted quadratic cost functional in the state deviations from targets and the control inputs. For an LTI system with dynamics given by Eq. (3.31), the infinite-horizon continuous-time LQR controller yields state feedback gains $\mathbf{K}$ to minimize the quadratic cost functional

$$J \quad = \quad \int_0^\infty \left(\mathbf{x}^T \, \mathbf{Q} \, \mathbf{x} \; + \; \Delta\mathbf{u}^T \, \mathbf{R} \, \Delta\mathbf{u} \right) dt \tag{3.33}$$

Where

$$\mathbf{x} \quad = \quad \left(\mathbf{y} \; - \; \mathbf{y}_{\text{target}} \right)$$

The state feedback controls are given by

$$\Delta\mathbf{u} \quad = -\mathbf{K} \, \mathbf{x}$$

The feedback gains are obtained from

$$\mathbf{K} \quad = \quad \mathbf{R}^{-1}\mathbf{B}^T\mathbf{P} \tag{3.34}$$

$\mathbf{P}$ is the unique positive definite steady-state solution of the continuous-time Riccati Equation

$$\frac{d\mathbf{P}}{dt} \; + \; \mathbf{A}^T\mathbf{P} \; + \; \mathbf{P}\mathbf{A} \; - \; \mathbf{P}\mathbf{B}\mathbf{R}^{-1}\mathbf{B}^T\mathbf{P} \; + \; \mathbf{Q} \quad = \quad \mathbf{0} \tag{3.35}$$

At steady-state, the time derivatives vanish, and the stabilizing solution satisfies the algebraic Riccati equation

$$\mathbf{A}^T\mathbf{P} \;+\; \mathbf{P}\mathbf{A} \;-\; \mathbf{P}\mathbf{B}\mathbf{R}^{-1}\mathbf{B}^T\mathbf{P} \;+\; \mathbf{Q} \quad = \quad \mathbf{0} \tag{3.36}$$

Taking transpose on both sides

$$\mathbf{A}^T\mathbf{P}^T \;+\; \mathbf{P}^T\mathbf{A} \;-\; \mathbf{P}^T\mathbf{B}\mathbf{R}^{-1^T}\mathbf{B}^T\mathbf{P}^T \;+\; \mathbf{Q}^T \quad = \quad \mathbf{0}$$

The vehicle and load rigid-body states are assigned non-zero weights, and the control inputs are penalized with a unit weight. All other states and off-diagonal weights (entries of $\mathbf{Q}$,$\mathbf{R}$) are assigned to zero. The diagonal form of the weighting matrices for controls and states allows for further simplification of the solution procedure to obtain the feedback gains $\mathbf{K}$ from the Riccati equation. The steady-state equation simplifies to

$$\mathbf{A}^T\mathbf{P}^T \;+\; \mathbf{P}^T\mathbf{A} \;-\; \mathbf{P}^T\mathbf{B}\mathbf{R}^{-1}\mathbf{B}^T\mathbf{P}^T \;+\; \mathbf{Q} \quad = \quad \mathbf{0} \tag{3.37}$$

Eq. (3.37) is very similar to Eq. (3.36), with $\mathbf{P}$ replaced by $\mathbf{P}^T$. Thus, if $\mathbf{P}$ is a stabilizing solution, $\mathbf{P}^T$ is also a stabilizing solution and if a unique stabilizing solution exists, the matrix $\mathbf{P}$ must be symmetric. For a matrix of size $n\times n$, the number of elements of $\mathbf{P}$ to find are $\frac{n(n+1)}{2}$. Thus, Eq. (3.35) can be integrated numerically from an initial condition towards the stabilizing solution by exploiting symmetry and updating the upper or lower-triangular elements of $\mathbf{P}$.

Practical Considerations

- **Controllability**

  A few candidate flight conditions (straight and turning flight at various speeds) were considered to determine whether the system is controllable, which is a necessary condition for a stabilizing solution of the Riccati equation to exist. In all cases, the Grammian was found to be full-rank.

- **Solving the Riccati Equation**

  A Runge-Kutta (fourth-order) scheme is used to advance the Riccati equation forward in time starting from $\mathbf{0}$. For computational efficiency, the time step is increased as the infinity-norm of $\dot{\mathbf{P}}$ decreases, and marching is terminated when it falls below a threshold value (10^{-8})

- **Computation efficiency**

  Additional time savings are obtained by marching the Riccati equation forward from the previous steady-state solution instead of the original initial condition ($\mathbf{0}$). In case the Riccati equation does not converge to a steady-state solution within a prefixed number of iterations (30000 in this case), the feedback gains from the previous update are used and the initial condition is reset to $\mathbf{0}$.

- **Gain Scheduling and Control Smoothness**

  It is possible, but practically cumbersome, to generate feedback gain matrices for a combination of speeds, climb angles, turn rates and altitudes. Every additional parameter (e.g. fin pitch settings) increases the number of potential

pre-computations exponentially. Instead, a dynamic update of the system **A** and **B** matrices is performed every 30 revolutions following a re-trim based on the current flight condition and altitude, and the feedback gains **K** are smoothly transitioned from the previous set to the current one over a few rotor revolutions to avoid abrupt changes in the control inputs.

- **Linearization with Simplified Cable Model**

  The linearized dynamical model in Eq. (3.31) is traditionally obtained using central differences and small perturbations from trim values of the state and control vectors. Obtaining the system **A** matrix using forward-difference based perturbations ensures that slackening effects during the linearization process are avoided and accuracy of the linearized model is retained.

3.8 Maneuvering Flight : Time Integration

A maneuver is a general unsteady flight condition which includes both trimmed flight and accelerating motions. While it is computationally more expensive to simulate compared to trim, the nature of the present formulation Eq. (3.1) used also renders it extremely straightforward to implement. Using an ODE solver (Ref. [103]), the values of $\mathbf{y}$ and $\dot{\mathbf{y}}$ are adjusted automatically at each time step by the solver (internally using polynomial interpolation up to order 5) until the relative and absolute errors fall below a user-specified threshold δ_{ODE}. Reducing this threshold, i.e. enforcing more precision increases the computational effort, but does not significantly affect the accuracy of the solutions beyond a certain numerical value of

δ_{ODE}. In this case, the point of diminishing returns was obtained at $\delta_{\text{ODE}} = 10^{-6}$.

3.9 Non-Dimensionalization

The analysis has been performed in a non-dimensional form to avoid overflow and underflow truncation errors. Table 3.1 shows the reference parameters used to nondimensionalize the relevant physical quantities. For non-rotating beams (cables), the reference rotational speed is set to unity. The reference mass per unit span m_0 and stiffness EI_0 are set to the corresponding values at the root of the beam.

Table 3.1: Non-Dimensionalization Constants

Physical Quantity	Reference Parameter
Length	Beam Length (R)
Mass per unit span	m_0
Bending Stiffness	EI_0
Velocity	$V_{tip} = \Omega R$
Force	$m_0\ \Omega^2\ R^2$
Moment	$m_0\ \Omega^2\ R^3$

4 Verification and Validation

This chapter discusses the test cases used to validate the present analysis. In the first section, verification tests are applied to the beam model by comparing it to analytical solutions for a cantilever beam. In the second section, test data obtained from ship-based towing of submerged loads is used to validate the cable (beam) model under static conditions. In the third section, the beam model is applied to rotor blades, and the coupled rotor-fuselage-inflow dynamics are validated under steady and transient conditions, using shaft power measurements and on-axis transfer functions from pilot inputs to vehicle response, respectively, for the UH-60 Blackhawk.

4.1 Verification : Beam Model

Consider the case of planar bending of a uniform cantilever beam. After bending, a point on the beam (x, 0, 0) is displaced to ($x + u$, v, w). The bending slope tangent, defined as the ratio of vertical displacement to horizontal *material* displacement is

$$\tan\alpha \quad = \quad \frac{w^+}{(x+u)^+}$$

The curvature is the spatial derivative of the angle α along r, given by α^+. Differentiate the expression for $\tan\alpha$ with respect to r to obtain

$$\alpha^+ \sec^2\alpha \quad = \quad \frac{w^{++}}{(x+u)^+} \quad - \quad \frac{w^+(x+u)^{++}}{(x+u)^{+^2}}$$

Using Eqn. 2.59, the expression for α^+ can be reduced to

$$\alpha^+ \quad = \quad \frac{w^{++}}{(x+u)^+} \quad = \quad \frac{w^{++}}{\sqrt{1-w^{+^2}}} \tag{4.1}$$

Pure Tip Moment

When the external load is a pure tip moment, the analytical solution for the beam deformed shape is a circular arc of radius $1/\alpha^+$, with bending coordinates

$$\begin{aligned} w &= \frac{1-\cos\theta}{\alpha^+} \\ x+u &= \frac{\sin\theta}{\alpha^+} \end{aligned}$$

These expressions can be substituted into Eqn. 4.1 to verify that the curvature is constant at all points along the beam. This test indicates that arbitrarily large curvatures can be represented using the spatial gradients of the deflection coordinates $(u,\, v,\, w)$.

Vertical Tip Load

Consider a cantilever beam subjected to a vertical tip load. As the magnitude of the load increases, the effects of transverse bending on axial displacement of the beam sections becomes increasingly important, changing the moment arm for the individual sections. Semi-analytical solutions for *elastica* (Ref. [104]), are available

for the vertical and axial displacements of the beam tip, and can be evaluated numerically using multi-point quadrature to provide a basis for validating the beam model. The vertical and axial deflection of a vertically loaded cantilever beam are shown for various tip loads in Fig. 4.1 for six equi-spaced finite elements.

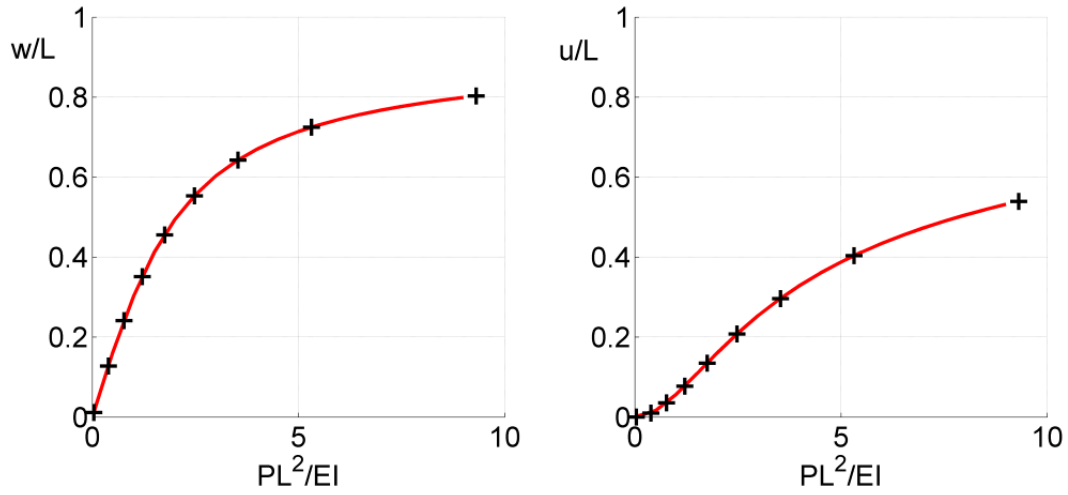

Figure 4.1: Deflection of a Tip-Loaded Cantilever. (+) : elastica (-) : FEM

Free Vibration Frequencies

Using Eq. (2.109), free-vibration frequencies for a non-rotating uniform cantilever beam with 20 equi-spaced elements are identified and compared to analytical solutions in Table 4.1. The frequencies are non-dimensionalized by $\sqrt{\frac{EI}{mL^4}}$. The comparisons indicate that the flap bending frequencies match almost exactly with the analytical solutions. The finite element method always results in a slight over-prediction of the natural frequencies. This over-prediction is a result of the assumptions associated with the finite element method, which imposes additional "stiffness" or "restraints" on a structure by replacing an inifinite number of degrees of freedom with a finite set of deflection parameters.

Table 4.1: Free-Vibration Frequencies of Non-Rotating Cantilever Beams

Mode No.	Analytical Solution	FEM solution
1	3.516	3.516
2	22.034	22.035
3	61.684	61.698
4	120.903	120.910
5	199.860	199.890
6	298.564	298.670

4.2 Ship-based Tow Tests

Experimental tests with submerged loads towed by ships using long cables have been documented in Ref. [71]. A schematic of the test configuration is shown in Fig. 4.2.

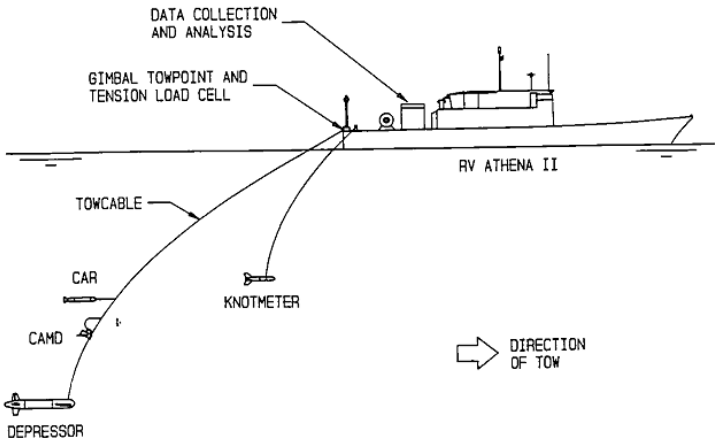

Figure 4.2: Ship-Based Tow Tests of Submerged Load - from Ref. [71]

The data available includes towed body depth, cable angles along the length

and at the tow point, and the total cable force at the tow point. Seven sets of test data are presented. Four datasets correspond to a thinner cable (called "small cable") of lengths 200, 400, 600 and 800 ft. The other three datasets correspond to a thicker cable (called "large cable") of lengths 300, 500 and 700 ft. The cross-section properties of the small and large cables are given in Tables. 4.2 and 4.3 respectively.

Table 4.2: Cross-section Properties of Small Cable

Property	Value	Units
Diameter	0.376 (9.55)	inch (mm)
Air weight per unit length	0.234 (3.41)	lb/ft (N/m)
Lengths	200, 400, 600, 800	ft

Table 4.3: Cross-section Properties of Large Cable

Property	Value	Units
Diameter	0.778 (19.76)	inch (mm)
Air weight per unit length	0.92 (13.42)	lb/ft (N/m)
Lengths	300, 500, 700	ft

The beam model is used to represent the dynamics of the tow cable, and the submerged load is treated as a tip mass with its own forces and moments, obtained from the Appendix of Ref. [71]. The tow system is simulated with both the small and large cables. All seven test cases are evaluated with the present model and compared to a static catenary analysis and experimental data.

Figure 4.3 shows the variation of the cable angle along the length of the 800-ft small cable. Each of the lines corresponds to a different tow speed. The solid lines show the predictions from the present work, while the dashed lines represent predictions from a static catenary analysis developed at the David Taylor Research Center (DTRC). Experimental measurements are represented by data points. Excellent agreement is observed with both the DTRC model and test data at all speeds. The geometrically accurate beam theory (without small angle restrictions) is essential to capture the large variation of slope from 80 deg at the tip to 15 deg near the water surface.

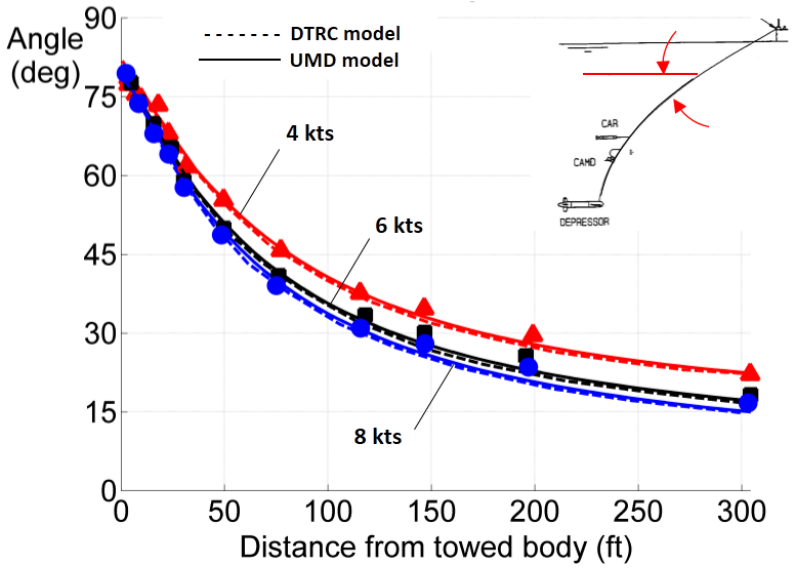

Figure 4.3: Angles along Length of 800 ft Small Cable

Figure 4.4 shows the depth of the towed body as a function of tow speed for various lengths of the small cable. The two analyses match each other almost exactly, while the correlation with test data is better for shorter cables. As the cable lengths increase, the effects of unmeasured cross-currents become significant and may cause reductions in the measured towed body depth.

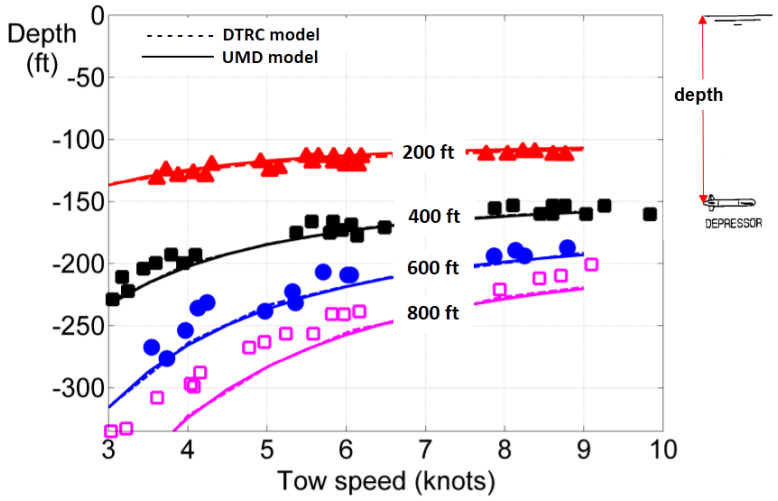

Figure 4.4: Towed Body Depth below Water Surface

Figure 4.5 shows the inclination of the cable to the horizontal at the root, i.e. attachment point on the ship for various cable lengths. Excellent agreement is again obtained, within 1-2 degrees with both test data and the DTRC analysis.

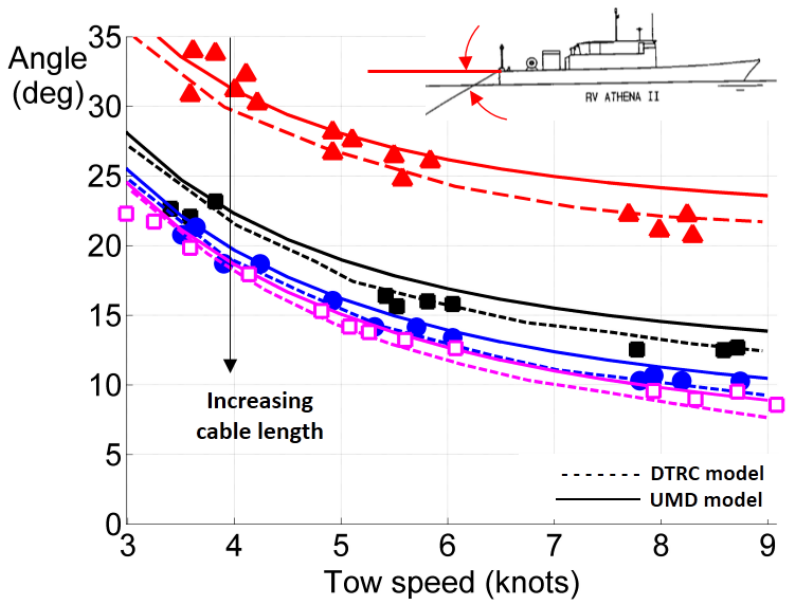

Figure 4.5: Cable Angle at the Tow Point

Figure 4.6 shows the total cable force at the tow point as a function of tow speed. Each of the lines represents a different cable length. The longer cables are heavier and experience more hydrodynamic drag, resulting in increased cable force

at the root. The difference between predicted and measured forces are within the range of experimental scatter. At very low speeds, the effects of water currents on cable force are significant, which may lead to increased data scatter.

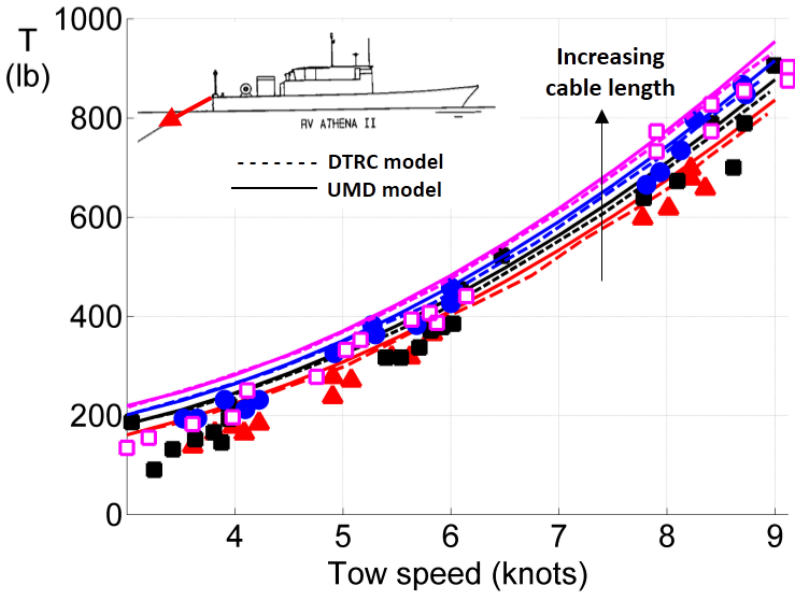

Figure 4.6: Cable Force at the Tow Point

The corresponding test cases for the large cable are shown below.

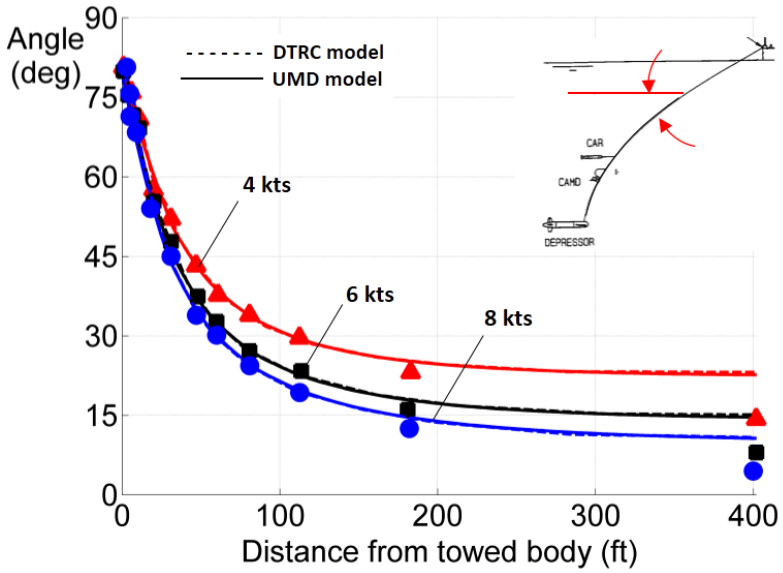

Figure 4.7: Angles along Length of 700 ft Large Cable

Figure 4.7 shows the variation of cable inclination to the horizontal as a func-

tion of distance from the towed body for three different tow speeds, for the 700-ft large cable. Near the towed body, excellent agreement is observed with experimental measurements. The error in predicted cable inclination close to the mid-point is 10 degrees at 4 knots, and 5 degrres at 8 knots. Figure 4.8 shows the variation of towed body depth with tow speed for three different lengths of the large cable. The present analysis shows excellent agreement with the DTRC model, and good agreement with experimental data at low speeds. A near-constant offset between experimental data and predictions exists above 7.5 knots.

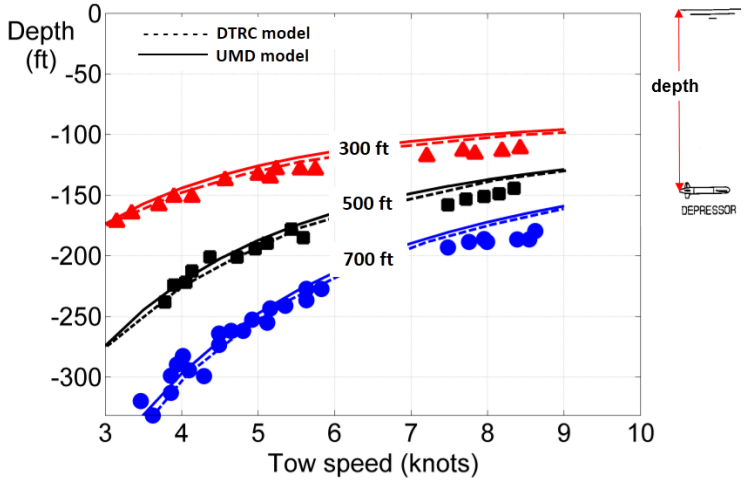

Figure 4.8: Towed Body Depth below Water Surface

Figure 4.9 shows the variation of cable root angle at the tow point with tow speed for various cable lengths. Excellent agreement is again obtained, within 1-2 degrees with both test data and the DTRC analysis. Figure 4.10 shows the variation of cable force at the tow point as a function of tow speed for various lengths of the large cable. The agreement with the DTRC model is excellent, and both analyses agree well with experimental data at low speeds. At tow speeds above 7.5 knots, the trendlines indicate a slight under-prediction from both analyses, but experimental

scatter also increases to almost 200 lb for the 700-ft large cable.

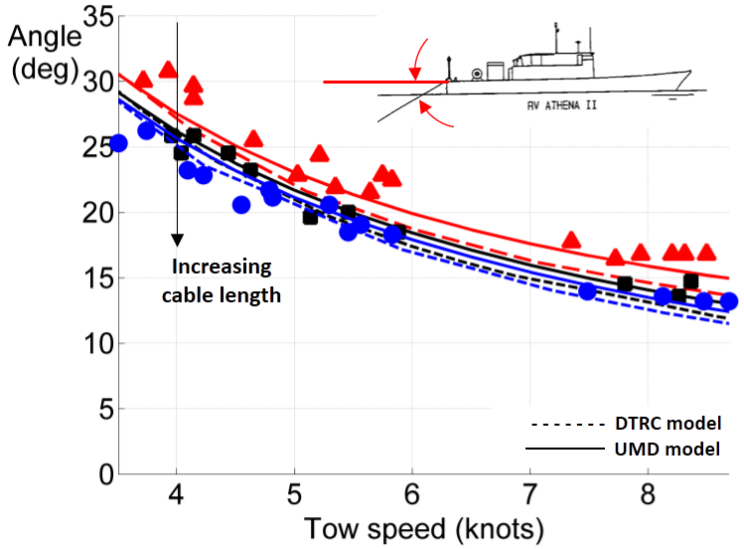

Figure 4.9: Cable Angle at the Tow Point

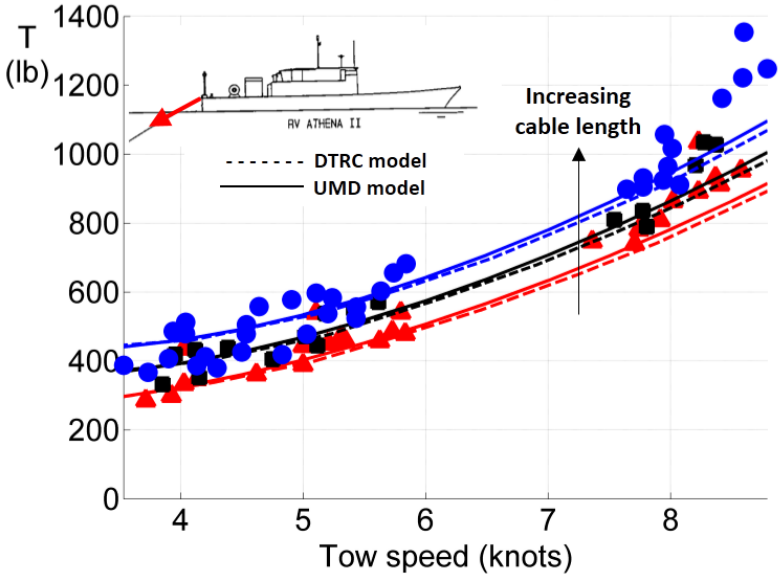

Figure 4.10: Cable Force at the Tow Point

4.3 Helicopter Configuration and Validation

The helicopter used in the present analysis is similar to the UH-60 Blackhawk. The relevant main rotor geometry parameters are given in Table 4.4, and the airframe parameters are given in Table 4.5. All other parameters, including airfoil section characteristics, are obtained from Ref. [26]. The blade structural properties are obtained from Ref. [105]. The swept tip section is considered rigid in the present analysis, with its own inertial and aerodynamic loads.

This section presents a validation of the coupled helicopter wake-flight dynamic model. Predictions of main rotor power required in steady forward flight are compared to flight test data (Ref. [106]) at five different density altitudes to establish the accuracy of the coupled model.

To obtain accurate predictions of helicopter performance at both low and high speeds, all relevant parameters that represent various aspects of the aerodynamics and structures must be chosen methodically. The most significant of these parameters are discussed below.

Fuselage Drag

Reference [106] observed that the baseline equivalent flat-plate area of the UH-60 fuselage (22-24 sq.ft) is not representative of the vehicle used for flight tests, due to additional fairings, wires and airframe appendages that were not added to the wind-tunnel model. A value between 33 and 36 sq.ft was found to be representative of the final configuration used during tests. Since the equivalent flat-plate area

is a measure of fuselage drag, this parameter significantly affects forward flight performance (above 70 knots), and must be chosen carefully.

The present flight dynamic model accounts for the aerodynamic drag from the tail surfaces and tail rotor separately from the fuselage drag. Since the empennage contributes 3 sq.ft to the equivalent flat-plate area of the helicopter (Ref. [106]), **the baseline fuselage flat-plate area was set to 30 sq.ft instead of the wind-tunnel test value of 24 sq.ft**.

Blade Flexibility

The frequencies of the first ten blade modes (computed in vacuum) are given in Table 4.7. Since these mode shapes and frequencies depend on the blade pitch setting, it is important to define the root angle used to determine the modes. **For finding the blade modes, the root angle is set so that the total pitch at 75% span is zero**.

The torsion frequencies (4.7/rev and 14.2/rev) are significantly affected by the pre-twist term θ^+ in the rotating beam equations. Without this term, these frequencies are shifted up to 5.04/rev and 16.1/rev, close to integer multiples of the rotor speed. Therefore, **the pre-twist term must be included in the modal analysis when checking for frequency coalescence, especially for elastic torsion**.

The first two modes correspond to rigid flap and lag motions with negligible bending curvatures and elastic twist. For the present blade, the blade section of

Table 4.4: Main Rotor Geometry

Parameter	Value	Units
Rotor Type	Single Rotor, ccw	
# blades	4	
Radius	26.83	ft
Rotation Speed	27	rad/s
Chord	1.73	ft
Blade weight	256.9	lbs
Shaft tilt aft relative to body	-3	degrees
Airfoil	SC1095	
Hinge offset	4.66	% Radius
Root cut-out	20	% Radius
Blade twist	Non-linear	
Swashplate control phase offset	-9.7	deg
Location of Swept tip	92.9	% Radius
Sweep Angle	20	deg
Pitch Link Stiffness	67900	ft-lb/rad

gravity is offset from the elastic axis towards the trailing edge from 14% to 72% (defined negative), and towards the leading edge between 72-100% span. This variation closely resembles the flap deflections for the second flap bending mode (2.837/rev), and is one of the primary reasons for elastic flap-twist coupling in this mode. The

Table 4.5: Airframe Parameters

Parameter	Value	Units
Roll Inertia I_{xx}	4658	slug-ft^2
Pitch Inertia I_{yy}	38512	slug-ft^2
Yaw Inertia I_{zz}	36796	slug-ft^2
Roll-Yaw Coupling Inertia I_{xz}	1882	slug-ft^2
Fuselage Station of vehicle CG	360	in
Fuselage Station of main rotor shaft	341.215	inch
Waterline Station of vehicle CG	243	in
Waterline Station of main rotor shaft	300	in
Atmosphere	ISA	

Table 4.6: Tail Rotor Geometry

Parameter	Value	Units
# blades	4	
Radius	5.5	ft
Rotation Speed	124.62	rad/s
Section lift-curve slope	5.73	/rad
Chord	0.81	ft
Cant angle with vertical	20	deg

Table 4.7: Main Rotor Blade Frequencies

Mode	Freq (/rev)	Mode	Freq(/rev)
1	0.267	6	5.222
2	1.035	7	7.923
3	2.837	8	11.567
4	4.600	9	12.426
5	4.710	10	14.214

torsion and flap-torsion modes (4.6/rev and 4.71/rev) introduce additional elastic twist, in addition to that from pitch link flexibility. The cumulative effect of elastic twist from modes # 3,4,5,6 results in a change in the near-wake distribution, since the section angles of attack are modified significantly (3° near the tip). Further, the tip vortex strength is altered, since it is obtained from the peak of the bound circulation distribution. At low speeds up to 30 knots, elastic twist is beneficial for rotor performance (3.5% power reduction with respect to a torsionally rigid blade), since the total blade twist along the span approaches the "optimum" (in a power loading sense) hyperbolic distribution. At high speeds, increased elastic twist results in increased rotor power requirements by 4% with respect to a torsionally rigid blade. This reduction in rotor efficiency is a result of airfoil sections along the blade operating at "non-optimal" (in a lift-to-drag ratio sense) angles of attack, incurring profile drag penalties to sustain the target rotor thrust. Therefore, **neglecting elastic twist results in an over-prediction of power at low speeds and**

under-prediction at high speeds.

Neglecting the contributions of distributed inertial moments in the flap and lag equations (e.g. through use of ordering schemes) exaggerates the flap-torsion couplings in the rigid flap mode (1.035/rev) when the cross-section CG is offset from the elastic axis. These assumptions result in artificially decreased levels of elastic twist in the blade motions, increasing power predictions at hover (0.6%) and reducing predictions in forward flight (0.7%).

Effect of Elastic Twist on Wake

Some level of modification is required to introduce elastic blade deflections into the free-wake model. The wake model assumes that rotor blades are rigid structures with flap motions. These blade motions are replaced with an equivalent flap angle obtained from the structural dynamics, similar to Refs. [20] and [101]. In the present work, an important update is introduced to improve consistency in the information exchange. **The wake model is modified to include elastic twist during computation of bound circulation along the span**. This has a significant effect on the predicted rotor power when using torsionally flexible blades. If the elastic twist is not included in the wake model (but included in the structural dynamics), the error in predicted rotor power at 120 knots is as much as 12%.

The airfoil zero-lift angle of attack α_0 (as given by tabulated data in Ref. [26]) changes as a function of Mach number. These characteristics in experimental data result in discrepancies in the near-wake model, which relies on a single zero-lift

angle of attack along the span. Further, changes in α_0 result in a constant offset in the bound vortex strength along the blade, which then affects the tip vortex strength (and therefore induced inflow) significantly. To avoid propagating the effect of these discrepancies into the wake model, the tip vortex strength was prescribed from blade lift distribution (computed from tables of Ref. [26]), using the Kutta-Joukowski theorem to directly relate the wake trailer strengths and the aerodynamic loads. When the near-wake strengths were assigned in a similar manner, the iterative convergence process was numerically unstable.

Root Cut-Out and Blade Spar Drag

Most rotor blades have cut-out sections near the root, where airfoil sections are absent and the blade spar is exposed to the free-stream flow in the root cut-out region (20% span in the present case). The spar experiences profile drag that has an increasingly significant effect on rotor power required. In the present case, it is assumed that the blade spar profile drag corresponds to a C_D=0.05 and a reference cross-section dimension of the root chord (1.73 ft). **Blade spar drag affects the rotor power prediction by as much as 3% at 100 knots**, and is one of the empirical parameters that must be chosen with care.

Comparison to Analyses with Traditional Ordering Schemes

Previous work (Refs. [19], [20]) utilized ordering schemes tailored for small or moderate rotations, to simplify the analysis and reduce the number of terms in

analytical expansions of the governing equations. These so-called "second-order" approximations introduce errors in the beam dynamics. A comparison of the rotor power predictions was obtained using ordering schemes and the geometrically exact approach, based on which the following conclusions are drawn

- Axial fore-shortening has no perceptible effect on rotor torque
- Contributions from aerodynamic loads to the tensile force computations have negligible effects on rotor power
- Small-angle assumptions have no effect on structural loads, due to inherently small curvatures in the blade
- Using second-order approximations to the inertial loads results in 0.8% (hover) to 1.5% (150 knots) under-prediction of power. The error scales with the magnitudes of the lag angles, and is minimum at 70 knots
- Using second-order approximations to the aerodynamic loads results in 2.5 to 3.5% under-prediction of power, depending on airspeed

Elimination of the individual higher-order terms one-at-a-time may result in negligible error in the final solution. However, these higher-order terms are so numerous, that their collective effect introduces second-order error in the inertial and aerodynamic loads.

Discretization

Grid convergence is important when using discretized models of continuous systems (in this case, the rotating beam equations and the wake model). For the structural dynamics, six blade modes (each with steady, 1/rev, 2/rev and 3/rev motions) were found to be sufficient to obtain accurate estimates of rotor power required. Using more than 6 modes increased the computational effort but yielded less than 1% change in the predicted power. Five finite elements with eight quadrature points in each element are needed to represent the bending and torsion of the flexible section of the rotor blade with six modes. Additional spatial resolution does not affect the predicted rotor power for the cases investigated. For trimming the rotorcraft, the blade loads are sampled at 40 azimuthal stations and averaged over the revolution. These 40 points can be conceptualized as five equal azimuthal subdivisions of the rotor disk, with eight quadrature points in each subdivision. These quadrature points are spaced similar to the radial locations along the blade finite element. A summary of the parameters used for the rotor blade is given in Table 4.8.

The wake model is modified to run on Graphics Processing Units (GPUs) with CUDA-Fortran. Use of GPUs greatly reduces the time required to obtain a trim solution by a factor of 20-25, while affecting the final trim solution (and power predictions) by less than 0.1% compared to CPU computations with double precision. The minor differences in CPU and GPU solutions stem from the fact that induced velocity computations involve the addition of millions of numbers for each

Table 4.8: Discretization for Rotor Blade Structures

Parameter	Value	Units
Azimuthal samples for trim	40	
Flexible finite elements	5	
Quadrature points / element	8	
Number of modes	6	
Blade harmonics per mode	3	

Table 4.9: Discretization for Rotor Wake

Parameter	Value	Units
Wake discretization	10	deg
Near-wake	30	deg
Blade bound vortex segments	40	
Number of wake turns	6	

wake collocation point, and *round-off errors are affected by the order of operations*, which are markedly different when using parallelized multi-stage binary reduction trees (GPU) vs. single-thread accumulation (CPU). Additional details of GPU parallelization are given in Appendix B. Parametric sweeps were used to determine the discretization for the wake model, given in Table 4.9.

Comparison with Test Data

Propulsive trim solutions are obtained for the helicopter in steady forward flight at five select density altitudes and vehicle gross weights, corresponding to flight test configurations (Ref. [106]). Predictions of main rotor power required (MRHPreq) are compared to flight test data to validate the coupled wake-flight dynamics model.

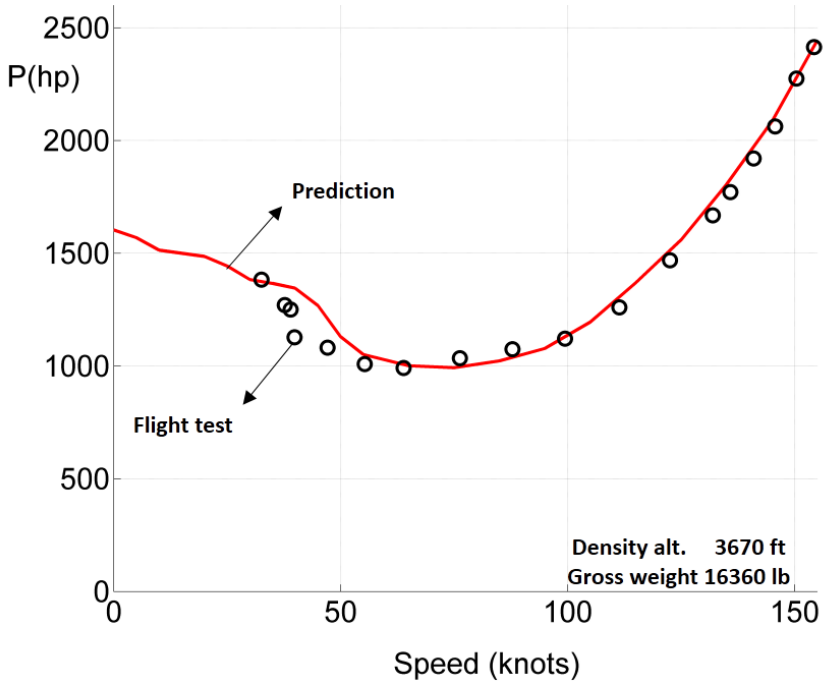

Figure 4.11: Main Rotor Power vs. Speed in Steady Forward Flight

Figure 4.11 shows the comparison of predicted main rotor power with test data from hover to 150 knots at a density altitude of 3670 ft. The comparisons show excellent agreement at speeds above 50 knots. At low speeds (below 30 knots), the predicted power curve exhibits discontinuities associated with rotor-wake interference typical of "transition" flight at $\mu \leq 0.1$. The "knee" in the power curve at 40 knots is captured by the coupled simulation, but instead of the sharp step, the power

curve corresponding to the converged simulation exhibits a gentler reduction with airspeed. The data also shows a linear range between 60 and 100 knots, whereas the predictions place this linear region between 70-100 knots with a higher slope.

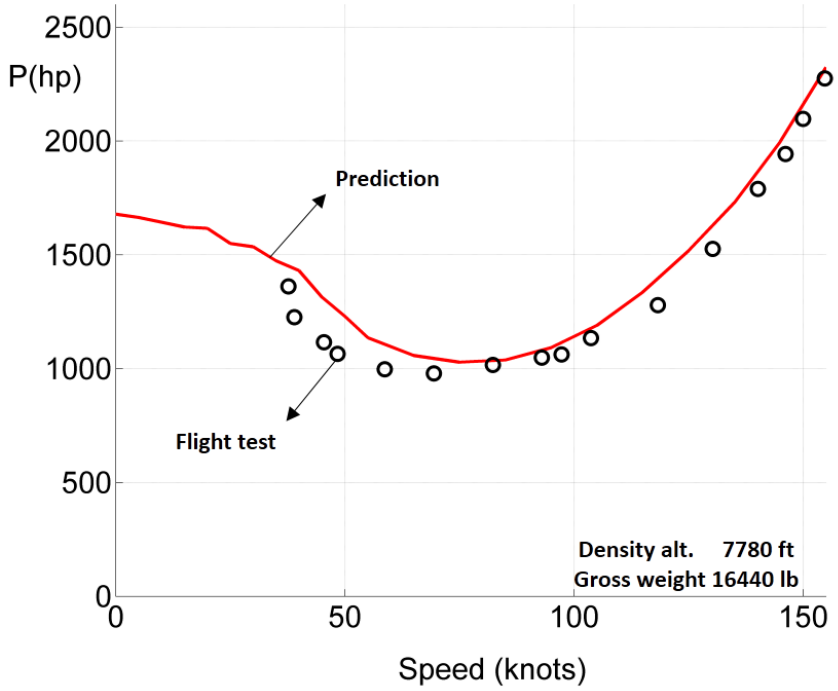

Figure 4.12: Main Rotor Power vs. Speed in Steady Forward Flight

Figure 4.12 shows the comparison of predicted main rotor power with test data from hover to 150 knots at a density altitude of 7780 ft. The comparisons show fair agreement at speeds above 50 knots, and predicted power shows a smooth trend. The step-like changes in rotor power required at low speeds are a result of rotor-wake interactions. Again, the "knee" in the power curve is captured at 40 knots, with maximum error due to over-prediction from 45-60 knots. To ensure that the power predictions and controls are insensitive the convergence process, repeated simulations of wake convection and rotor-body trim are performed until the cumulative error in controls, steady and 1/rev blade motions *and* rotor power

reduces to 1% or smaller.

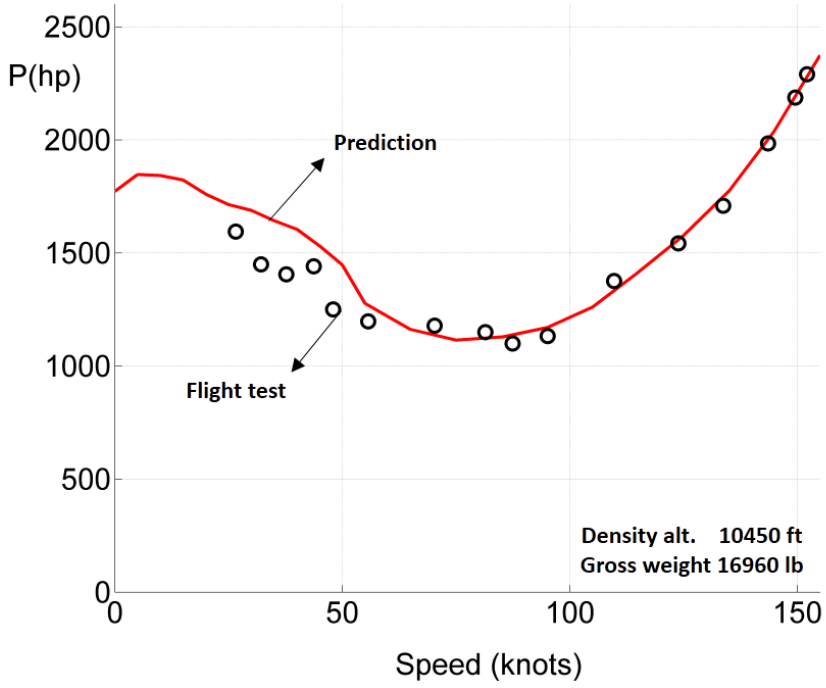

Figure 4.13: Main Rotor Power vs. Speed in Steady Forward Flight

Figure 4.13 shows the comparison of predicted main rotor power with test data from hover to 150 knots at a density altitude of 10450 ft. The comparisons show excellent agreement throughout, except between 30-45 knots. At this altitude, the "knee" in the flight test data is replaced with two step changes at 25 and 40 knots that may be a result of experimental error. The linear region in the flight test still persists from 50-90 knots. The predicted power exhibits smooth trends from 40-150 knots with negligible error ($\leq 1\%$).

Figure 4.14 shows the comparison of predicted main rotor power with test data from hover to 150 knots at a density altitude of 13230 ft. The comparisons again show excellent agreement at speeds above 50 knots. There exist two distinct steps in the flight test data, one at 30 knots and another at 40 knots that are not predicted

by the present model. The linear region in the flight test is present between 60-100 knots, together with significant data scatter (14%) from 90-100 knots. The predicted power exhibits smooth trends above 40 knots.

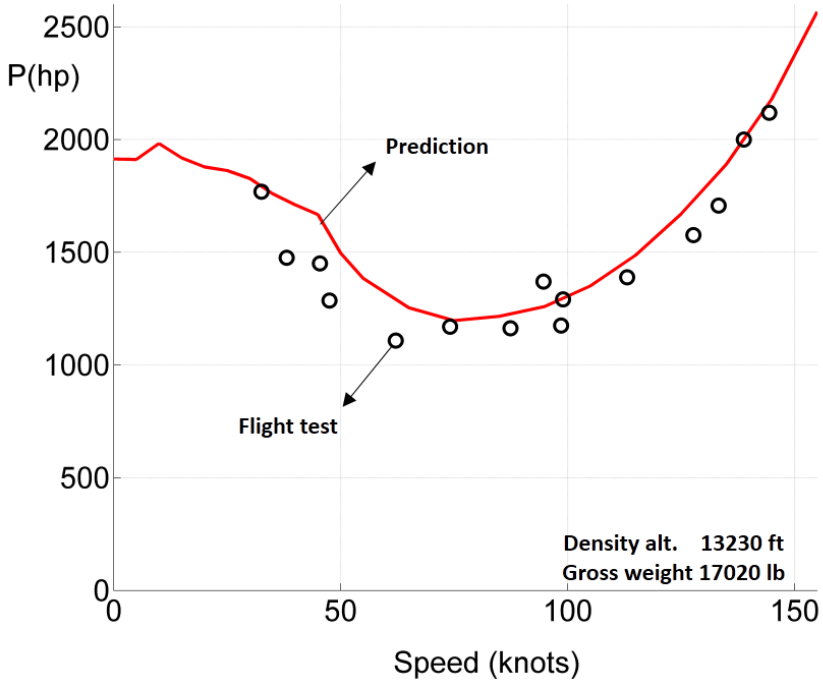

Figure 4.14: Main Rotor Power vs. Speed in Steady Forward Flight

Figure 4.15 shows the comparison of predicted main rotor power with test data from hover to 150 knots at a density altitude of 16770 ft. The comparisons show excellent agreement at speeds above 70 knots. The flight test data exhibits two steps at 35 and 45 knots, together with an *increase* in power with airspeed from 35 to 45 knots. The linear region in the flight test is present between 60-110 knots. The predicted power exhibits smooth trends throughout. At this altitude, the density is 60% of that at sea-level and so the rotor tip vortex strengths (and induced velocities) increase significantly (30% more at hover compared to sea level). The wake is convected away from the rotor quickly at this high thrust condition

($\frac{C_T}{\sigma} = 0.123$), and results in faster convergence without oscillations. The differences between predictions and flight test data is largest at 45 knots (20%) between the two step changes in the flight data.

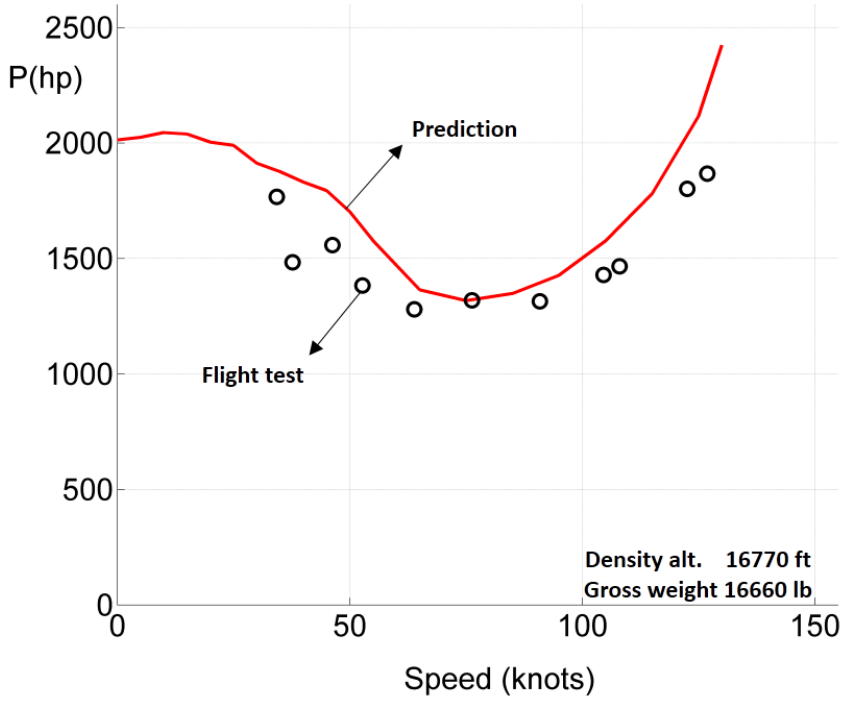

Figure 4.15: Main Rotor Power vs. Speed in Steady Forward Flight

Sources of Error

The term "error" is used here as a measure of discrepancy between flight tests and predictions, which are susceptible to inaccuracies in measurement and mathematical modeling, respectively. The step changes in measured power at 40 knots are indicative of data scatter due to environmental disturbances, or the difficulty associated with obtaining trimmed flight at low speeds, especially the transition region between hover and forward flight ($\mu \leq 0.15$).

Several modeling assumptions have been made to recast the governing equa-

tions into forms that yield engineering solutions in reasonable times. The blade dynamics are assumed to be represented using beam models, except at the swept tip, which is treated as a rigid attachment. Airframe-wake interactions are neglected and a single trailer is used to model the rolled-up wake emanating from a rotor blade with a swept tip. Further, unsteady aerodynamics of rotor blades and the effects of blade-vortex intersections (i.e. viscous interactions between the blade boundary layer and tip vortex core) are neglected.

4.4 Validation of Helicopter Frequency Response to Pilot Inputs

After obtaining trim configurations for the helicopter at hover, 80 knots and 120 knots (steady forward flight), the linearized rotor-airframe dynamics around equilibrium are extracted numerically using finite-difference perturbations and used to construct transfer functions. In this section, these transfer functions from pilot stick inputs to vehicle response outputs are compared to test data (also provided as transfer functions) to validate the helicopter flight dynamic model. The free-vortex wake equations, in their present form, are currently incompatible with a state-space representation of the coupled rotor-airframe dynamics. Therefore, dynamic inflow models are used to compute vehicle frequency responses for validation, observed in Ref. [39] to be sufficient for predicting the on-axis vehicle response.

Figure 4.16 shows the helicopter heave acceleration response to collective stick inputs at hover, while Figs. 4.18, 4.17 and 4.19 show the vehicle pitch, roll and yaw rate responses to lateral stick, longitudinal stick and foot pedal inputs respectively.

These four transfer functions are the "on-axis" vehicle responses, since they represent the primary helicopters motions for each of the corresponding pilot controls.

The on-axis transfer functions at 80 knots are shown in Figs. 4.20, 4.22, 4.21 and 4.23. The on-axis transfer functions at 120 knots are shown in Figs. 4.24, 4.26, 4.25 and 4.27. In forward flight, the heave acceleration along the helicopter $\boldsymbol{k}_{\text{B}}$ axis is given by $\dot{w} + pv - qu$, where v and u are evaluated at the trim condition. The reductions in helicopter roll rate response magnitude between 10-20 rad/s corresponds to the coupling of body motions and rotor blade lag. The nonlinearities in the damper force characteristics and the linearization technique (azimuthal averaging for fixed-frame rotor dynamics) result in prediction errors in the magnitude at higher frequencies. Overall, agreement is very good in the regions marked "accurate flight tests' for all on-axis vehicle responses.

This range of "accurate flight tests" indicates regions where the input-output coherence is above a cutoff value of 0.6, to ensure that dynamic nonlinearities and effects of other pilot inputs on the vehicle response parameter of interest are small. At very high frequencies, the human pilot cannot apply consistent stick inputs of sufficient amplitude reliably. At very low frequencies, inputs amplitudes that are sufficient to excite a measurable response also cause the helicopter to drift away from equilibrium, and the linearized dynamic model is no longer valid. Therefore, intermediate frequencies between 0.5 rad/s to 15 rad/s is a good range for using frequency-domain data to validate the dynamic model.

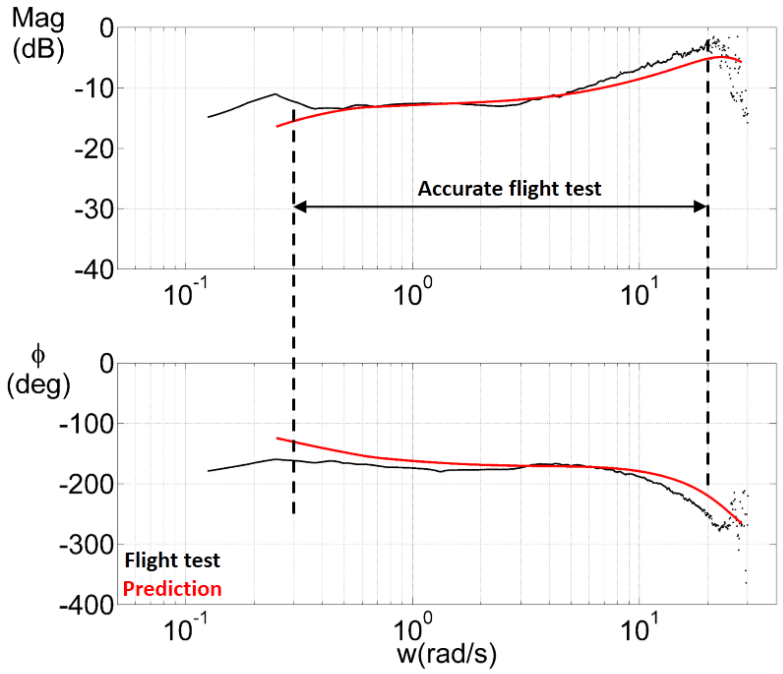

Figure 4.16: Heave Acceleration Response to Collective Stick Inputs at Hover

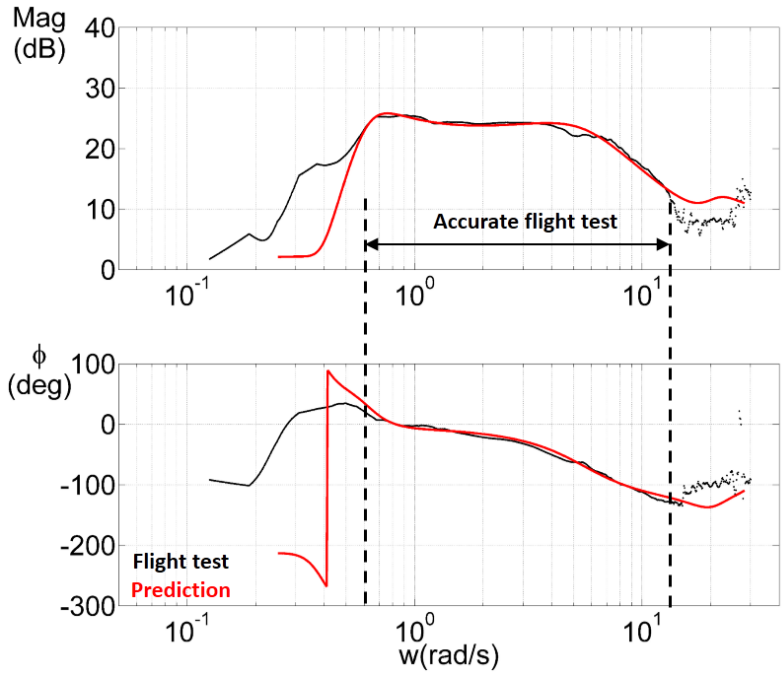

Figure 4.17: Roll Rate Response to Lateral Stick Inputs at Hover

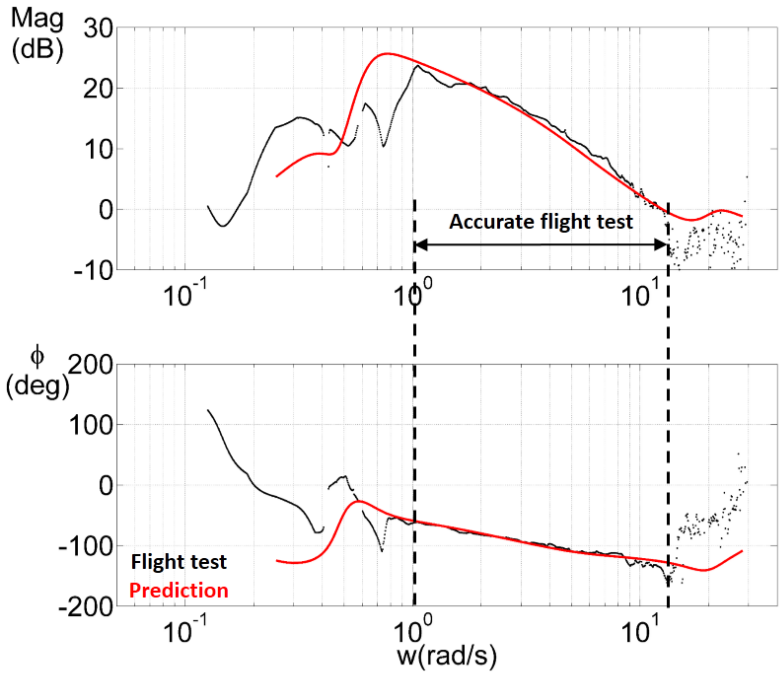

Figure 4.18: Pitch Rate Response to Lateral Stick Inputs at Hover

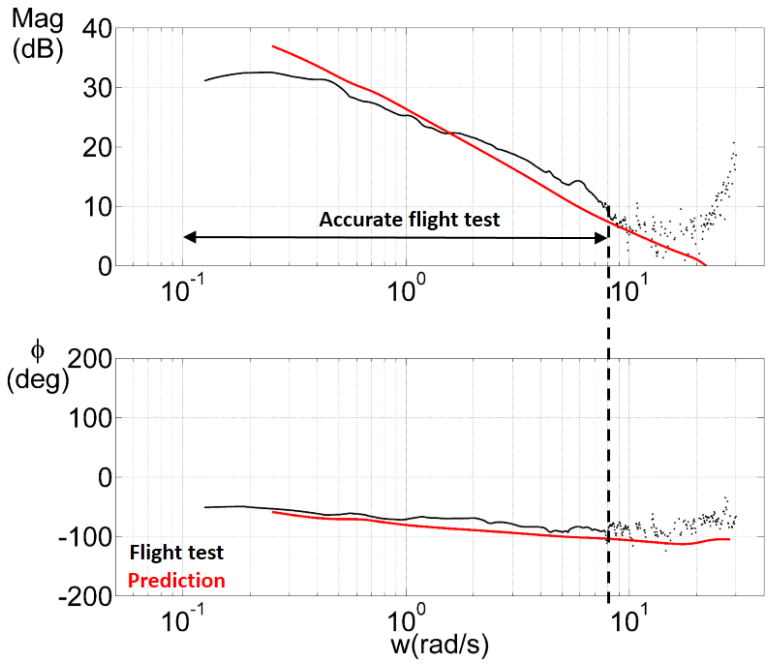

Figure 4.19: Yaw Rate Response to Lateral Stick Inputs at Hover

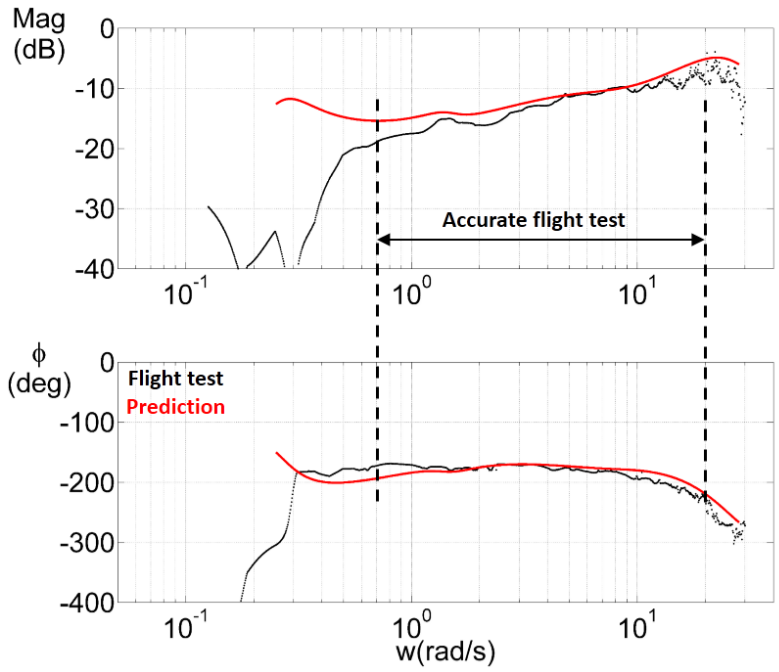

Figure 4.20: Heave Acceleration Response to Collective Stick Inputs at 80 knots

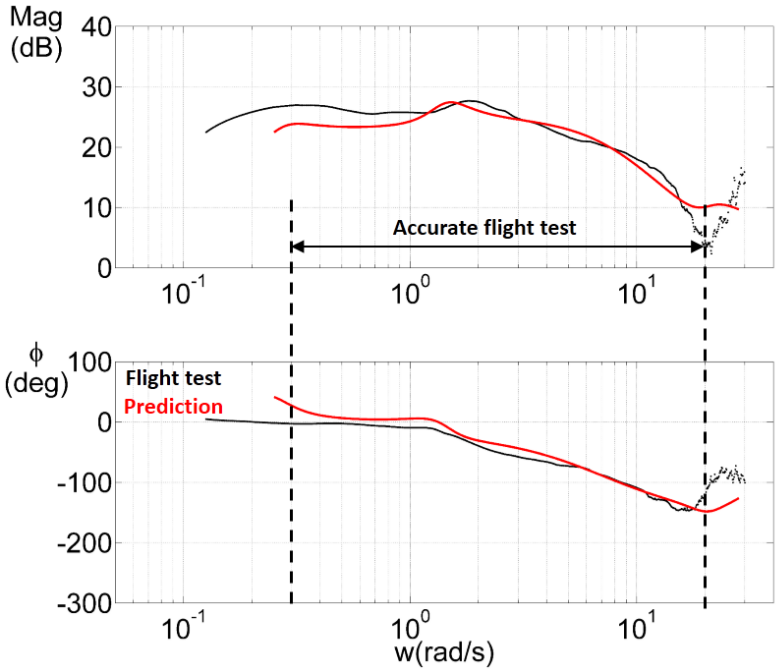

Figure 4.21: Roll Rate Response to Lateral Stick Inputs at 80 knots

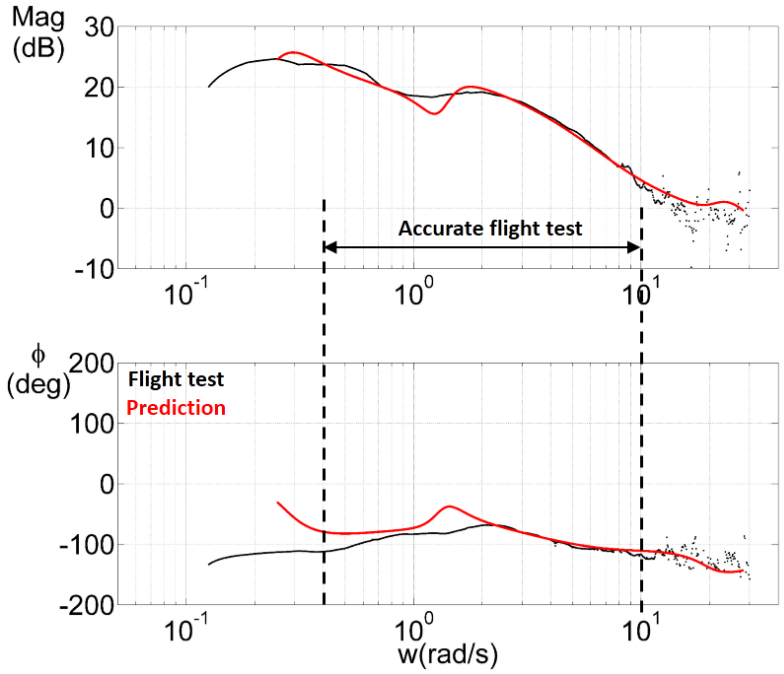

Figure 4.22: Pitch Rate Response to Lateral Stick Inputs at 80 knots

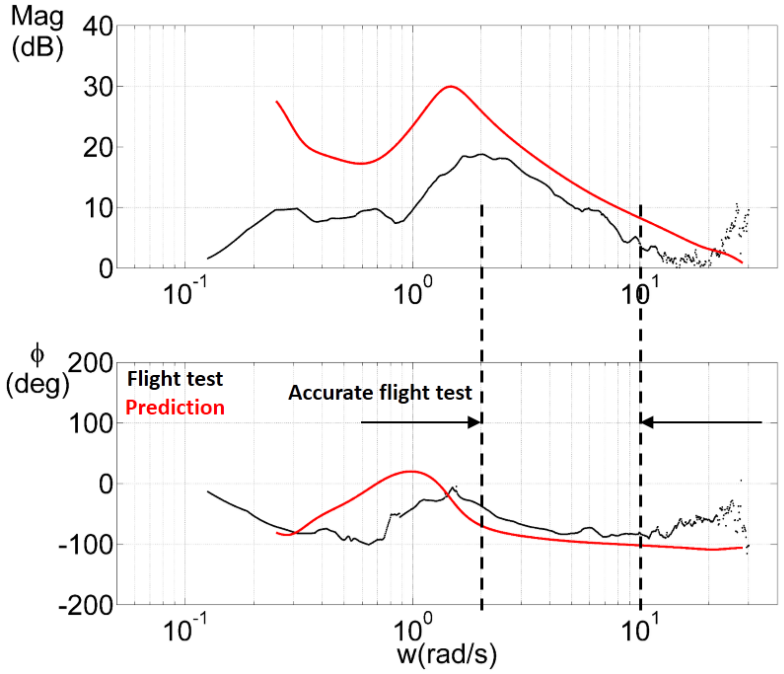

Figure 4.23: Yaw Rate Response to Lateral Stick Inputs at 80 knots

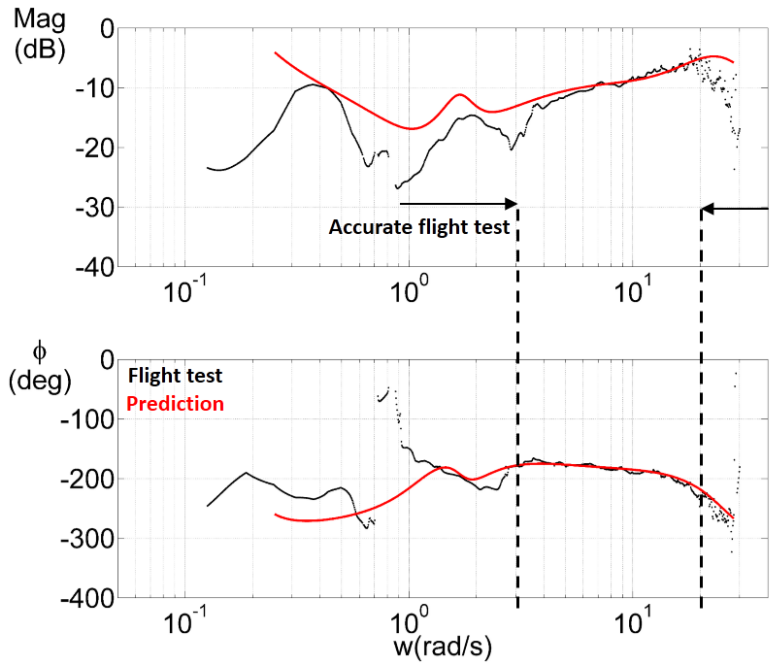

Figure 4.24: Heave Acceleration Response to Collective Stick Inputs at 120 knots

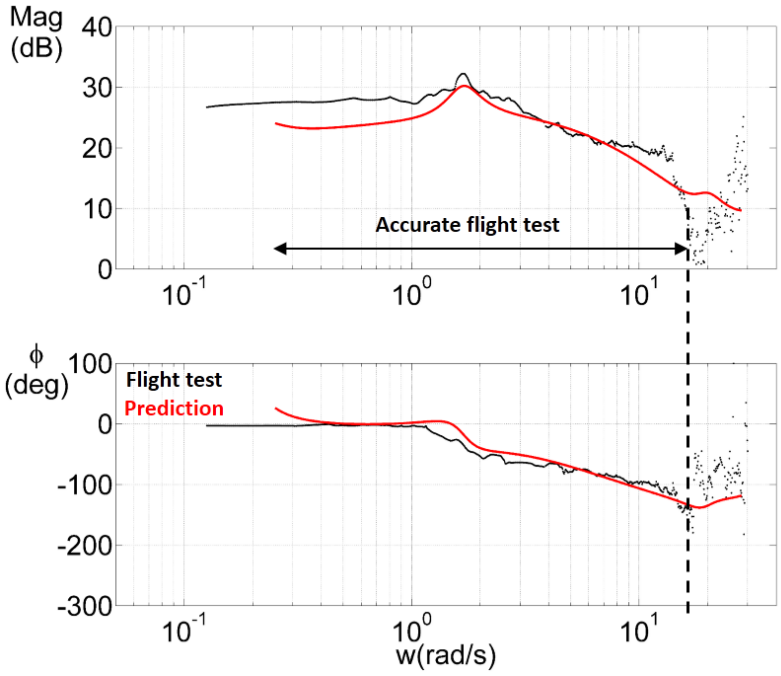

Figure 4.25: Roll Rate Response to Lateral Stick Inputs at 120 knots

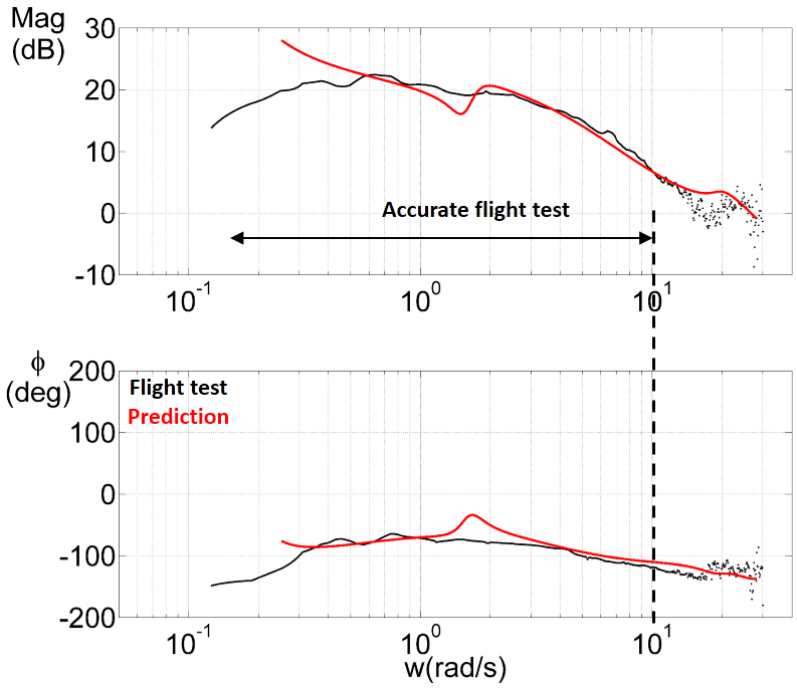

Figure 4.26: Pitch Rate Response to Lateral Stick Inputs at 120 knots

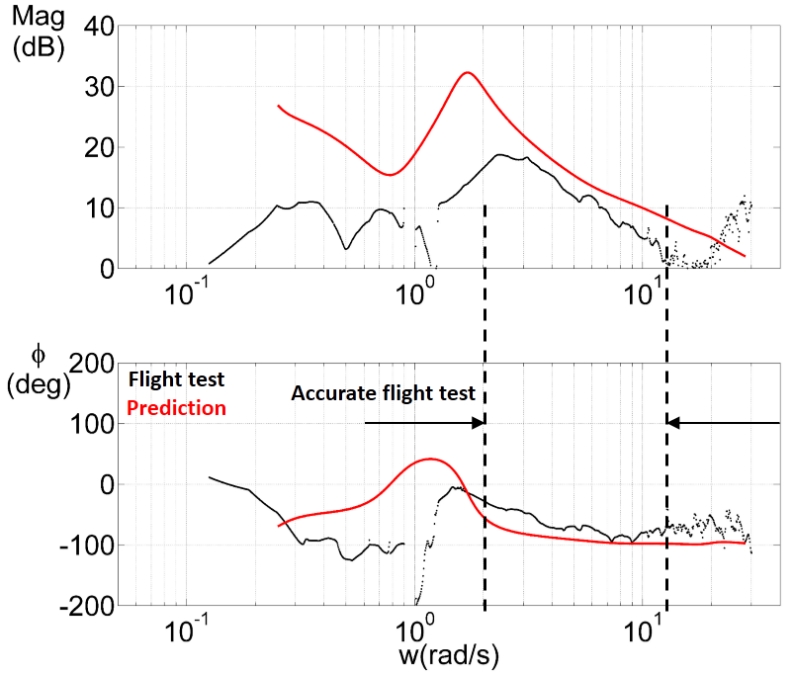

Figure 4.27: Yaw Rate Response to Lateral Stick Inputs at 120 knots

5 Trim Characteristics

This chapter discusses the trim configurations of the coupled helicopter-cable-towed body system in steady level flight. The first section covers results for steady forward flight, and the second section covers steady turning flight. The implications of towing a submerged load on helicopter steady-state performance are explored through parametric studies. These sweeps are performed by perturbing relevant physical quantities one-at-a-time, centered on a baseline helicopter, towed body and cable configuration. Initial predictions with dynamic inflow models are used to illustrate the effects of various cable and towed body parameters on the forces transmitted to the helicopter and trim depths of the submerged load. These dynamic inflow models are also used to gain qualitative insight into the helicopter trim configurations and rotor power requirements, which are subsequently refined using a free-vortex wake model of the rotor flowfield.

Baseline Configuration

The baseline helicopter is similar to the UH-60 Blackhawk, with relevant physical parameters given in Chapter 4. The baseline helicopter weight is 18000 lb, discounting the air weight of the towed body and cable. The trim density altitude

for the helicopter is set to 150 ft above sea level. The tow point on the airframe is vertically offset below the vehicle CG as given in Table 5.1.

Table 5.1: Helicopter Tow Point Location

Parameter	Value	Units
Fuselage station	361	inches
Buttline station	0	inches
Waterline station	208	inches

The physical parameters for the baseline cable are given in Table 5.2. Based on anecdotal evidence, the cable is assumed to be fitted with a hydrofoil fairing that reduces its diameter-based drag coefficient to 0.1, instead of the bare-cable value of 1.73 as given in Ref. [71]. The elastic axis is assumed to coincide with the center of gravity of the cable cross-section. Five finite elements, each with eight quadrature points are sufficient to represent the flexure of the cable.

Table 5.2: Baseline Cable Parameters

Parameter	Value	Units
Lengths	350, 500, 700	ft
Mass/length	0.64	kg/m
Diameter	0.025	m
Bending stiffness	4×10^4	Nm^2

Table 5.3: Baseline Towed Body

Parameter	Value	Units
Weight in air	4454 (1000)	N (lb)
Hull diameter	0.25	m
Hull length	2.0	m
Roll inertia I_{xx}	3.5	kg-m^2
Pitch inertia I_{yy}	150	kg-m^2
Yaw inertia I_{zz}	150	kg-m^2
Coupling inertias I_{yz}, I_{xz}, I_{xy}	0	kg-m^2
Drag coefficient (frontal area)	1.0	
Lift coefficient (frontal area)	0.0	
# main fins	2	
Longitudinal offset from CG	0	m
Vertical offset from CG	0	m
Main fin span	0.4	m
Main fin chord	0.2	m
# tail fins	3	
Placement of tail fins	inverted-Y	
Longitudinal offset of tail fins from nose	1.9	m
Tail fin span	0.2	m
Tail fin chord	0.1	m

The 3-view of the baseline towed body is shown in Fig. 5.1, and the relevant physical parameters are given in Table 5.3. The center of gravity and center of buoyancy of the baseline towed body are each assumed to coincide with the geometric center, i.e. on the axis of cylindrical hull at 1 m from the nose. The cable attachment point lies 0.125 m above the geometric center, on the surface of the hull.

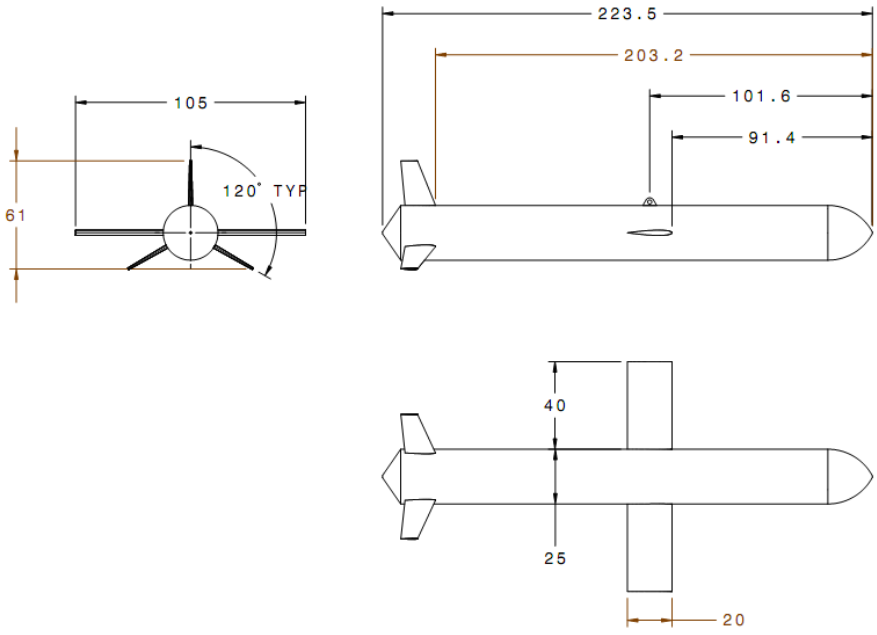

Figure 5.1: Baseline Towed Body. All dimensions are in cm

5.1 Trim in Steady Forward Flight

The effects of the towed body on helicopter performance in steady forward flight are inferred from trim solutions, and the performance during tow is compared to that of an isolated helicopter with the same gross take-off weight. A tow cable of length 700 ft and weight 300 lb is considered, with different deployed lengths. A deployed length of 350 ft corresponds to a 150 lb cable of length 350 ft used

to tow the baseline submerged load, and the rest of the cable weight (150 lb) is carried inside the airframe. Thus, the additional weight of the undeployed length of the 700-ft cable is accounted for in the following results. The trim attitudes of the towed body are examined first, since they are independent of both cable and helicopter parameters.

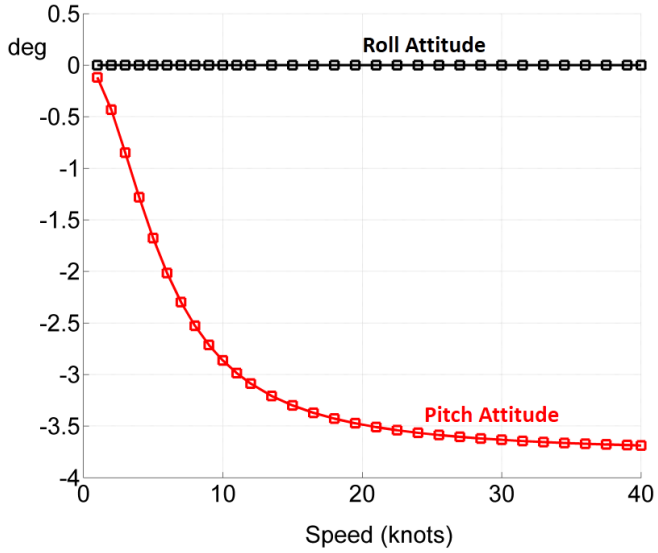

Figure 5.2: Towed Body Trim Attitudes in Steady Forward Flight

Figure 5.2 shows the trim pitch and roll attitudes of the fully submerged baseline towed body in steady forward flight. The roll attitude is zero due to symmetric loading on the fins, and the pitch attitude is increasingly nose-down (hence negative, by sign convention) with increases in tow speed. The reason for this trim pitch attitude variation with tow speed lies in longitudinal moment balance for the submerged load. To counter increasing hydrodynamic drag at higher tow speed, the forward component of cable force must increase. Since the cable attachment point is vertically offset above the load CG, the cable force component parallel to the water surface produces a nose-down pitching moment. This nose-down pitching moment

from cable forces can be countered *only* by nose-up pitching moments (down-force) from the tail fins, achieved by trimming the towed body to a nose-down pitch attitude. When the main fins (mounted near the load CG) are fixed at their zero pitch setting, they experience down-forces proportional to the trim pitch attitude of the submerged load. Therefore, increases in tow speed result in increased cable loads transmitted to the helicopter due to two dominant phenomena

- **Increase in cable force component parallel to the tow direction (drag)**
- **Increase in cable force component normal to the tow direction (down-forces) from the main fin, arising from longitudinal moment balance**

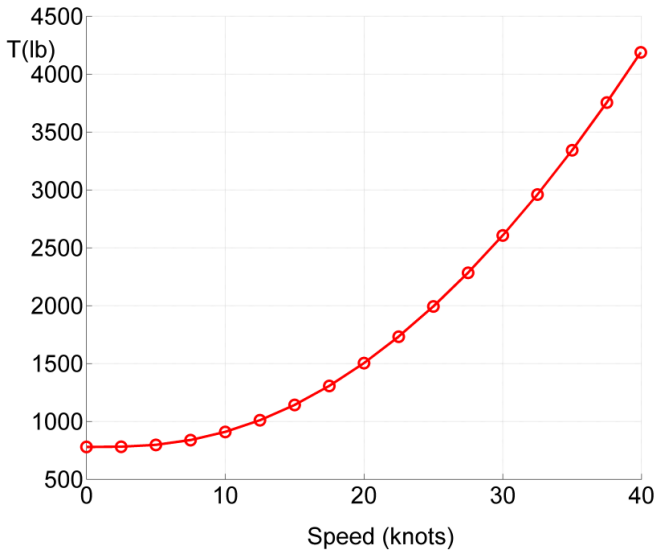

Figure 5.3: Cable Force in Steady Forward Flight

These effects cause an increase in the resultant cable force with tow speed, as shown in Fig. 5.3 for a 350-ft cable. In this case, the effects of cable drag and buoyancy have been neglected. Since the helicopter ultimately provides the aerodynamic loads necessary to maintain trim, thrust requirements on the rotor increase, leading to

increased engine power consumption during tow procedures as shown in Fig. 5.4.

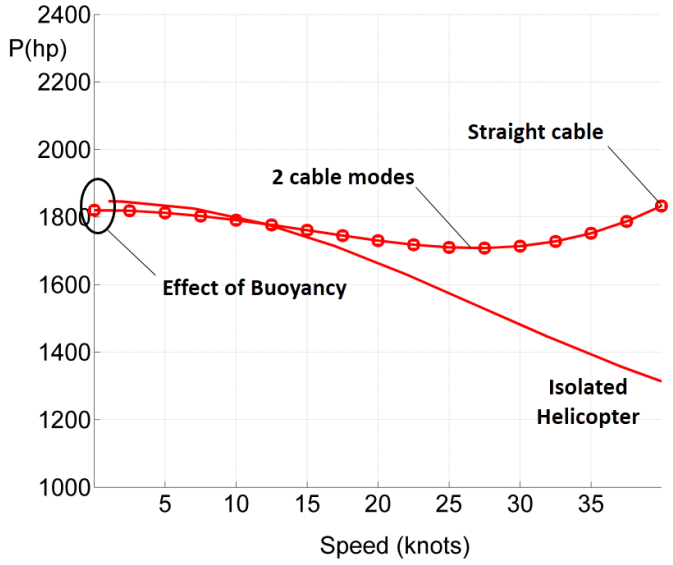

Figure 5.4: Main Rotor Power Required in Steady Forward Flight, No Cable Drag

Also shown in Fig. 5.4 are the power requirements for the isolated helicopter. The effects of buoyancy are apparent between 0-5 knots, where an isolated helicopter with the same GTOW requires more power to hover than a tow system with the submerged load and part of the cable immersed in water. **The towed body hydrodynamic forces manifest as increases in weight and equivalent flat-plate area on the helicopter.** Thus, the main rotor thrust vector must increase in magnitude and tilt into the tow direction to counter hydrodynamic drag and downforce. To simultaneously maintain longitudinal moment balance for the airframe, the helicopter CG must lie close to lines of action of rotor thrust and cable force at the tow point. Therefore, the trim pitch attitudes of the helicopter are increasingly nose-down (negative, by sign convention) with increasing tow speed compared to an isolated helicopter, as shown in Fig. 5.5. The trim roll attitudes are insensitive to towed body drag up to 25 knots, and show slight differences at 40 knots due to

additional rolling moments induced by increasing tail rotor thrust (coupled with the vertical offset of the tail rotor above the helicopter CG).

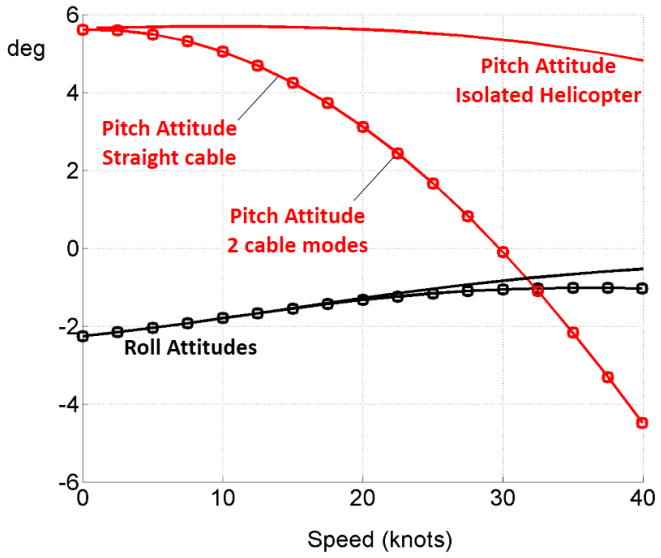

Figure 5.5: Helicopter Attitudes in Steady Forward Flight, No Cable Drag

Figs. 5.4 and 5.5 also serve as verification tests of the present implementation. Since the first two modes of a hinged beam correspond to rigid-body rotations, reduction of cable dynamics to two normal modes is equivalent to using a straight cable. Various cable and load parameters influence the total force transmitted to the airframe. The dominant parameters are discussed in the following sections.

5.1.1 Effect of Cable Hydrodynamics

The previous section discussed the effect of towed body hydrodynamics on the trim characteristics of the tow system. In this section, cable drag and buoyancy are introduced to identify their effect on trim with straight cables.

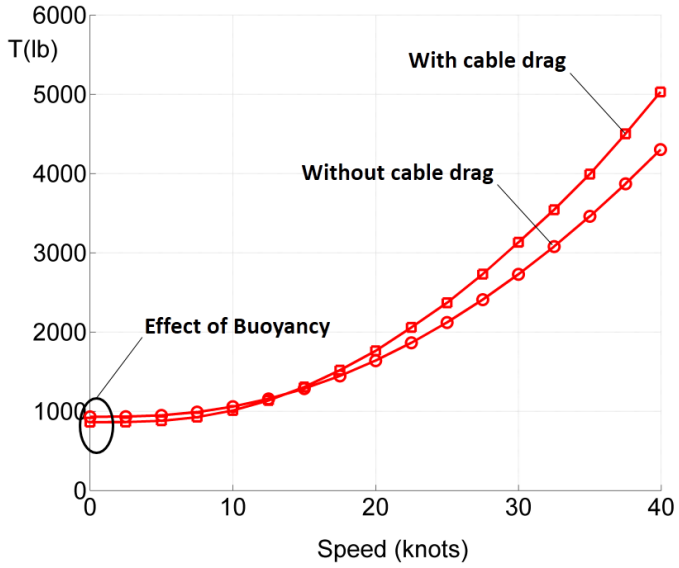

Figure 5.6: Helicopter Tow Tension, Steady Forward Flight, 350-ft Straight Cable

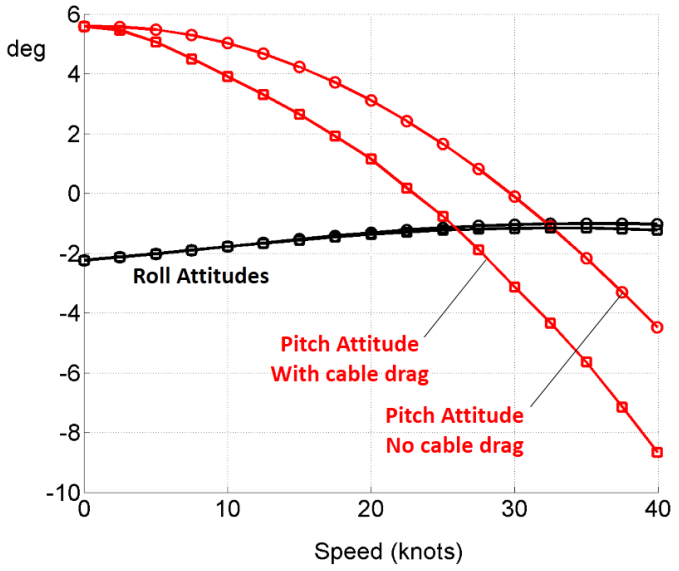

Figure 5.7: Helicopter Attitudes in Steady Forward Flight, 350-ft Straight Cable

Figure 5.6 shows the variation of the total force transmitted to the helicopter for the baseline submerged load towed by a 350-ft cable. When cable buoyancy is ignored, the force is slightly over-predicted at hover. When cable drag is ignored, force is under-predicted in forward flight by 16%. Ignoring cable drag also propagates

the error to helicopter trim attitudes, as shown in Fig. 5.7. When hydrodynamic loads are ignored for a 700 ft cable, the cable force is under-predicted by 65%, rotor power is under-predicted by 20% and the trim pitch attitude is under-predicted by 12° at 40 knots. Under-prediction of trim attitudes is significant for choosing configurations that offer higher levels of pilot comfort, since operating at trim pitch attitudes in excess of -6° may lead to fatigue (Ref. [66]).

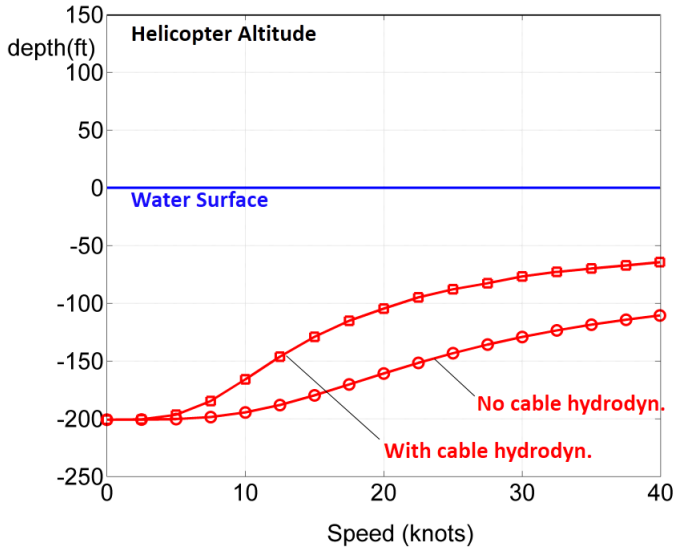

Figure 5.8: Towed Body Depth in Steady Forward Flight, 350-ft Straight Cable

The variation of submerged load depth (measured as distance from water surface) with tow speed is shown in Fig. 5.8 for a 350-ft cable. With increasing speed, hydrodynamic drag and down-force increase, the interplay between which determines towed body depth. Ignoring cable drag erroneously increases the relative magnitude of vertical forces, resulting in over-prediction of depth by 68% for a 350-ft cable and 81% for a 700-ft cable at 40 knots.

5.1.2 Effect of Cable Curvature

Cable curvature introduces variations along the cable span, of the angle of the flow inclination to the cable axis and modifies the force distributions normal to the local cable axis. For a 350-ft cable, the changes in helicopter trim attitudes, total cable force transmitted to the helicopter, trim controls and rotor power required is less than 1% from hover to 40 knots. The error in prediction of towed body trim depth is at most 5% (4 ft). When the cable length increases to 700 ft, ignoring cable curvature results in 3% under-prediction of cable force and 1.6% under-prediction of rotor power at 40 knots. Helicopter trim attitudes are unaffected by cable curvature for the cases investigated. The primary effect of curvature is on towed body depth, shown in Fig. 5.9.

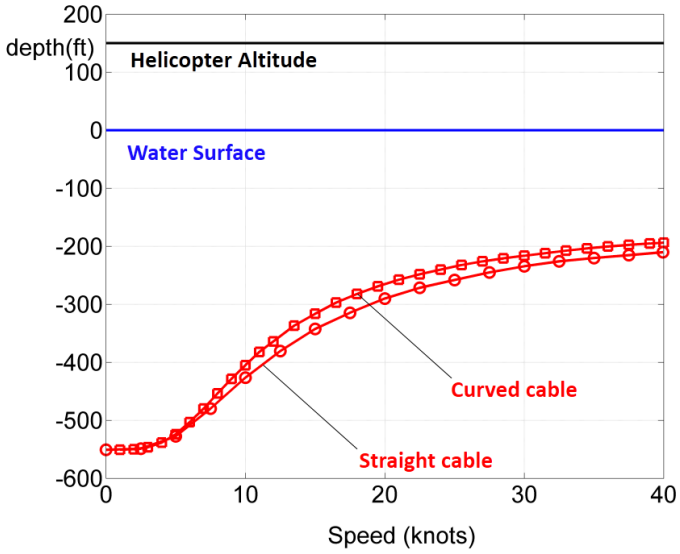

Figure 5.9: Towed Body Depth with 700-ft Cable

Neglecting cable curvature for the 700-ft cable results in at most 9.3% over-prediction of towed body depth. As the cable lengths increase, effects of curvature

become increasingly significant. Perturbing the bending stiffness of the cable by one order of magnitude in each direction about the baseline value produced insignificant changes in the trim state of the vehicle for all cable lengths considered. This insensitivity to cable flexural stiffness indicates that the axial force always dominates the stiffening term in the cable bending equations, due to the large spans involved.

5.1.3 Cable Attachment Point on the Towed Body

The location of the cable attachment point on the towed body plays a dominant role in determining the towed body trim depth, cable force, rotor power required and helicopter trim pitch attitudes. The baseline value of the hook offset is 2 inches above the CG. The effects of increasing this vertical offset by 2 and 4 inches on the trim pitch attitudes of the towed body are shown in Fig. 5.10 for the baseline towed body.

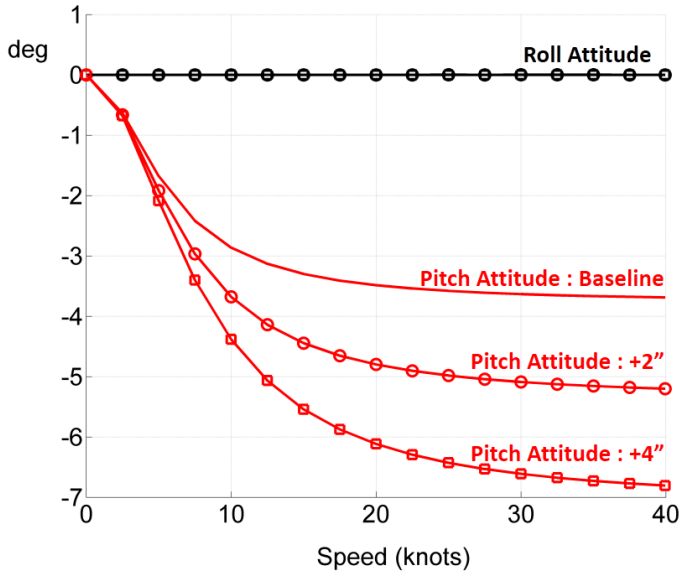

Figure 5.10: Towed Body Trim Attitudes, Various Cable Attachment Offsets

As the moment arm for the horizontal component of the cable force increases,

the nose-up moments from the tail fins must increase to maintain equilibrium, necessitating additional nose-down pitch attitudes. The main fins experience additional down-force, increasing the depth of the towed body as shown in Fig. 5.11.

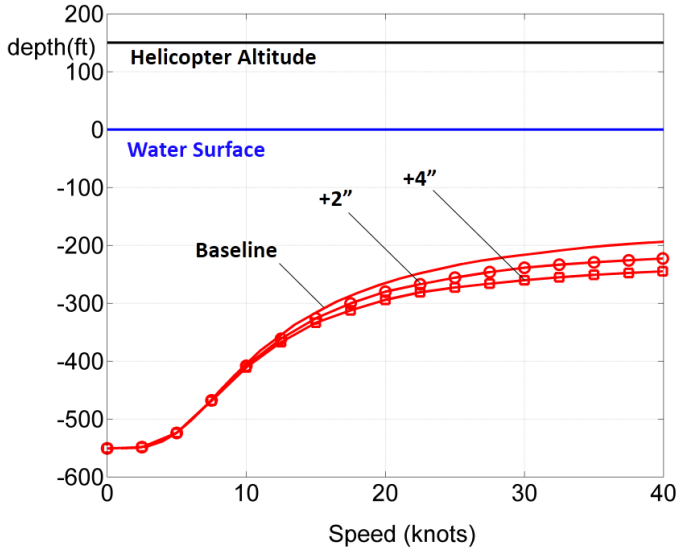

Figure 5.11: Towed Body Depth, Various Cable Attachment Offsets, 700-ft Cable

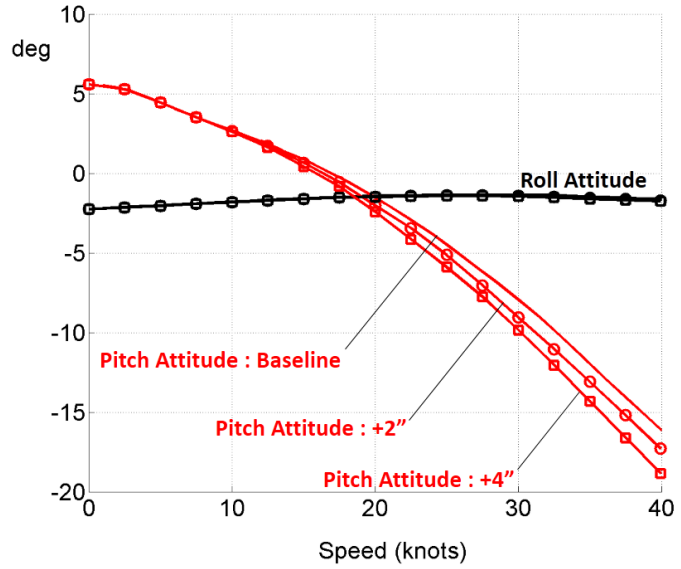

Figure 5.12: Helicopter Attitudes, Various Cable Attachment Offsets, 700-ft Cable

At 40 knots, 4 inches of additional vertical offset of the cable attachment point results in a 25% increase in towed body depth. Down-forces on the main fin also

orient larger sections of the cable normal to the tow direction, increasing hydrodynamic drag. The helicopter assumes an increasingly nose-down pitch attitude to overcome the additional cable drag, while roll attitudes are unaffected as shown in Fig. 5.12. The increase in down-force and cable drag together impose higher thrust requirements on the helicopter rotor to maintain trim, resulting in higher power consumption (6% for an additional 2 inches and 15% for an additional 4 inches at 40 knots) as shown in Fig. 5.13.

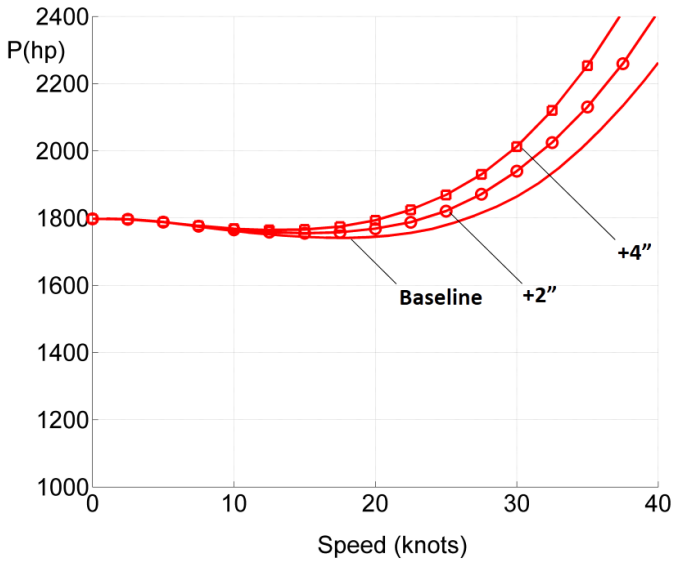

Figure 5.13: Main Rotor Power Required, Various Cable Attachment Offsets on the Towed Body, 700-ft Cable

5.1.4 Cable Attachment Point on the Helicopter

The longitudinal position of the cable attachment point on the helicopter is a key parameter that determines the fuselage trim attitudes, shown in Fig. 5.14. Rearward displacement of this point allows for closer spacing between the lines of action of the cable force and rotor thrust, resulting in smaller fuselage trim pitch

attitudes. Roll attitudes and hub rolling moments are unaffected by longitudinal rearward translation of the tow point on the helicopter, shown in Figs. 5.14 and 5.15.

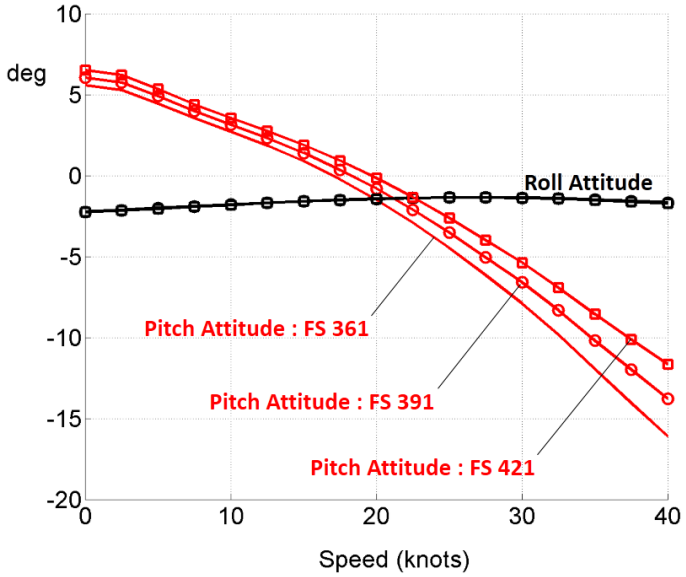

Figure 5.14: Helicopter Trim Attitudes : Effect of Tow Point Location

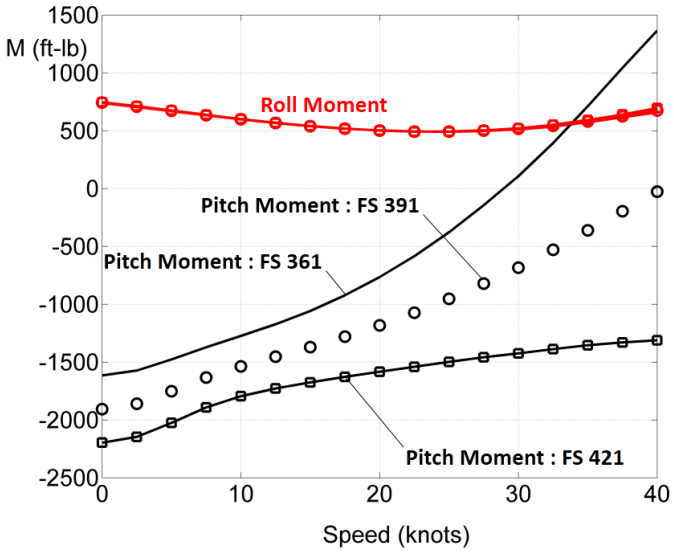

Figure 5.15: Helicopter Hub Moments : Effect of Tow Point Location

The reduction in fuselage pitch attitude is accompanied by incrementally higher rotor longitudinal flapping (0.5°) and additional nose-down hub pitching

moments, shown in Fig. 5.15 to preserve longitudinal moment equilibrium. This parameter does not affect rotor thrust and power, and can be engineered to improve pilot comfort levels by reducing pitch attitudes in forward flight.

5.1.5 Effect of Cable Length

A side view (plane containing longitudinal and vertical dimensions) of the cable shapes in trim at various speeds is shown in Figs. 5.16, 5.17 and 5.18 for the 350, 500 and 700-ft cables, respectively. Each of the black curves represents the shape of the cable at a particular tow speed when the system is moving from left to right, and the red dots represent the tip of the cable (i.e. location of towed body). The numbers next to the red dots represent the trim tow speed in knots corresponding to a particular line/dot combination. Curvature above the water surface is negligible for all three cases.

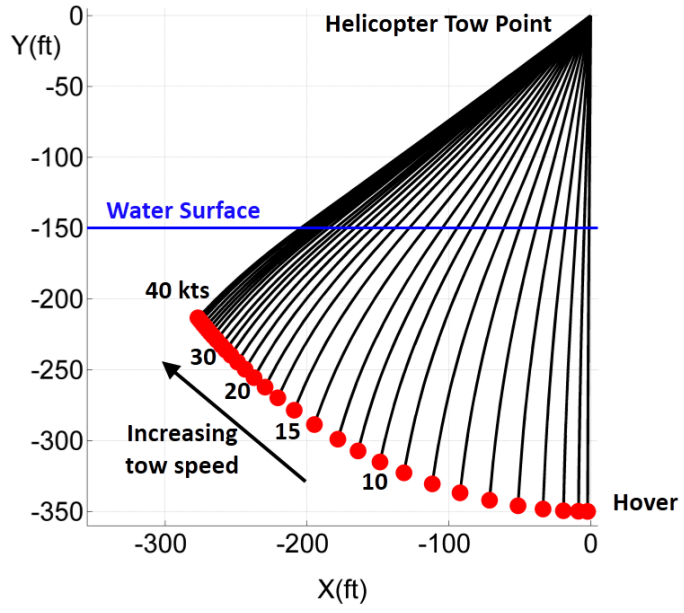

Figure 5.16: Shape of 350-ft Cable in Steady Forward Flight, Various Speeds

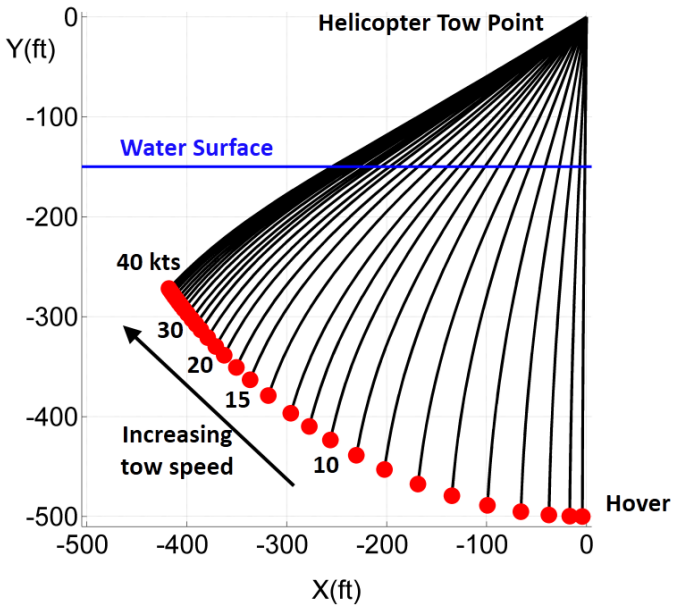

Figure 5.17: Shape of 500-ft Cable in Steady Forward Flight, Various Speeds

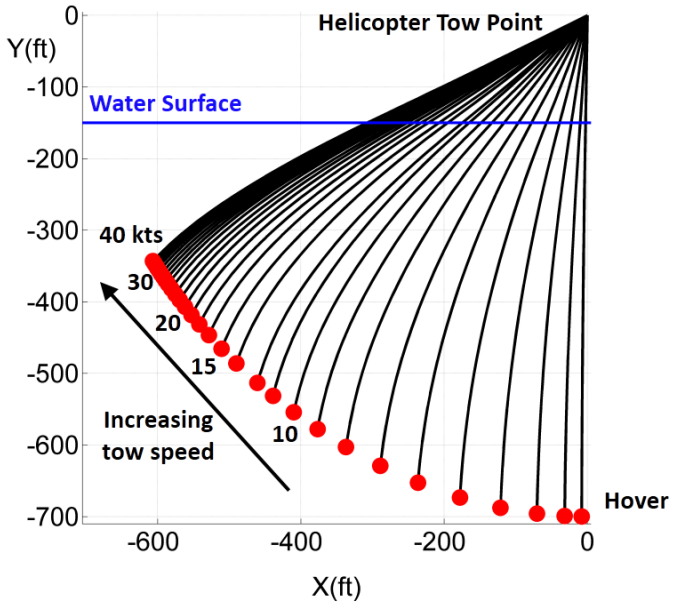

Figure 5.18: Shape of 700-ft Cable in Steady Forward Flight, Various Speeds

Consider first the 350-ft cable (Fig. 5.16). As the tow speed increases, the trim depth of the submerged load below the water surface changes from 200 ft at hover to 150 ft at 12 knots, to 100 ft at 22 knots. Above 20 knots, the trim depth is less

sensitive to tow speed, asymptoting to 70 ft at 40 knots, indicating that the total hydrodynamic forces in the horizontal (drag) and vertical (down-force) directions are well-balanced. When the deployed length increases to 500 ft (Fig. 5.17), the total depth below the water surface increases. However, increased hydrodynamic drag on the cable results in higher initial sensitivity of the trim depth to tow speed from 0 to 20 knots. As the deployed length increases to 700 ft (Fig. 5.18), the effects of curvature become more apparent in the shape of the cable, and the range of trim depths varies from 550 ft at hover to 200 ft at 40 knots.

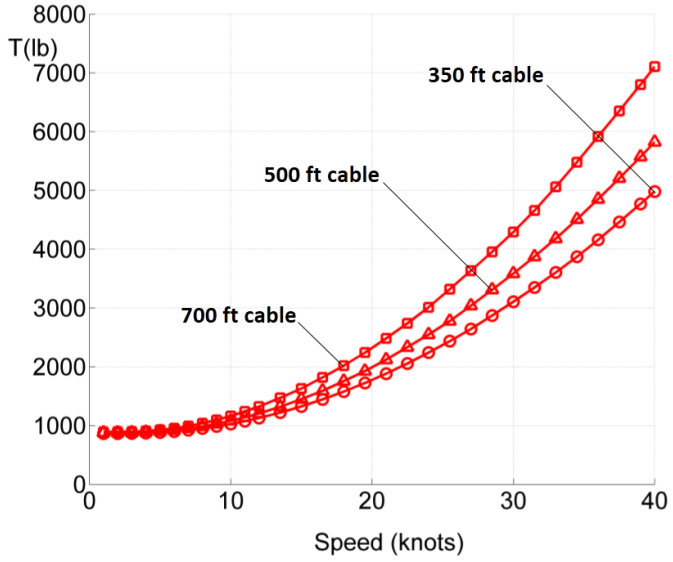

Figure 5.19: Cable Force in Steady Forward Flight, Various Cable Lengths

Longer cables (700 ft) experience additional hydrodynamic drag that result in increased depth variations with tow speed, and transmit up to 42% more cable force to the helicopter than shorter cables (350 ft) with identical properties. Figure 5.19 shows the variation of total cable force with tow speed for the three different deployed lengths. At very low speeds, the cable force is near-identical among the three cases except for imperceptible variations due to

buoyancy. As the tow speed increases, hydrodynamic drag on the cable (even with fairings) is comparable to that on the towed body, and forms a significant fraction of the total force transmitted to the helicopter. The helicopter must assume an increasingly nose-down pitch attitude to overcome both towed body and cable drag while simultaneously maintaining longitudinal moment equilibrium, as shown in Fig. 5.20. Increasing the cable length from 350 to 700 ft results in a 100% increase in the helicopter pitch attitude from -8° to -16° at 40 knots.

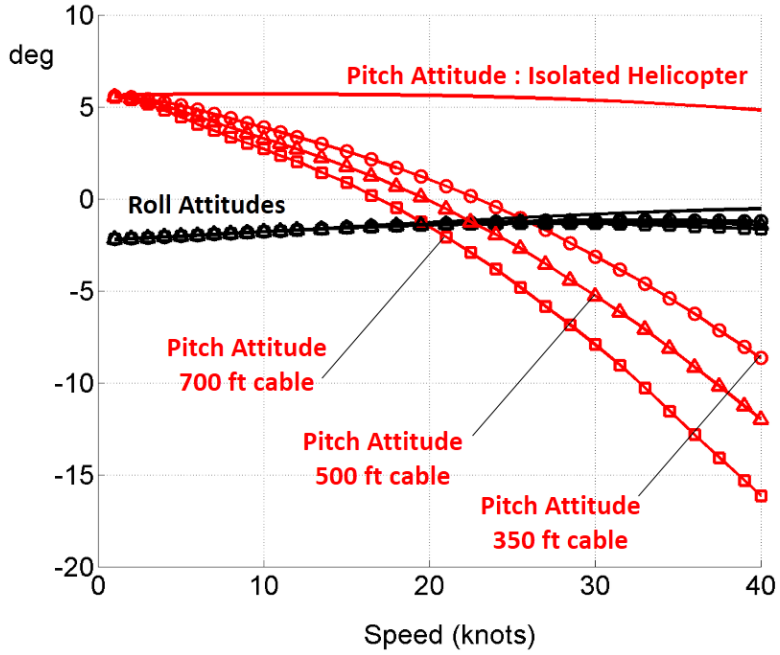

Figure 5.20: Helicopter Trim Attitudes in Steady Forward Flight, Dynamic Inflow

The increases in hydrodynamic drag and down-force with tow speed are so large that the minimum power speed is reduced from 65 knots to 20 knots for the 700-ft cable. With increasing rotor thrust, the rotor power required to maintain trim increases with flight speed, as shown in Fig. 5.21. Minor differences in the hover power (between various deployed cable lengths) arise from cumulative buoyancy loads acting on the submerged sections of the tow cable. Since longer cables undergo

additional weight alleviation due to buoyancy at low speed but larger hydrodynamic drag at high speeds, the power curves intersect each other at 16 knots. Above 20 knots, the effects of hydrodynamic drag on the cables dominates the total cable force acting on the helicopter, resulting in 75% higher power compared to an isolated helicopter with the same GTOW for the 700-ft cable, and 46% for the 350-ft cable. At 40 knots, the 350-ft cable case has exceeded the rated Maximum Continuous Power (MCP = 1900 Hp) of the aircraft, not including tail rotor power.

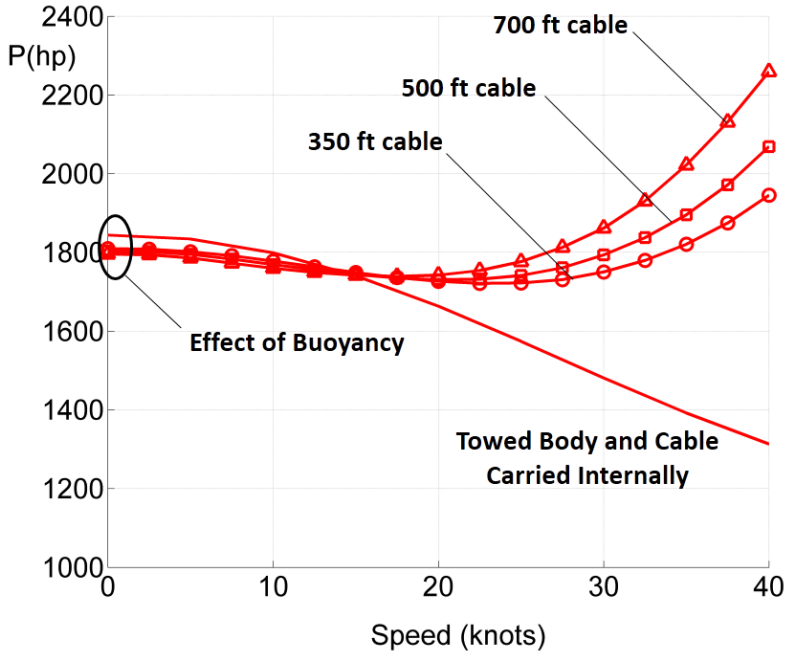

Figure 5.21: Main Rotor Power Required in Steady Forward Flight, Dynamic Inflow

5.1.6 Predictions with Free-Vortex Wake Models

The trim state of the cable and towed body are completely uncoupled from that of the helicopter. Therefore, towed body depth, cable force transmitted to the helicopter and the shape of the cable are independent of the tow platform. For all

three cable lengths considered, the trim attitudes of the helicopter are completely unaffected by choice of induced inflow models, as indicated by Figs. 5.20 and 5.22. The steady and 1/rev flap response of the blade tip is near-identical between predictions made using dynamic inflow and free wake.

The differences in predictions between dynamic inflow and free wake models appear in rotor performance, since vortex models of the rotor wake accurately represent most non-ideal physical effects, such as blade tip losses and non-uniform inflow distributions over the rotor disk. Using a free-vortex wake model of the rotor aerodynamics yields quantitatively different power curves for the helicopter rotor, compared to predictions based on dynamic inflow.

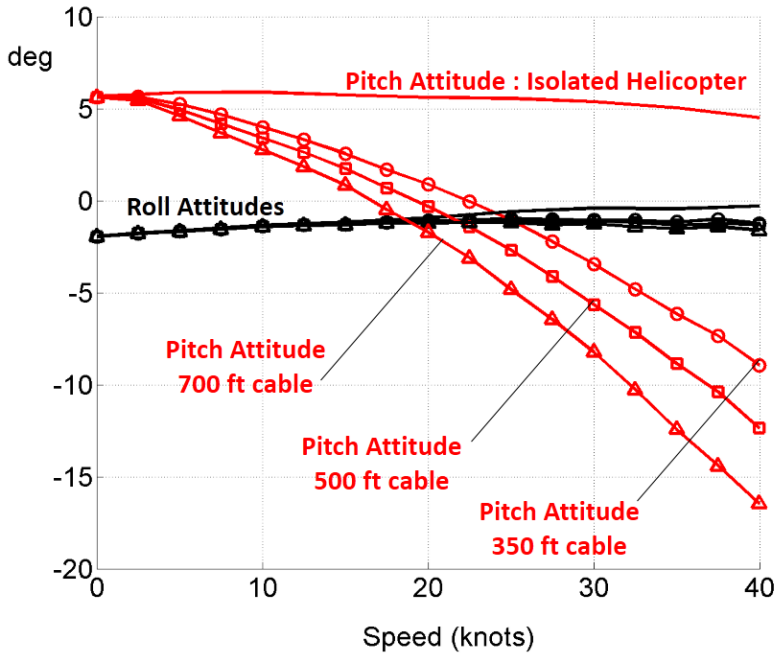

Figure 5.22: Helicopter Trim Attitudes in Steady Forward Flight, Free Wake

Consider the solid lines without markers in Figs. 5.21 and 5.23. Dynamic inflow models under-predict rotor induced power between 0-40 knots, and show steeper reductions in rotor power requirements with airspeed, since they do not

capture rotor-wake interactions below $\mu \leq 0.1$.

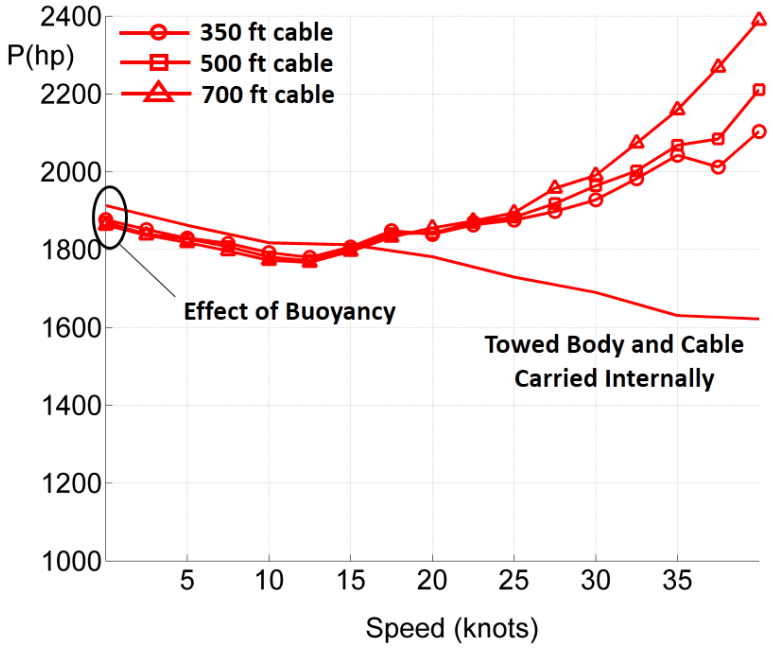

Figure 5.23: Main Rotor Power Required in Steady Forward Flight, Free Wake

When towing the baseline submerged load, the shape of the power curve changes depending on the deployed cable length. Up to 15 knots, the reductions in induced power with airspeed dominate the power requirements. Above 15 knots, hydrodynamic drag on the cable and submerged load increase rapidly, and the power curves for all three tow configurations (of various cable lengths) increase monotonically.

Reductions in the rotor induced power with airspeed are similar between the three tow configurations and an isolated helicopter with the same GTOW. Since part of the weight is supported by buoyancy, rotor power requirements for tow configurations are reduced compared to the isolated helicopter carrying the tow system inside the airframe. As airspeed increases, larger sections of the cable raise out of the water, simultaneously reducing buoyancy and wetted area, but increasing the

dynamic pressure on both the cable and towed body. This interplay between cable buoyancy, hydrodynamic drag and rotor induced power variations with airspeed result in the power curves crossing each other at different speeds corresponding to their deployed lengths. The effective differences in power requirements between the three cables are small, and near-identical up to 25 knots. Above 25 knots, the effects of hydrodynamic drag dominate power requirements, and shorter cables are more power-efficient in steady forward flight.

5.1.7 Depth Regulation using Pitching Fins

In this section, the effects of depth regulation on the trim state of the tow system are examined. To achieve depth regulation independent of the helicopter altitude, the submerged load is fitted with two main fins that are capable of pitch actuation relative to the hull. **When the fins are rotated nose-up or nose-down, the trim configuration of both the cable and load change simultaneously**.

As the main fins exert hydrodynamic down-forces, they also experience significant induced drag due to their small aspect ratio (2). As a result, the horizontal component of the cable force increases to maintain equilibrium, thereby increasing the nose-down pitching moments on the towed body. To maintain longitudinal moment balance, the submerged load trims with an additional nose-down pitch attitude for larger down-forces, i.e. nose-down main fin pitch angle as shown in Fig. 5.24. The towed body pitch attitude is negative even when the fin angle is increased above zero. At 3-4° of fin nose-up actuation, the surfaces produce incremental levels of

hydrodynamic lift. Due to the incremental drag created by the tail fins, the point of minimum towed body pitch attitude is not attained at the negative value of the fin angle.

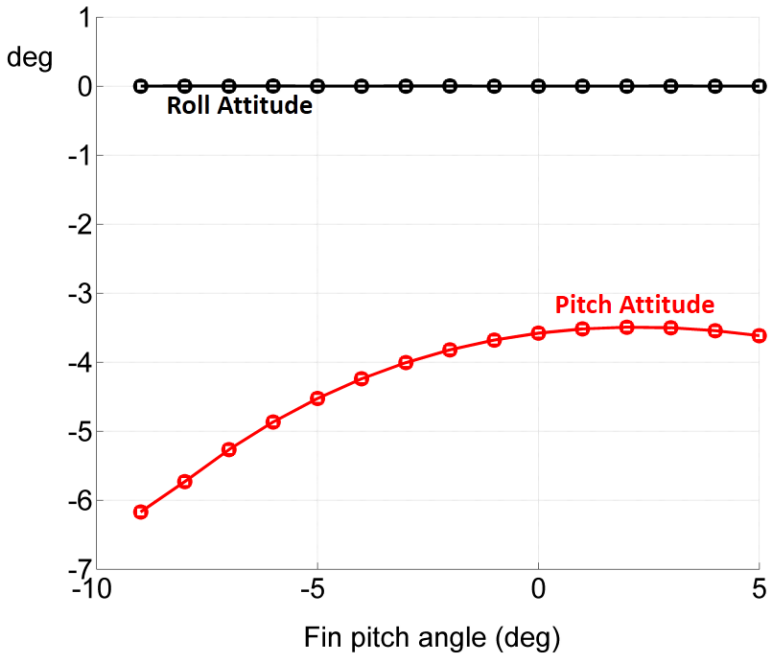

Figure 5.24: Towed Body Trim Attitudes at 25 knots

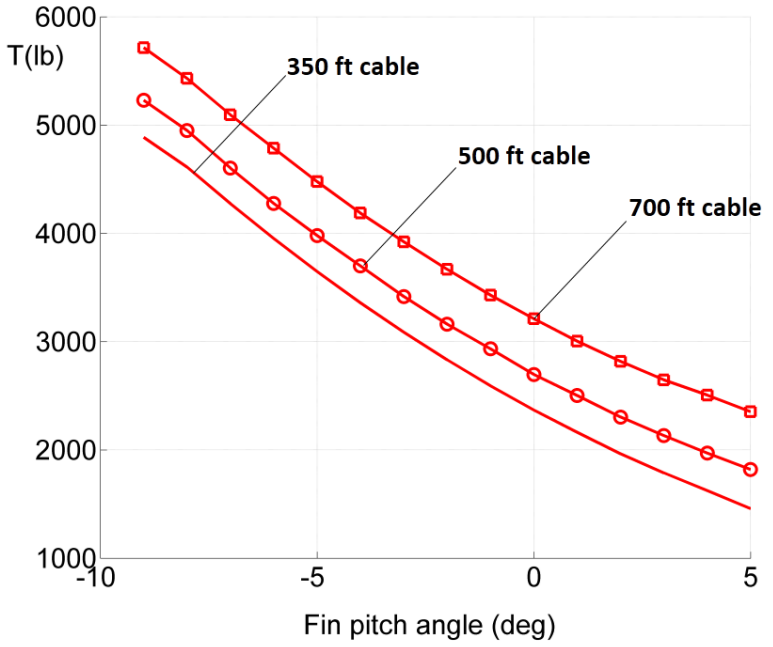

Figure 5.25: Cable Force at 25 knots for Various Cable Lengths

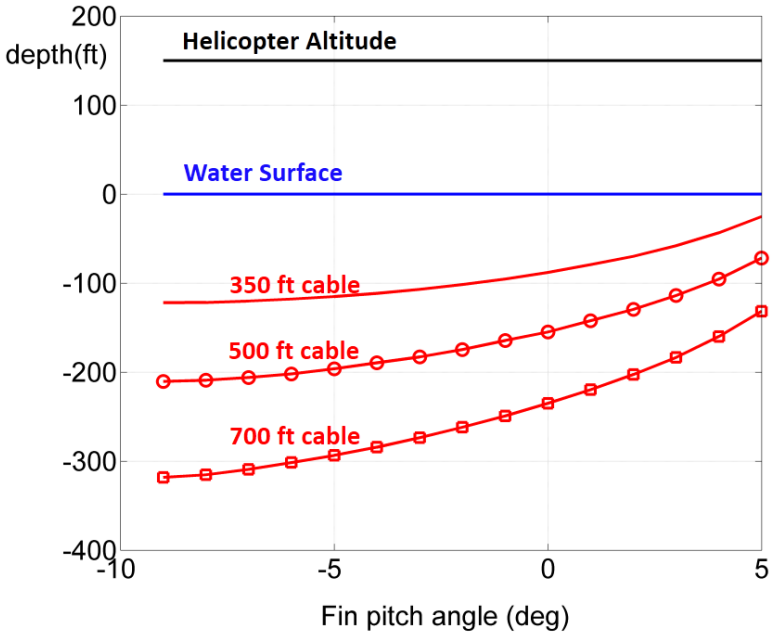

Figure 5.26: Towed Body Depths at 25 knots for Various Cable Lengths

When the fin exerts down-forces through pitch actuation, larger sections of the cable are aligned normal to the tow direction, increasing hydrodynamic drag *and* down-force. Conversely, **reducing fin down-force alleviates both vertical force and hydrodynamic drag**, resulting in significant reductions in the cable force, as shown in Fig. 5.25.

The corresponding towed body depth variation with fin angle is shown in Fig. 5.26. A target depth of 200 ft below the water surface can be achieved using a 500-ft cable with a fin angle of -6°, or a 700-ft cable with a fin angle of +2°. The corresponding values of cable force and power from Figs. 5.25 and 5.27 are (4200 lb, 1900 Hp) for the 500-ft cable, and (2900 lb, 1700 Hp) for the 700-ft cable. **For the same trim depth, the longer cable with hydrodynamic fairings is a more power-efficient choice than an equivalent shorter cable**. Thus, using the 700-ft cable can yield significant power savings in forward flight (10% to track

200 ft at 25 knots) in addition to providing a larger achievable depth range.

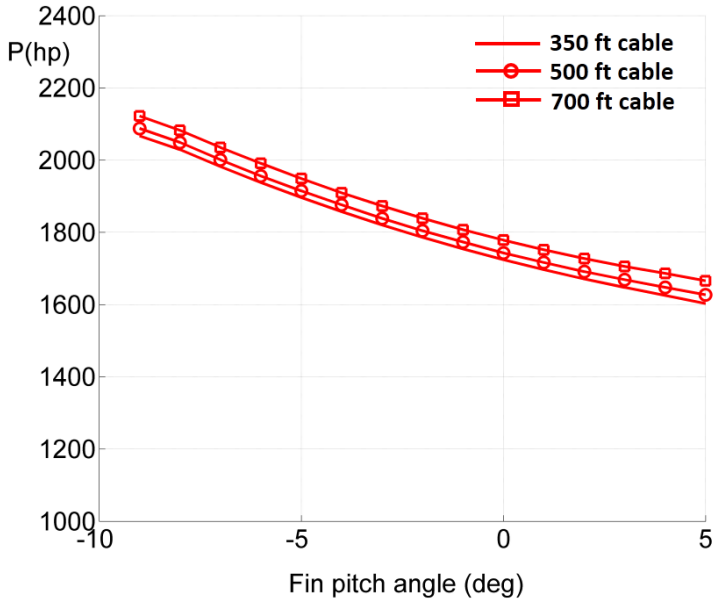

Figure 5.27: Main Rotor Power Required at 25 knots, Dynamic Inflow

5.1.8 Effect of Fin Pitch Angle on Curvature

Figure 5.28 shows the trim configurations of the cable and towed body for the 350-ft cable at 25 knots, at various fin pitch settings. As the fin angle increases, hydrodynamic down-force reduces and the cable trail angle increases, since modifying the vertical-axis forces by manipulating the fins changes the relative magnitudes of external forces in the vertical and longitudinal directions. The corresponding cable shapes for the 500-ft and 700-ft cables are shown in Figs. 5.29 and 5.30 respectively. As fin angle increases, the towed body depth reduces and simultaneously, the cable assumes a straight-line shape. **The effects of cable curvature vanish when there is no down-force from the submerged load**.

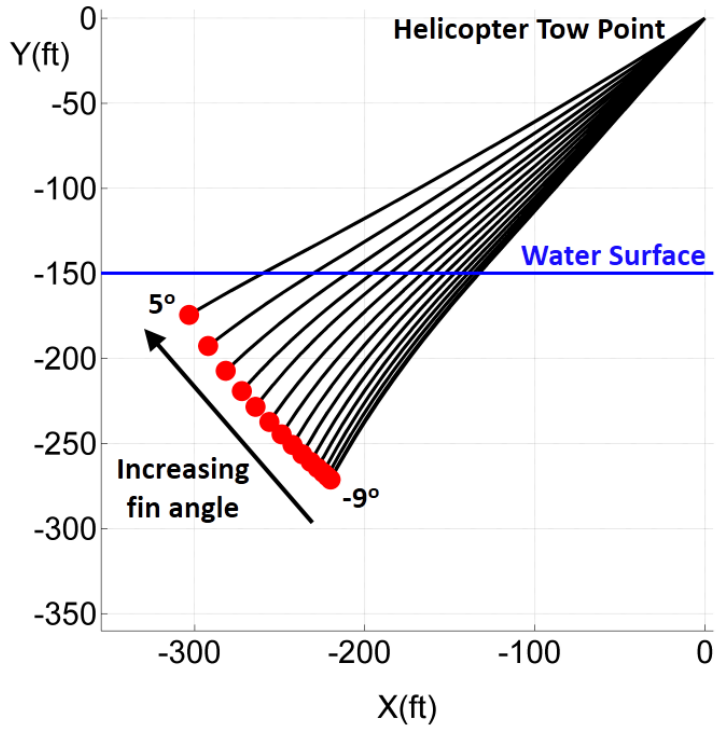

Figure 5.28: Shapes of the 350-ft Cable, 25 knots, Various Fin Pitch Orientations

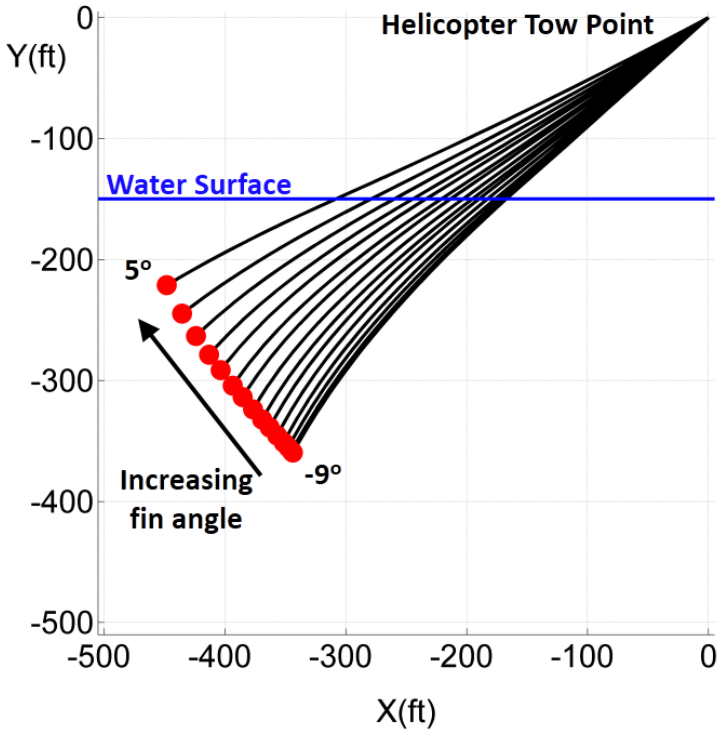

Figure 5.29: Shapes of the 500-ft Cable, 25 knots, Various Fin Pitch Orientations

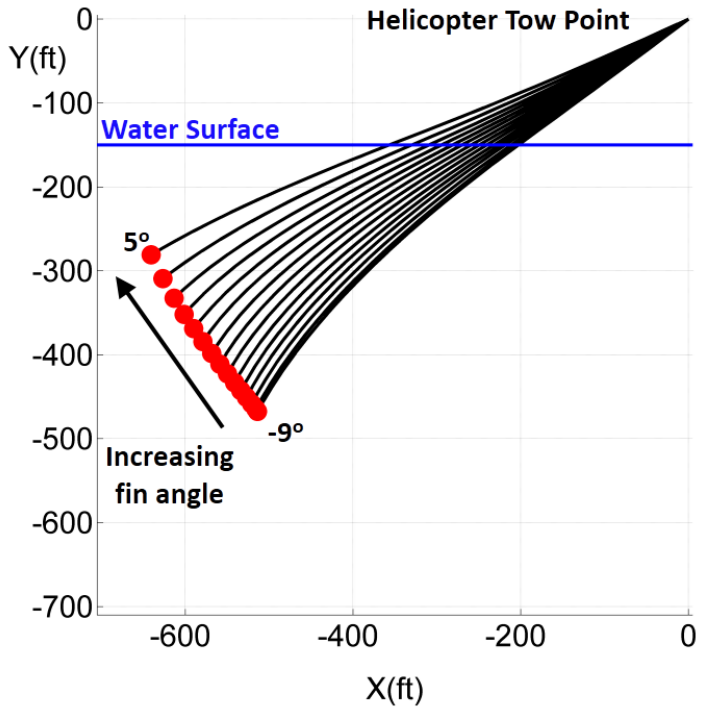

Figure 5.30: Shapes of the 700-ft Cable, 25 knots, Various Fin Pitch Orientations

5.1.9 Effect of Fin Pitch on Helicopter Trim

Figure 5.31 shows the helicopter trim attitudes for varying fin pitch angles. The pitch attitude is a measure of total drag acting on the cable and towed body. As the fin pitch angle increases, larger sections of the cable emerge from the water. These reductions in the total drag result in corresponding changes in the airframe pitch attitudes. Using a 700-ft cable requires -3.5° of pitch attitude, while achieving the same trim depth with a 500-ft cable requires -5.5°. Using a longer cable is a more power-efficient choice while simultaneously allowing the pilot to operate the aircraft at more benign orientations.

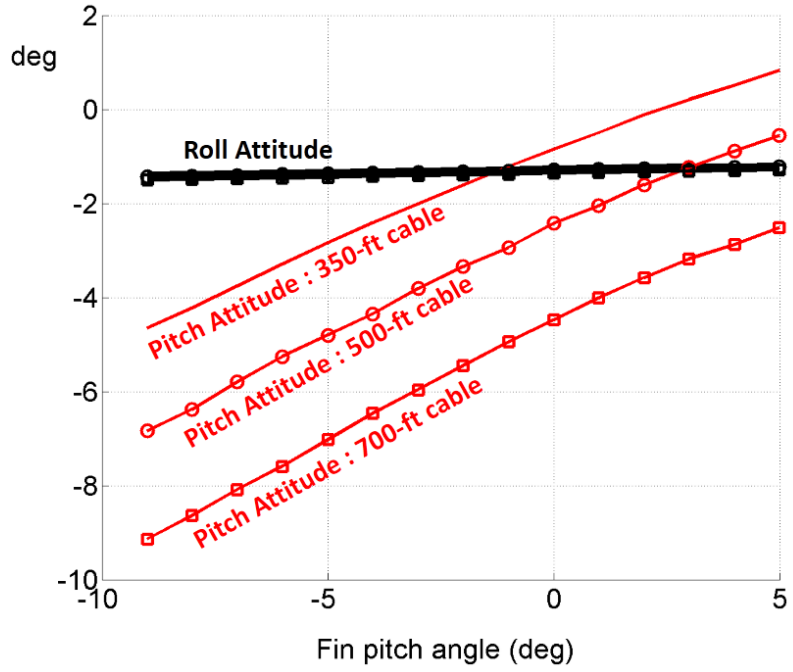

Figure 5.31: Helicopter Trim Attitudes at 25 knots, Dynamic Inflow

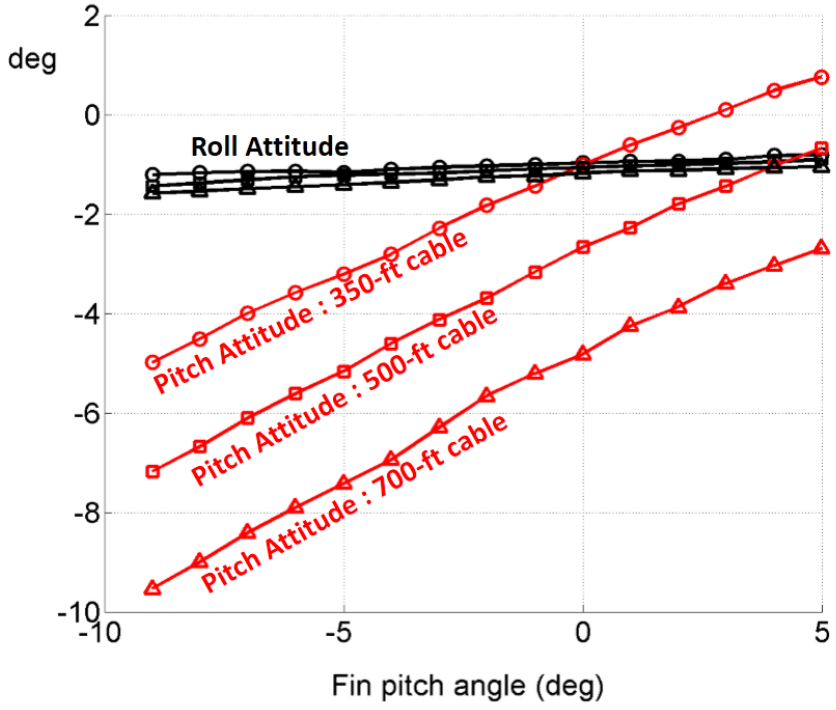

Figure 5.32: Helicopter Trim Attitudes at 25 knots, Free Wake

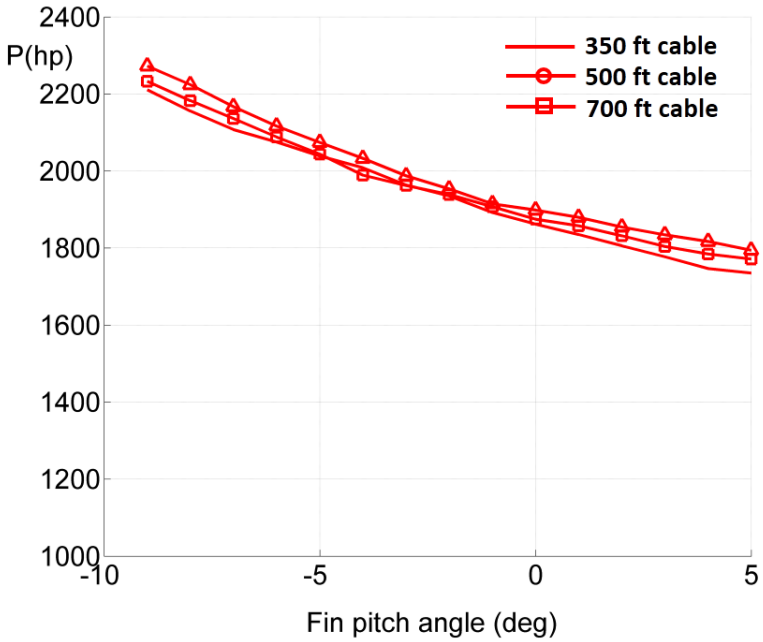

Figure 5.33: Main Rotor Power Required at 25 knots, Free Wake

The use of free-vortex wake models does not significantly alter predictions of the trim attitudes, as shown in Figs. 5.31 and 5.32. The attitudes predicted using the two inflow models differ by less than 1°. Main rotor power predictions obtained using the free wake model are shown for the three cables at 25 knots in Fig. 5.33. Cable drag differences between the three deployed lengths results in increased power requirements for longer cables at all fin angles. Performance improvements as predicted by dynamic inflow still hold, and 10% power reduction (now 200 Hp) may indeed be realized by using a 700-ft cable to track 200 ft depth instead of a 500-ft cable.

5.2 Trim in Steady Turning Flight

In this section, the characteristics of the tow system will be examined in steady level turning flight at 25 knots. At this low speed, the vertical tail of the helicopter is ineffective in providing sufficient lateral forces and yawing moments necessary for turn coordination. Instead, the helicopter is trimmed to fly with zero sideslip angle (β_{F}=0). For the individual cable lengths (350, 500, 700 ft) the magnitude of the peak turn rate is limited so that the smallest turn radius is always less than or equal to the length of the cable.

The towed body trim state is unaffected by that of the cable and helicopter, and is shown in Fig. 5.34 for turning flight at 25-knots of helicopter airspeed. With increasing turn rate, the pitch attitude does not change appreciably, indicating that the total drag on the towed body remains nominally constant. The submerged load rolls into the turn, with left roll attitude (negative) for nose-left turns, and right roll attitude for nose-right turns. The linear variation of roll angle with turn rate is a result of symmetry of the load geometry about the load X-Z plane.

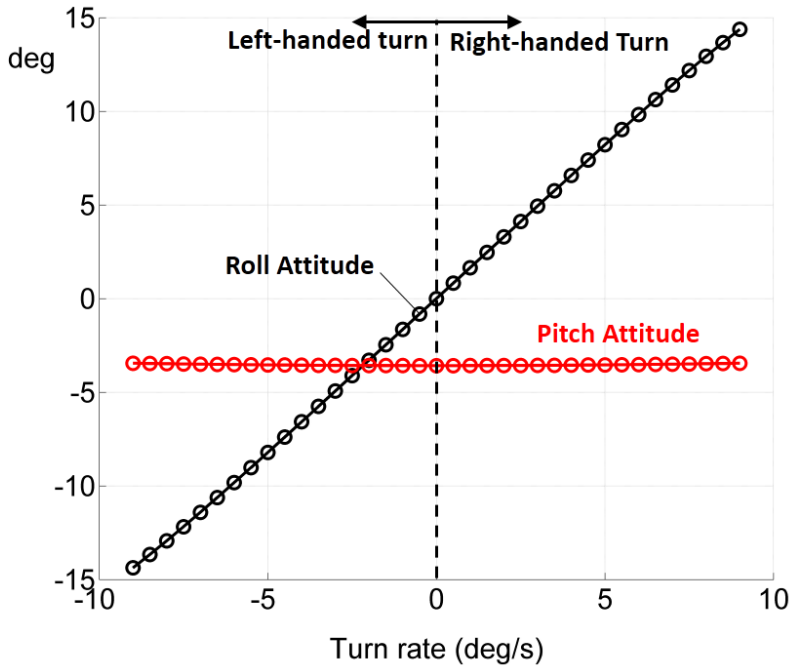

Figure 5.34: Towed Body Trim Attitudes in Turning Flight, 25 knots

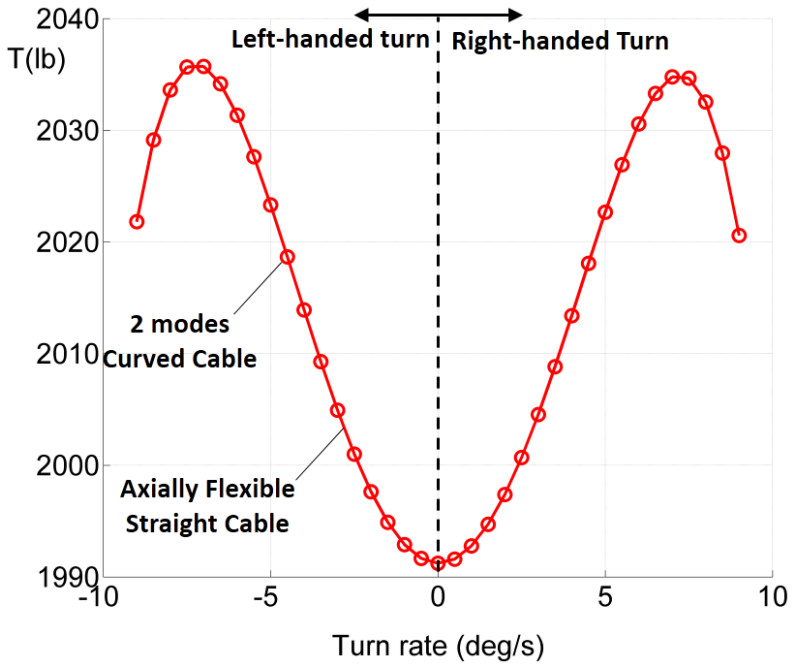

Figure 5.35: Helicopter Tow Tension in 25-knot Turn, 350-ft Straight Cable : Axially Flexible vs. Reduced Curved Cable Model, No Cable Hydrodynamics

Figure 5.35 shows the variation of the cable force transmitted to the airframe at

25 knots for a 350-ft straight cable, without cable hydrodynamics. With increasing turn rate magnitude, the turn radius of the towed body initially increases up to 7.5°/sec, resulting in higher dynamic pressure on the fins and hull and larger drag. Above 7.5°/sec, the cable force reduces because the turn radius of the submerged load reduces, and at extremely high turn rates, the path of the submerged load asymptotes to the center of the turn. These trends are qualitatively similar to phenomena observed in the previous work with aircraft-based sling load operations. When loads are suspended from flying platforms that maintain a steady turn, they migrate to the center of the turn with sufficient aerodynamic drag (Ref. [56]).

The results in Fig. 5.35 were obtained two different methods : the axially flexible straight cable, and a two-mode solution of the curved cable. The excellent agreement between the two predictions serves as another cross-validation of the two formulations and indicates that axial stretching effects are negligible.

The trim attitudes of the helicopter are shown in Fig. 5.36 for steady turning flight at 25 knots. When towing the submerged load, the airframe nose-down pitch attitude increases by 4° in comparison to an isolated helicopter with the same GTOW. The roll attitudes, while still linearly varying with turn rate, are smaller in magnitude when towing the submerged load. Since the tow point is offset below the helicopter CG, the vertical component of the cable force (due to fin down-force and towed body weight) serves as a stabilizing mechanism for the airframe roll attitude. Towed body drag and down-force result in elevated rotor power requirements at 25 knots in comparison to an isolated helicopter. However, the variation of rotor power with turn rate (up to 9°/sec, without cable hydrodynamics) is less than 1%.

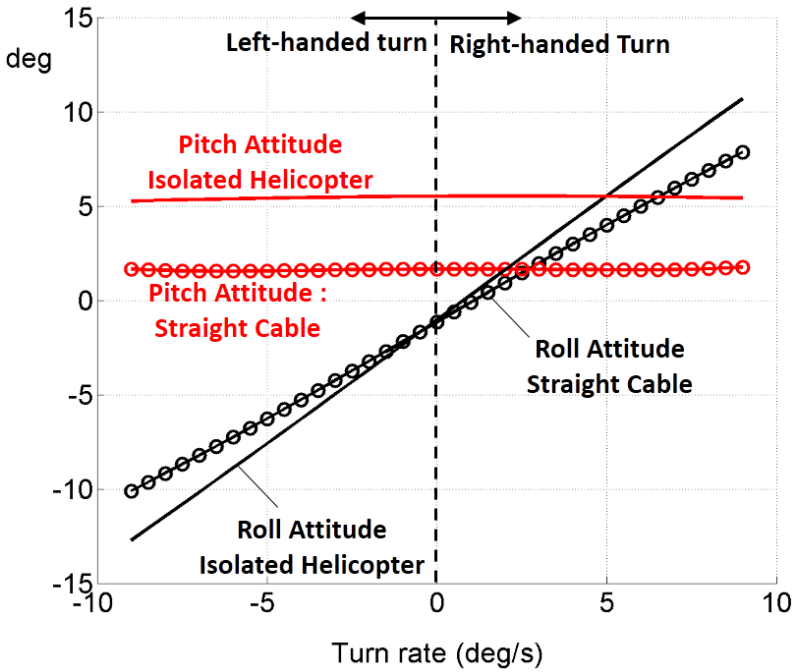

Figure 5.36: Helicopter Trim Pitch Attitudes in Turning Flight, 25 knots

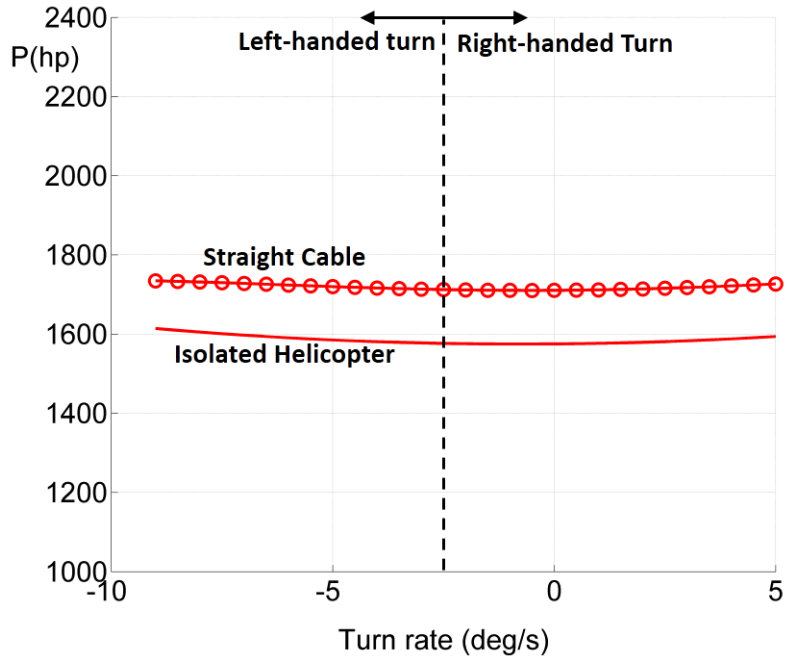

Figure 5.37: Main Rotor Power Required in Turning Flight, 25 knots

5.2.1 Effect of Cable Hydrodynamics

Cable hydrodynamic forces significantly influence the trim state of the towed body in turning flight, in addition to altering the forces transmitted to the airframe and therefore the helicopter trim state. The variation of total cable force with turn rate is shown in Fig. 5.38 for a 350-ft straight cable. With increasing turn rate, the effect of cable drag (in combination with towed body drag) is to reduce the turn radius of the submerged load even for incrementally small turn rates, resulting in lowered cable force levels for increasing turn rate. When cable drag is neglected, the trend predictions (as seen in the previous section) are reversed : an initial increase in load turn radius, followed by a decrease above 7.5°/sec.

If cable drag is neglected, the errors cascade into the helicopter trim state, as shown in Fig. 5.39. Without cable forces, the roll attitudes are over-predicted by 2° at 5°/sec of turn rate. With increasing turn rate, the turn radius of the towed body reduces, and the errors associated with neglecting cable drag cancel those due to over-predicting towed body drag. As a result, the total horizontal force transmitted to the helicopter is not grossly altered, resulting in lower differences in the trim pitch attitudes and 3.6% error in the rotor power required.

The most significant impact of cable drag is on the predictions of trim depth of the towed body. Neglecting cable drag results in almost 50% error in depth prediction, as shown in Fig. 5.40.

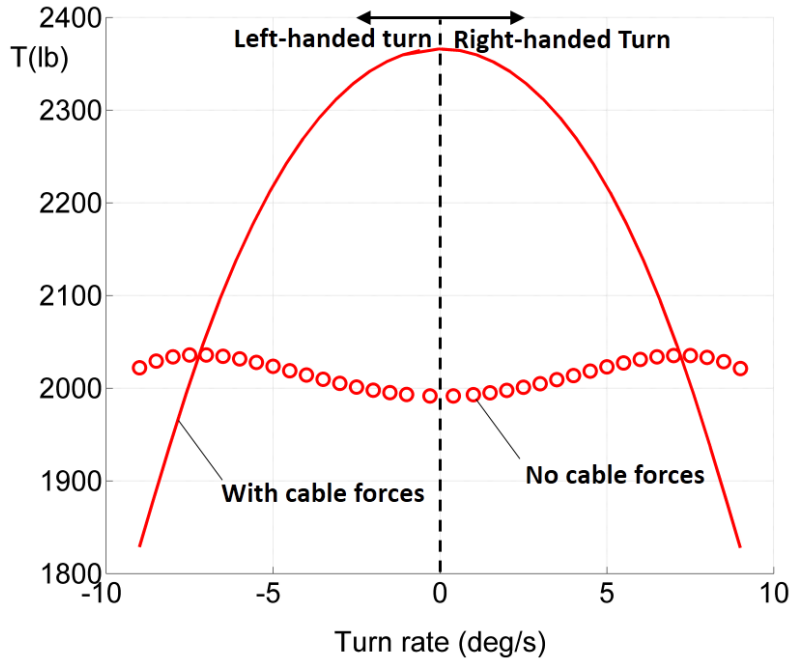

Figure 5.38: Cable Force in 25-knot Turn, 350 ft straight cable

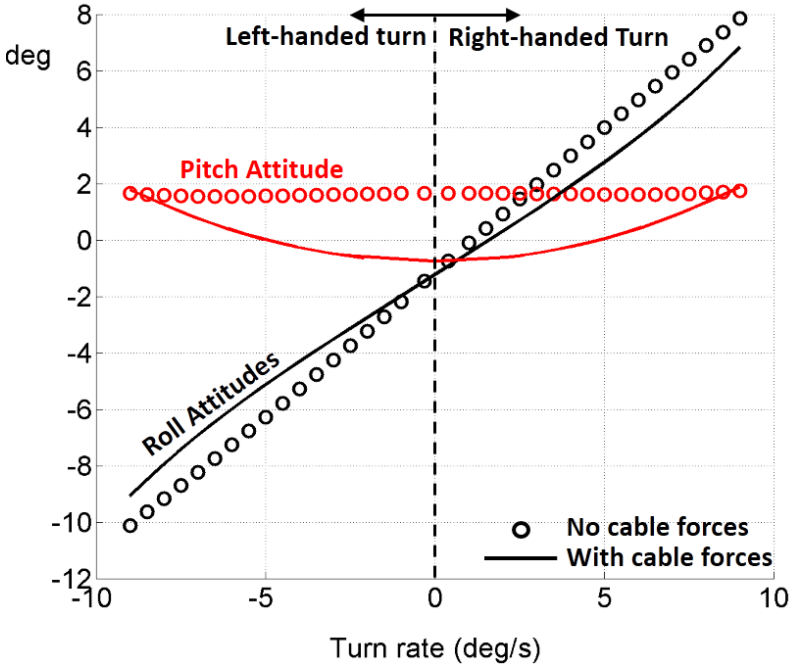

Figure 5.39: Helicopter Trim Pitch Attitudes in 25-knot Turn, 350 ft straight cable

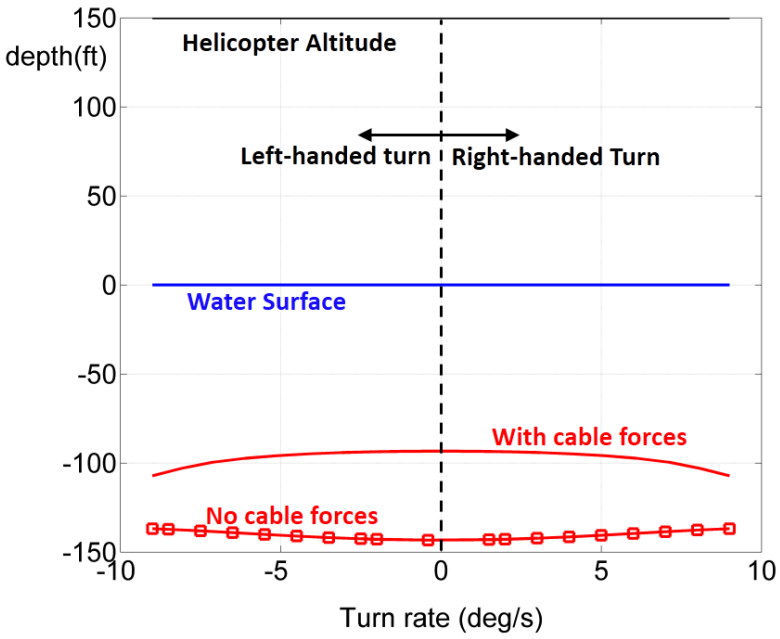

Figure 5.40: Towed Body Trim Depth in 25-knot Turn, 350 ft Straight Cable

5.2.2 Effect of Cable Curvature in Turning Flight

Tow cable curvatures are small at 25 knots with the depth control system turned off. When the tow system executes turning flight at this helicopter speed, the effects of cable curvature on the turn radius of the towed body are negligible. Ignoring curvature results in 3% over-prediction of cable force transmitted to the helicopter at the peak turn rate (9°/sec), with negligible changes in predictions of rotor power requirements and helicopter trim controls. Cable flexural stiffness and axial stiffness play do not noticeably influence trim predictions, again highlighting the dominance of the axial force terms in the cable dynamics over the bending resistance afforded by the cross-section considered.

5.2.3 Effect of Cable Length

In steady forward flight, the trim state of the submerged load is influenced *only* by its own geometry. In turning flight, the trim state of the towed body depends on its own geometry *and* the parameters of the cable, due to effects of cable drag on the turn radius of the submerged load.

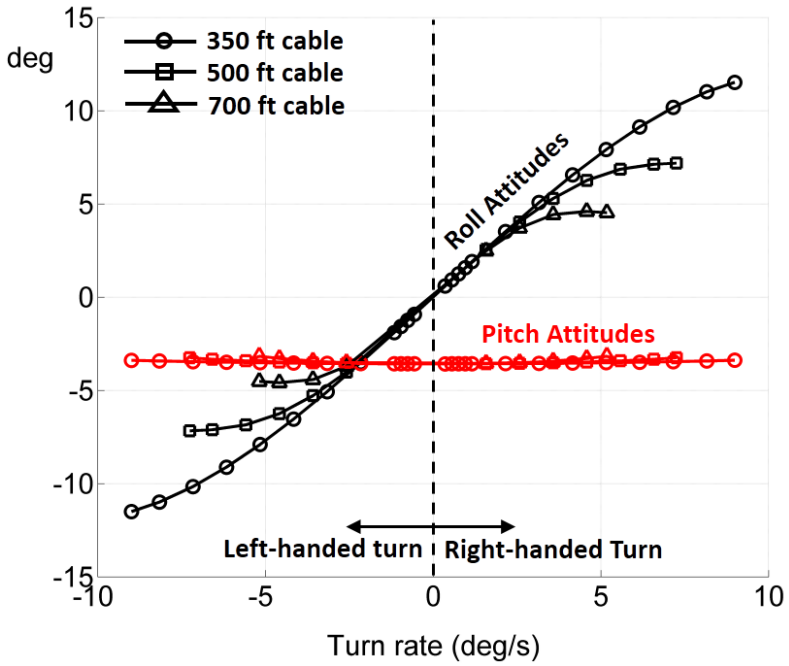

Figure 5.41: Towed Body Trim Attitudes in Turning Flight, V_{HELO}=25 knots

Figure 5.42 shows the variation of trim roll and pitch attitudes of the submerged load with different cable lengths. The trim pitch attitude is independent of cable length, indicating that the hull drag (and hence, forward speed) is unchanged. The roll attitude is constant for all three cables until the turn radius approaches the cable length. When the helicopter turn rate increases, the towed body turn radius decreases as it asymptotes to the center of the turn. At this limit, the increase in lateral force with turn rate almost vanishes, and the roll attitude trends exhibit

nonlinearities. The trim depths of the submerged load are shown in Fig. 5.42. The variations of trim depth across the range of turn rates are 10 ft (3% length), 60 ft (12% length) and 90 ft (13% length) for the 350, 500 and 700-ft cables respectively.

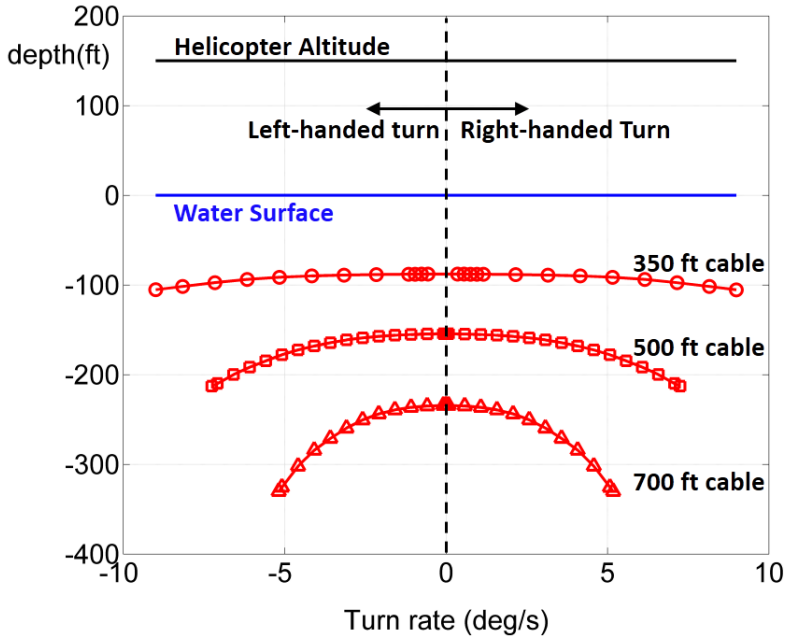

Figure 5.42: Towed Body Trim Depth in Turning Flight, V_{HELO}=25 knots

Top views of the tow system in turning flight are shown in Figs. 5.43, 5.44 and 5.45 for the 350, 500 and 700-ft cables respectively. The shapes of the 700-ft cable at the peak turn rates display visible levels of lateral curvature, which is absent in the 350 and 500-ft cables. For the 350-ft cable, turning flight at the peak rate of 9°/sec results in significant towed body lateral offset from the helicopter (160 ft or 45% of cable length). The corresponding numbers for the 500-ft cable at 7.25°/sec and 900-ft cable at 5°/sec are 250 ft (50%) and 420 ft (60%) respectively. **Increasing cable length in turning flight reduces the load turn radius, resulting in three dominant effects on the tow system : reduction of main fin down-force, reduction of hull hydrodynamic drag and reduction in cable drag.**

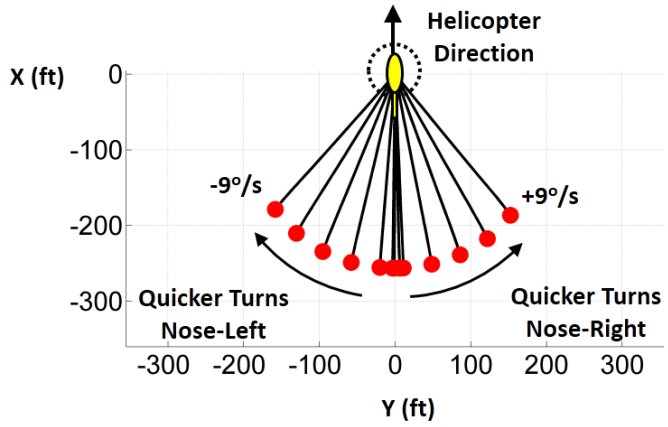

Figure 5.43: Top View in Turning Flight, V_{HELO}=25 knots, 350 ft cable

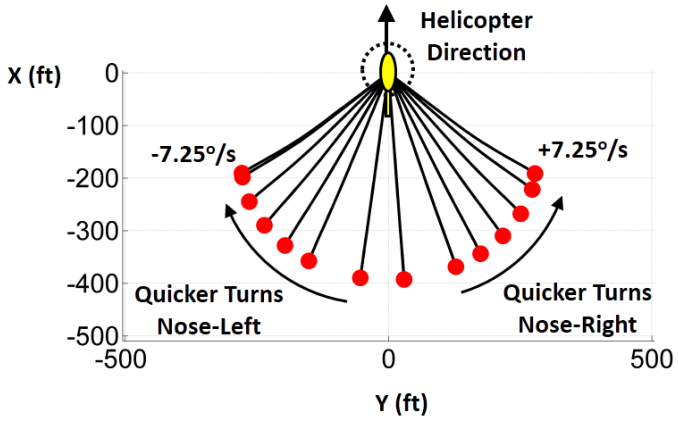

Figure 5.44: Top View in Turning Flight, V_{HELO}=25 knots, 500 ft cable

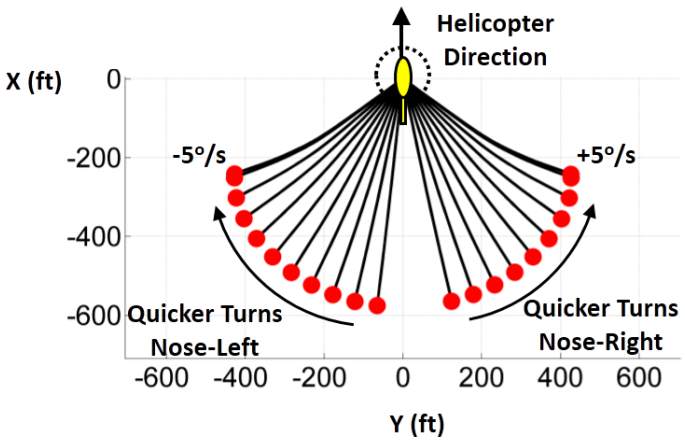

Figure 5.45: Top View in Turning Flight, V_{HELO}=25 knots, 700 ft cable

The corresponding cable forces transmitted to the helicopter are shown in Fig.

5.46 for various cable lengths and helicopter turn rates. In forward flight (zero turn rate), hydrodynamic drag on the immersed lengths of the cables results in higher tow tension for longer cables. With increasing turn rate, the towed body moves closer to the center of the turn when using longer cables, reducing hydrodynamic drag on both the submerged load *and* the sections of the tow cable close to the towed body. Thus, **hydrodynamic drag on the cable causes higher cable forces at low turn rates, and lower cable forces at high turn rates for long cables**.

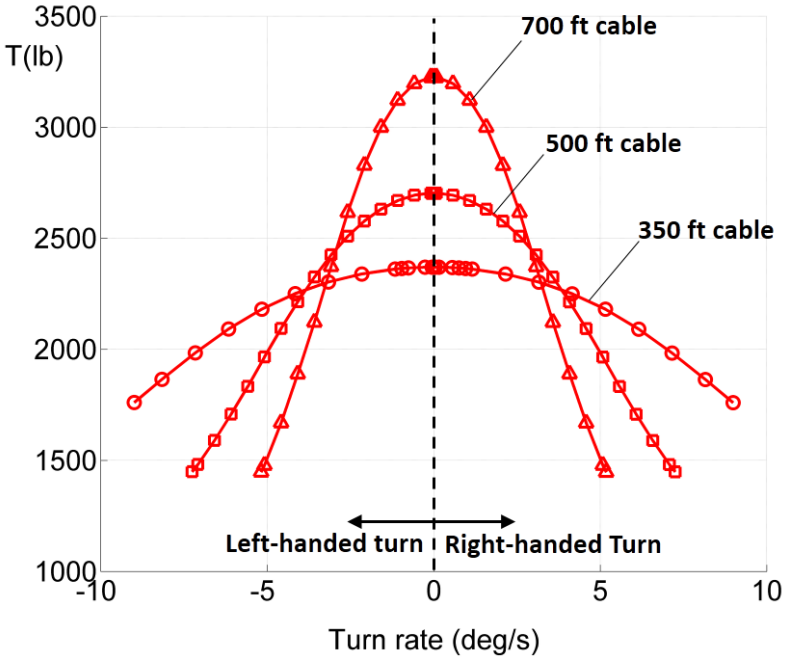

Figure 5.46: Helicopter Tow Tension in Turning Flight, V_{HELO}=25 knots

The trend of reducing hydrodynamic drag with turn rate is clearly visible in the pitch attitude of the helicopter, shown in Fig. 5.47. As the hydrodynamic drag on the cable and towed body decreases, the reduction in horizontal component of cable drag causes the fuselage to trim with an increasingly nose-up pitch attitude with increasing turn rate. The power required by the rotor to sustain flight reduces with increasing turn rate, as shown in Fig. 5.48. The differences in power predictions

between the three cables at steady forward flight (zero turn rate) stem from the effects of hydrodynamic drag on elevated rotor thrust requirements for longer cables.

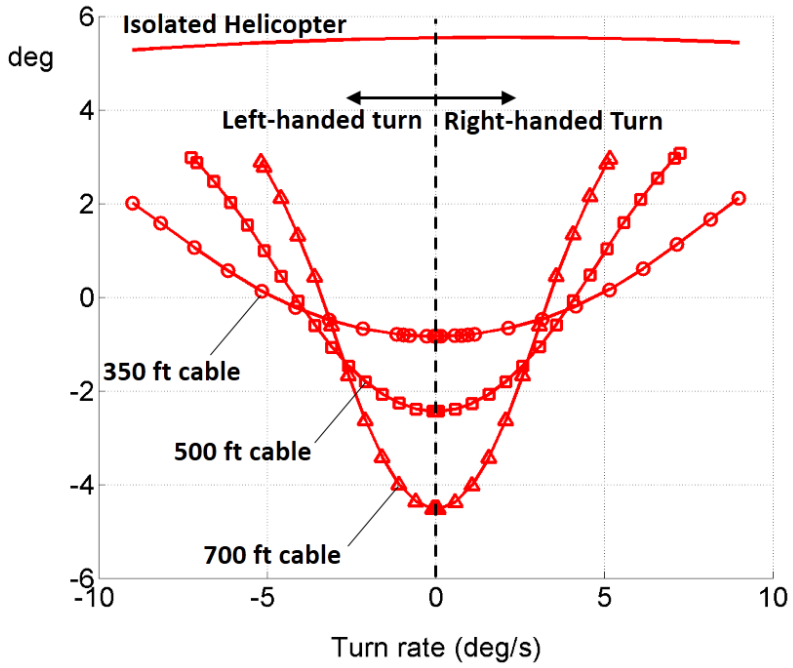

Figure 5.47: Helicopter Pitch Attitude in Turning Flight, V_{HELO}=25 knots

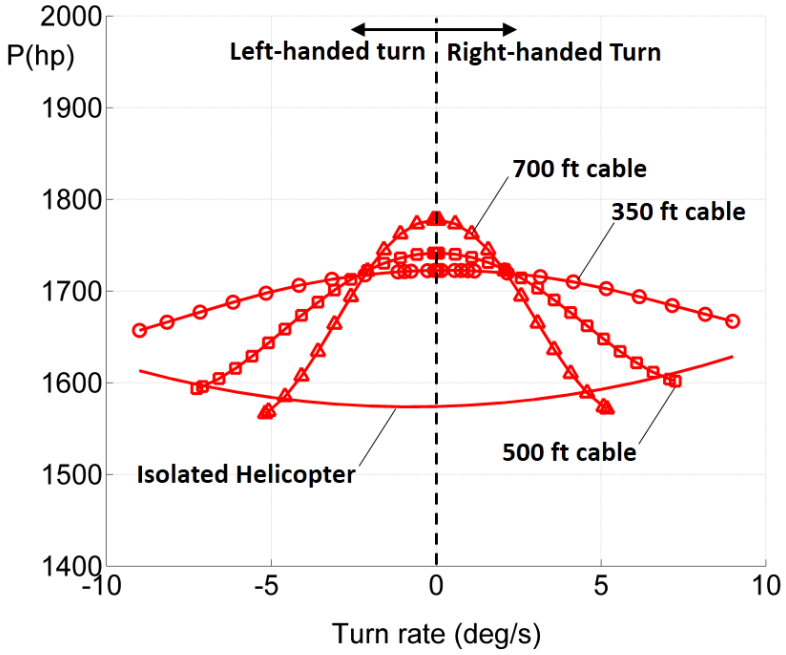

Figure 5.48: Main Rotor Power Required in Turning Flight, V_{HELO}=25 knots

5.2.4 Predictions with Free-Vortex Wake

The simulations for the three curved cables were repeated with a vortex wake model of the main rotor aerodynamics to obtain refined performance predictions. Since the rotor model is completely uncoupled from the *trim* solutions of the cable and towed body, inclusion of free-vortex wake does not affect predictions of towed body depth, cable shape or total cable force at the helicopter tow point. Potential differences may occur in the trim state of the helicopter. However, Figs. 5.47 and 5.49 shows that the helicopter trim pitch attitude as predicted by free wake is almost identical to the corresponding results obtained using dynamic inflow.

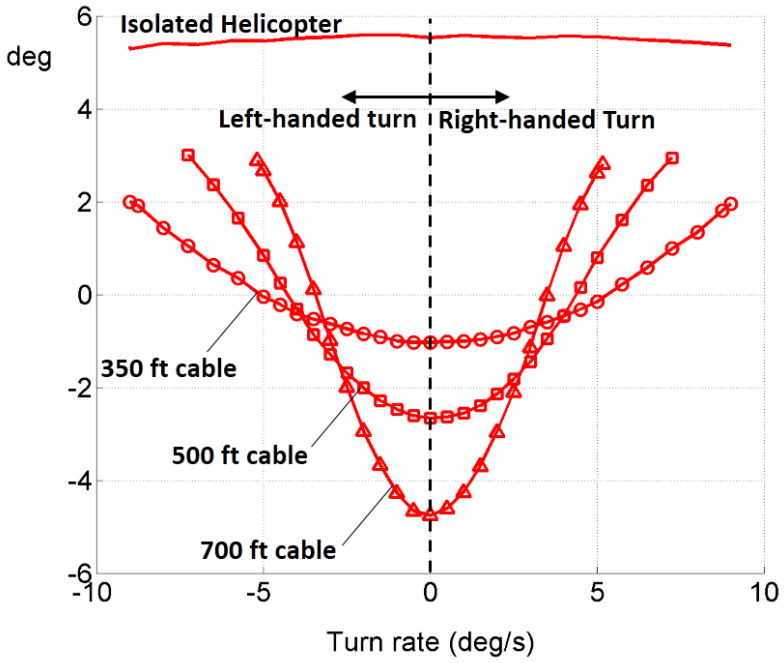

Figure 5.49: Helicopter Pitch Attitude in Turning Flight, V_{HELO}=25 knots

Capturing non-uniform inflow distributions with free wake yields more accurate predictions of rotor power, shown in Fig. 5.50 compared to dynamic inflow. The apparent lack of smoothness in the power curve for the isolated helicopter is

the outcome of an oscillatory convergence process, and is exaggerated by the scale of the plot. To avoid terminating the trim process prematurely, alternate updates of wake geometry and vehicle retrim are continuously performed until the cumulative normalized change in rotor power, trim controls, rotor response, airframe attitudes, towed body orientations and cable deflections is less than 1% between two iterations. The maximum change in rotor power at the last trim iteration was less than 0.5% (less than 10 Hp).

The longest cable (700 ft) initially requires maximum power in steady forward flight due to cable drag. With increasing turn rate, the trim turn radius of the submerged load reduces faster for longer cables, resulting in lower power consumption. The dynamic inflow model indicates that nose-right turns require incrementally more power than nose-left turns for the isolated helicopter, but power requirements for the tow system exhibit less asymmetry. The free wake model highlights that these differences are larger for both the isolated helicopter and the tow system, and scale with rotor thrust requirements. **Steady turns of the tow system require lesser rotor power compared to straight-line tow at the same helicopter speed.** Therefore, steady level turns do not impose additional performance penalties on the tow system and are not restricted by available power. Engine power limits determine the maximum straight-line tow speeds, while the maximum turn rate is determined by cable length and hydrodynamics.

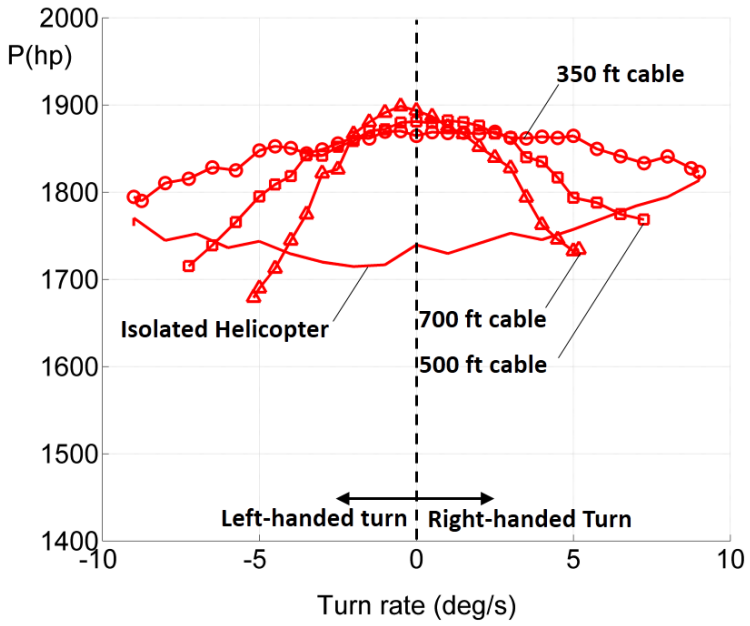

Figure 5.50: Main Rotor Power Required in Turning Flight, V_{HELO}=25 knots

5.2.5 Depth Regulation using Pitching Fins

In this section, the effects of depth regulation using pitching of the main fins on the towed body on trim configurations in turning flight are investigated at the peak turn rate (as dictated by cable length) for the helicopter-cable-load system in turning flight at 25 knots, with three cable lengths. For a given cable length and helicopter turn rate, the trim pitch attitude of the submerged load varies from -6° at -9° of fin pitch to -4° at 5° of fin pitch, and is similar to the corresponding results in steady forward flight. The trim roll attitude varies by less than 2° (with respect to the trim state at zero fin pitch) across the range of fin pitch angles investigated. The changes in trim pitch attitudes of the towed body arise from induced drag on the pitching fins, while the changes in the trim roll attitude stem from an altered trim turn radius for the submerged load.

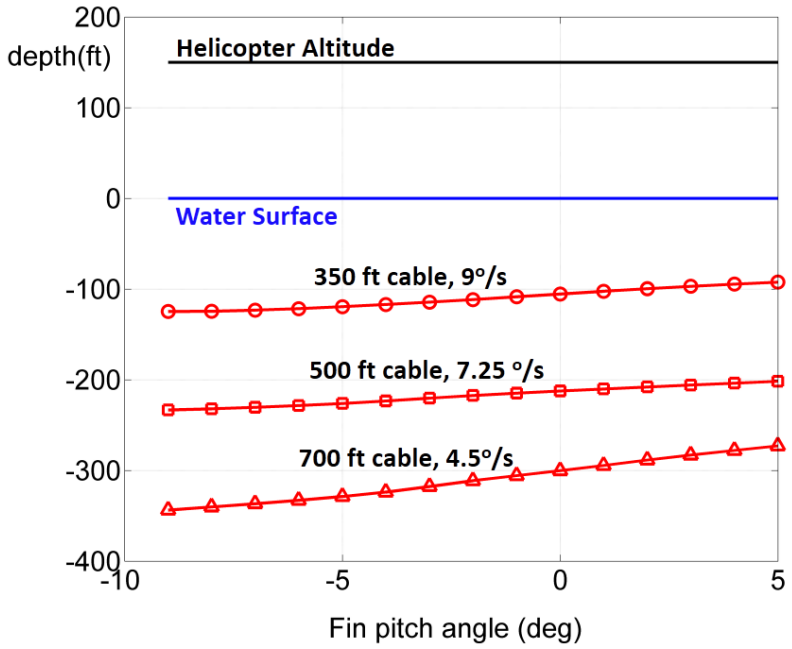

Figure 5.51: Towed Body Depth in Turning Flight, V_{HELO}=25 knots

The trim depth of the towed body is shown in Fig. 5.51 for tow systems in a 25-knot turn with three different cable lengths, at the peak turn rates for each cable. While fin pitch is useful in forward flight to track various depths, it is less effective in turning flight due to the reduced dynamic pressures experienced by the towed body and its hydrofoils. For the 350-ft cable, the range of available depths is restricted to 90-120 ft, while in straight-line tow, the same range of fin actuation allows for 30-120 ft. As the cable lengths increase, two aspects of depth control begin to interact with each other. While longer cables allow for larger ranges of trim depths to be reached in forward flight, the influence of cable drag on towed body turn radius reduces fin effectiveness, restricting the range of available depths. As a result of this interplay, the 500 and 700-ft cables can track 200-230 ft and 280-340 ft, respectively, at their peak turn rates. The corresponding depth ranges in forward flight for the two cables are, in order, 80-210 ft and 130-310 ft.

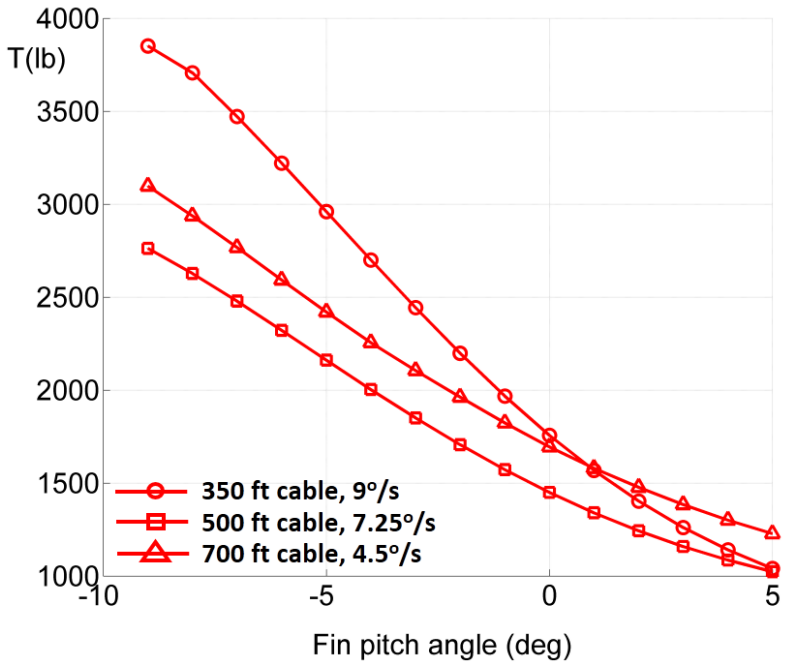

Figure 5.52: Helicopter Tow Tension in Turning Flight, V_{HELO}=25 knots

The cable force variations with fin angle for the three cables at their peak turn rates are shown in Fig. 5.52. When the hydrofoils produce down-force, the turn radius of the towed body increases, resulting in larger hydrodynamic drag. In this operating condition, the 350-ft cable transmits the maximum tow tension to the airframe. For nose-up fin pitch angles, the 700-ft cable transmits the maximum tension, due to increased hydrodynamic drag on the cable. The combination of smaller load turn radius, peak turn rate, cable buoyancy and hydrodynamic drag on the 500-ft cable results in minimum tow tension throughout the range of fin angles investigated. The main variations in towing tension between the three cables arise from differences in hydrodynamic drag. To compensate for this increased cable drag, the helicopter trims to an increasingly nose-down pitch attitude, as shown in Fig. 5.53.

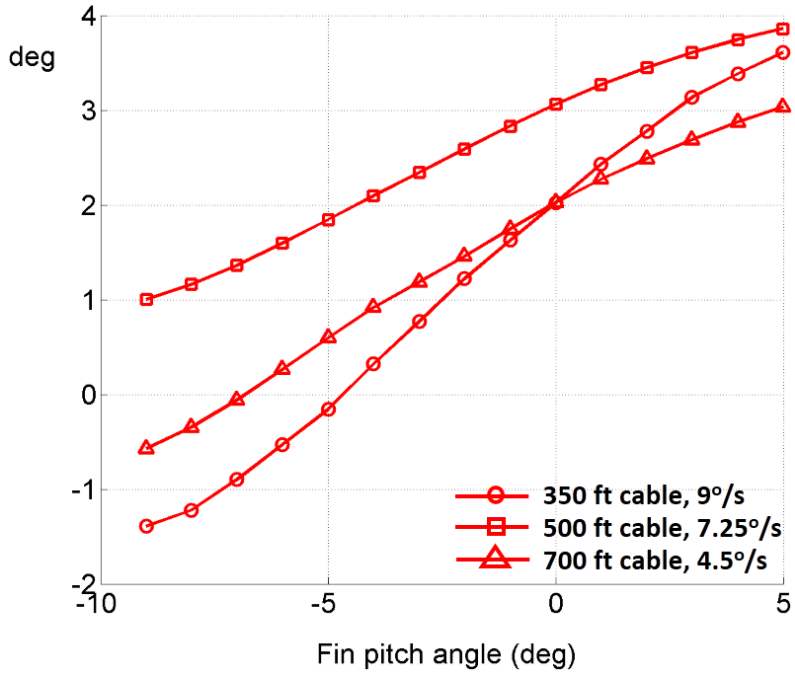

Figure 5.53: Helicopter Pitch Attitude in Turning Flight, V_{HELO}=25 knots

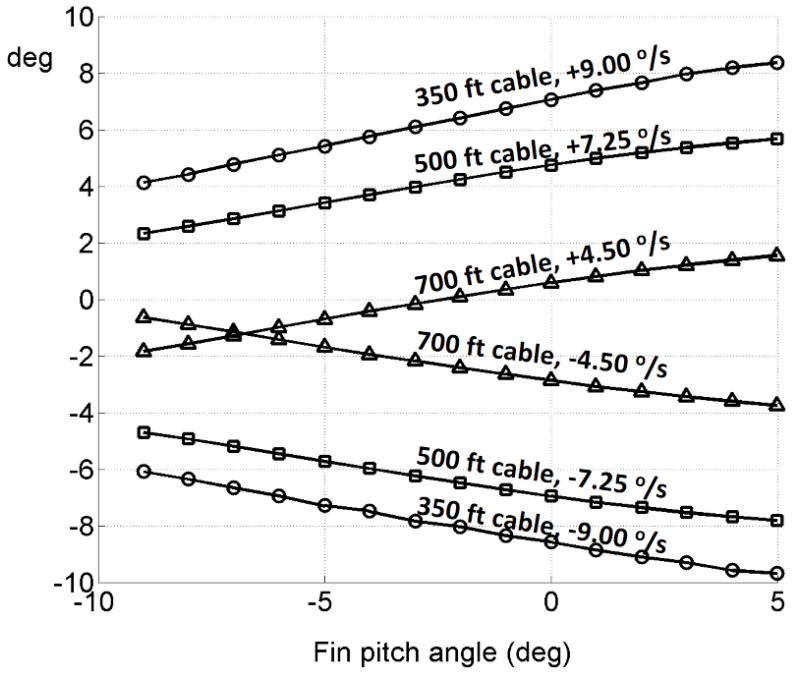

Figure 5.54: Helicopter Roll Attitude in Turning Flight, V_{HELO}=25 knots

The helicopter roll attitudes at the peak nose-left and nose-right turn rates for the three cables are shown in Fig. 5.54. The roll attitudes of the helicopter are

antisymmetric about $\phi_F = -1°$. With increasing fin pitch angle, the towed body down-force increases. Since the magnitude of the towed body trim roll attitude at the peak turn rate increases with cable length, down-forces from the main fins cause increased lateral forces on the helicopter. To counter these lateral forces and simultaneously maintain roll moment equilibrium, the helicopter rolls away from the turn (i.e. roll right in a left-handed turn and roll left in a right-handed turn).

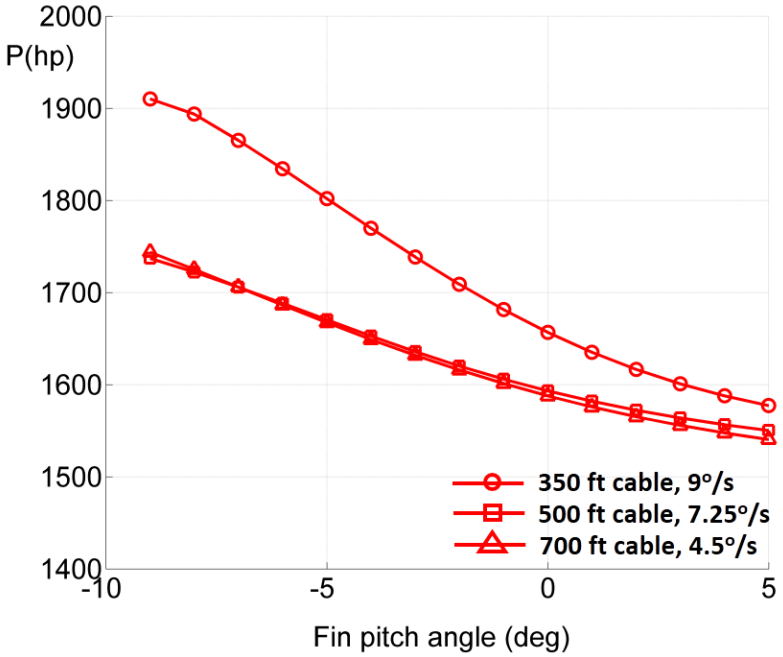

Figure 5.55: Main Rotor Power Required in Turning Flight, V_{HELO}=25 knots

The main rotor power required to maintain a 25-knot turn is shown in Fig. 5.55, as predicted by dynamic inflow. The 350-ft cable requires the maximum power among the three lengths investigated, since the towed body experiences the smallest reductions in turn radius at this cable length. Predictions for the 500-ft and 700-ft cables are near-identical, with near-identical thrust requirements. For these two cable lengths, weight alleviations due to buoyancy are offset by increases in hydrodynamic drag. The crossing of the power curves is a result of the rotor operating at

two different turn rates.

5.2.6 Predictions with Free-Vortex Wake

The trim configurations of the cable and towed body, and total tow-point tension at the helicopter are unaffected by the rotor dynamics model, since turn kinematics (and not kinetics) determines the equilibrium solution. Predictions of trim attitudes obtained using dynamic inflow and free wake are near-identical and differ by less than 0.5°.

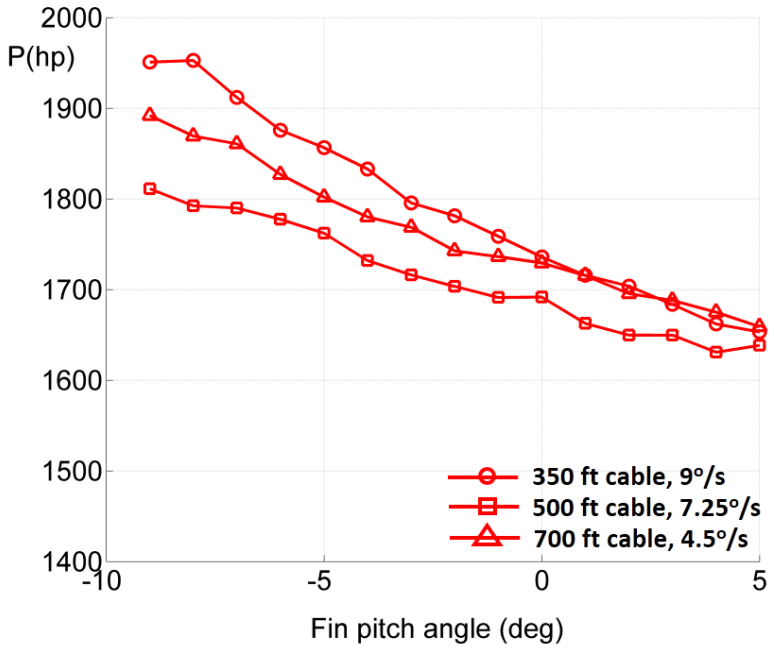

Figure 5.56: Main Rotor Power Required in Turning Flight, V_{HELO}=25 knots

The rotor power requirements as predicted using free wake are shown in Fig. 5.56. The power required to maintain a 25-knot turn for the helicopter at the peak turn rates are obtained for various fin pitch settings. The 500-ft cable requires the least power at all fin pitch angles, consistent with the results obtained using dynamic

inflow. However, dynamic inflow does not penalize the increased thrust requirements due to increased cable forces from the 700-ft cable (compared to the 500-ft cable) among the two flight conditions. When the free wake model is used, the difference in thrust requirements between the 500-ft and 700-ft cables is clearer, indicating that induced power penalties due to increasing cable forces are more dominant than the corresponding thrust alleviations obtained by operating at lower turn rates.

Maintaining a steady turn at the same helicopter speed at 9°/sec with a 350-ft cable is the most power-inefficient configuration among the three cases investigated (up to 3° of fin pitch), since the reduction in turn radius of the towed body (and therefore the hydrodynamic drag) is the smallest for this deployed cable length. The crossing of the power curves for the 700-ft cable and 350-ft cable is a result of an interplay between decreasing hydrodynamic drag and cable buoyancy with increasing fin pitch angle, and its corresponding effect on rotor thrust requirements.

6 Analysis of Linearized Models

This chapter discusses the analysis of linearized system dynamics in the neighborhood of equilibrium (trim) conditions in steady forward flight. The extraction of linearized models presents certain difficulties for the tow system, which has specific nonlinearities. All conclusions drawn from these studies are valid for specific operating conditions and combination of parameters that ultimately result in dominantly linear tow system dynamics.

The primary source of nonlinearities is the sharp discontinuity at the water/air free surface, where aerodynamic loading on the cable changes abruptly to hydrodynamic forces. This discontinuity in cable force distribution along the span and the variation of section normal force with flow angle are the dominant sources of cable curvature.

For the purposes of extracting linearized models, the first two blade modes (corresponding to "rigid" flap and lag) are used. Fixed-frame frequencies of the flexible blade modes for this articulated rotor are sufficiently large that they do not interact with the airframe modes and do not affect flight dynamic frequencies (up to 30 rad/s). The open-loop eigenvalues of the isolated helicopter are given in Table 6.1. The high-frequency modes (large imaginary part) corresponding rotor

fixed-frame flap and lag motions, while the low-frequency rotor modes (lag and regressive flap) are coupled with airframe motions. All open-loop modes are stable except modes # 15 and # 17. Mode 15 is an oscillatory divergent translation (longitudinal, lateral and vertical) with small contributions from body roll, pitch and yaw. The dominant motions in mode 17 consist of divergent longitudinal, vertical and lateral translations, and is stabilizing or destabilizing depending on the blade mode shapes (specifically, the flap-torsion coupling terms in the beam equations). Thus, accurate modeling of the blade dynamics (including the so-called higher order terms) is required for coupled rotor-airframe stability analysis. The mode with zero eigenvalue corresponds to the heading pole, i.e. there is no preferential heading for the airframe.

6.1 Tow System : Eigenvalues

The eigenvalues for the tow system at 25 knots obtained without cable hydrodynamics are given in Table 6.2. The introduction of rigid-body position states for the helicopter, required for tracking towed body depth, results in three additional poles at the origin. These modes indicate that the dynamics are unaffected by the position of the system in space so long as the towed body remains submerged. At hover, the heading pole is unchanged for the helicopter, and an identical pole at the origin is introduced corresponding to the towed body direction. In forward flight, the heading pole for the entire system is preserved. The mode shape corresponding to the heading pole is transformed into rigid translations along the earth-fixed axes

Table 6.1: Helicopter Bare Airframe Eigenvalues at 25 knots

Mode #	Real part (rad/s)	Imaginary part (rad/s)	Mode #	Real part (rad/s)	Imaginary part (rad/s)
1	0	0	2	-12.9	47.03
3	-34.57	0	4	-3.10	37.91
5	-30.67	7.76	6	-12.34	20.05
7	-2.63	18.31	8	-15.18	0
9	-15.02	22.48	10	-3.56	7.82
11	-3.43	4.40	12	-3.79	0
13	-1.93	0	14	-0.22	0.86
15	0.27	0.42	16	-0.22	0
17	0.0185	0	18	-3.02	7.34

contained in the $\boldsymbol{i}_{\mathrm{B}}$-$\boldsymbol{j}_{\mathrm{B}}$ plane, since the helicopter heading modifies the (non-zero) earth-fixed velocity components.

The rotor modes are altered as a result of operating at a higher thrust condition, required to overcome hydrodynamic drag. The real part of the unstable airframe eigenvalue is unchanged, while the second marginally unstable mode with a small positive real part (mode 17 for the isolated helicopter case) is stabilized. The overdamped mode # 6 for the tow configuration corresponds to longitudinal translation and pitch motions for the towed body. The tow cable and submerged load do not introduce any unstable modes when attached to the helicopter, *when*

including effects of cable drag. If cable drag is neglected, the cable mode predictions turn unstable, and the eigenvalues have real positive components. The same cable drag that stabilizes the coupled helicopter translation-transverse vibration modes introduces (for large-amplitude motions) nonlinearities into the system through the discontinuous load at the water interface, and the variation of normal loading with flow inclination to the cable axis.

6.2 Analysis of Tethered Helicopters

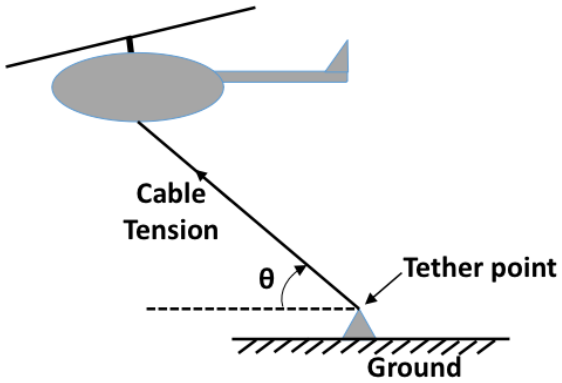

Figure 6.1: Tethered Helicopter Schematic

To understand the nature of the helicopter frequency response when used as a tow platform, a systematic approach is followed to isolate the contributions of various physical parameters. An idealized system is initially considered, and gradually augmented with additional degrees of freedom until the tow system is obtained. The idealized system considered here consists of a helicopter tethered to the ground as shown in Fig. 6.1. Using this system, the effects of vertical and forward components of rotor thrust, hook offset, forward flight and cable properties are examined to determine the effect of the operating conditions on the vehicle

response sensitivities over a range of frequencies. To extract linearized dynamics, equilibrium solutions are required. The tethered system is trimmed so that the cable inclination and force are equal to prescribed values (θ=θ_{trim} and T_C=$\text{T}_{C_{\text{trim}}}$).

6.3 Effect of Thrust in Hover

For this case alone, the cable deflections are defined with respect to a vertical reference axis. The system is trimmed to various values of cable force up to 4000 lb, and the frequency response characteristics are compared at hover. The cable angle is θ=90°, and the attachment point is coincident with the helicopter CG.

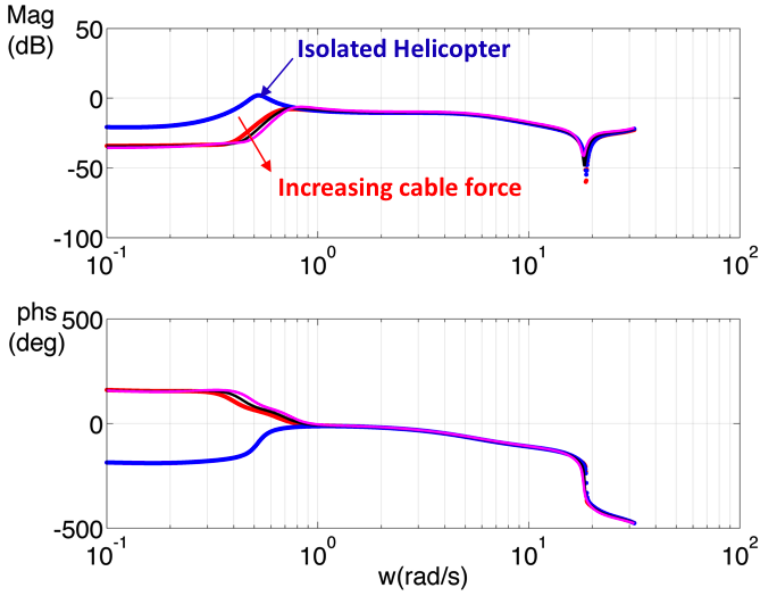

Figure 6.2: Helicopter Roll Rate Response to Lateral Stick

Figure 6.2 shows the on-axis roll response for the isolated helicopter and the tethered systems for increasing trim cable force. Above 1 rad/s, the frequency responses are identical except in the vicinity of the notch at 20 rad/s corresponding to lag-roll air resonance. This notch is sensitive to the nonlinearities in the lag

damper force characteristics. Both the roll and pitch response (Fig. 6.3) show reductions in the low-frequency magnitude compared to the isolated helicopter case, while the yaw rate response is unaffected as shown in Fig. 6.4.

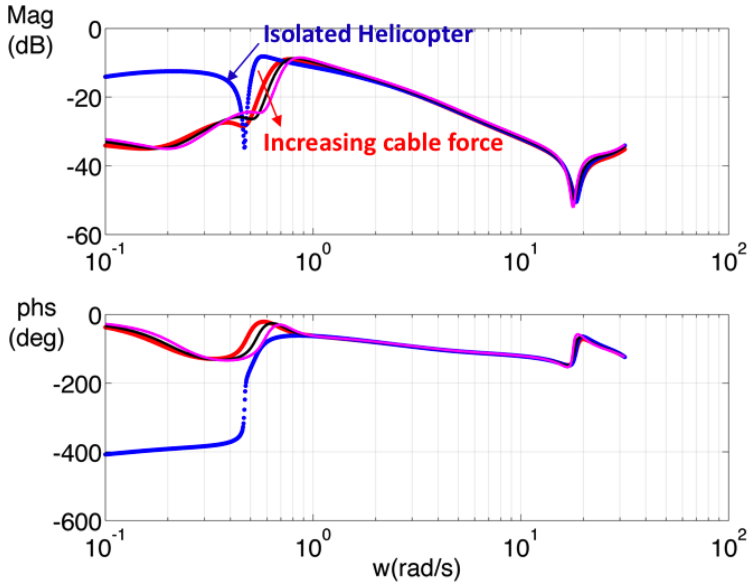

Figure 6.3: Helicopter Pitch Rate Response to Longitudinal Stick

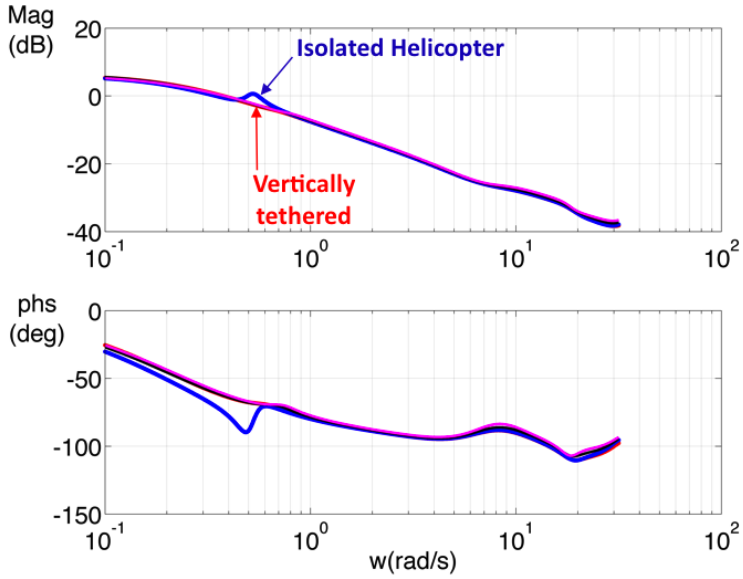

Figure 6.4: Helicopter Yaw Rate Response to Pedal

The vertical offset of the rotor hub above the helicopter center of gravity provides a stabilizing effect to the attitudes. When the aircraft rolls or pitches, this

offset acts as a moment arm for the rotor thrust which aligns with the line of action of the cable force, and stabilizes the helicopter. Dynamics above 1 rad/s do not show effects of this stabilization since the aircraft does not translate significantly for inputs at this frequency. Since the cable connection is a spherical bearing, the yaw dynamics are largely unaffected by vertical tethers for the helicopter.

6.4 Horizontal Tether

Cable deflections are defined with respect to the earth-fixed axes. The system is trimmed to various values of cable force up to 4000 lb, and the frequency response characteristics are compared at hover. The cable angle is θ=0°, and the attachment point is coincident with the helicopter CG. Since the excess force is in the horizontal direction perpendicular to gravity, the total rotor thrust is less than the sum of the two forces and so increases in power with increasing cable force are minimal compared to the vertical tether case.

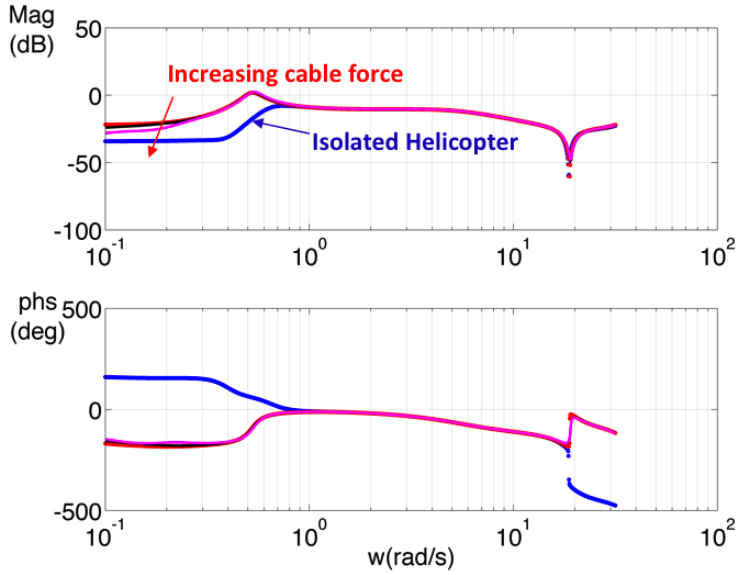

Figure 6.5: Helicopter Roll Rate Response to Lateral Stick

Figures 6.5 and 6.6 show the helicopter on-axis roll response for increasing trim cable force up to 4000 lb. Compared to the isolated helicopter, the frequency response is unaffected above 1 rad/s, while the low-frequency magnitude is larger. In the horizontally tethered configuration, the cable force and rotor forward thrust create a couple that increase the aircraft response magnitude in pitch, since the cable under tension acts as a restraint for translations. The yaw dynamics are unaffected as in the previous case, since the helicopter is free to rotate about its vertical axis, and are not shown.

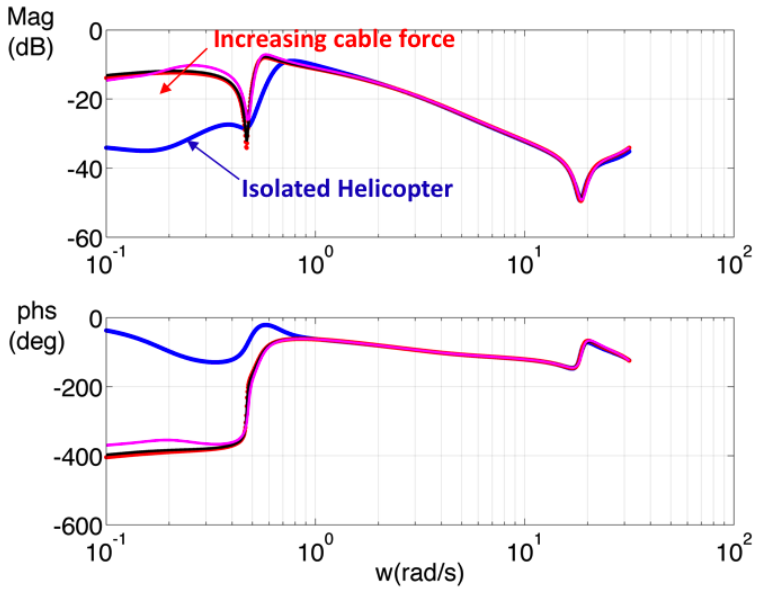

Figure 6.6: Helicopter Pitch Rate Response to Longitudinal Stick

Vertical tethers reduce the aircraft pitch and roll rate response magnitudes at low frequency, while horizontal tethers increase these response magnitudes at the same frequencies in comparison to an isolated helicopter. The effect of cable angle will be examined next to see the effect of an angled tether.

6.4.1 Effect of Tether Angle

The system is trimmed to various values of cable force up to 4000 lb and various cable angles, and the frequency response characteristics are compared at 25 knots. The attachment point is still coincident with the helicopter CG. The trim cable angle is set to 10° to determine the effect of a dominantly horizontal force and a small vertical component at hover.

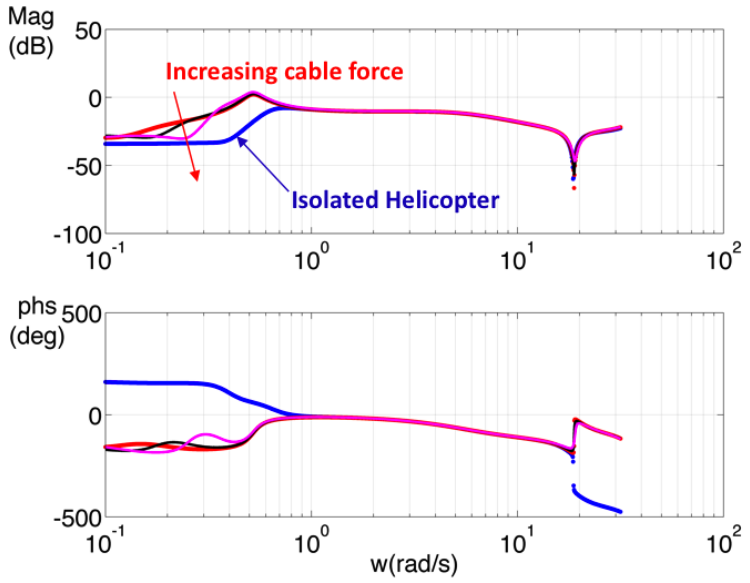

Figure 6.7: Helicopter Roll Rate Response to Lateral Stick

Figures 6.7 and 6.8 show the aircraft on-axis pitch and roll responses, respectively for a tether angle of 10° and increasing cable force up to 4000 lb. Due to the small cable inclination and dominantly horizontal force, the aircraft low-frequency response magnitudes are larger than the baseline helicopter, but these increases over the isolated helicopter response are perceptibly diminished compared to the horizontal tether. While roll response does not show as much sensitivity to the cable force at 0.1 rad/s, the effects of the vertical component of cable force on pitch are visible.

With increasing cable force, the reduction in aircraft pitch response is perceptible even for 10° of cable angle. Yaw dynamics remain unaffected, and are not shown.

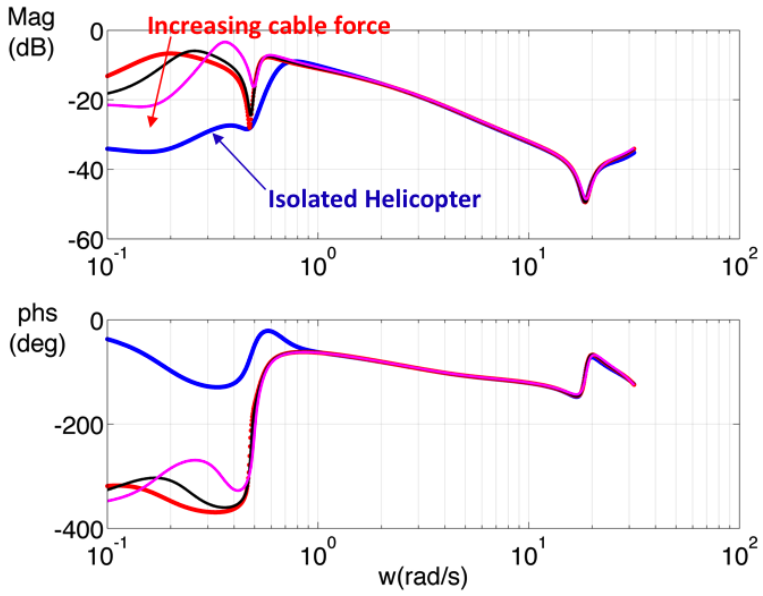

Figure 6.8: Helicopter Pitch Rate Response to Longitudinal Stick

Cable Angle of 30°

As the cable angle is increased to 30°, the vertical component of cable force increases and horizontal component decreases, resulting in the expected behavior of further reduction in magnitude of aircraft on-axis response. Figures 6.9 and 6.10 show the helicopter on-axis pitch and roll responses for a tether angle of 30° for increasing cable force. The increase in vertical component of the tether force results in further reductions of the aircraft response magnitude due to stabilization from the couple system set up by the rotor and the tether cable.

Cable Angle of 45°

Further increases in the cable angle to 45°, as shown in Figs. 6.11 and 6.12 causes the roll rate response magnitude to decrease to 5dB above the aircraft response and

remains insensitive to cable force. The pitch response magnitude decreases until it falls below the isolated helicopter value except for the largest cable force (4000 lb).

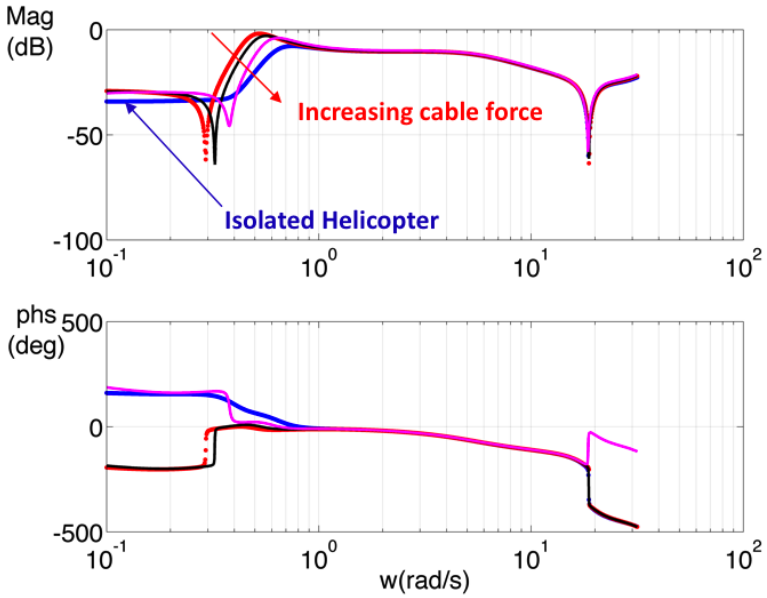

Figure 6.9: Helicopter Roll Rate Response to Lateral Stick

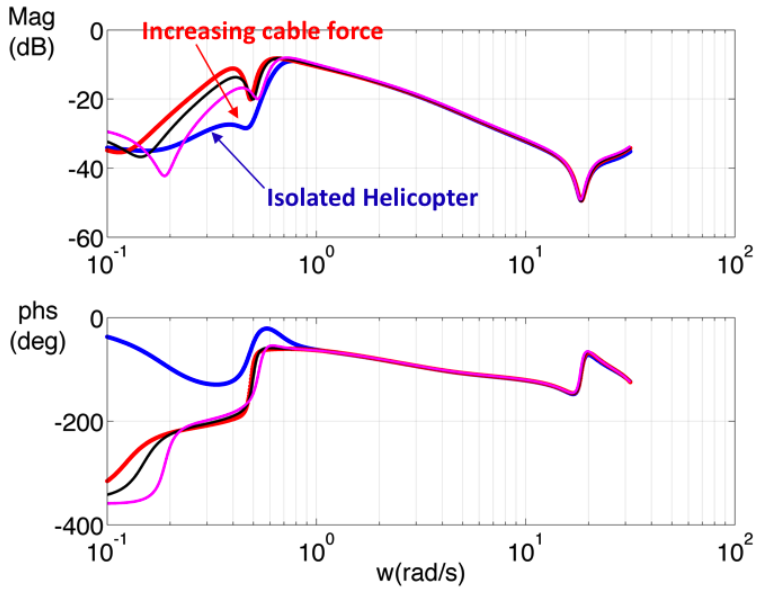

Figure 6.10: Helicopter Pitch Rate Response to Longitudinal Stick

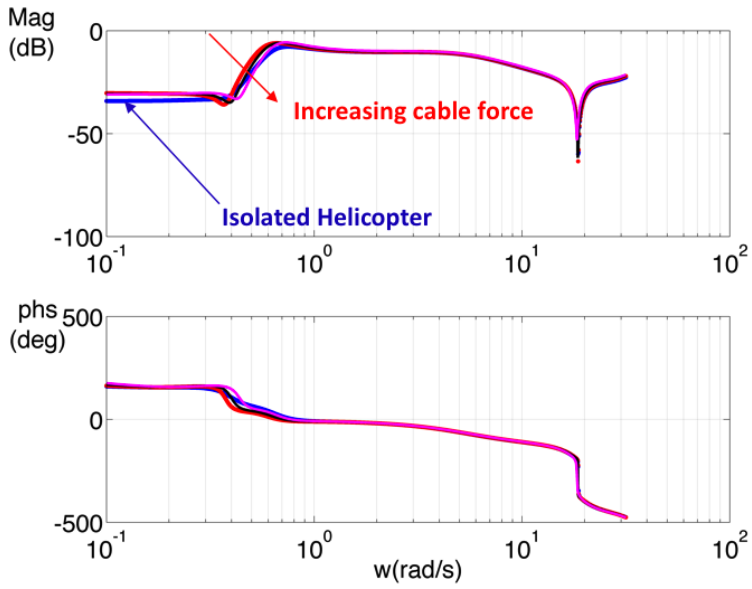

Figure 6.11: Helicopter Roll Rate Response to Lateral Stick

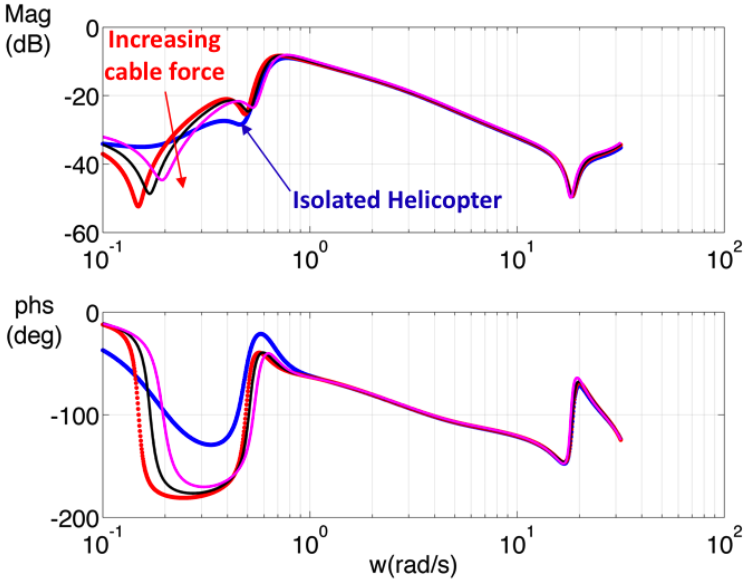

Figure 6.12: Helicopter Pitch Rate Response to Longitudinal Stick

6.4.2 Effect of Rotor Flight Condition

The results in the previous section were obtained for hovering flight conditions. During the tow mission, the helicopter operates in forward flight at 25 knots.

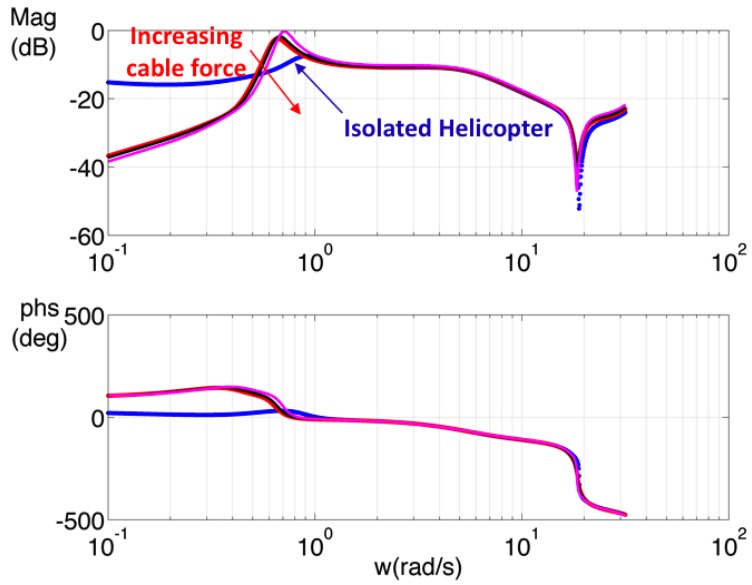

Figure 6.13: Helicopter Roll Rate Response to Lateral Stick

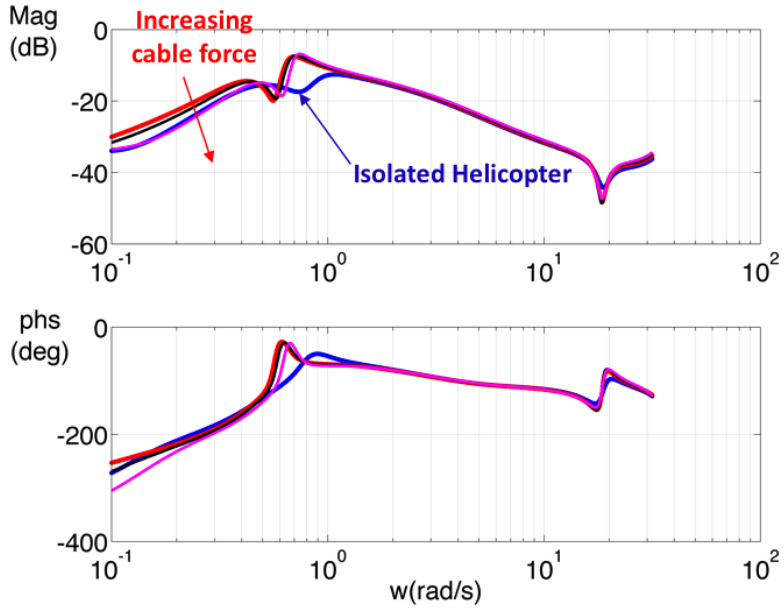

Figure 6.14: Helicopter Pitch Rate Response to Longitudinal Stick

To simulate forward flight, the on-axis responses of a tethered helicopter are studied with a 25-knot head wind at the previously investigated tether angle of 45°. Figure 6.13 shows the helicopter on-axis response with a 25-knot head wind, comparing an isolated helicopter to a tethered configuration. The magnitude of the

isolated helicopter response increases with speed, from -35dB to -16dB while the tow configuration response decreases slightly to -38dB. The combination of increase in magnitude for the isolated helicopter and marginal reduction for the towed body manifests as a relative decrease of the tow system response when going from hover to forward flight. The pitch on-axis response with a 25-knot head wind is shown in Figure 6.14. The low-frequency magnitudes remain unchanged with airspeed. However, the effects of cable force are reversed, and tether configurations with higher trim tensions suffer larger reductions in the low-frequency response magnitude. Figure 6.15 shows that the helicopter yaw on-axis response is insensitive to increasing cable force. In forward flight, pitch-yaw couplings manifest for the UH-60 through the tail rotor, and the dynamic couplings are evident through the local minima in the pitch and yaw on-axis responses between 0.5-0.6 rad/s.

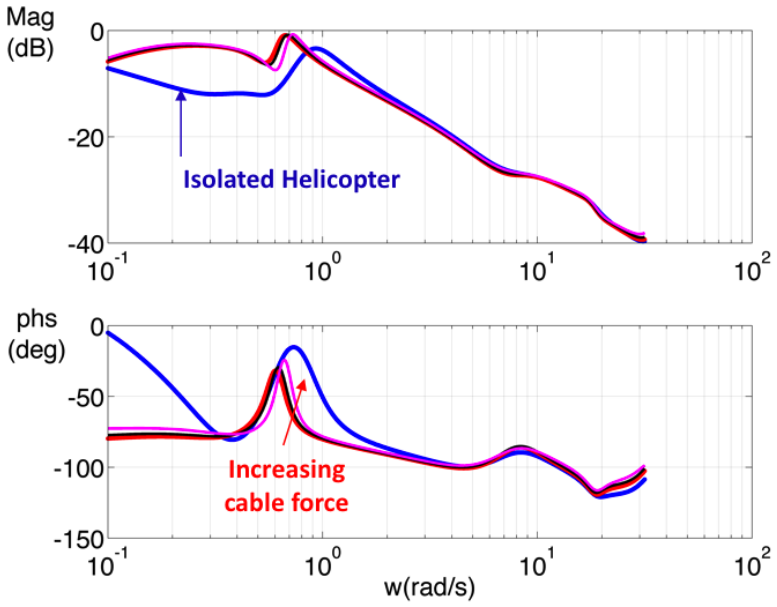

Figure 6.15: Helicopter Yaw Rate Response to Pedal

6.4.3 Effect of Hook Offset

The previous results were obtained assuming that the cable was attached to the helicopter CG. The effects of vertical downward translation of this attachment point are investigated in this section.

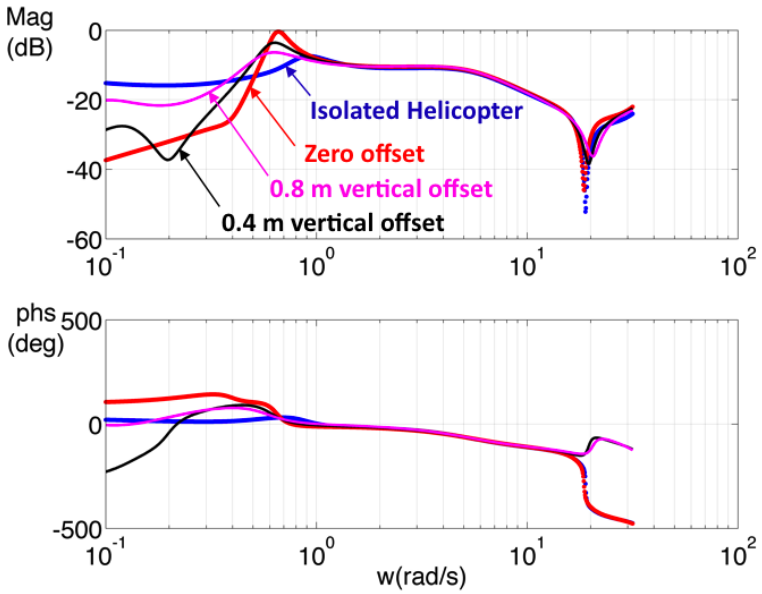

Figure 6.16: Helicopter Roll Rate Response to Lateral Stick

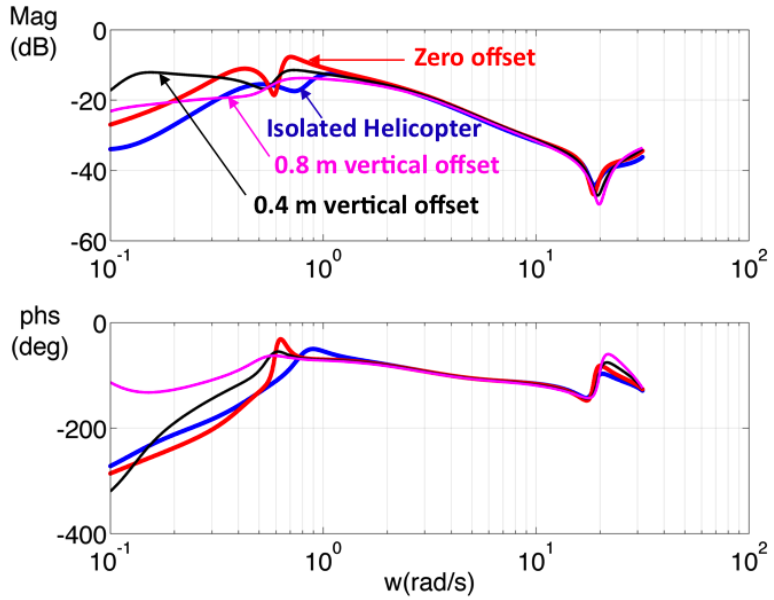

Figure 6.17: Helicopter Pitch Rate Response to Longitudinal Stick

Figure 6.16 shows the helicopter on-axis roll response for various vertical offsets of the tow point from the CG in a 25 knot head wind. For increasing vertical offset of the tow point, the magnitude of the roll response at low frequencies increases. The magnitude of the pitch on-axis response initially increases with hook vertical offset and then decreases as shown in Figure 6.17. This trend reversal is due to conflicting contributions from the vertical and horizontal components of cable force, which reduce and increase, respectively, the on-axis pitch response magnitude.

6.4.4 Effect of Cable Flexibility

All previous linearized analyses were performed using modal reduction with 2 cable modes. The final perturbation performed for the tethered helicopter configuration is the introduction of cable flexibility.

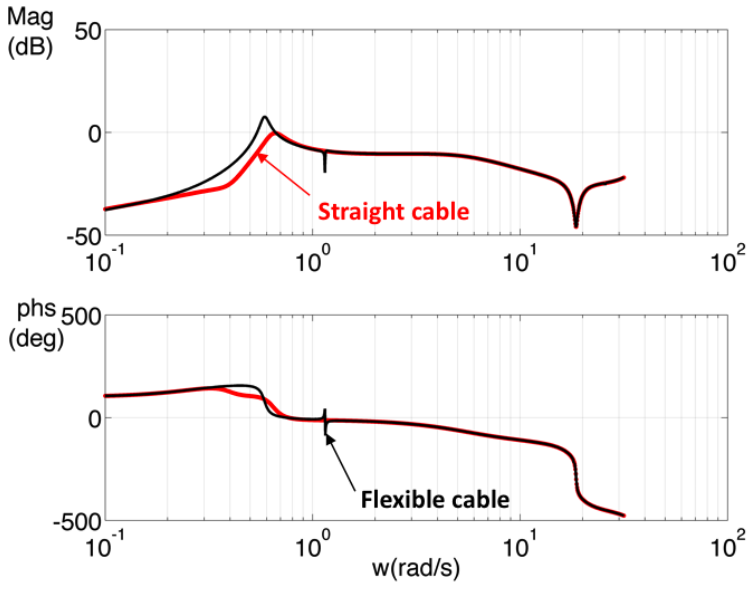

Figure 6.18: Helicopter Roll Rate Response to Lateral Stick

Figure 6.18 shows the comparison of helicopter roll on-axis response for inelastic and flexible cables. A single cable frequency couples with the helicopter roll

mode at 1.2 rad/s and changes the peak of the magnitude response from 0dB at 0.6 rad/s to 8 dB at 0.5 rad/s, but otherwise does not affect the helicopter response. The helicopter on-axis pitch response exhibits multiple resonance points as shown in Fig. 6.19.

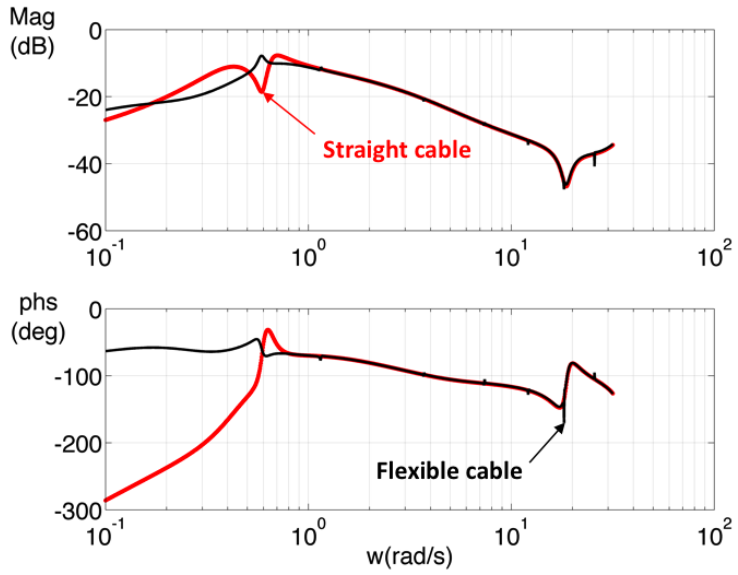

Figure 6.19: Helicopter Pitch Rate Response to Longitudinal Stick

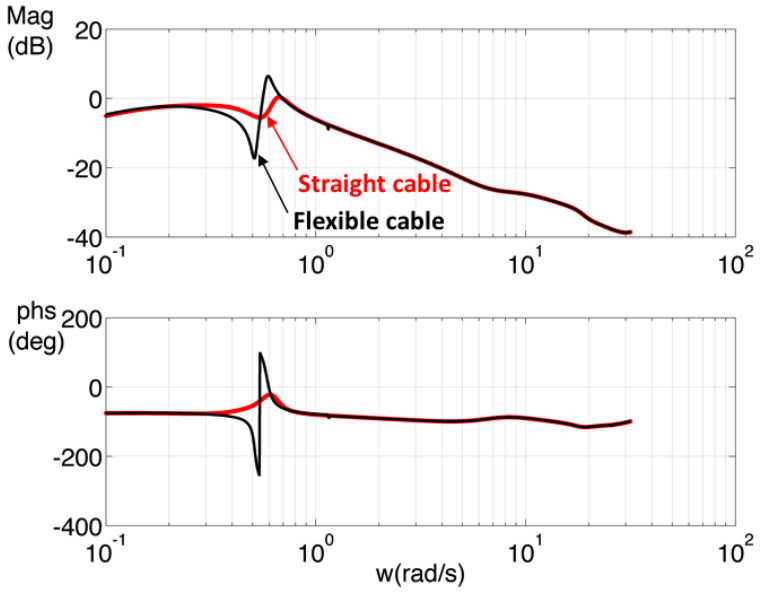

Figure 6.20: Helicopter Yaw Rate Response to Pedal

The on-axis yaw response exhibits a single cable resonance point at 1.2 rad/s,

identical to the roll response. The reduction in magnitude at these cable resonance frequencies may interfere with flight control systems when towing hydroplaning sleds.

6.4.5 Comparison between Tethered and Tow Systems

The tethered helicopter system is trimmed to a cable force of 2000 lb at 45° to the horizontal, to mimic the cable shape under tow when ignoring cable drag at 25 knots. The helicopter on-axis roll response is shown in Fig. 6.21 for the isolated helicopter, tethered system and tow system. The primary difference between the tethered helicopter and tow configuration is the introduction of a free boundary condition (i.e. submerged load) with hydrodynamic loads. The additional drag on the towed body results in lowered response magnitude at low frequencies compared to the isolated helicopter, similar to the response of the tethered helicopter.

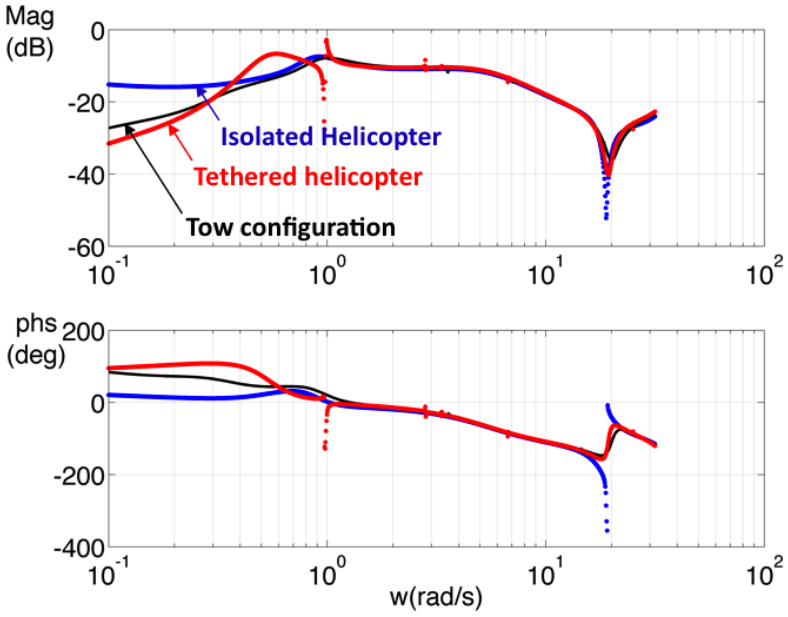

Figure 6.21: Helicopter Roll Rate Response to Lateral Stick

In the presence of hydrodynamic damping on the towed body, the sharp resonance peaks corresponding to cable vibration disappear, and are replaced by less pronounced notches corresponding to cable vibration dipoles. The number of cable resonance frequencies in the on-axis roll response reduces from five points at 1, 2.8, 3.1, 6.8 and 25 rad/s, to a single point at 3.6 rad/s.

An examination of the on-axis pitch response in Fig. 6.22 reveals that the multiple resonance points at 1,2.8, 6.8, 10.2, 10.8 and 25 rad/s for the tethered helicopter case disappear in the presence of towed body drag, with cable drag set to zero. In the absence of cable drag, the on-axis pitch and yaw responses of the helicopter tow platform at 25 knots are similar to the corresponding values for the isolated helicopter case, as shown in Fig. 6.23. The yaw response for the tethered helicopter exhibits four resonance points at 1, 2.8, 6.8 and 25 rad/s at 25 knots, which are attenuated by hydrodynamic damping from towed body drag.

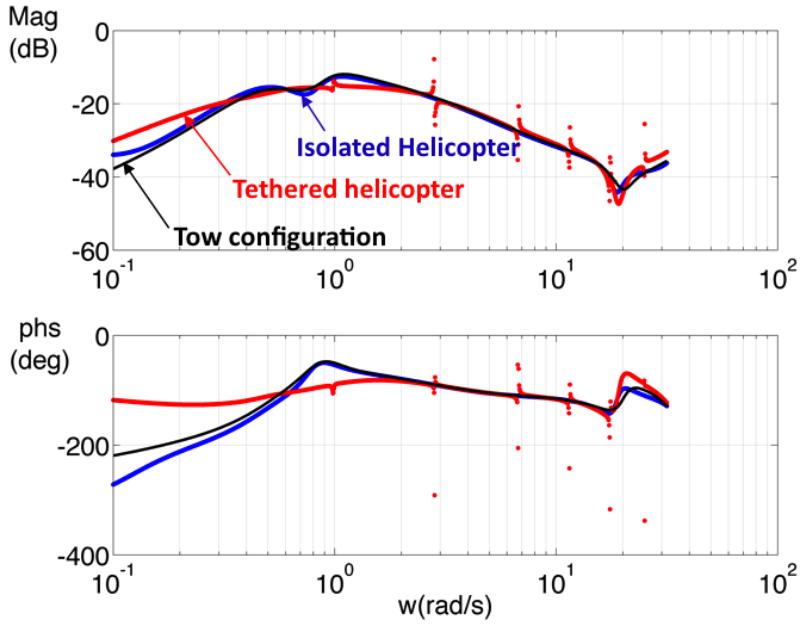

Figure 6.22: Helicopter Pitch Rate Response to Longitudinal Stick

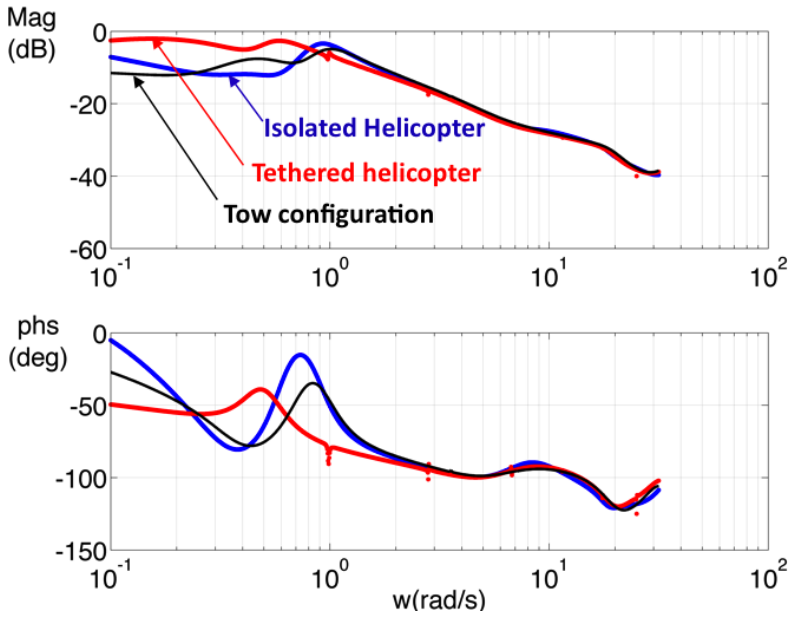

Figure 6.23: Helicopter Yaw Rate Response to Pedal

6.5 Effect of Cable Drag

Cable hydrodynamics provides damping to the purely oscillatory cable modes that lie on the imaginary axis. The high density of water results in an overdamped system for cable vibrations, and the dipole signature in the helicopter on-axis roll response disappears, as shown in Fig. 6.24. The isolated helicopter response is also shown as a reference. Cable drag also decreases the magnitude of the helicopter roll response further in comparison to the case with only towed body drag, but does not affect the frequency response above 1 rad/s.

Figure 6.25 shows the effect of cable drag on the helicopter on-axis pitch response. Cable drag has a similar effect, and damps out cable oscillations (shown as notches in the magnitude plot). The low-frequency magnitude of the pitch response is reduced by 10dB in the presence of cable drag. The effects of cable drag

on the yaw response are minimal, as shown in Fig. 6.26. In the presence of cable drag, cable structural properties have no effect on the helicopter pitch, roll or yaw responses since hydrodynamic drag results in an overdamped system and does not allow steady-state oscillations to develop.

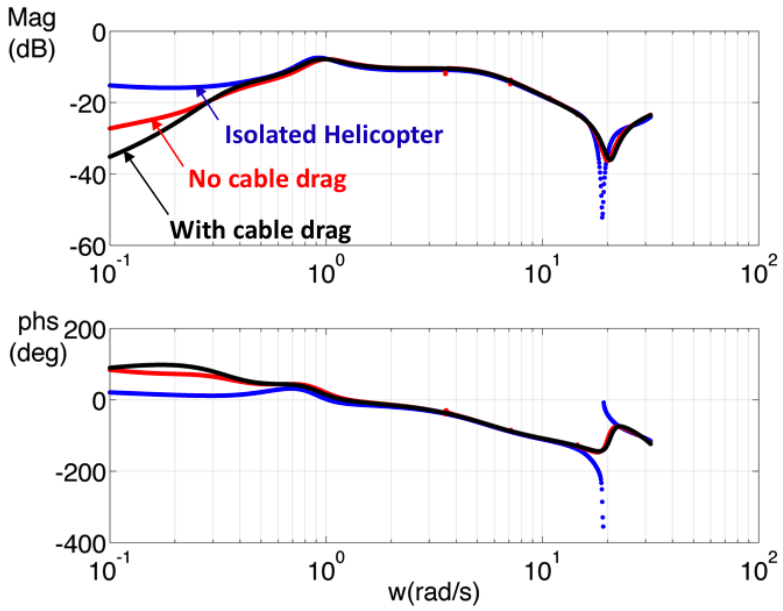

Figure 6.24: Helicopter Roll Rate Response to Lateral Stick

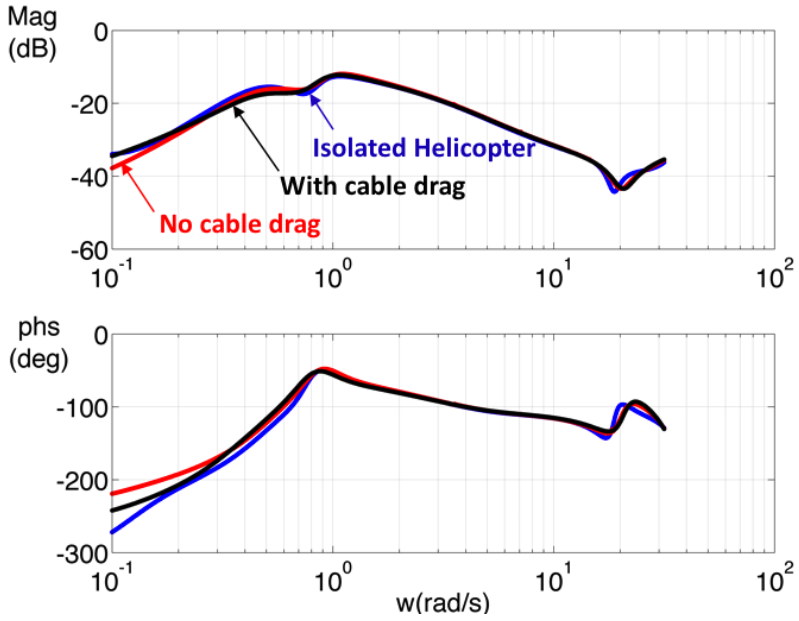

Figure 6.25: Helicopter Pitch Rate Response to Longitudinal Stick

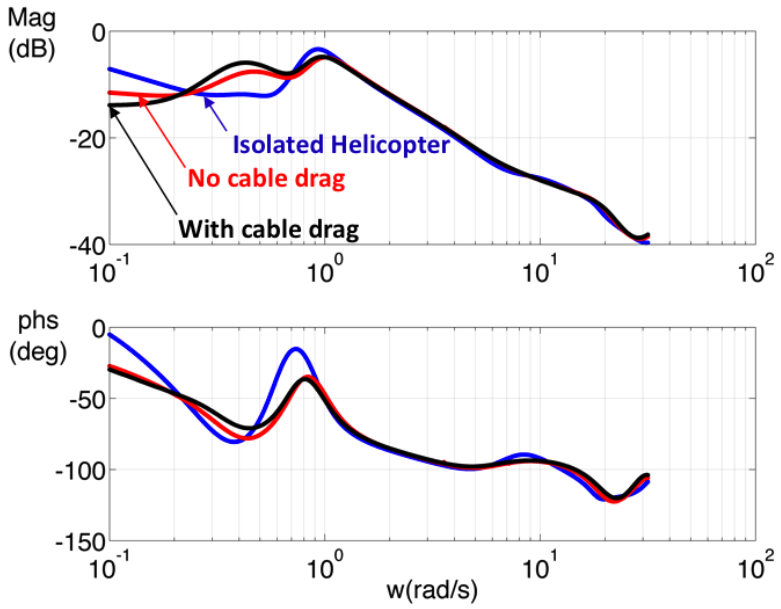

Figure 6.26: Helicopter Yaw Rate Response to Pedal

Predictions of helicopter Handling Qualities are based on characteristics of the vehicle frequency response to pilot stick inputs. The effect of a sling load (carried in air) is characteristic of a dipole - a reduction in the response magnitude and a sharp reduction/recovery in the phase close to the load pendulum frequency. However, the enormous damping afforded by water eliminates the dipole signature. The low-frequency response magnitude reduces as a result of hook vertical offset below the helicopter CG stabilizing the helicopter roll and pitch attitudes. In the absence of cable drag, a dipole signature is present close to the natural frequency of the cable under tension (3.5 rad/s). Therefore, bandwidth deformation parameters developed for sling load operations are not applicable for the tow system.

Table 6.2: Tow System Eigenvalues at 25 knots

Mode #	Real part (rad/s)	Imaginary part (rad/s)	Mode #	Real part (rad/s)	Imaginary part (rad/s)
1	0	0	2	0	0
3	0	0	4	0	0
5	-12.83	46.55	6	-131.33	0
7	-7.61	36.21	8	-36.8	0
9	-31.5	8.48	10	-5.63	20
11	-12.1	19.9	12	-15.1	22.28
13	-17.2	0	14	-16.48	0
15	-1.19	15.2	16	-1.66	14.83
17	-1.59	10.59	19	-1.79	10.31
18	-7.44	4.16	20	-3.02	7.12
21	-3.24	5.54	22	-3.58	5.15
23	-3.39	4.26	24	-0.53	5
25	-1.31	4.38	26	-6.6	4.49
27	-4.31	0.00	28	-2.85	0
29	-1.33	1.50	30	-1.77	0.00
31	-0.25	0.87	32	0.27	0.37
33	-0.18	0.31	34	-0.32	0
35	-0.27	0	36	-0.12	0

7 The Tear-Drop Maneuver

This chapter discusses unsteady time-marching simulations of the tow system. The objective is to obtain the helicopter swashplate inputs required to guide the submerged load along a prescribed trajectory, shaped like a tear-drop as shown in Fig. 7.1. Knowledge of the tow system dynamics is used to subdivide the trajectory tracking problem for the *towed body* into two stages. In the first stage, the tow point trajectory that guides the submerged load along the target path is determined using an optimization process. In the second stage, a feedback control system is used to determine the swashplate and tail rotor pitch angles that guide the helicopter along the *target tow point trajectory*. The trajectory of the cable and towed body depend on the motions of the tow point only, and are independent of the nature of the tow system. If another tow platform is to be analyzed for the same maneuver, the results from the first stage (i.e. motions of the tow point) would be identical, and only the second stage needs to be analyzed for the new vehicle.

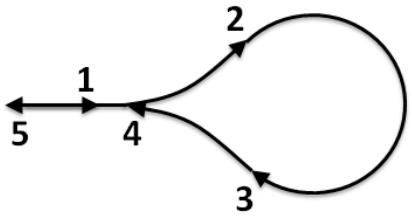

Figure 7.1: Schematic of a Tear-Drop Trajectory

7.1 Mathematical Representation of the Tear-Drop Trajectory

A "tear-drop" trajectory is a typical maneuver executed with a helicopter-based tow system. The objective is to guide the towed body along the tear-drop shaped path shown in Fig. 7.1. The path can be broken down into the following turn sequences, with steady forward flight represented as a special case with zero heading change.

- Approach point 1 at steady level flight
- Heading change -$\Delta\psi$ from 1-2 (nose-left)
- Heading change $180° + 2\Delta\psi$ from 2-3 (nose-right)
- Heading change -$\Delta\psi$ from 3-4 (nose-left)
- Approach point 5 at steady level flight

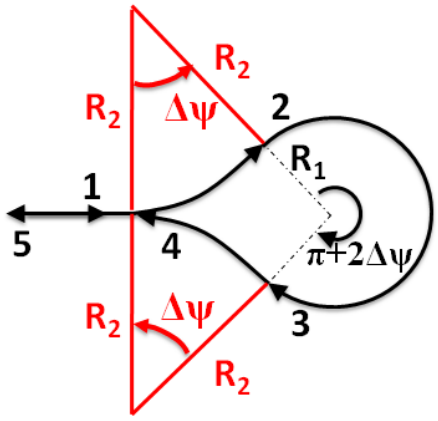

Figure 7.2: Tear-Drop Sequences as Idealized Circular Arcs

The tear-drop trajectory is idealized as arcs of two circles of different radii, as shown in Figure 7.2.

7.1.1 Turn Sequence Characterization

During tow procedures, the tow point motions are assumed to be contained in a horizontal plane parallel to the water surface, to allow the helicopter to remain at constant altitude. Any reductions in altitude may compromise safety of flight by encroaching further into the "avoid" regions of the height-velocity curve. Tow missions are executed on the boundaries of these avoid regions, where the combination of low altitudes and reduced forward speeds precludes the possibility of safe autorotation in case of single engine failures. Increasing helicopter altitude will reduce the towed body depth, necessitating fin down-force which results in increased rotor thrust requirements, elevated fuel consumption and reduced stall margins.

The altitude of the helicopter tow point is constrained from changing by safety requirements on the lower side, and by efficiency of flight/rotor stall margins on the higher side.

While multiple helicopter control input time histories may exist that each achieve near-identical tear-drop trajectories, special focus is given in the present work to the class of solutions that require the minimum necessary adjustments to the controls as the helicopter transitions from one flight condition to another. Since control input changes are unavoidable during transitions between turn sequences, the problem then reduces to holding the controls nominally fixed for as long as possible during a sequence (turn). Therefore, each sequence is further subdivided into three sections as follows

- Maintain constant airspeed while increase turn rate smoothly

- Maintain steady turn and increase airspeed, if required
- Maintain new airspeed and reduce turn rate smoothly

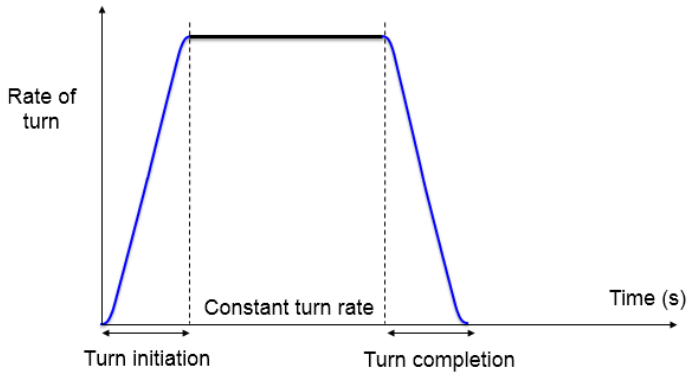

Figure 7.3: Variation of Turn Rate during a Sequence

Specifically, the build-up and reduction of turn rate are constructed using cubic splines to ensure C_0 and C_1 continuity as shown in Fig. 7.3, necessary for consistent ODE solutions. During the second section of a turn sequence, it may be necessary to increase (or decrease) the helicopter speed in a turn. As seen in Chapter 5, hydrodynamic drag on the towed body and cable cause the submerged load to trim with a smaller turn radius (and hence lower translation speed) than the tow point (helicopter). To compensate for this speed reduction, the helicopter may be required to fly faster to maintain the same turn radius for the towed body. Since the translational acceleration need not be differentiable but only continuous, a linear variation of airspeed is assumed during the second section of each turn sequence, as shown in Fig. 7.4.

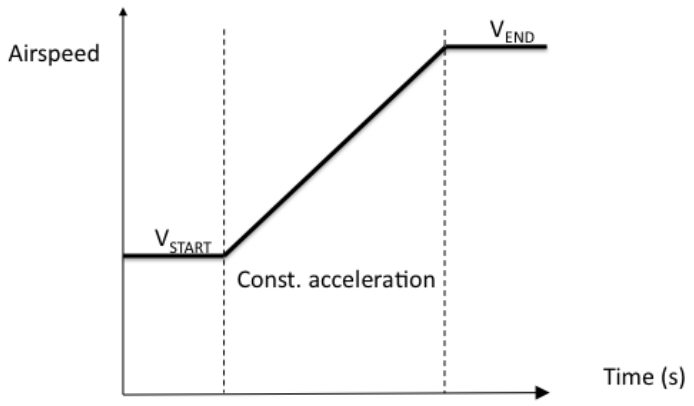

Figure 7.4: Variation of Airspeed during a Sequence

The following parameters are used to precisely define the variation of airspeed and turn rate during each sequence :

- Allotted Time T_i - the total duration of each sequence, measured in seconds. This is equal to the duration of the corresponding sequence in the target trajectory.

- Time fraction f_i - a non-dimensional measure of the time spent in a sequence for entering and exiting a turn. If the value of f_i is 0.3, it implies that 30% (100 f_i) of the time interval T_i seconds in sequence $\#i$ is spent attaining a steady rate of turn, 40% (100 - 200f_i) of the sequence is spent holding a constant turn rate and the last 30% (100 f_i) is spent to transition back to steady forward flight. The maximum allowable value of f_i is 0.5, and the minimum value is set to 0.1, based on the physical turn acceleration limits of the helicopter. Since the turn rate is not constant throughout the sequence, the steady-state turn rate is compensated to account for the spline ramps during first and third sections. A larger time fraction f_i implies a slower transition to steady-state

turns and smaller turn accelerations, but a higher peak turn rate that may influence the turn radius of the submerged load.

- Heading change $\Delta\psi_i$ - the total heading change during the sequence measured in degrees. It is defined positive for nose-right turns and negative for nose-left turns. The heading change of the helicopter (tow point) and the towed body need not be necessarily equal, and so this parameter needs to be identified.

- Velocity change ΔV_i - the total airspeed change during a sequence, measured in knots. It is positive for airspeed increases and negative for speed decreases. The speed change occurs during the second section of a turn sequence, when the turn rate is held steady between f_i T_i and (1-f_i) T_i. This is the second parameter that needs to be identified.

The methodology used to determine the parameters ΔV_i and $\Delta\psi_i$ is described in the following section.

7.1.2 Stage I : Definition of Optimization Problem

The tow point motions in each turn sequence are parameterized using two quantities : the heading change within a sequence $\Delta\psi_i$, and the airspeed change ΔV_i. The turn sequence parameters that determine the motions of the tow point

$$\mathbf{X} \quad \stackrel{\text{def}}{=} \quad (\Delta\psi_1, \Delta V_1, \quad \Delta\psi_2, \Delta V_2, \quad \cdots \quad \Delta\psi_N, \Delta V_N) \tag{7.1}$$

are determined using an optimization process. Here N is the number of sequences. An optimization problem is formally defined as follows:

$$\text{Find } \mathbf{X} \text{ such that } \mathrm{F}(\mathbf{X}) \rightarrow \min \tag{7.2}$$

$$\text{subject to : } \mathbf{F}_C(\mathbf{X}) \leq \mathbf{0} \tag{7.3}$$

$\mathbf{X}$ is the vector of design variables defined in Eq. (7.1). $\mathbf{F}_C(\mathbf{X})$ represents a set of constraints specific to the design problem. Each design variable is constrained with both lower and upper bounds. The upper bounds on the heading change in sequence i, i.e. $\Delta\psi_i$ are given by

$$\mathbf{F}_{\mathrm{C}}^{\mathrm{heading,U}}(i) = \begin{cases} \Delta\psi_i - \Delta\psi_i^{\mathrm{target}} - \Delta\psi_{\mathrm{tol}} & : \Delta\psi_i^{\mathrm{target}} > 0 \\ \Delta\psi_i & : \Delta\psi_i^{\mathrm{target}} < 0 \\ \Delta\psi_i - \Delta\psi_{\mathrm{tol}} & : \Delta\psi_i^{\mathrm{target}} = 0 \end{cases} \tag{7.4}$$

The corresponding lower bounds on $\Delta\psi_i$ are

$$\mathbf{F}_{\mathrm{C}}^{\mathrm{heading,L}}(i) = \begin{cases} -\Delta\psi_i & : \Delta\psi_i^{\mathrm{target}} > 0 \\ \Delta\psi_i^{\mathrm{target}} - \Delta\psi_{\mathrm{tol}} - \Delta\psi_i & : \Delta\psi_i^{\mathrm{target}} < 0 \\ -\Delta\psi_{\mathrm{tol}} - \Delta\psi_i & : \Delta\psi_i^{\mathrm{target}} = 0 \end{cases} \tag{7.5}$$

Here, $\Delta\psi_i^{\mathrm{target}}$ represents the heading change targets used to generate the desired towed body trajectory, and $\Delta\psi_{\mathrm{tol}}$ is a tolerance band that allows the tow point to deviate from the target path for the submerged load. The value of $\Delta\psi_{\mathrm{tol}}$ used is 25° for the first left turn sequence, and 45° for the other turn sequences. The upper and lower bounds for the speed change in sequence i, i.e. ΔV_i dictate that the speed change during a sequence be no more or less than two knots, and are given by

$$\mathbf{F}_{\mathrm{C}}^{\mathrm{speed,U}}(i) = \Delta V_i - 2 \tag{7.6}$$

$$\mathbf{F}_{\mathrm{C}}^{\mathrm{speed,L}}(i) \quad = -\Delta V_i - 2 \tag{7.7}$$

The constraints are used to guide the analysis to physically meaningful solutions. F($\mathbf{X}$) is the objective function to be minimized, defined as follows:

$$F(\mathbf{X}) \quad = \quad \sum_{i=1}^{N_p} d_i \tag{7.8}$$

N_p is the number of points used to discretize the target and candidate trajectories. The i^{th} distance function d_i between the candidate trajectory and the target trajectory is defined as

$$d_i \quad = \quad \min\, d_n(i,j), \qquad j = i - \Delta i, i - \Delta i + 1, \cdots, i + \Delta i - 1, i + \Delta i \tag{7.9}$$

Where $d_n(i,j)$ is normal distance from the i^{th} point on the candidate trajectory to the straight line joining points (j, $j+1$) on the target trajectory. Δi is an integer parameter (5 in this case) that allows the candidate trajectory to be flown slightly slower or faster in segments, and relaxes the criterion that that points on the candidate and target trajectories match at every instant in time. A schematic for Δi=2 is shown in Fig. 7.5.

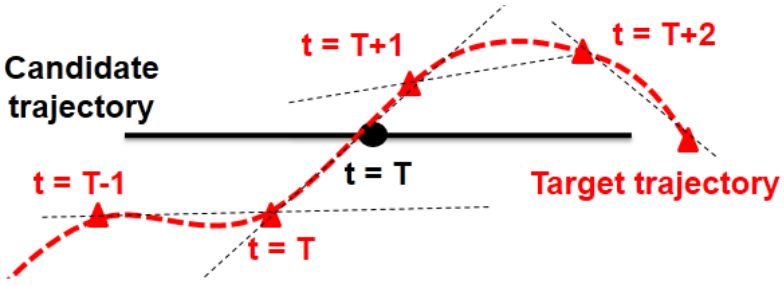

Figure 7.5: Computation of Distance Function

In summary,

- **Heading and velocity changes that describe the tow point motions during each turn sequence are selected as the design variables. A time marching simulation is performed with these prescribed tow point motions, and the resulting towed body trajectory is obtained**.

- **The objective function is the aggregate normal distance between the candidate and target trajectories, relaxed to allow slower or faster completion of individual segments.**

- **Inequality constraints are imposed to limit the allowable heading and velocity changes within a turn sequence to $\pm$ 30° and $\pm$ 2 knots respectively, centered on the corresponding parameters that define the target trajectory**.

7.1.3 Approximate Optimization using Response Surfaces

Trajectory optimization problems suffer from multiple local minima (Ref. [107]), which restrict the applicability of gradient-based optimizers that converge to different local minima depending on the initial design. To circumvent these difficulties, the approach of Ref. [108], (used in Ref. [109]) is adapted for the present problem. The key idea is to avoid optimizing the "true" objective function (Eq. 7.8) which is computationally expensive to simulate. Instead, optimizations are performed on *an approximate response surface*, constructed by sampling the *true objective function* at a few points, and continuously refined as the optimization proceeds. The sequence of operations is as follows:

1. **Sample the true objective function over the design space** : this is the initialization step of the optimization process. An equispaced grid with three points along each design variable coordinate is generated. At each of these points, the true objective function is evaluated. This step is performed once, and when completed, the number of precise function evaluations N_F is equal to N_{DV}^4. This step allows for construction of a global approximation of the true objective function (response surface) prior to optimization.

2. **Construct approximate response surface based on available precise function evaluations** : this is the first step in the convergence process used for approximate optimizations. The response surface $F_{app}(\mathbf{X})$ is constructed using multi-quadric radial basis functions as follows

$$F_{app}(\mathbf{X}) \quad = \quad \sum_{i=1}^{N_F} \lambda_i \phi(||\mathbf{X} - \mathbf{X}_{p,i}||) + p(\mathbf{X}) \tag{7.10}$$

N_F is the number of precise function evaluations at designs ($\mathbf{X}_{p,i}$, $i = 1, 2, \cdots N_F$) that are used to construct the approximate response surface. p($\mathbf{X}$) are lower-order polynomial functions (here linear) that improve the representation of the approximate objective function. The basis function ϕ is given by

$$\phi(r, \gamma) \quad = \quad \sqrt{r^2 + \gamma^2} \tag{7.11}$$

γ is a predefined constant (here unity), and r is the N_{DV}-dimensional distance metric between the trial design $\mathbf{X}$ and the design $\mathbf{X}_{p,i}$ at which precise values of the objective function are available, given by

$$r \quad = \quad ||\mathbf{X} - \mathbf{X}_{p,i}|| \quad = \quad \sum_{j=1}^{N_{\text{DV}}} (\mathbf{X}(j) - \mathbf{X}_{p,i}(j))^2 \tag{7.12}$$

$\mathbf{X}(j)$, $\mathbf{X}_{p,i}(j)$ represent the j^{th} entries in the vectors of design variables $\mathbf{X}$, $\mathbf{X}_{p,i}$ respectively. The coefficients λ_i are obtained by equating the values of the approximate objective function $\mathrm{F}_{app}(\mathbf{X})$ to their precise values $\mathrm{F}(\mathbf{X})$ at designs $\mathbf{X}_{p,i}$, effectively inverting a set of linear equations

$$F_{app}(\mathbf{X}_{p,i}) \quad = \quad F(\mathbf{X}_{p,i}) \tag{7.13}$$

3. **Perform optimization on most recent response surface and determine approximate minimum** : genetic algorithms offer distinct advantages over gradient-based optimizers, such as the ability to identify global minima even in the presence of multiple local minima, and are an excellent choice for the present problem. Using MATLAB's global optimization toolbox, an initial population of 1000 designs is evaluated and propagated for 128 generations. Characteristic crossover and mutation are also implemented. The crossover feature selects "genes" at random from the preceding generation of designs ("parents") and combines them to create "children". "Mutations" are introduced by adding pseudo-random numbers extracted from a Gaussian distribution to the "genes". An elite count of 2 is used to ensure that the algorithm propagates the "best" 2 designs forward with each generation. Finally, the best design $\mathbf{X}_{\min}$ that represents the minimum of the approximate objective function is obtained.

4. **Obtain precise function evaluation at approximation minimum obtained in previous step** : this step is similar to the first, and consists of the following sequence of operations

- Generate the trajectory of the tow point from the design variables
- Numerically integrate the equations of motion governing the cable and towed body dynamics forward for the duration of the maneuver to obtain the candidate trajectory of the submerged load
- Use the candidate trajectory to obtain the precise value of the objective function given in Eq. (7.8)

5. **Compare optimum of the approximate response surface between iterations** : when the distance between $\mathbf{X}_{\min}$ falls below a threshold δ_{opt} and the design space has been sufficiently sampled (i.e. empty regions of the design space have been sampled a minimum number of times), the optimization process is terminated. If not, steps 2-6 are repeated until convergence.

7.1.4 Adaptation for Tear-Drop Maneuvers

The computational cost of evaluating the response surface using radial basis functions scales as N_F^2, where N_F is the number of data points at which the precise value of the objective function is available. With an increasing number of design variables, the number of these data points required for an accurate representation increases, and the computational cost of the optimization algorithm approaches that of the objective function. As the optimization proceeds, the number of available data points increases and *the cost escalates as the response surface improves in accuracy.* Further, the parameters corresponding to later turn sequences do not affect the trajectory *until that sequence is initiated.* For this reason, it is valid (and

computationally efficient) to restrict the optimization process to two sequences at a time, as shown in Fig. 7.6. In the first stage, the design variables are assigned to the heading and velocity changes corresponding to the first two sequences, i.e.

$$\mathbf{X}_1 \quad = \quad (\Delta\psi_1, \Delta V_1, \Delta\psi_2, \Delta V_2) \tag{7.14}$$

The optimization problem is solved numerically until an optimal solution for the hook motion parameters corresponding to the first two sequences are obtained. The parameters for the first sequence are frozen at their optimal values, and the second stage is initiated. In the second stage, the design variables are assigned to the heading and velocity changes for the second and third sequence, i.e.

$$\mathbf{X}_2 \quad = \quad (\Delta\psi_2, \Delta V_2, \Delta\psi_3, \Delta V_3) \tag{7.15}$$

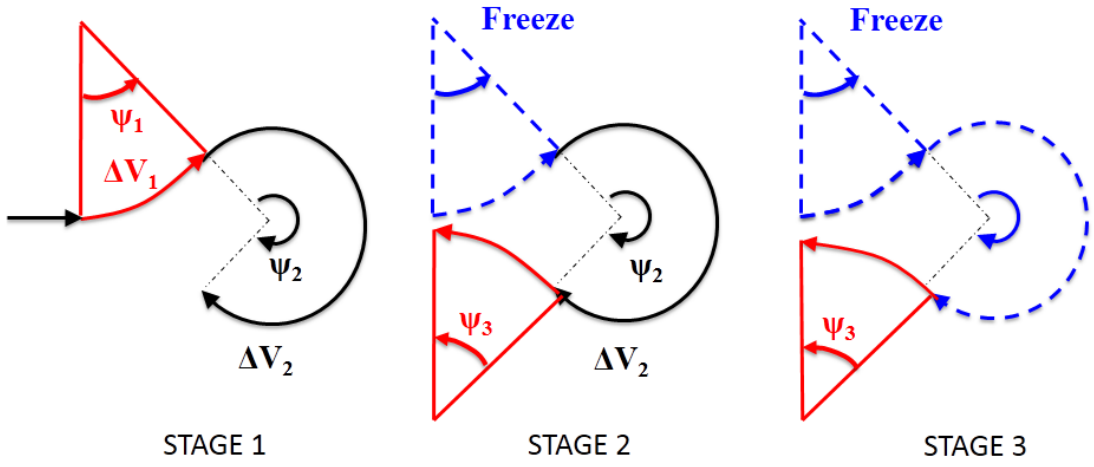

Figure 7.6: Trajectory Optimization Stages

This "leap-frogging" process is repeated as many times as necessary, optimizing the trajectory over two turn sequences after freezing the preceding sequence until the maneuver is complete. Thus, the effect of a turn sequence on the trajectory over the succeeding sequence is taken into account during the optimization process

without elevating computational costs to impractical levels.

7.1.5 Results : Trajectory Optimization

Two different optimization techniques were evaluated using the RBF-based response surfaces. The first method uses a gradient-based optimizer that yields valid solutions and requires the least computational effort, but is extremely sensitive to both the initial condition and the constraints. The second method utilizes a genetic algorithm, and is computationally expensive but is relatively immune to local minima. The parameters used to construct the target path of the towed body are given in Table 7.1.

Table 7.1: Towed Body Target Path Parameters

Sequence	Time (seconds)	Time Fraction f	Heading Change $\Delta\psi_i$(deg)	Speed Change ΔV_i(knots)
1	16	0.3	-40.0	0.0
2	48	0.1	-260.0	0.0
3	16	0.3	-40.0	-0.0
4	08	0.2	0.0	0.0

The best trajectories obtained using the gradient-based optimizer and the genetic algorithm are shown in Figs. 7.7 and 7.8 respectively.

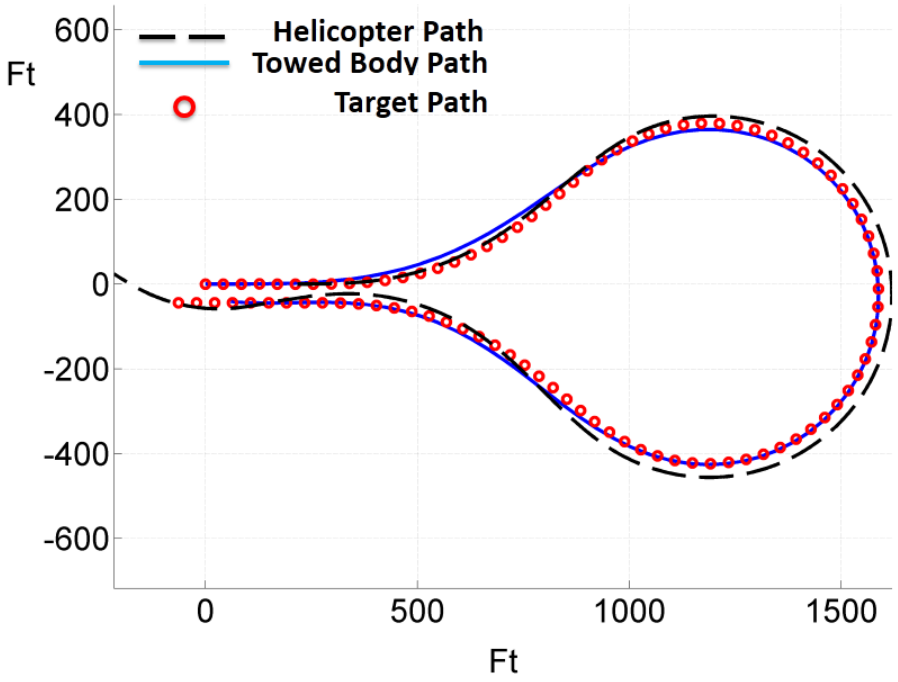

Figure 7.7: Top View of Best Path : Gradient-Based Optimizer

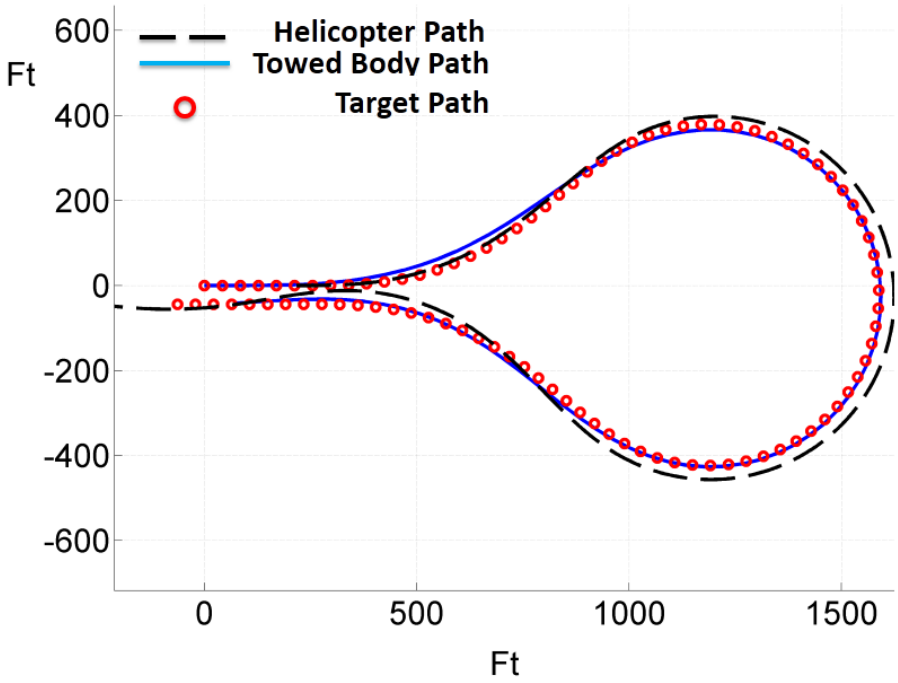

Figure 7.8: Top View of Best Path : Genetic Algorithm

The heading and velocity change targets for the helicopter tow point in Tables 7.2 and 7.3 are obtained using the gradient-based optimizer and the genetic

algorithm respectively.

Table 7.2: Tow Point Targets : Gradient-Based Optimizer

Sequence	Time (seconds)	Time Fraction f	Heading Change $\Delta\psi_i$(deg)	Speed Change ΔV_i(knots)
1	16	0.3	-40.0	1.42
2	48	0.1	264.7	1.17
3	16	0.3	-54.7	-0.66
4	08	0.2	42.4	0.97

Table 7.3: Tow Point Targets : Genetic Algorithm

Sequence	Time (seconds)	Time Fraction f	Heading Change $\Delta\psi_i$(deg)	Speed Change ΔV_i(knots)
1	16	0.3	-40.0	1.59
2	48	0.1	265.4	1.14
3	16	0.3	-55.1	-0.80
4	08	0.2	14.7	-1.82

Based on the optimal trajectories, the following conclusions can be drawn

- **The optimal tow point motions obtained using the two algorithms are near-identical for the first three turn sequences**. Sampling the true objective function prior to optimization is essential for the gradient-based optimizer to converge to a valid solution. While this pre-processing step is not

strictly required for the genetic algorithm, it allows for faster convergence of the response surface.

- **The helicopter must move incrementally faster, and turn along a path whose radius is larger than that of the towed body**. Since the turn rate changes sign across sequences, the path of the helicopter and towed body cross multiple times.

- **The helicopter must lead the towed body during the entire maneuver**. Further, the tow point speed must increase slightly for the first two turn sequences, over-shoot the nose-right turn by 4-5 degrees and over-shoot the second nose-left turn by 15°.

- **The gradient-based optimizer is trapped inside a local minimum** during the fourth sequence (departure from tear-drop) and erroneously over-predicts the heading change required to correct the overshoot from the third turn sequence. This error leads to 32° of residual nose-right heading overshoot and 3 knots of speed gain. The genetic algorithm identifies a gentler end to the tear-drop maneuver as begin "optimal", with 3° of residual nose-right heading overshoot and 0.1 knots of total speed change.

7.2 Stage II : Helicopter Simulation

The breakdown of a maneuver into sequences, and sequences into sections is particularly useful for the tear-drop maneuver, which has multiple changes in the

sign of the turn rate. The end-points of each section within a sequence correspond to equilibrium (trim) conditions, obtained using the techniques described in Chapter 3. The trim variables corresponding to these equilibrium solutions are interpolated smoothly using cubic splines between trim states, and assigned as targets for the feedback controller. The maneuver is simulated with a 350-ft cable and the baseline towed body using the targets given in Table 7.3. Based on these inputs, the total maneuver time is 80 seconds. Two optional seconds of lead buffer are introduced to eliminate transients that may arise when starting from a trim solution. The trajectories obtained with dynamic inflow are discussed first, followed by an investigation of blade flexibility effects. These results are re-examined with the free-wake inflow model.

Simultaneous tracking of all three linear velocities and fuselage attitudes is essential for three-dimensional trajectory following using control systems. The relative LQR weights for states and controls must be chosen carefully to ensure smooth and bounded controls, together with accurate state tracking. A top-down view ($X_G - Y_G$ plane) of the resulting tear-drop trajectory is shown in Fig. 7.9, together with the path of the helicopter over the entire maneuver and target path for the submerged load.

The corresponding helicopter attitudes are shown in Fig. 7.10. The airframe roll overshoots the target during the transition between the first two sequences. The maximum pitch tracking error is less than 1°, and the helicopter heading lags the target value by 1 second.

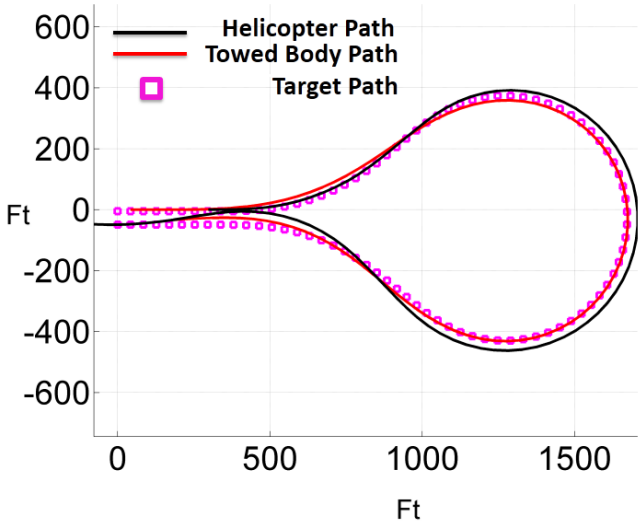

Figure 7.9: Closed-loop tear-drop simulation at 25 kts. The total depth change over the duration of the maneuver is 15 ft, less than 0.5% of the total distance traveled.

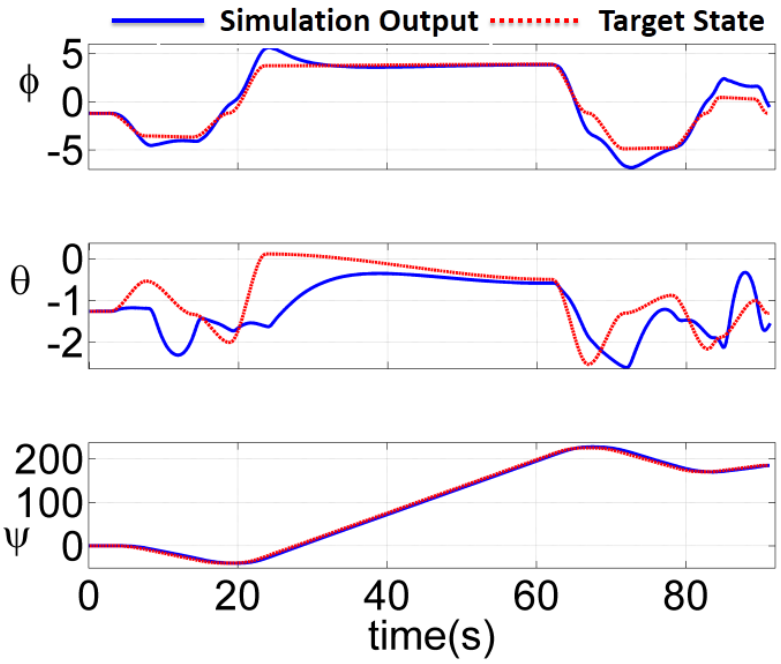

Figure 7.10: Helicopter Attitudes in Degrees

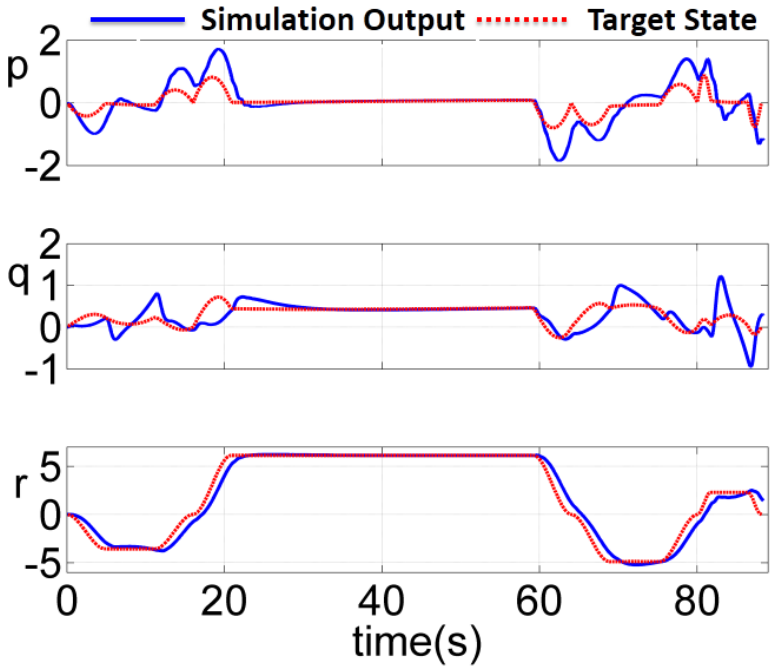

Figure 7.11: Helicopter Angular Velocities in Degrees/s

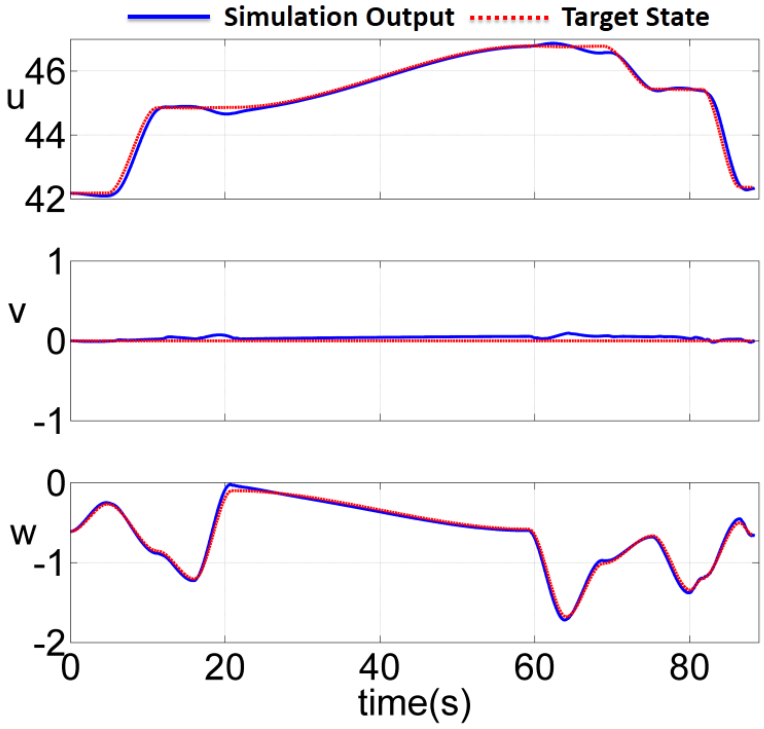

Figure 7.12: Helicopter Body-Axes Velocities in ft/s

The helicopter body-axes angular velocities are shown in Fig. 7.11. All three

rates show excellent tracking, with less than 1°/s error. The near-zero lateral velocity v indicates that the maneuver is executed with negligible sideslip. The maximum turn rate for the helicopter is 5.5°/s, less than the peak turn rate of 9°/s as determined by the cable length. The body-axes velocity components are shown in Fig. 7.12. The tracking for translation velocities is excellent with negligible error.

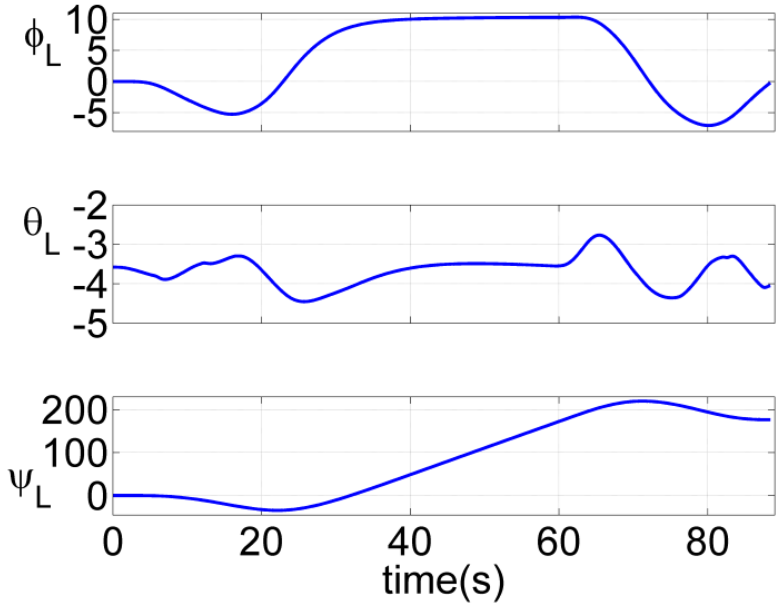

Figure 7.13: Submerged Load Attitudes in Degrees

The attitudes of the submerged load are shown in Fig. 7.13. The load heading lags that of the helicopter by 5 seconds. Hydrodynamic forces in water result in overdamped dynamics for the submerged load, resulting in perceptible delays between tow point motion and towed body response. The pitch attitude of the towed body varies by less than 2° over the entire maneuver, and is near-constant over the steady section of the nose-right turn (40-60 seconds). The towed body rolls left between 10-16 seconds (nose-left turn) and then to the right between 22-70 seconds during the nose-right turn. The overshoot for the third turn sequence (nose-left)

results in additional left roll at 80 seconds.

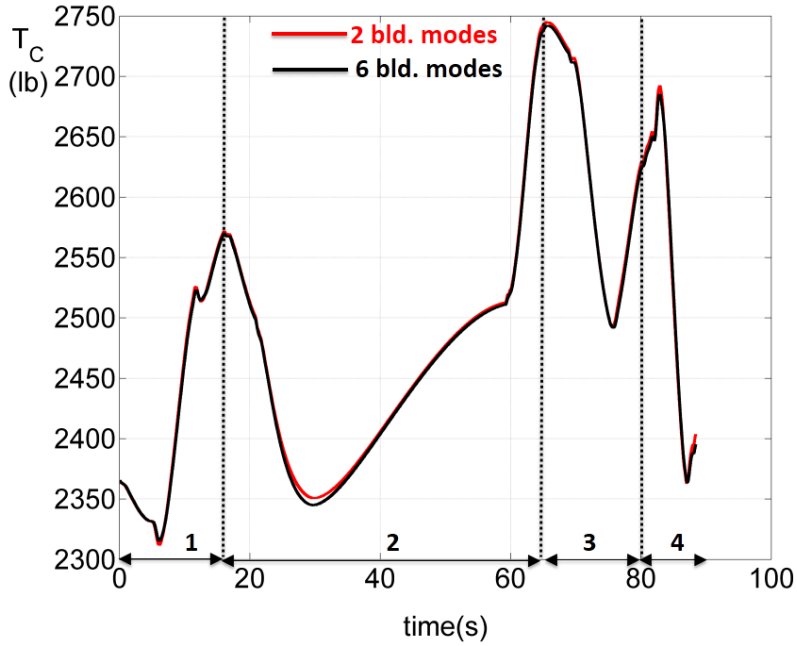

Figure 7.14: Cable Force

Fig. 7.14 shows the variation of cable force over the duration of the tear-drop maneuver. The time durations for each of the turn sequences at 16,64 and 80 seconds are indicated on the plot. For the first turn sequence (left turn), the cable force initially decreases as the tow system enters the left turn and then increases with hydrodynamic drag as the helicopter speed increases from 25 to 26.6 knots. During the transition to the second sequence (nose-right turn), the cable force initially reduces due to reduction in hydrodynamic drag with turn radius of the submerged load. As the helicopter airspeed increases, the hydrodynamic drag on the tow cable and submerged load increases, resulting in increasing cable force from 30-60 seconds. When the helicopter transitions back to forward flight before the third turn sequence, the towed body turn radius and speed increase, transmitting larger cable forces. As the helicopter enters the third turn sequence, the combination of turn radius and

speed reduction result in smaller cable forces. Finally, as the turn rate reduces from 75-80 seconds during the transition to the fourth turn sequence, the cable force increases with hydrodynamic drag. The reduction of helicopter airspeed causes a corresponding drop in hydrodynamic drag and cable force.

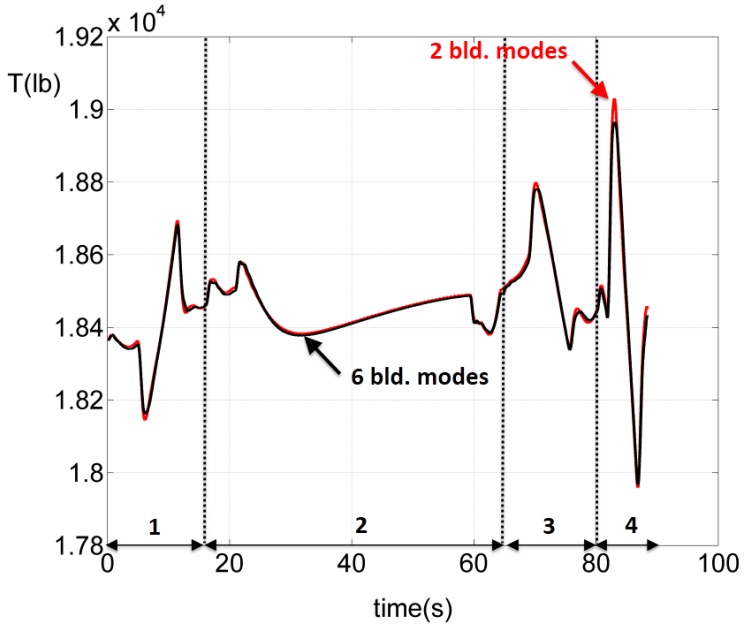

Figure 7.15: Main Rotor Thrust

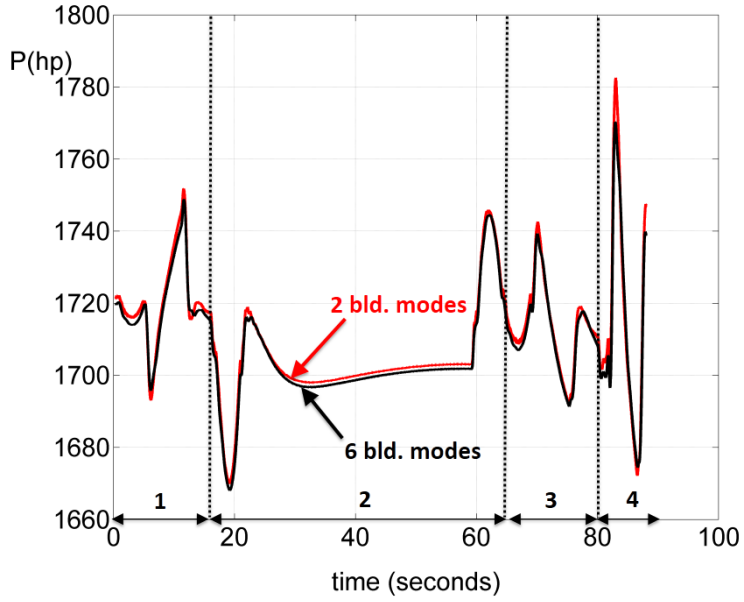

Figure 7.16: Main Rotor Power

The corresponding rotor thrust and power time histories are shown in Figs. 7.15 and 7.16 respectively. The local peaks correspond to changes in the helicopter turn rate, when the hydrodynamic drag of the towed body fluctuates with turn radius and helicopter airspeed. The effects of blade flexibility on cable force and rotor thrust are not apparent, with the 6-mode solution being near-identical to the 2-mode solution. With the dynamic inflow model, the rotor power shows no sensitivity to blade flexibility.

Swashplate Controls

The 4/rev vibratory loads signal from the rotor causes high-frequency helicopter oscillations (especially in roll). To avoid spurious feedback based on rotor vibrations, a low-pass filter is applied to the helicopter rigid-body states prior to computing the control inputs. This filtering ensures that higher-harmonic (of the order of the rotor frequency) control inputs are avoided, and the input time histories are smooth.

The trends in the rotor collective pitch inputs reflect those present in the thrust, as shown in Fig. 7.17. The effects of blade flexibility manifest in the main rotor collective pitch input angles. When elastic twist is ignored, the pitch angle distribution along the span of the rotor blade is higher, requiring smaller collective inputs for rigid blades. When blade torsion is included, the structural response includes a nose-down twist angle and the root collective must increase to maintain the same thrust.

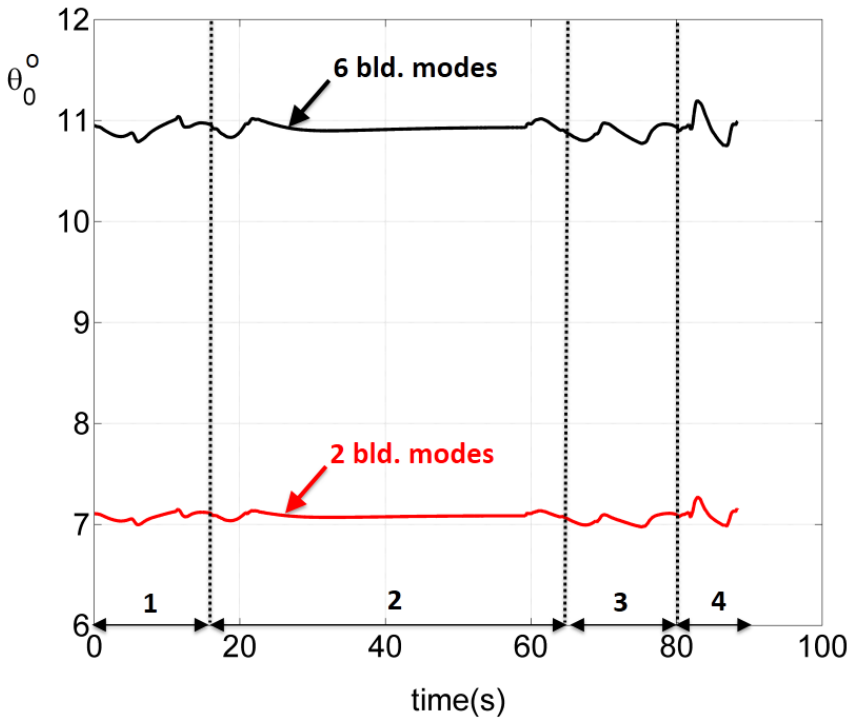

Figure 7.17: Main Rotor Collective Pitch

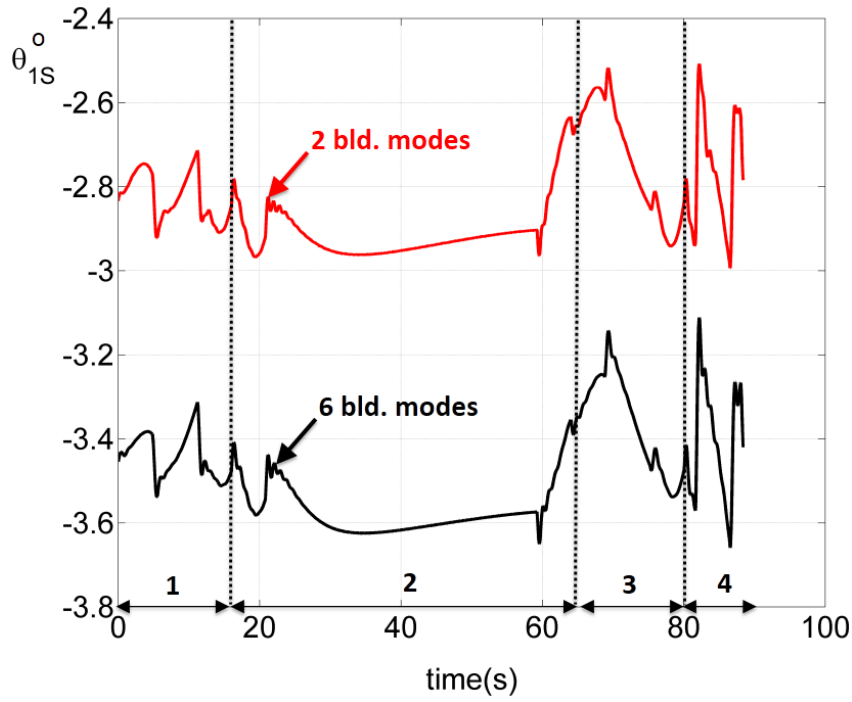

Figure 7.18: Main Rotor Longitudinal Cyclic Pitch

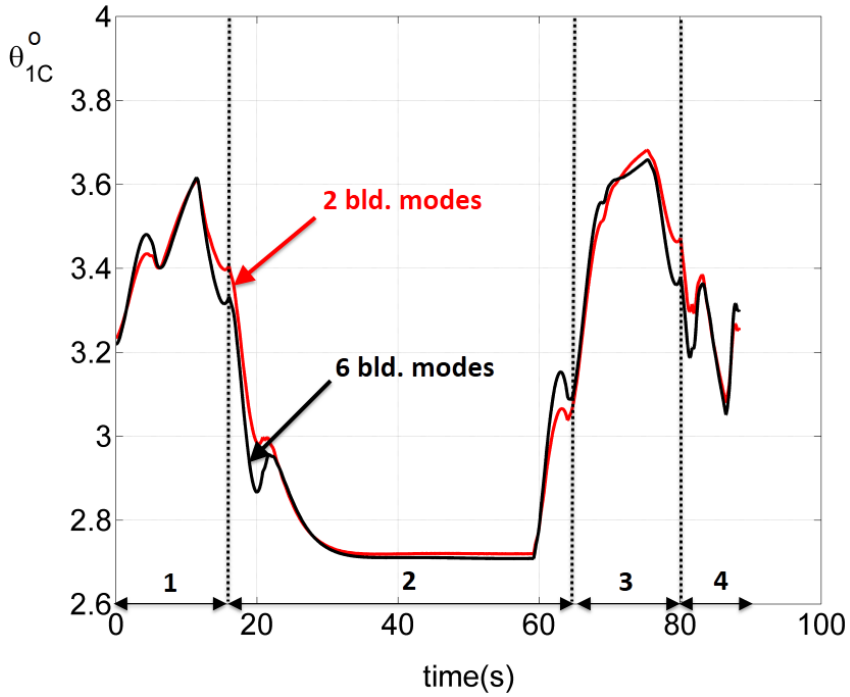

Figure 7.19: Main Rotor Lateral Cyclic Pitch

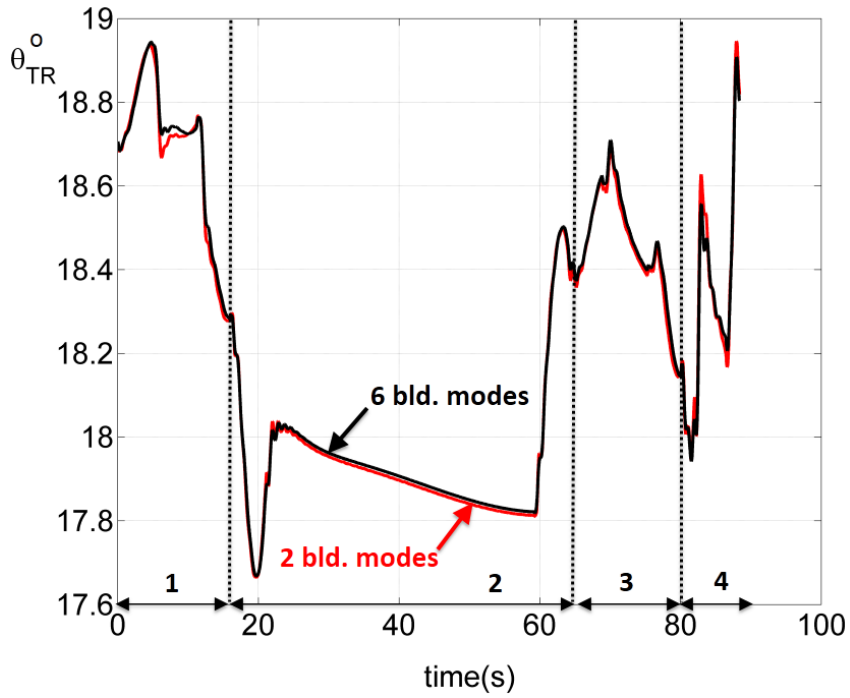

Figure 7.20: Tail Rotor Collective Pitch

Blade twist also modifies the required longitudinal cyclic pitch inputs, as shown

in Fig. 7.18. With elastic twist, the 1/rev torsional response results in 0.6° of additional cyclic. The lateral cyclic is unaffected, as shown in Fig. 7.19. The tail rotor collective is a measure of anti-torque required to maintain yawing moment equilibrium. Since dynamic inflow predicts identical solutions for the main rotor torque, the tail rotor collective pitch inputs are identical between 2 blade modes and 6 blade modes, as shown in Fig. 7.20.

Hub Loads

The hub in-plane forces are shown in Figs. 7.21 and 7.22, and the rolling and pitching moments are shown in Figs. 7.23 and 7.24. During the nose-left turn over the 8-16 second interval, the helicopter airspeed increases by 1.6 knots, and the individual hub loads change in the following manner

- The hub lateral force decreases (i.e. more force towards port) to counter the centrifugal forces in a nose-left turn. The hub rolling moment increases (i.e. more left roll moment) to counter the rolling moment induced by the lateral component of cable force on the helicopter.

- The hub longitudinal force increases (i.e. more force towards the tail) in conjunction with nose-down body pitch of 1° to maintain the same airspeed. The hub pitching moment is nose-down (with respect to the trim value) to compensate for the helicopter pitch attitude *and* the reduced pitching moments from the cable when the towed body enters a turn and travels along a smaller turn radius.

The second sequence consists of three sections : transition from steady forward flight to a nose-right turn (16-20 seconds), steady turn rate with slight increase in airspeed (20-60 seconds) and transition back to steady forward flight (60-64 seconds).

- During the transition from steady forward flight to a steady right turn, the hub lateral force increases (i.e. more force towards starboard) to initiate the turn and maintain the force component required to counter centrifugal force. The hub rolling moment decreases (i.e. roll-right moment) to counter the moments induced by the lateral component of cable forces and maintain equilibrium in turning flight.

- The hub longitudinal force is near-constant over the steady right turn. The pitching moment variation reflects the trends in longitudinal cyclic, and increases slightly (more nose-up moments) to counter the pitching moments induced by the cable and towed body with increasing tow speed.

The third turn sequence consists of a nose-left turn (faster than sequence 1) and the helicopter overshoots the towed body target path.

- The hub rolling moment increases (roll-left) above the peak value for the first sequence, since the turn rate is higher. The lateral force reduces (i.e. more force towards port) to counter centrifugal forces in a turn.

- The hub longitudinal force decreases (i.e. more force towards the nose) to compensate for the increased cable drag as the towed body transitions from a right-handed turn to a left-handed turn. During the steady nose-left turn,

the hub longitudinal force decreases (more force towards the tail) to reduce the helicopter airspeed by 0.8 knots. As the tip-path-plane tilts aft, the hub pitching moment increases (i.e. nose-up).

The fourth and final turn sequence consists of a nose-right turn with an airspeed reduction of 1.8 knots.

- The hub lateral force increases (i.e. more force towards starboard) to compensate for centrifugal loads, and the rolling moment decreases (i.e. rotor induces roll-right moments) as a result of tip-path-plane tilt into the turn.

- The hub longitudinal force decreases (i.e. more forces towards the tail) to decelerate the vehicle, and the hub pitching moments increase (i.e. more nose-up moments) as a result of aft tilt of the tip-path-plane.

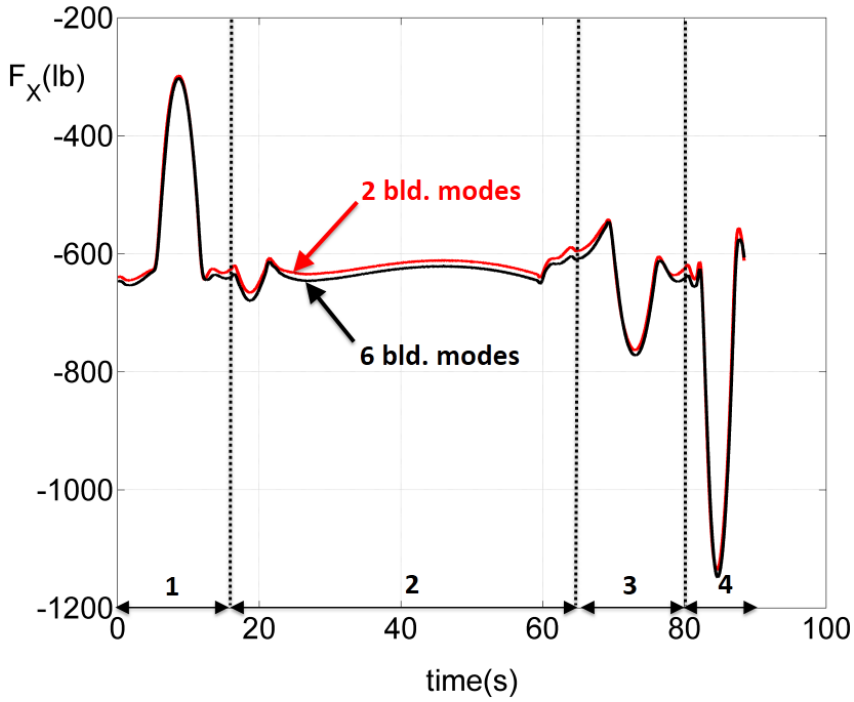

Figure 7.21: Hub In-Plane Longitudinal Force

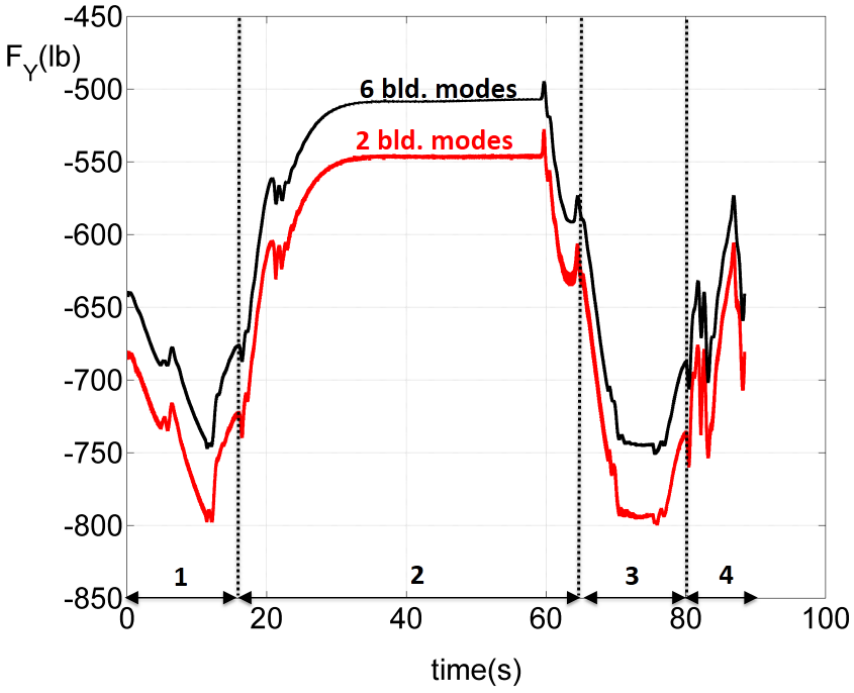

Figure 7.22: Hub In-Plane Lateral Force

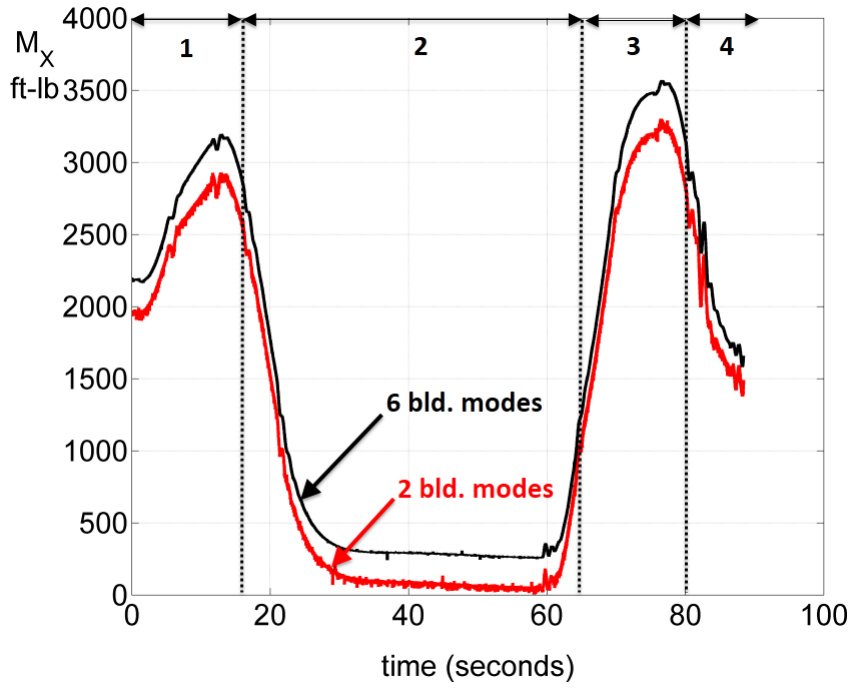

Figure 7.23: Hub Rolling Moment

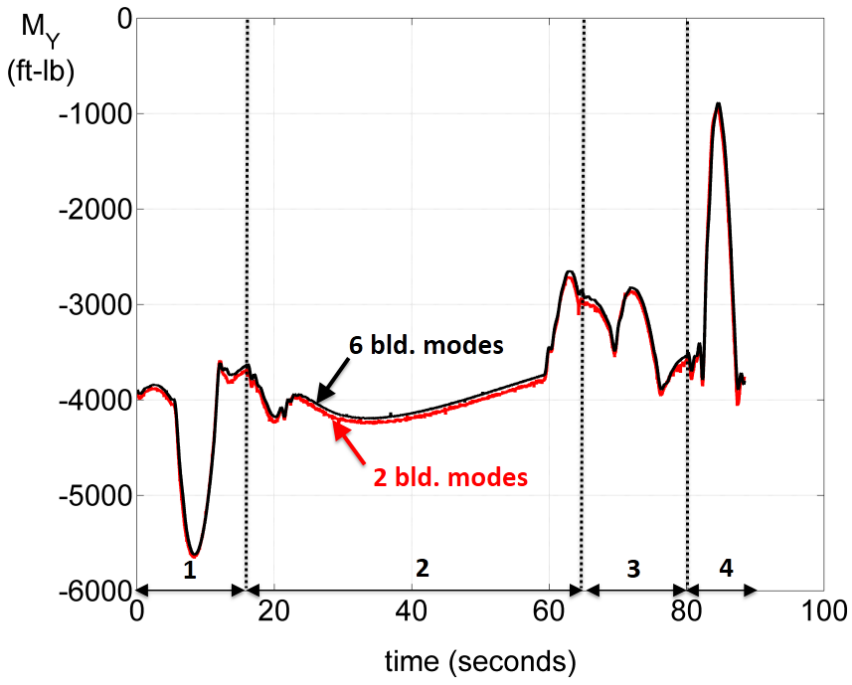

Figure 7.24: Hub Pitching Moment

7.2.1 Predictions with Free-Vortex Wake

The following strategies were employed to couple the wake and flight dynamics models for time integration. The Conventional Serial Staggered (CSS) approach exchanges information between flight dynamics and aerodynamics at every time step. The flight dynamics solution is advanced forward in time with the structural dynamics frozen, and the flowfield is advanced assuming the structural dynamics are frozen. No problems exist while simulating the closed-loop flight dynamics with a frozen flowfield or advancing the flowfield with frozen blade motions. The following approaches were evaluated in simulating the closed-loop coupled aero-flight dynamics solution, all with limited or no success:

- **Tight coupling** - The CSS scheme is numerically unstable both at hover and

25 knots (the maneuver speed of interest) with the LQR controller. While this approach was used by Ref. [20] for simulating open-loop simulations with prescribed controls, it was not evaluated for closed-loop simulations with feedback control. Absolute and relative errors across time steps could not be preserved after 15 seconds of simulation time, and the integration process terminated prematurely. When the trim solution is provided as an initial condition and the maneuver targets are assigned to the trim states, the solutions for the first 10-20 revolutions displayed oscillations in rotor power of the order of 1000 Hp. These oscillations were traced back to a 0.5/rev fluctuation in the trim induced velocities, a result of operating in transition flight. If the low-pass filter is used to filter out signals at this frequency, the associated delays result in a destabilized system. If the low-pass filter is not used, these fluctuations permeate into the feedback controls and magnify the wake strength variations over successive revolutions.

- Information is exchanged every quarter, half or full revolution instead of at every time step. However, this method suffers from the same (in)stability issues as the CSS scheme, and similar power fluctuations were observed.

- **Relaxation :** The time history of differences in the induced velocities from free-vortex wake and dynamic inflow are stored, applied as "delta" corrections and updated over successive maneuvers. However, this method is also numerically unstable and settles into limit-cycle oscillations with a steady vertical descent after 15 seconds of simulation time.

The feedback controller for the closed-loop system is built assuming the structure of a certain (dynamic) inflow model. When that model is replaced with a vortex wake representation of the flowfield *and* the rotor is operated at low speeds, the coupled closed-loop linearized dynamics are not stable. To circumvent these instabilities and obtain a first-order effect of the vortex wake, a static "delta" correction to the inflow is applied as follows:

- At each of the equilibrium points used to determine the target states for the maneuver, the "delta" inflows between dynamic inflow and free wake are obtained in trim. At these points, the controller is expected to establish equilibrium, and the delta-corrected inflows will be exactly equal to the free-flight inflows *instantaneously*

- The trim states at the equilibrium points as obtained using the free wake model are used to construct the target states

- The delta inflow is applied as a correction to the induced velocities given by the dynamic inflow model, and the system $\mathbf{A}$, $\mathbf{B}$ matrices are obtained

- The controller is formulated with these $\mathbf{A}$, $\mathbf{B}$ matrices (as obtained with delta inflows) at 25 knots

- The delta inflows are interpolated linearly between the trim points and applied as corrections at every time step to the original dynamic inflow model over the duration of the maneuver

Results with Delta-Corrected Inflow

For the same helicopter tow point motions, the cable force, towed body trajectory and attitudes are identical. However, non-uniformities in the free wake induced velocities cause fluctuating loads on the rotor which excite vehicle roll and pitch motions. These oscillations result in small deviations of the towed body motions from the target trajectory as shown in Fig. 7.25. The tow point motions exhibit oscillations at the rotor frequencies, which introduces oscillations in the cable forces. Changes in the rotor inflow distribution introduce oscillations in the cable forces as shown in Fig. 7.26. The effect of blade flexibility on cable force is minimal, indicating that rigid-body motions excited by the first two rotor modes (rigid blade flap and lag) are sufficient for predicting the cable loads.

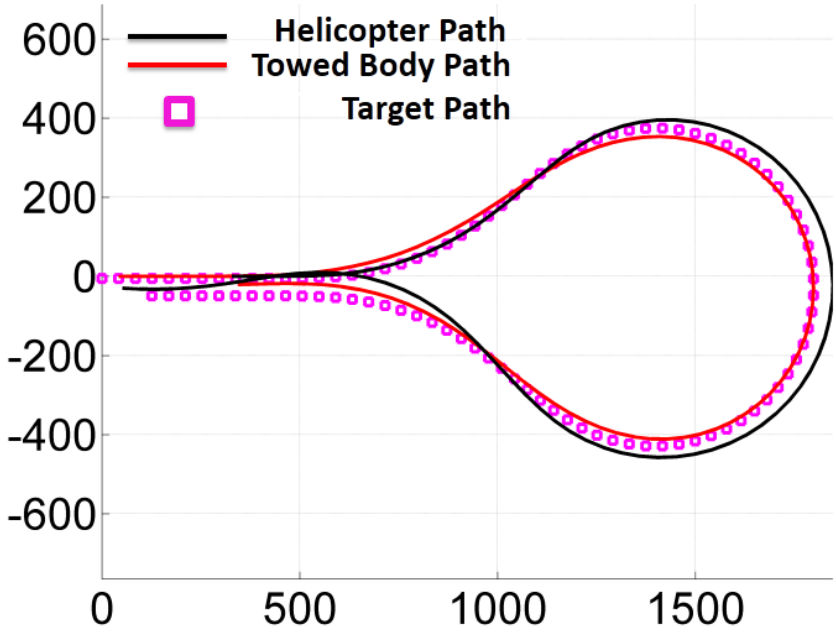

Figure 7.25: Top-View of Towed Body Trajectory. The total depth reduction over the 80-second maneuver is 20 ft, less than 0.5% of the total distance traveled.

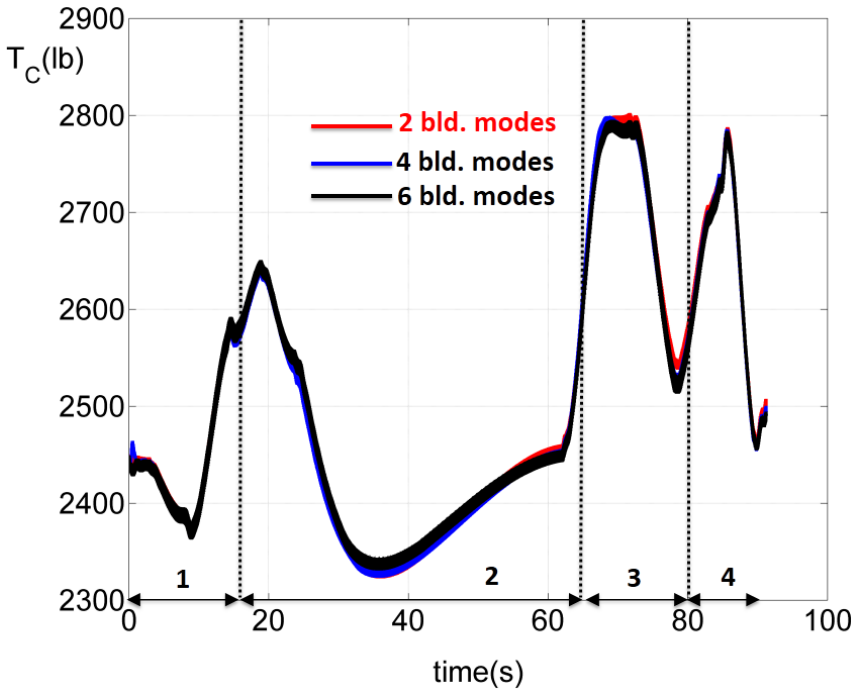

Figure 7.26: Cable Forces

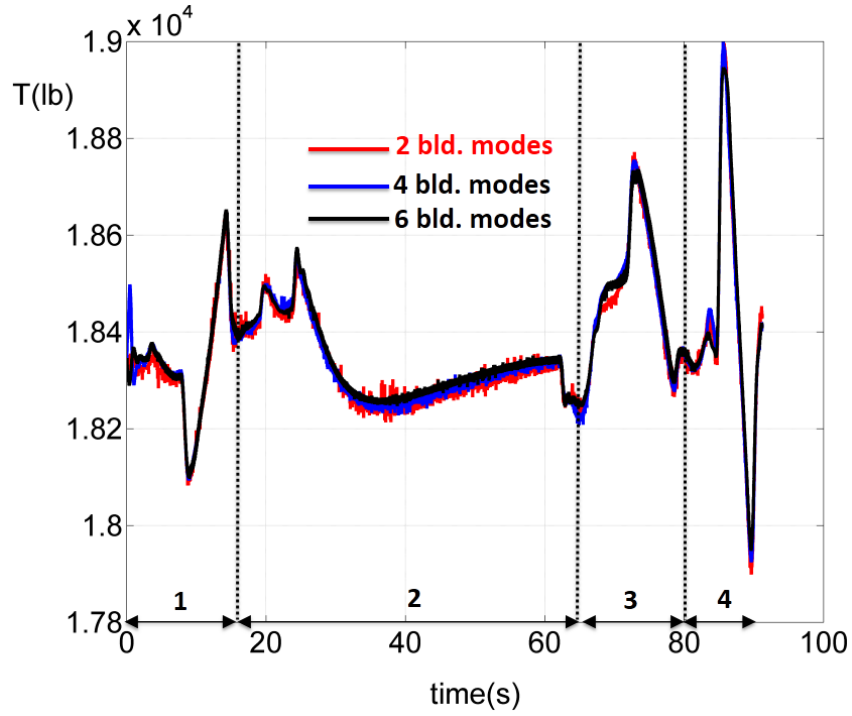

Figure 7.27: Rotor Thrust

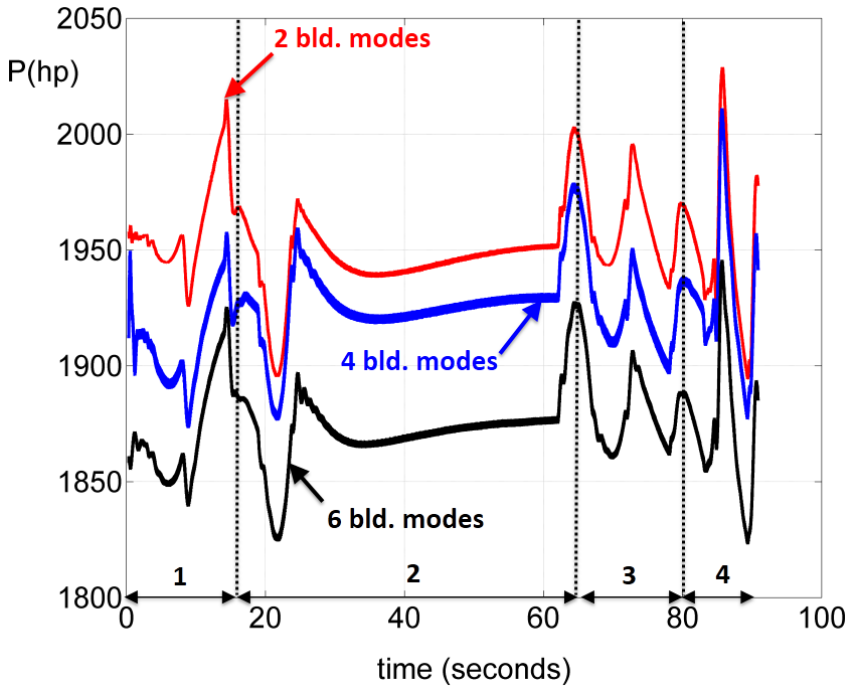

Figure 7.28: Main Rotor Power Required

The rotor thrust over the duration of the maneuver is shown in Fig. 7.27 for 2,4 and 6 rotor blade modes. The non-vibratory thrust component is unchanged for all three cases, and the effects of blade flexibility are not apparent since the controller modifies the collective and cyclic pitch inputs to maintain the required thrust mangnitude and direction. The effects of blade flexibility are apparent in the predictions of main rotor power, shown in Fig. 7.28. When blade flexibility is neglected (2 modes), the elastic twist is ignored and rotor power is over-predicted by 5.5%. The over-predictions of power are especially relevant for the UH-60 Blackhawk, with an MCP (Maximum Continuous Power) rating of 1900 Hp. The variations of rotor power over the duration of the maneuver do not entirely reflect the trends of rotor thrust or cable force. Rotor induced power increases with cable force, increases when entering a turn and reduces when transitioning back to steady forward flight. The

resulting power requirements exhibit low-frequency oscillations during transitions between turn sequences. The magnitude of these oscillations scales with the trim rotor torque which depends on elastic torsion of the blade.

Swashplate Controls

The effects of blade flexibility are apparent in the rotor control inputs especially for the collective pitch, shown in Fig. 7.29. When blade torsion is ignored, the collective pitch input is underpredicted by 5° in trim, and persist over the entire maneuver. The trends in collective variation with time reflect those in rotor thrust and cable force, discussed earlier.

The longitudinal cyclic input time histories are shown in Fig. 7.30. The use of rigid blades results in an under-prediction of 0.4°, and under-predicts the peak control inputs during transients between turn sequences by 0.5°. The lateral cyclic inputs are shown in Fig. 7.30. Neglecting blade torsion results in 1° over-prediction of cyclic inputs. When the elastic twist response is included in the predictions, the required peak-to-peak cyclic range reduces from 1.4° to 1°. The predictions of tail rotor collective pitch input reflects the trends in rotor power variation over the duration of the maneuver. When blade flexibility is ignored, the tail rotor collective pitch is over-predicted by 0.5°. **Neglecting blade flexibility introduces maximum error in the rotor collective and lateral cyclic.**

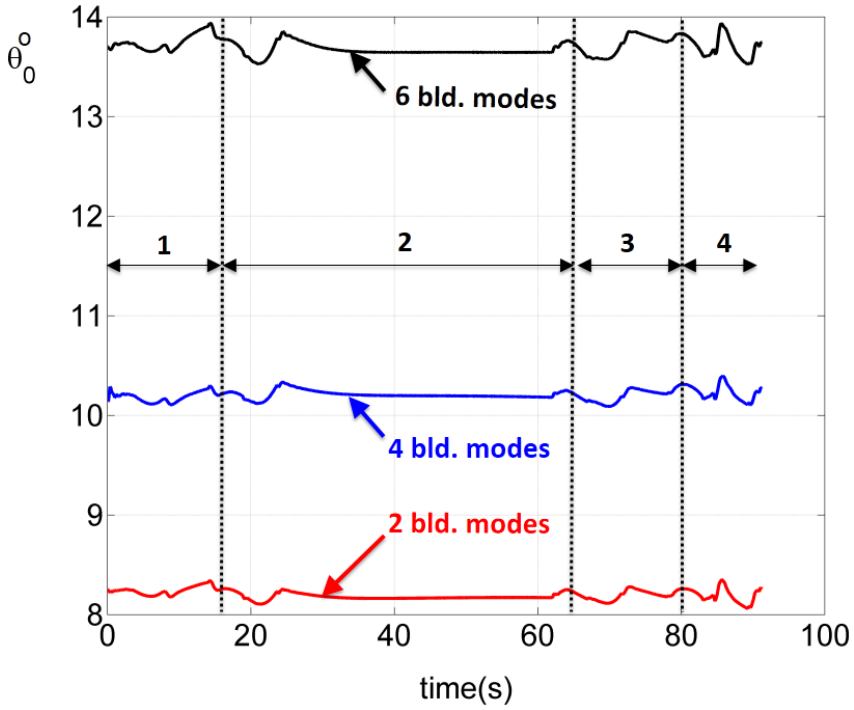

Figure 7.29: Main Rotor Collective Pitch

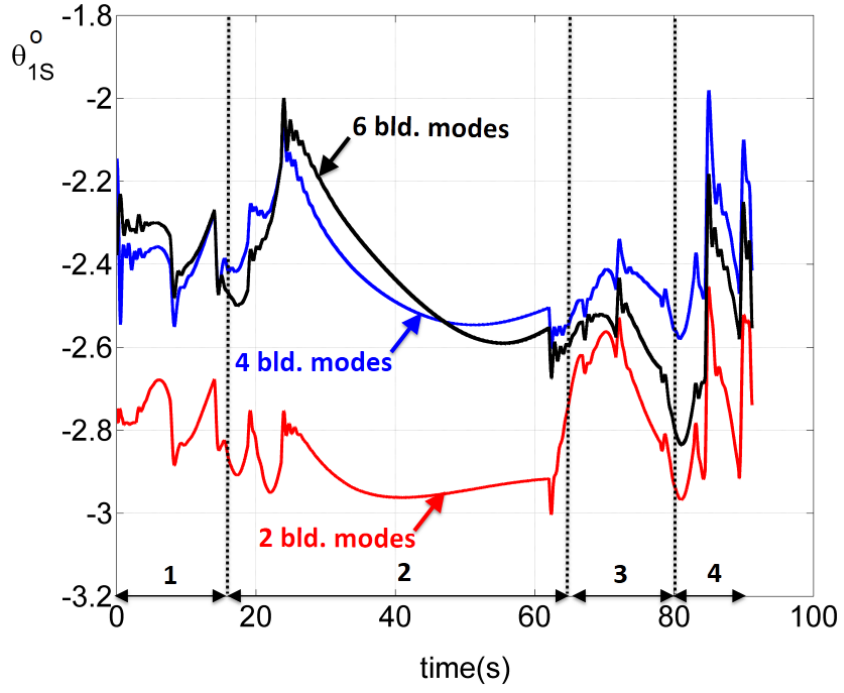

Figure 7.30: Main Rotor Longitudinal Cyclic Pitch

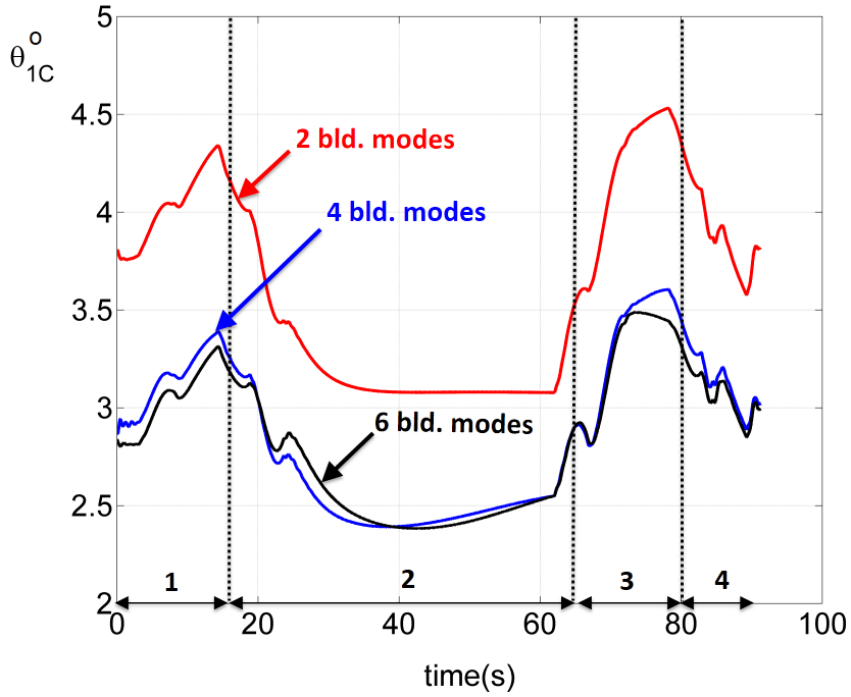

Figure 7.31: Main Rotor Lateral Cyclic Pitch

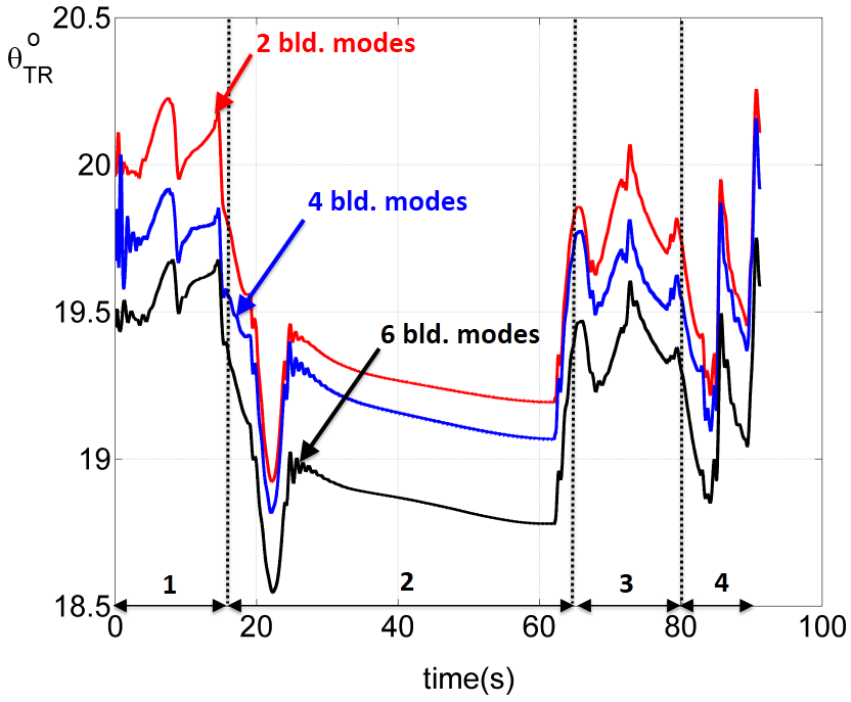

Figure 7.32: Tail Rotor Collective Pitch

Hub Loads : Effect of Blade Flexibility

The hub longitudinal force is shown in Fig. 7.33 for the tear-drop maneuver with 2, 4 and 6 blade modes. The predictions for 2 modes and 6 modes are very close. However, this is not an indication that blade flexibility is unimportant. The lateral hub forces, shown in Fig. 7.34, are near-identical for the 2 and 4 blade modes cases. However, the 6 blade modes case shows that elastic twist alters the hub lateral force by 50 lb.

With increasing fidelity in modeling the blade flexibility, the low-frequency components of the hub moment time histories remain unaltered, as shown in Figs. 7.35 and 7.36. However, **predictions of the *vibratory* component of the hub moments is reduced when flexible blade models are used.** The dominant contribution to the fixed-frame hub moments from an articulated rotor blade is from the azimuthal distribution of vertical hub shear (aerodynamic pitching moments and blade torsional oscillations play a secondary role in determination of fixed-frame hub loads). When blade elasticity is ignored, error is introduced into predictions of both aerodynamic lift and rotor response (flap motions and inertial loads), resulting in larger azimuthal variations of total forces at the hinge. Thus, **rotor blades behave as vibration absorbers by virtue of their elasticity.** These predictions are valid within the realm of applicability of the quasi-steady rotor aerodynamic model, and a quantitatively accurate analysis of vibratory loads requires the use of unsteady aerodynamic models.

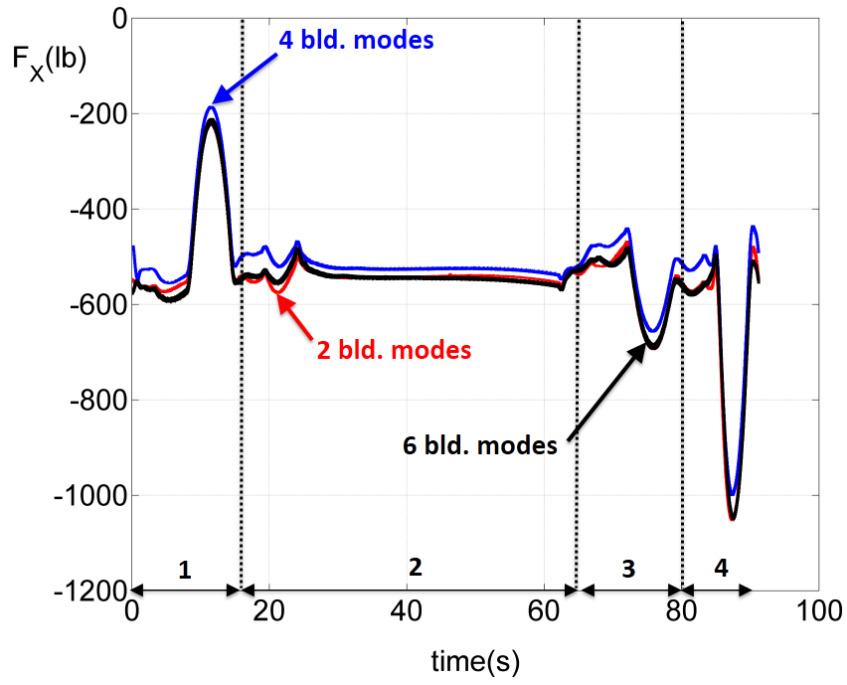

Figure 7.33: Main Rotor Hub Longitudinal Force

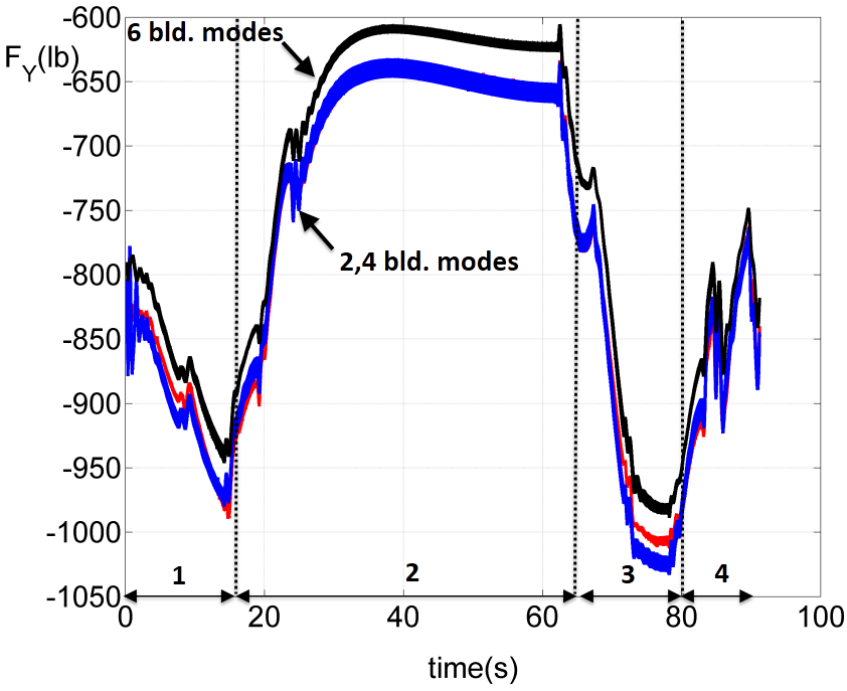

Figure 7.34: Main Rotor Hub Lateral Force

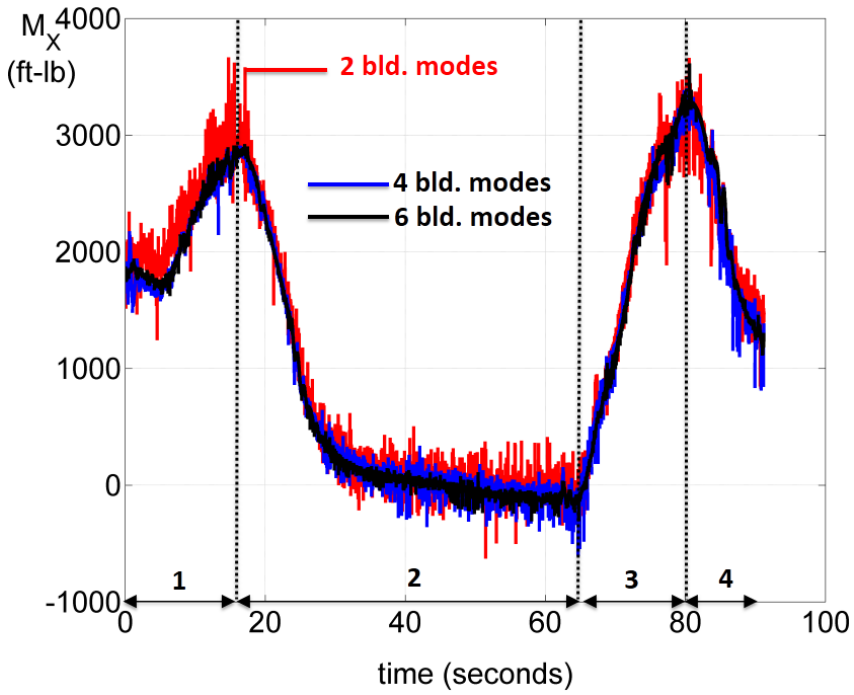

Figure 7.35: Main Rotor Hub Roll Moment

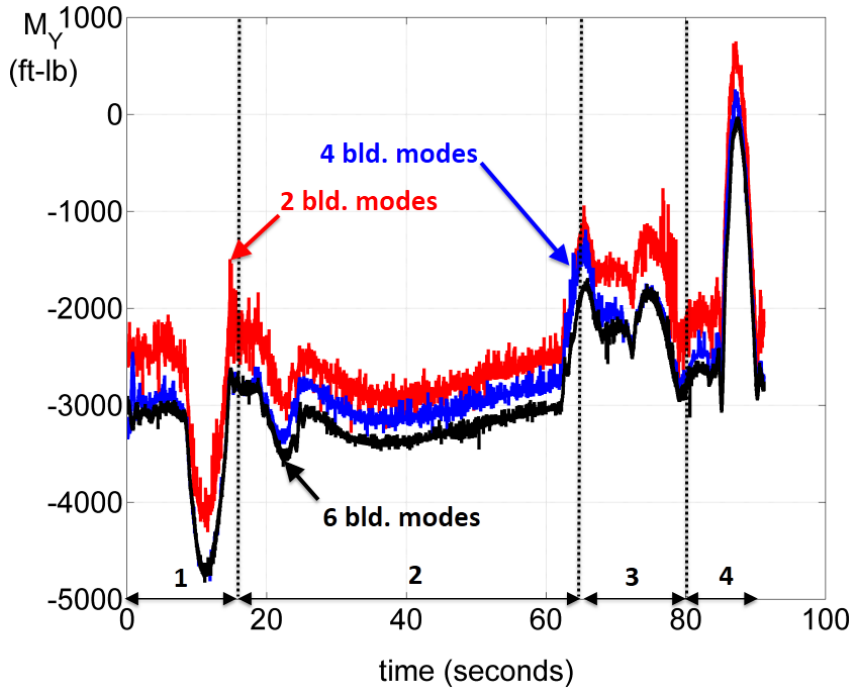

Figure 7.36: Main Rotor Hub Pitch Moment

8 Summary and Conclusions

8.1 Summary

This document has described the formulation of a coupled helicopter wake-rotor-airframe-cable-towed body flight dynamic model with flexible blades, rigid airframe, free-vortex wake, curved cables and a rigid submerged load. The coupled flexible body dynamics of the rotor and cable, and the rigid-body dynamics of the airframe and towed body are preserved in state-space form. The airframe and submerged load are treated as rigid bodies, while the flexible structures (rotor blades and cable) are modeled using a fully numerical geometrically exact quasi-multibody rotating beam dynamics formulation developed in this work. This beam model does not require ordering schemes and is not subject to small-angle or moderate-rotation restrictions, and is valid up to 90° of transverse bending slope. All flap-lag-torsion couplings are accounted for, including the kinematic integral twist and axial foreshortening without expansion/truncation of trigonometric functions. While a modal coordinate transformation is applied to rotor blades to reduce computational effort, the cable nodal degrees of freedom are preserved in their original form to accurately capture the loading discontinuity at the water/air free surface.

Boundary conditions coupling the motions of the helicopter, cable and towed

body are formulated for spherical bearings that transmit zero moments. The present formulation may be extended in a straightforward manner to apply additional constraints at the ends of the cable. Trim conditions in a steady ascending/descending helical turn are formulated for two different cable models : an axially flexible straight cable, and an axially inextensible curved cable and serve as cross-validations for each other. For the straight cable, explicit expressions are derived assuming that the towed body maintains a constant separation from the helicopter. For the curved cable, the towed body is treated as a tip mass, and the root motions are obtained from helicopter hook motions. The only necessary condition for the curved cable to maintain trim in turning flight is that its transverse deflections as defined in a rotating reference frame aligned with the helicopter heading remain constant. This formulation accounts for centrifugal accelerations on the cable and towed body numerically without resorting to analytical expansions.

The swashplate controls required to guide the towed body along a target gentle maneuver are obtained using a two-stage process. In the first stage, the tow point (helicopter) motions are parameterized and identified using an optimization process. The tow point motions are converted to target states in stage II, and an LQR controller is used with a low-pass filter to obtain smoothly varying controls that guide the helicopter along the target tow point path obtained in stage I. Induced inflow from the vortex wake model is applied as a "delta" correction to the dynamic inflow model at select equilibrium points and interpolated to yield a more representative variation of inflow over the duration of the tear-drop maneuver.

8.2 Conclusions

- The CG-EA offset of the UH-60 blade couples the second flap bending mode to the elastic twist. Accurate modeling of rotor blade elastic twist and its effect on the near-wake is the key to accurate rotor power predictions.

- The use of ordering schemes and small-angle assumptions in the rotor dynamics may result in negligible error when *individual* third-order terms are neglected. However, when *all* third-order terms are neglected, it results in 0.8-1.5% error in inertial loads, and 3-4% error in the aerodynamic loads. The error in inertial loads scales with the steady value of the blade root lag angle.

- The profile drag of the blade spar in the root cut-out region and inclusion of fuselage drag additions to flight test instrumentation plays a major role in accuracy of forward flight performance predictions.

- Trim longitudinal dynamics of the submerged load results in the towed body trimming with nose-down pitch attitude and creating a down-force on the cable. This down-force manifests as an apparent increase in weight for the helicopter, increasing thrust and power requirements. The dominant parameters that govern the magnitude of this down-force are the cable attachment point on the towed body and longitudinal placement of the fins.

- Hydrodynamic drag on the towed body and cable manifest as apparent increases in the equivalent flat-plate area for the tow system, and result in the helicopter trimming to nose-down pitch attitudes in excess of -6°. These pitch

attitudes can be reduced by aft offset of the tow point and using longer cables with fin pitching to regulate depth.

- When the fin pitch is positive, the down-force is alleviated and longer sections of the cable raise out of the water as the longitudinal trail angle increases. Coupled with the alignment of cable cross-sections parallel to the flow, the reduction in total cable drag outweighs the reduction in buoyancy, resulting in more efficient operations for tracking the same depth with longer cables and up-force than shorter cables and down-force.

- Neglecting cable drag can result in 42% error in predictions of tow tension for the longest cable, while neglecting curvature results in 5% prediction error in rotor power for the shortest cable.

- In turning flight, hydrodynamic drag on the cable and towed body result in the submerged load turning with a consistently smaller radius than the helicopter. The power requirements reduce with increasing turn rate as the load moves closer to the center of the turn, and this tendency increases with cable length. As the turn rate increases and the turn radius approaches the length of the cable, the variation of trim attitudes is no longer linear and the towed body increasingly "lags" behind the helicopter (in turn azimuth) as it approaches the center of the turn. Peak turn rates are limited by cable length, and maximum tow speeds are limited by available cable length and engine power.

- Depth variation with turn rate increases with the length of the cable. Fin

pitch actuation in turning flight is not as effective as in forward flight due to cable drag countering the effects of fin down-force in modifying the load trim depth and turn radius.

- Cable flexural stiffness does not significantly influence the steady-state performance, indicating that the dominant source of stiffening is from the tensile forces.

- Analysis of linearized models indicates that the helicopter frequency response to pilot stick inputs is unchanged above 1 rad/s when the cable and towed body are attached to the airframe. At low frequencies (below 0.3 rad/s), the magnitude of the aircraft response reduces with increasing hydrodynamic drag on the cable and towed body, and is unaffected by cable structural properties due to over-damped stabilization afforded by hydrodynamics.

- The 2-stage approach yields smooth controls that guide the towed body along the desired path. The variation of towed body depth over the duration of the maneuver is 20 ft, less than 0.5% of the total distance traveled.

- Blade elastic torsion plays an important role in determining the steady-state performance and low-frequency variation of hub loads, while flap bending elasticity acts as a vibration absorber to attenuate the oscillatory airloads transmitted to the hub.

8.3 Recommendations for Future Work

This section suggests a few areas of related research areas that will result in a significant improvement in understanding the dynamics of the tow system. In particular,

1. The effects of rotor-wake-airframe interaction at this low flight speed is an area with great potential for in-depth exploration, especially when operating at large nose-down pitch attitudes and elevated rotor thrust levels. Recent advancements in hardware and software solutions for accelerated computing (GPUs and multicore CPUs) may be exploited to solve larger-scale problems in an efficient manner to understand the fundamental aerodynamics of rotor-wake-airframe interaction at this speed.

2. Towing of hydroplaning sleds with time-varying immersion depths represents a numerically challenging task. Integrating the relatively large system of equations forward in time while introducing a time-varying free-surface boundary condition is another potential problem, the solution of which will push the envelope of state-of-the-art in flight dynamic simulations.

3. The flight dynamic model may be coupled with CFD for the rotor, airframe, cable, towed body and optionally ship air wake to study trim configurations and maneuvering flight. The presence of different time and length scales of fluid flow over the blades, airframes and hydrofoils presents a challenging simulation task. Progress towards this goal will promote the development of

universal fluid dynamic solvers that can handle multi-phase flow phenomena, including the effects of the free-surface.

4. Full-fledged trajectory optimization using inverse simulation with free-vortex wake methods is a computationally intensive process, with an estimate of 1 year and 3 months of computational time to obtain a good approximation to the objective function. Recasting the entire solver, including airframe and rotor dynamics to execute on GPUs, together with CPU-GPU load balancing has the potential to reduce run times by a factor of 50, and represents a worthwhile initial investment for the potential long-term gains.

5. The cable resonance frequencies are pertinent for missions involving towing of hydroplaning sleds, where hydrodynamic damping on the cable is absent. The coupling between vehicle flight dynamics and cable/towed body motions creates resonance frequencies at which the pilot inputs can excite transverse vibrations of the tow cable. This phenomenon occurs at flight dynamic frequencies of interest, may interact adversely with the flight control system and requires further analysis to determine the nature of the interaction (unstable divergent or limit-cycle).

A Time Derivatives of Euler Angles

The rigid-body angular states that are conventionally used are the Euler angles ψ,θ,ϕ and the body-axis angular rates p,q,r. Using consistency equations, the time derivatives of the Euler angles can be found as follows.

$$\dot{\phi} = p + q\sin\phi\tan\theta + r\cos\phi\tan\theta \tag{A.1}$$

$$\dot{\theta} = q\cos\phi - r\sin\phi \tag{A.2}$$

$$\dot{\psi} = (q\sin\phi + r\cos\phi)\sec\theta \tag{A.3}$$

Differentiating Eq. (A.1) once with respect to time, we obtain

$$\ddot{\phi} = \dot{p} + (\dot{q}\sin\phi + \dot{r}\cos\phi)\tan\theta + (q\sin\phi + r\cos\phi)\,\dot{\theta}\sec^2\theta + (q\cos\phi - r\sin\phi)\,\dot{\phi}\tan\theta$$

Substituting from Eqs. (A.2) and (A.3), we obtain

$$\ddot{\phi} = \dot{p} + (\dot{q}\sin\phi + \dot{r}\cos\phi)\tan\theta + \dot{\theta}\sec\theta\left(\dot{\psi} + \dot{\phi}\sin\theta\right) \tag{A.4}$$

Differentiating Eq. (A.2) once with respect to time, we obtain

$$\ddot{\theta} = \dot{q}\cos\phi - \dot{r}\sin\phi + \dot{\phi}\,(-q\sin\phi - r\cos\phi)$$

Substituting from Eq. (A.3), we obtain

$$\ddot{\theta} = \dot{q}\cos\phi - \dot{r}\sin\phi - \dot{\phi}\dot{\psi}\cos\theta \tag{A.5}$$

Differentiating Eq. (A.3) once with respect to time, we obtain

$$\ddot{\psi} = (\dot{q}\sin\phi + \dot{r}\cos\phi)\sec\theta + (q\sin\phi + r\cos\phi)\,\dot{\theta}\sec\theta\tan\theta + (q\cos\phi - r\sin\phi)\,\dot{\phi}\sec\theta$$

Substituting from Eqs. (A.2) and (A.3), we obtain

$$\ddot{\psi} = (\dot{q}\sin\phi + \dot{r}\cos\phi)\sec\theta + \dot{\theta}\sec\theta\left(\dot{\psi}\sin\theta + \dot{\phi}\right) \tag{A.6}$$

B Parallelization

Recent advancements in parallel computing have been used to accelerate the simulations using existing multi-core CPUs and NVIDIA Graphics Processing Units (GPUs). The nature of the rotorcraft analysis is such that the complete dynamics can be partitioned into contributions from multiple components which interact selectively with each other. Parallel computing can be applied in these situations, but care must be taken to minimize the time delays (overhead) incurred by transferring information across processors.

Consider first the structural/flight dynamics. At a given time instant, the loads on the rotor blades, airframe, empennage, tail rotor, cable and towed body can be calculated simultaneously. Applying a code profiler revealed that computation of blade loads and beam equation residuals creates a speed bottleneck. Given that the number of blades for a helicopter are typically 4-8 (in this case 4), CPU parallelization is applied using OPENMP directives. The loads on each of the blades are computed using independent parallel threads. It is also possible to implement GPU parallelization for the rotor dynamics. However, since the solver routines are executed on the CPU, any potential speed-ups must take into account the time delay overhead due to back-and-forth transfers across devices at each time step.

The free-vortex wake analysis requires approximately 750,000 simultaneous induced velocity computations at every time instant when using 6 wake turns with 10° discretization. The scale of the problem is ideal for the use of CUDA-Fortran GPU parallelization. At every time step, the locations and vortex strengths of each wake marker are transferred from CPU to GPU. Using multi-stage parallelized binary reduction trees, the total induced velocity on each wake marker is computed on the GPU, and transferred back to the CPU. Even with the transfer overhead, 20-25x speed is obtained using an Nvidia 560Ti GPU compared to a serial implementation on an Intel Core i7 3.2GHz processor. The specific speedup depends on the number of wake turns and discretization chosen. As the number of wake markers increases, the speedup offered by this implementation increases, since the transfer overhead (scaling with N, the number of particles) diminishes in comparison to the cost of induced velocity computations (scaling with N^2). Additional savings may be obtained, depending on the problem size, by using shared memory storage to reduce memory access latency.

C Implementation Details - Beam Theory

The third Euler angle θ_1 used to determine the $\mathbf{T}_{DU}$ matrix is given by

$$\theta_1 \quad = \quad \theta_t \; + \; \phi \; - \; \int_0^r \; \xi_1^+ \; w^+ \; dr$$

- θ_t represents the beam geometric twist, obtained from the input data from table look-up
- ϕ is the elastic twist of the beam and w^+ the spatial derivative of the flap deflection, obtained from the shape functions and nodal degrees of freedom
- ξ_1^+ is obtained as follows from Eqs. (2.35)

$$\begin{aligned} w^+ &= \sin\beta_1 \\ \Rightarrow \quad \beta_1^+ &= \frac{w^{++}}{\cos\beta_1} \\ v^+ &= \sin\xi_1 \; \cos\beta_1 \\ \Rightarrow \quad v^{++} &= \cos\xi_1 \cos\beta_1 \; \xi_1^+ \; - \; \sin\xi_1 \; \sin\beta_1 \; \beta_1^+ \\ \xi_1^+ &= \frac{v^{++} \; + \; \sin\xi_1 \; \sin\beta_1 \; \beta_1^+}{\cos\xi_1 \; \cos\beta_1} \end{aligned}$$

Differentiate Eq. (2.44) once with respect to time to obtain

$$\dot{\theta}_1 \quad = \quad \dot{\phi} \; - \; \int_0^r \; \left(\xi_1^+ \; \dot{w}^+ \quad + \quad \dot{\xi}_1^+ \; w^+ \right) \; dr$$

The time derivatives $\dot{\xi}_1^+$ can be obtained by differentiating the expression for β_1^+ and ξ^+ above once with respect to time

$$\begin{aligned}
\dot{\beta}_1^+ &= \frac{\dot{w}^{++} + \beta_1^+ \dot{\beta}_1 \sin\beta_1}{\cos\beta_1} \\
\dot{\xi}_1^+ &= \frac{1}{\cos\xi_1 \cos\beta_1}\Big[\dot{v}^{++} + \dot{\beta}_1^+ \sin\xi_1 \sin\beta_1 + \sin\xi_1 \cos\beta_1 \left(\beta_1^+ \dot{\beta}_1 + \xi_1^+ \dot{\xi}_1\right) \\
&\qquad + \cos\xi_1 \sin\beta_1 \left(\beta_1^+ \dot{\xi}_1 + \xi_1^+ \dot{\beta}_1\right)\Big]
\end{aligned}$$

Differentiate Eq. (2.44) twice with respect to time to obtain

$$\ddot{\theta}_1 = \ddot{\phi} - \int_0^r \left(\xi_1^+ \ddot{w}^+ + \ddot{\xi}_1^+ w^+ + 2\,\dot{\xi}_1^+ \dot{w}^+\right) dr$$

The term $\ddot{\xi}_1^+$ is obtained by differentiating the expressions for $\dot{\beta}_1^+$ and $\dot{\xi}_1^+$ once with respect to time to obtain

$$\begin{aligned}
\ddot{\beta}_1^+ &= \frac{\ddot{w}^{++} + \beta_1^+ \ddot{\beta}_1 \sin\beta_1 + 2\,\dot{\beta}_1 \dot{\beta}_1^+ \sin\beta_1 + \beta_1^+ \dot{\beta}_1^2 \cos\beta_1}{\cos\beta_1} \\
\ddot{\xi}_1^+ &= \frac{1}{\cos\xi_1 \cos\beta_1}\Big[\ddot{v}^{++} + \sin\xi_1 \cos\beta_1 \left(2\,\dot{\xi}_1 \dot{\xi}_1^+ + 2\,\dot{\beta}_1 \dot{\beta}_1^+ + \ddot{\beta}_1 \beta_1^+ + \ddot{\xi}_1 \xi_1^+\right) \\
&\qquad + \cos\xi_1 \sin\beta_1 \left(2\,\dot{\beta}_1 \dot{\xi}_1^+ + 2\,\dot{\xi}_1 \dot{\beta}_1^+ + \ddot{\xi}_1 \beta_1^+ + \ddot{\beta}_1 \xi_1^+\right) \\
&\qquad + \sin\xi_1 \sin\beta_1 \left(\ddot{\beta}_1^+ - \dot{\beta}_1^2 \beta_1^+ - 2\,\dot{\beta}_1 \xi_1^+ \dot{\xi}_1 - \beta_1^+ \dot{\xi}_1^2\right) \\
&\qquad + \cos\xi_1 \cos\beta_1 \left(2\,\dot{\beta}_1 \dot{\xi}_1 \beta_1^+ + \dot{\xi}_1^2 \xi_1^+ + \dot{\beta}_1^2 \xi_1^+\right)\Big]
\end{aligned}$$

Finally, $\dot{\beta}_1$, $\ddot{\beta}_1$, $\dot{\xi}_1$ and $\ddot{\xi}_1$ are obtained by differentiating the expressions for w^+ and v^+ with respect to time

$$\begin{aligned}
\dot{\beta}_1 &= \frac{\dot{w}^+}{\cos\beta_1} \\
\dot{\xi}_1 &= \frac{\dot{v}^+ + \sin\xi_1 \sin\beta_1 \dot{\beta}_1}{\cos\xi_1 \cos\beta_1} \\
\ddot{\beta}_1 &= \frac{\ddot{w}^+ + \dot{\beta}_1^2 \sin\beta_1}{\cos\beta_1} \\
\ddot{\xi}_1 &= \frac{\ddot{v}^+ + \sin\xi_1 \cos\beta_1 \left(\dot{\xi}_1^2 + \dot{\beta}_1^2\right) + 2\,\dot{\xi}_1 \dot{\beta}_1 \cos\xi_1 \sin\beta_1 + \ddot{\beta}_1 \sin\xi_1 \sin\beta_1}{\cos\xi_1 \cos\beta_1}
\end{aligned}$$

Numerical Integration

The external loads on rotating and non-rotating beams are integrated numerically along the span of the blades to determine the forces and moments transmitted to the hub. These integrals are computed numerically using Gaussian Quadrature using weighted summation of the integrand values at specific points along the span.

$$\mathbf{I} \quad = \quad \int f(r)\ dr$$

I denotes the integral, f the integrand and r the spanwise coordinate along the deformed elastic axis. Using numerical quadrature,

$$\mathbf{I} \quad \approx \quad \sum_{i=1}^{n} w_i\ f(r_i)$$

The points r_i are the zeros of the Legendre polynomials, which obey some recurrence relations. The first relation is known as Bonnet's recursion formula, given by

$$n\ P_n(x) \quad = \quad (2n-1)\ x\ P_{n-1}(x) \quad - \quad (n-1)\ P_{n-2}(x)$$

$P_n(x)$ is a Legendre polynomial of order "n", given by Rodrigues' formula

$$P_n(x) \quad = \quad \frac{1}{2^n\ n!}\ \frac{d^n}{dx^n}\ \left[\left(x^2\ -\ 1\right)^n\right]$$

Another recurrence relation is

$$\frac{x^2\ -\ 1}{n}\ \frac{dP_n(x)}{dx} \quad = \quad (2n+1)\ x\ P_n(x) \quad - \quad n\ P_{n-1}(x)$$

n is the user-specified number of quadrature points. The Gauss-Legendre quadrature weights corresponding to each of the locations is given by (Ref. [110])

$$w_i \quad = \quad \frac{2}{(\ 1\ -\ x_i^2\ )\ \ [P_n{}'(x_i)]^2}$$

Using iterative convergence, the quadrature locations and the slope of the Legendre polynomial may be identified by using the recurrence relations, starting from an initial guess given by

$$x_i \quad = \quad \cos\left[\pi \frac{4i-1}{4n+2}\right] \qquad\qquad i = 1, 2, 3, \cdots, n$$

These locations are generated assuming that the integration range is $[-1, 1]$. The quadrature locations and weights may be transformed for use over other limits using a change of coordinates along x.

Intermediate Quadrature

The simulation of beam dynamics requires the computation of the accumulated external loads, from the tip to a certain location of interest. Additionally, the axial fore-shortening u and the Euler rotation angle θ_1 require the accumulated values of certain integrations from the root value to the radial location at which these quantities are evaluated. These "intermediate" integrals (so labelled because the limits lie between nodes of finite elements) are evaluated by fitting a polynomial to the sampled values of the integrand within the finite element, and integrating the *fitted* polynomial to reduce computational cost.

Assume that the integrand f is sampled at n points x_1, x_2, $\cdots$, x_n. Let the corresponding values of f at these points be f_1, f_2, $\cdots$, f_n. Let the *approximate* integrand $g(x)$ be represented using a polynomial, given by

$$f(x) \quad \approx \quad g(x) \quad = \quad \sum_{i=1}^{n} a_{i-1}\, x^{i-1}$$

The coefficients a_i, $i = 1, 2, \cdots, n$ are determined from the sampled values of the true integrand $f(x)$ at locations x_i using polynomial interpolation. If the approximate integrand matches the true integrand at $(x_1, x_2, \cdots, x_n)$ then

$$\begin{Bmatrix} f(x_1) \\ f(x_2) \\ . \\ . \\ f(x_n) \end{Bmatrix} = \begin{bmatrix} 1 & x_1 & x_1^2 & \cdots & x_1^{n-1} \\ 1 & x_2 & x_2^2 & \cdots & x_2^{n-1} \\ . & . & . & . & . \\ . & . & . & . & . \\ 1 & x_n & x_n^2 & \cdots & x_n^{n-1} \end{bmatrix} \begin{Bmatrix} a_0 \\ a_1 \\ . \\ . \\ a_{n-1} \end{Bmatrix}$$

This system of linear equations may be written as a matrix-vector product

$$\mathbf{f} = \mathbf{C}\,\mathbf{a}$$

$\mathbf{C}$ is invertible as long as all quadrature locations are unique. The polynomial coefficients $\mathbf{a}$ are obtained by inverting $\mathbf{C}$ to yield

$$\mathbf{a} = \mathbf{C}^{-1}\,\mathbf{f}$$

The approximate integrand may be integrated along the span of the element using different limits, depending on the quantity of interest. For displacement quantities (Euler rotation θ_1 and axial fore-shortening u) the integration limits are from the left end of the element to the quadrature point of interest. The integrated value is

$$\mathrm{I}_{\mathrm{inboard}}(x_1) = \int_0^{r_1} g(r_1)\, dr_1 = \frac{dr}{dx} \sum_{i=1}^{n} a_{i-1}\, \frac{x_1^i}{i}$$

$\frac{dr}{dx}$ represents the scale factor between the non-dimensional coordinate x and the dimensional coordinate r. The summation may be written as a matrix-vector product

$$\mathrm{I}_{\mathrm{inboard}}(x_1) \quad = \quad \frac{dr}{dx} \quad \left\{ x_1 \quad \tfrac{1}{2}x_1^2 \quad \cdots \quad \tfrac{1}{n-1}x_1^{n-1} \right\} \left\{ \begin{array}{c} a_0 \\ a_1 \\ . \\ . \\ a_{n-1} \end{array} \right\}$$

Using the same notation for the integrals at the other quadrature points, we obtain

$$\left\{ \begin{array}{c} \mathrm{I}(x_1) \\ \mathrm{I}(x_2) \\ . \\ . \\ \mathrm{I}(x_n) \end{array} \right\}_{\mathrm{inboard}} = \frac{dr}{dx} \left[\begin{array}{cccc} x_1 & \tfrac{1}{2}x_1^2 & \cdots & \tfrac{1}{n-1}x_1^{n-1} \\ x_2 & \tfrac{1}{2}x_2^2 & \cdots & \tfrac{1}{n-1}x_2^{n-1} \\ . & . & . & . \\ . & . & . & . \\ x_n & \tfrac{1}{2}x_n^2 & \cdots & \tfrac{1}{n-1}x_n^{n-1} \end{array} \right] \left\{ \begin{array}{c} a_0 \\ a_1 \\ . \\ . \\ a_{n-1} \end{array} \right\}$$

The vector of integrals $\mathbf{I}$ may be written as another matrix vector product as

$$\mathbf{I}_{\mathrm{inboard}} \quad = \quad \frac{dr}{dx}\, \mathbf{E}\, \mathbf{a} \quad = \quad \frac{dr}{dx}\, \mathbf{E}\, \mathbf{C}^{-1}\, \mathbf{f}$$

Similarly, the vector of integrals with limits from the current radial position to the outboard end of the finite element is

$$\mathbf{I}_{\mathrm{outboard}} \quad = \quad \frac{dr}{dx}\, \mathbf{F}\, \mathbf{C}^{-1}\, \mathbf{f}$$

The entries in row i and column j of $\mathbf{E}$ and $\mathbf{F}$ are

$$E(i,j) \quad = \quad E_{ij} \quad = \quad \frac{1}{j} x_i{}^j \qquad \text{and} \qquad F(i,j) \quad = \quad F_{ij} \quad = \quad \frac{1}{j}\left(1 - x_i{}^j\right)$$

The matrices $\mathbf{E}\, \mathbf{C}^{-1}$ and $\mathbf{F}\, \mathbf{C}^{-1}$ are independent of loads and can be pre-computed.

The term $\frac{dr}{dx}$ is the dimensional length of the finite element l_e.

Bibliography

[1] R. E. Malatino, "U.S. Navy Helicopter Operational Flight Spectrum Survey Program - Past and Present," in *AGARD Specialists Meeting on Helicopter Design Mission Load Spectra*, no. CP-206, August 1976.

[2] J. A. Miller, "Airship Mine Countermeasure System - The Cost Effective Solution," in *AIAA Lighter-Than-Air Systems Technology Conference, 10th*, vol. 14, 1993.

[3] T. R. Weber, "An Analysis of Lemmings: A Swarming Approach to Mine Countermeasures in the VSW/SZ/BZ," Master's thesis, The Naval Postgraduate School, Monterey, CA, 1995.

[4] K. L. Schmitz, "LCAC versus LCU: Are LCAC Worth the Expenditure," tech. rep., DTIC Document, 1996.

[5] T. H. Choi, "Out of Sight, Out of Mind: The United States Navy and Mine Warfare in the 21st Century," Master's thesis, Center for Military and Strategic Studies, 2013.

[6] "MH-60S Airborne Mine Counter-Measures Continues Development." `http://www.mccaskill.senate.gov/ndaa/Supporting%20Docs/67%20-%20Franks/MH-60S%20Airborne%20Mine%20Counter-Measures%20Continues%20Development.html`, Nov 2011.

[7] Anonymous, "General Helicopter Discussions." `http://www.justhelicopters.com/COMMUNITY/JHFORUMS/JHAlternateForum/tabid/180/forumid/1/postid/20106/view/topic/Default.aspx`, 2009.

[8] W. Archaeology, "Sidescan Sonar." `http://ets.wessexarch.co.uk/recs/how-we-study-the-seafloor/geophysical-survey/`, 2010.

[9] M. C. Staff Sgt. Cooley, "664th Ordn Co Conducts Sling Load Training." `http://www.forthoodsentinel.com/story.php?id=6073`, 2011.

[10] D. H. Hodges and E. H. Dowell, "Nonlinear Equations of Motion for the Elastic Bending and Torsion of Twisted Nonuniform Rotor Blades," Tech. Rep. TN D-7818, NASA, December 1974.

[11] A. Rosen and P. P. Friedmann, "Nonlinear Equations of Equilibrium for Elastic Helicopter or Wind Turbine Blades undergoing Moderate Deformation," Tech. Rep. CR 159478, NASA, December 1978.

[12] D. H. Hodges, R. A. Ormiston, and D. A. Peters, "On the Nonlinear Deformation Geometry of Euler-Bernoulli Beams," Tech. Rep. 1566/80-A-1, NASA/AVRADCOM, April 1980.

[13] W. Johnson, "Aeroelastic Analysis for Rotorcraft in Flight or in a Wind Tunnel," Tech. Rep. TN D-8515, NASA, 1977.

[14] R. Celi and P. P. Friedmann, "Rotor Blade Aeroelasticity in Forward Flight with an Implicit Aerodynamic Formulation," *AIAA Journal*, vol. 26, no. 2, pp. 1425–1433, 1988.

[15] R. Celi, "Helicopter Rotor Blade Aeroelasticity in Forward Flight with an Implicit Structural Formulation," *AIAA Journal*, vol. 30, no. 9, pp. 2274–2282, 1992.

[16] D. L. Kunz, "Survey and Comparison of Engineering Beam Theories for Helicopter Rotor Blades," *Journal of Aircraft*, vol. 31, no. 3, pp. 473–479, 1994.

[17] D. H. Hodges, "A Mixed Variational Formulation Based on Exact Intrinsic Equations for Dynamics of Moving Beams," *International Journal of Solids and Structures*, vol. 26, no. 11, pp. 1253–1273, 1990.

[18] D. H. Hodges, H. Saberi, and R. A. Ormiston, "Development of Nonlinear Beam Elements for Rotorcraft Comprehensive Analyses," *Journal of the American Helicopter Society*, vol. 52, no. 1, pp. 36–48, January 2007.

[19] A. Datta, *Fundamental Understanding, Prediction and Validation of Rotor Vibratory Loads in Steady Level Flight*. PhD thesis, University of Maryland, 2004.

[20] M. Ribera, *Helicopter Flight Dynamics Simulation with a Time-Accurate Free-Vortex Wake Model*. PhD thesis, University of Maryland, 2007.

[21] A. Abhishek, *Analysis, Validation, Prediction and Fundamental Understanding of Rotor Blade Loads in an Unsteady Maneuver*. PhD thesis, University of Maryland, 2010.

[22] W. Johnson, "Rotorcraft Aerodynamics Models for a Comprehensive Analysis," in *54^{th} Annual National Forum of the American Helicopter Society*, AHS, May 1998.

[23] H. Saberi, K. M, R. A. Ormiston, and M. J. Rutkowski, "Overview of RCAS and Application to Advanced Rotorcraft Problems," in *American Helicopter Society 4th Decennial Specialist's Conference on Aeromechanics*, January 2004.

[24] J. M. Wang and T. R. Norman, "Correlation of Flatwise and Chordwise Bending Moments for a Sikorsky Full-Scale Bearingless Main Rotor," in *American Helicopter Society 3rd Decennial Specialist's Conference on Aeromechanics*, Jan 1994.

[25] R. Sopher and D. W. Hallock, "Time-History Analysis for Rotorcraft Dynamics Based on a Component Approach," *Journal of the American Helicopter Society*, vol. 31, no. 1, 1986.

[26] J. J. Howlett, "UH-60A Black Hawk Engineering Simulation Program: Volume I - Mathematical Model," Tech. Rep. CR 166309, NASA, December 1981.

[27] J. G. Leishman, *Principles of Helicopter Aerodynamics*. Cambridge University Press, 2002.

[28] H. Werle, "On the Flow of Fluids Made Visible," *Leonardo*, vol. 8, no. 4, pp. 329–331, 1975.

[29] D. M. Pitt and D. A. Peters, "Theoretical Prediction of Dynamic Inflow Derivatives," *Vertica*, vol. 5, pp. 21–34, 1987.

[30] C. He and D. A. Peters, "Comparison of Measured Induced Velocities with Results from a Closed-form Finite State Wake Model in Forward Flight," in *45th Annual National Forum of the American Helicopter Society*, AHS, May 1989.

[31] A. J. Landgrebe, "An Analytical Method for Predicting Rotor Wake Geometry," *Journal of the American Helicopter Society*, vol. 14, no. 4, pp. 20–32, October 1969.

[32] A. J. Landgrebe, "The Wake Geometry of a Hovering Rotor and its Influence on Rotor Performance," *Journal of the American Helicopter Society*, vol. 17, no. 4, pp. 2–15, October 1972.

[33] M. P. Scully, "A Method of Computing Helicopter Vortex Wake Distortion," Tech. Rep. ASRL TR 138-1, MIT, June 1967.

[34] J. D. Kocurek and B. L. F, "Velocity Computing : A New Concept or Hover and Axial Flow Wake Analysis and Design," Tech. Rep. CP-334, AGARD, May 1982.

[35] T. S. Beddoes, "A Wake Model for High Resolution Airloads," in *2nd International Conference on Basic Rotorcraft Research*, 1985.

[36] A. Bagai and J. G. Leishman, "Free-Wake Analysis of Tandem, Tilt-Rotor and Coaxial Rotor Configurations," *Journal of the American Helicopter Society*, vol. 41, no. 3, pp. 196–207, July 1996.

[37] W. Johnson, "Wake Model for Helicopter Rotors in High Speed Flight," Tech. Rep. CR 177507, NASA, November 1988.

[38] W. Johnson, "A General Free Wake Geometry Calculation for Wings and Rotors," in *51st Annual National Forum of the American Helicopter Society*, AHS, May 1995.

[39] C. Theodore, *Helicopter Flight Dynamic Simulation with Refined Aerodynamic Modeling*. PhD thesis, University of Maryland, 2000.

[40] F. Kim, *Formulation and Validation of High-Order Mathematical Models of Helicopter Flight Dynamics*. PhD thesis, University of Maryland, 1991.

[41] S. R. Turnour, *Flight Dynamics Modeling of Hingeless and Bearingless Rotor Helicopters*. PhD thesis, University of Maryland, 1996.

[42] A. Bagai, *Contributions to the Mathematical Modeling of Rotor Flow-Fields using a Pseudo-Implicit Free-Wake Analysis*. PhD thesis, University of Maryland, 1995.

[43] D. Fusato, *Design Sensitivity Analysis and Optimization for Helicopter Handling Qualities Improvement*. PhD thesis, University of Maryland, 2002.

[44] M. J. Bhagwat, *Mathematical Modeling of the Transient Dynamics of Helicopter Rotor Wakes Using a Time-Accurate Free-Vortex Method*. PhD thesis, University of Maryland, 2001.

[45] D. A. Wachspress, T. R. Quackenbush, and B. A. H, "Rotorcraft Interactional Aerodynamics with Fast Vortex/Fast Panel Methods," *Journal of the American Helicopter Society*, vol. 48, no. 4, pp. 223–235, October 2003.

[46] "Flight Lab." `http://www.flightlab.com/flightlab.html`, Feb 2008.

[47] T. Ronen, *Dynamics of a Helicopter with a Sling Load*. PhD thesis, Stanford University, 1985.

[48] V. Sahasrabuddhe, A. Faynberg, M. Pozdin, R. Cheng, M. B. Tischler, A. Stumm, and M. Lavin, "Balancing CH-53K Handling Qualities and Stability Margin Requirements in the Presence of Heavy External Loads," in *63rd Annual National Forum of the American Helicopter Society*, May 2007.

[49] L. S. Cicolani and M. G. E. Ehlers, "Modeling and Simulation of a Helicopter Slung Load Stabilization Device," in *58th Annual National Forum of the American Helicopter Society*, June 2002.

[50] B. Gassaway, K. Strope, L. Cicolani, J. Lusardi, C. He, and D. Robinson, "Predictive Capabilities of a UH-60 FLIGHTLAB ® Model with an External Sling Load," in *62nd Annual National Forum of the American Helicopter Society*, May 2006.

[51] J. A. Lusardi, C. L. Blanken, and M. S. R. Braddom, "UH-60 External Load Handling Qualities Evaluation," in *35th European Rotorcraft Forum*, September 2009.

[52] D. Fusato, G. Guglieri, and R. Celi, "Flight Dynamics of an Articulated Rotor Helicopter with an External Slung Load," *Journal of the American Helicopter Society*, vol. 46, no. 1, pp. 3–13, 2001.

[53] R. H. Hoh, R. K. Heffley, and D. G. Mitchell, "Development of Handling Qualities Criteria for Rotorcraft with Externally Slung Loads," Tech. Rep. CR-2006-213488, NASA, October 2006.

[54] J. A. Lusardi, C. L. Blanken, L. S. R. Braddom, L. S. Cicolani, and E. L. Tobias, "Development of External Load Handling Qualities Criteria for Rotorcraft," in *66th Annual National Forum of the American Helicopter Society*, May 2010.

[55] R. A. Skop and Y.-I. Choo, "The Configuration of a Cable Towed in a Circular Path," *Journal of Aircraft*, vol. 8, no. 11, pp. 856–862, November 1971.

[56] J. J. Russell and W. J. Anderson, "Equilibrium and Stability of a Circularly Towed Cable Subject to Aerodynamic Drag," *Journal of Aircraft*, vol. 14, no. 7, pp. 680–686, July 1977.

[57] P. Lapthorne, *Experimental Studies on Circularly Towed Aerial Tethers*. PhD thesis, RMIT University, 2012.

[58] D. Sgarioto, *Non-linear Dynamic Modeling and Optimal Control of Aerial Tethers for Remote Delivery and Capture of Payloads*. PhD thesis, RMIT University, 2006.

[59] J. E. Cochran Jr, M. Innocenti, T. S. No, and A. Thukral, "Dynamics and Control of Maneuverable Towed Flight Vehicles," *Journal of Guidance, Control and Dynamics*, vol. 15, no. 5, pp. 1245–1252, 1992.

[60] A. S. Bourmistrov, R. D. Hill, and P. Riseborough, "Nonlinear Control Law for Aerial Towed Target," *Journal of Guidance, Control and Dynamics*, vol. 18, no. 6, pp. 1232–1238, 1995.

[61] P. Williams, D. Sgarioto, and P. Trivailo, "Optimal Control of an Aircraft-Towed Flexible Cable System," *Journal of Guidance, Control and Dynamics*, vol. 29, no. 2, pp. 401–410, 2006.

[62] E. H. Handler, "The Helicopter-Towed Hydrofoil Sea Pallet," *Journal of the American Helicopter Society*, vol. 6, no. 3, pp. 22–26, July 1961.

[63] H. Xin and C. He, "A High Fidelity Simulation Model for Comprehensive Analysis of Rotorcraft Towing Operations," in *59th Annual National Forum of the American Helicopter Society*, AHS, 2003.

[64] LCDR J. R. Kennedy, "Helicopter Tow Tests of the U.S. Coast Guard's Air Delivery Container for Oil Spill Containment Barrier," Tech. Rep. NCSL 198-73, U.S. Naval Coastal Systems Laboratory, December 1973.

[65] L. R. M. Larrabee and R. Ward, "Fast Surface Delivery System for Pollution Response Equipment," in *International Oil Spill Conference*, no. 1, pp. 417–421, March 1977.

[66] LCDR J. E. Ludwig, LT F F. A. Pinegar, LCDR G. Serotsky, J. H. Edris and G. E. Clark, "Development of a Tow Capability for the HH-3F Helicopter," Tech. Rep. CG-D-51-76, U.S. Naval Air Test Center, April 1976.

[67] A. G. Strandhagen and C. F. Thomas, "Dynamics of Towed Underwater Vehicles," Tech. Rep. 219, U.S. Navy Mine Defense Laboratory, November 1963.

[68] R. L. Huston and J. W. Kamman, "Validation of Finite Segment Cable Models," *Journal of Computers and Structures*, vol. 15, no. 6, pp. 653–660, 1982.

[69] S. Huang, "Dynamic Analysis of Three-Dimensional Marine Cables," *Ocean Engineering*, vol. 21, no. 6, pp. 587–605, 1994.

[70] J. W. Kamman and R. L. Huston, "Modeling of Variable Length Towed and Tethered Cable Systems," *Journal of Guidance, Control and Dynamics*, vol. 22, no. 4, pp. 602–608, August 1999.

[71] R. K. Knutson and K. C. Eisenberg, "At-Sea Hydrodynamic Evaluation of Bare Double-Armored Tow Cables," Tech. Rep. R025967, David Taylor Research Center, July 1991.

[72] J. V. Sanders, "A Three-Dimensional Dynamic Analysis of a Towed System," *Ocean Engineering*, vol. 9, no. 5, pp. 483–499, 1982.

[73] T. N. Delmer, T. C. Stephens, and J. M. Coe, "Numerical Simulation of Towed Cables," *Ocean Engineering*, vol. 10, no. 2, pp. 119–132, 1983.

[74] J. W. Schram and S. P. Reyle, "A Three-Dimensional Dynamic Analysis of a Towed System," *Journal of Hydronautics*, vol. 2, no. 4, pp. 213–220, October 1968.

[75] F. Milinazzo, M. Wilkie, and S. A. Latchman, "An Efficient Algorithm for Simulating the Dynamics of Towed Cable Systems," *Ocean Engineering*, vol. 14, no. 6, pp. 513–526, 1987.

[76] C. M. Ablow and S. Schechter, "Numerical Simulation of Undersea Cable Dynamics," *Ocean Engineering*, vol. 10, no. 6, pp. 443–457, 1983.

[77] T. N. Delmer, T. C. Stephens, and J. A. Temills, "Numerical Simulation of Cable-Towed Acoustic Arrays," *Ocean Engineering*, vol. 15, no. 6, pp. 511–548, 1988.

[78] L. Petzold, "Automatic Selection of Methods for Solving Stiff and Nonstiff Systems of Ordinary Differential Equations," Tech. Rep. SAND80-8230, Sandia National Laboratory, 1980.

[79] F. R. Driscoll, R. G. Lueck, and M. Nahon, "Development and Validation of a Lumped-Mass Dynamics Model of a Deep-Sea ROV System," *Applied Ocean Research*, vol. 22, pp. 169–182, 2000.

[80] C. Evangelinos, D. Lucor, C. H. Su, and G. E. Karniadakis, "Flow-Induced Vibrations of Non-Linear Cables. Part I: Models and Algorithms," *International Journal for Numerical Methods in Engineering*, vol. 55, pp. 535–556, 2002.

[81] C. T. Howell, *Investigation of the Dynamics of Low-Tension Cables*. PhD thesis, Massachusetts Institute of Technology, 1992.

[82] A. A. Tjavaras, *The Dynamics of Highly Extensible Cables*. PhD thesis, Massachusetts Institute of Technology, 1996.

[83] J. I. Gobat and M. A. Grosenbaugh, "Time-domain Numerical Simulation of Ocean Cable Structures," *Ocean Engineering*, vol. 33, no. 10, pp. 1373–1400, 2006.

[84] M. A. Grosenbaugh, "Transient Behavior of Towed Cable Systems during Ship Turning Maneuvers," *Ocean Engineering*, vol. 35, no. 11-12, pp. 1532–1542, 2007.

[85] K. J. Horton, C. M. Ferrer, K. P. Watson, and D. Charvoz, "Measurements of the Hydrodynamic Force and Strum Characteristics of Stranded Cables," Tech. Rep. NCSC TM 471-87, Naval Coastal Systems Center, Panama City, Florida, December 1987.

[86] M. Seto, G. Watt, and D. Hopkin, "A Fully Interactive Dynamic Simulation of a Semi-submersible Towing a Large Towfish," in *OCEANS'99 MTS/IEEE. Riding the Crest into the 21st Century*, vol. 3, IEEE, 1999.

[87] B. Buckham, M. Nahon, M. Seto, X. Zhao, and C. Lamber, "Dynamics and Control of a Towed Underwater Vehicle System, part I: Model Development," *Ocean Engineering*, vol. 30, no. 3, pp. 453–470, 2003.

[88] B. Buckham, M. Nahon, M. Seto, X. Zhao, and C. Lamber, "Dynamics and Control of a Towed Underwater Vehicle System, part II: Model Validation and Turn Maneuver Optimization," *Ocean Engineering*, vol. 30, no. 4, pp. 471–485, 2003.

[89] E. Kreyszig, "Advanced Engineer Mathematics," 1997.

[90] W. Johnson, *Helicopter Theory*. Dover Books on Aeronautical Engineering Series, Dover Publications, 1994.

[91] R. T. N. Chen, "A Survey of Nonuniform Inflow Models for Rotorcraft Flight Dynamics and Control Applications," Tech. Rep. Technical Memorandum 102219, NASA, November 1989.

[92] S. Ananthan, *Analysis of Rotor Wake Aerodynamics During Maneuvering Flight Using a Free-Vortex Wake Methodology*. PhD thesis, University of Maryland, 2006.

[93] D. A. Wachspess and T. R. Quackenbrush, "BVI Noise Predictions Using a Comprehensive Rotorcraft Analysis," in *57th Annual National Forum of the American Helicopter Society*, May 2001.

[94] S. Gupta and J. G. Leishman, "Accuracy of the Induced Velocity of Wind Turbine Wakes using Vortex Segmentation," in *23rd ASME Wind Energy Symposium and the 42nd AIAA Aerospace Sciences Meeting*, January 2004.

[95] P. G. Saffman, *Vortex Dynamics*. Cambridge University Press, 1992.

[96] F. J. Bailey, "A Simplified Theoretical Method of Determining the Characteristics of a Lifting Rotor in Forward Flight," Tech. Rep. 716, NACA, 1941.

[97] M. B. Tischler, "Flight Dynamics Analysis and Simulation of Heavy Lift Airships," Tech. Rep. TM-166471, NASA, December 1982.

[98] R. Celi, "Implementation of Rotary-Wing Aeromechanical Problems Using Differential-Algebraic Equation Solvers," *Journal of the American Helicopter Society*, vol. 45, no. 4, pp. 253–262, October 2000.

[99] R. Celi, "Helicopter Rotor Dynamics in Coordinated Turns," *Journal of the American Helicopter Society*, vol. 36, no. 4, pp. 39–47, October 1991.

[100] J. J. More, B. S. Garbow, and K. E. Hillstrom, "User's Guide for MINPACK-1," Tech. Rep. ANL-80-74, Argonne National Laboratory, August 1980.

[101] J. Alfred, "Rotorcraft Brownout Mitigation through Flight Path Optimization using a High-Fidelity Rotorcraft Simulation Model," Master's thesis, University of Maryland, 2012.

[102] D. E. Kirk, *Optimal Control Theory : An Introduction*. Prentice-Hall, USA, 1970.

[103] K. E. Brenan, S. L. Campbell, and L. R. Petzold, *The Numerical Solution of Iniitial Value Problems in Differential-Algebraic Equations*. Elsevier Science Publishing Co., 1989.

[104] J. M. Gere and S. P. Timoshenko, *Mechanics of Materials*. Springer, 1991.

[105] S. J. Davis, "Predesign Study for a Modern 4-Bladed Rotor for the RSRA," Tech. Rep. CR 166155, NASA, March 1981.

[106] H. Yeo, W. G. Bousman, and W. Johnson, "Performance Analysis of a Utility Helicopter with Standard and Advanced Rotors," *Journal of the American Helicopter Society*, vol. 49, no. 3, pp. 250–270, 2004.

[107] R. Celi, "Optimization-Based Inverse Simulation of a Helicopter Slalom Maneuver," *Journal of Guidance, Control and Dynamics*, vol. 23, no. 2, pp. 289–297, 2000.

[108] J. Tritschler, *Contributions to the Characterization and Mitigation of Rotorcraft Brownout*. PhD thesis, University of Maryland, 2012.

[109] S. Hersey, A. Sridharan, and R. Celi, "Multiobjective Performance Optimization of a Coaxial Compound Rotorcraft Configuration," in *Fifth Decennail AHS Aeromechanics Specialists Conference, San Francisco, CA*, no. 1, Jan 2014.

[110] M. Abramowitz and I. A. Stegun, *Handbook of Mathematical Functions with Formulas, Graphs, and Mathematical Tables*, vol. 55 of *National Bureau of Standards Applied Mathematics Series*. Superintendent of Documents, U.S. Government Printing Office, Washington, D.C., 1964.